THÈSE DE DOCTORAT

de l'Université de recherche Paris Sciences et Lettres
PSL Research University

Préparée au Laboratoire de Géologie de l'École Normale Supérieure de Paris

Extensional collapses in the overpressured frictional upper crust based on Limit Analysis

Ecole doctorale n°560

École Doctorale des Sciences de la Terre

Spécialité Sciences de la Terre et de l'environnement

COMPOSITION DU JURY :

M. MOURGUES Régis
Univ. du Maine, Rapporteur

Mme. COOKE Michele
Univ. Massachusetts, Rapporteur

M. VENDEVILLE Bruno
Univ. Lille 1, Examinateur

M. PUBELLIER Manuel
CNRS, ENS, Examinateur

Mme. CUBAS Nadaya
UPMC, Examinateur

M. BOUZIAT Antoine
IFPEN, Invité

M. GUÉGUEN Yves
ENS, Directeur de thèse

M. MAILLOT Bertrand
Univ. Cergy-Pontoise, Directeur de thèse

Soutenue par Xiaoping YUAN
le 04 juillet 2016

Dirigée par **Yves GUÉGUEN et Bertrand MAILLOT**

PSL RESEARCH UNIVERSITY PARIS

Extensional collapses in the overpressured frictional upper crust based on Limit Analysis

Xiaoping Yuan

A thesis submitted in partial fulfilment for the
degree of Doctor of Philosophy
in the
Laboratoire de Géologie,
École Normale Supérieure, Paris

Soutenance prévue le 4 juillet 2016
au laboratoire de Géologie de l'École normale supérieure

Yves Guéguen (Pr. ENS) ..... Directeur de thèse
Bertrand Maillot (Pr. Univ. Cergy-Pontoise) Directeur de thèse
Régis Mourgues (Pr. Univ. du Maine) ..... Rapporteur
Michele Cooke (Pr. Univ. Massachusetts) ..... Rapporteur
Bruno Vendeville (Pr. Univ. Lille 1) ..... Examinateur
Manuel Pubellier (D.R. CNRS, ENS) ..... Examinateur
Nadaya Cubas (M.C. UPMC) ..... Examinateur
Antoine Bouziat (Ingénieur IFPEN) ..... Invité

Abstract

There are many studies on structural geology in compressive contexts (e.g. fold-and-thrust belts, accretionary wedges and mountain building) in last several decades, from field geology study, sandbox analogue experiments to numerical and mechanical analyses. In contrast with the studies in compressive contexts, the contributions on extensional deformation are few although the existence of extension is widespread, especially in sedimentary basins and passive margins. The extensional deformation develops from large-scale problems such as continental rifting to small-scale landslides in the shallow depth. This manuscript uses a mechanical approach to examine the extensional failures in the frictional upper crust resulting from normal faulting. There are many interesting topics related to the extensional deformation such as (1) the roles of fluid overpressures, topographic process, material and fault properties on the stability of extensional structures; (2) the formation of low-angle and listric normal fault; (3) the deformation pattern due to slip on a low-angle fault; and (4) the influence of fault softening and sedimentation processes on this deformation pattern.

A two-dimensional kinematic approach of Limit Analysis is proposed to study two kinds of extensional collapses. The first extensional collapse is the gravity instability of a frictional cover overlying a weak, inclined detachment. The second extensional collapse is tectonic extension triggered by downdip slip on a detachment following the retreat of a back wall. The mechanical approach applied to wedge prototypes is validated by the critical Coulomb wedge (CCW) theory. Additionally, this approach generalizes the CCW theory allowing us to investigate the influence of material cohesion, fluid overpressure and complex topography on the Mejillones peninsula, Northern Chile. For example, details of the topography are responsible for a short-length scale instability corresponding to a frontal gravitational collapse. A reasonable amount of cohesion (5 MPa) leads to a stability transition with a long-length mode.

There is a sequential version of this Limit Analysis combining mechanical equilibrium and

a geometrical construction as an half-graben, to predict the extensional deformation pattern. This method opens new ways to envision the structural evolution through time resulting from normal faulting. The simulations show that the normal fault and axial surface of the half-graben are rotating during extension, forming a region of Foot-to-Hanging Wall (FHW) where the material in the footwall is sheared upon entering the hanging wall. The creation of the FHW region is illustrated by sandbox experiments and field examples. Fault softening leads to the discontinuous rotations of normal fault and axial surface, and as a result, the FHW contains internal blocks. Sedimentation slows down the rotations and thus reduces the extent of the FHW. These two processes, fault softening and sedimentation, are essential to recreate the final geometry in Southern Jeanne d'Arc Basin, offshore Newfoundland. A simple sedimentation history with a slow sedimentation rate in the Lower Jurassic followed by an increasing rate up to present time is proposed to obtain the observed single block in the FHW region bounded by two faults.

The Limit Analysis is also applied to investigate gravity instability of offshore deltas by linking down-slope compressional to up-slope extensional failures through a deep detachment. The failure in Niger Delta is widely recognized by geologists as a gravity-driven instability resulting from sedimentation overloading and fluid overpressures. On the contrary, *Bilotti and Shaw* [2005] and *Suppe* [2007; 2014] examined the stability of Niger Delta by using the CCW theory which is, by default, considering the failure in this region as compressional (or tectonic-driven) collapse. The Limit Analysis applied to the Niger Delta predicts much higher fluid pressures within the delta materials and on the detachment than the predictions from the CCW theory. For example, we predict a pore-fluid pressure in the range of 80 to 90% of the lithostatic pressure within the bulk material (Hubbert-Rubey fluid-pressure ratio $0.8 - 0.9$), and in the range 97 to 99% of the lithostatic pressure within the detachment.

Additionally, this Limit Analysis methodology is applied to investigate the shape of normal fault linking a low detachment to the surface. The formations of listric fault and low-angle normal fault are of interest because Andersonian theory predicts a normal fault dipped at $\sim 60^\circ$ in the extensional context. The low detachment is assumed to be frictional, with a lower friction angle than the frictional bulk materials. A widespread fluid pressure in sedimentary basins is introduced. The fluid pressures is assumed hydrostatic above a fluid-retention depth and overpressured below this depth. The results of Limit Analysis reveal that the low-angle

normal fault and the listric fault can be achieved in prototypes with a gently dipping surface slope ($\leq 3^{\circ}$). This type of fluid overpressure is essential in determining the shape of a normal fault. Our methodology applied to the Gulf of Mexico shows that the fault shape depends much on the dip of the detachment. For example, a detachment dipped at 5° results in a strong curved normal fault and a 17° dipped detachment leads to a bi-linear fault when the fluid-retention depth is deep. The application to Niger Delta suggests that the formation of low-angle and listric faults are resulting from a shallow fluid-retention depth.

Résumé

Dans ce manuscrit nous développons l'approche cinématique 2D du calcul à la rupture pour examiner les effondrements en extension (ou failles normales) de la croûte supérieure cassante qui résultent de surpressions de fluides. Les sujets d'intérêt liés à la déformation en extension sont (1) les roles de la pression des fluides, des processus de surface, et des propriétés des matériaux et des failles sur la stabilité des structures d'extension; (2) la formation de failles normales à faible pendage et de failles listriques; (3) la distribution de la déformation au dessus d'un glissement à faible pendage; et (4) l'influence de l'adoucissement mécanique des failles et des processus de sédimentation sur cette distribution.

Cette approche mécanique est vérifiée par la théorie du prisme critique de Coulomb, et la généralise pour étudier la topographie complexe de la péninsule de Mejillones dans le Nord du Chili. Cette approche est aussi appliquée à l'instabilité gravitaire dans le delta du Niger en reliant les structures compressives en bas de pente aux structure extensives en amont par un détachement profond. Nous prédisons des surpressions de fluides beaucoup plus élevée que celles obtenues par application du prisme de Coulomb. Enfin, cette méthodologie est appliquée à l'étude de la forme de failles normales reliant un détachement profond à la surface. Dans le cas du delta du Niger, nous montrons que les failles à faible pendage et les failles listriques impliquent que la profondeur de rétention des fluides est faible. La version séquentielle de l'analyse limite ouvre de nouvelles voies pour suivre l'évolution structurale dans le temps du jeu sur les failles normales. Les simulations montrent en particulier qu'une faille normale tourne vers des pendage plus faibles au fur et à mesure de la dénudation du mur, formant une région qui passe du mur au toit de la faille active en rotation. La prédiction de cette région est illustrée par des expériences analogiques et des exemples de terrain.

Acknowledgements[1]

After almost four years of study in France, I am appreciating too many people who gave me much support on my *Mission: Impossible*. I appreciate my supervisor, Prof. Yves M. Leroy, who helped me during my doctoral studies, teaching me the inspiration on a difficult topic and meanwhile leaving me a lot of independence. He always directs me to make sure my work is on the right track. His broad knowledge in geology, excellence in solid mechanics and research enthusiasm really open my minds in the research. I am impressed by the moments of deriving equations with him in Paris on many Saturday afternoons. I will not forget his generous invitation to TOTAL and took me to travel the Pyrénées mountain.

I also would like to thank Prof. Bertrand Maillot who helps me throughout of my doctoral work. He is always very patient to answer my questions. In order to improve my writing ability, he read though my communications, did careful corrections several times, and taught me how to improve them. He supported me to attend several international conferences, which greatly broaden my scientific horizons. I also thank Prof. Yves Guéguen for helping me to take care of the administration things. Without their insightful supervision and continuous supports, I would not have been able to complete this thesis. Their broad knowledge and kind personality have been and will be inspiring in my future work and life.

I would also like to thank the rest of my thesis committee : Manuel Pubellier, Régis Mourgues, Michele Cooke, Bruno Vendeville, Nadaya Cubas and Antoine Bouziat. I have several discussions with Manuel, Régis and Michele about the geology and mechanics which was really helpful to my thesis work. Nadaya gave me many suggestions to my research on the gravity instability by linking down-slope compressional to up-slope extensional failures.

I appreciate Prof. John Suppe (National Taiwan University) for his valuable exchanges on

[1]The research presented in this thesis was supported by the China Scholarship Council during my doctoral studies in France.

the topic of fluid overpressure in relation to the strength of upper crust in EGU2014, and his great advice for the failure mechanism in offshore deltas by email. Many thanks to Baptiste Mary who always helps me on SLAMTec when I have some technical problems. He also teaches me to develop a new version of SLAMTec in Python. I would like to thank Geoffroy Mohn for building the relationship and opening my research to Michael Nirrengarten and Prof. Gianreto Manatschal in Strasbourg.

I also thank Aurelien Nicolas, Lucas Pimienta, Aurdrey Bonelye, François Passelegue, Celine Mallet, Thomas Ferrand, Sarah Incel, Pauline Souloumiac, Jean-Baptiste Regnet, Typhaine Caer, Thibault Harlé, Romain Robert, Josselin Berthelon for the happiness that I enjoyed during my studies in France. My appreciation also goes to Prof. Huai Zhang in the University of Chinese Academy of Sciences, who gave me much help and hospitality when I was in China for visiting.

My endless love goes to my parents and sister who have always encouraged and supported me, without them I would not be here today. They give me material and spirit support, and teach me independence to complete my studies. I express my greatest gratitude to Mss Botao who has the similar experience on competing the thesis. I enjoy the moment to chat with her every day. After almost four years, she should know more on the 'triangle' of half-graben in my modelling.

Contents

1 General Introduction **5**

1.1 Geology of extensional collapses 5

1.1.1 Natural examples of gravity and tectonic extensional modes 5

1.1.2 Kinematic model in extension 8

1.1.3 Analogue modeling 10

1.2 Mechanics of extensional collapses 12

1.2.1 Fluid Pressure 13

1.2.2 The Critical Coulomb Wedge (CCW) theory 14

1.2.3 Numerical modeling 18

1.3 Methodology used here : Limit Analysis and Sequential Limit Analysis 19

1.4 Manuscript content 22

2 Tectonic and gravity extensional collapses in over-pressured cohesive and frictional wedges[2] **24**

2.1 Introduction 25

2.2 Limit analysis for extension 27

2.2.1 Prototype and collapse mechanisms 28

2.2.2 Theorem of effective virtual powers 28

2.2.3 Maximum strength theorem (MST) 30

2.3 Gravitational collapse 32

2.3.1 General stability conditions based on the MST 32

[2]Published as: Yuan, XP, Leroy YM, Maillot B. Tectonic and gravity extensional collapses in over-pressured cohesive and frictional wedges, Journal of Geophysical Research - Solid Earth, 2015, 120, doi:10.1002/2014JB011612.

2.3.2 Comparison with CCW theory . . . 34
2.3.3 The role of cohesion in a triangular wedge . . . 37
2.3.4 Experimental validation . . . 39
2.4 Tectonic extensional collapse . . . 44
2.4.1 Mechanism (1): decollement fully activated . . . 44
2.4.2 Mechanism (2): a normal fault rooting at the back-wall . . . 46
2.4.3 Mechanism (3): a normal fault and a shear plane rooting on the decollement 46
2.4.4 Comparison with CCW theory for extensional collapse . . . 47
2.4.5 Experimental validation . . . 48
2.5 Application to North Chile . . . 53
2.6 Conclusion . . . 57

3 Deformation pattern during normal faulting: a sequential limit analysis 59
3.1 Introduction . . . 60
3.2 Sequential Limit Analysis of a Homogenous Wedge under Extension . . . 62
3.3 Simulation Results and Interpretation by the CCW Theory . . . 66
3.3.1 Numerical Results for the Case of a Dry Wedge . . . 66
3.3.2 Internal Deformation Pattern for the Case of a Dry Wedge . . . 69
3.3.3 Numerical Results for the Case of an Overpressured Wedge . . . 70
3.4 Roles of Fault Softening and of Sedimentation . . . 72
3.4.1 Reference Simulations . . . 74
3.4.2 Fault Softening . . . 76
3.4.3 Sedimentation and No Fault Softening . . . 79
3.4.4 Combined Effects of Sedimentation and Fault Softening . . . 81
3.5 Application to Jeanne d'Arc Basin, Grand Banks, Newfoundland . . . 84
3.6 Conclusions . . . 89

4 Reappraisal of gravity instability conditions for offshore wedges: consequences for overpressures in the Niger Delta 92
4.1 Introduction . . . 93
4.2 Gravity instabilities with Limit Analysis . . . 95
4.2.1 General prototype . . . 95

4.2.2 Application of Limit Analysis . . . 97
4.3 Validation for an inclined layer . . . 99
4.3.1 Comparison with other analytical results . . . 101
4.3.2 Validation with sandbox experiments in fluid overpressured conditions . . . 104
4.4 Application to the offshore Niger Delta . . . 105
4.4.1 Stability conditions . . . 105
4.4.2 Stability Analysis of Niger Delta . . . 110
4.5 Concluding discussions . . . 112

5 Role of fluid overpressures on the shape of normal faults in brittle, upper crust 118

5.1 Introduction . . . 119
5.2 The prototype . . . 122
5.2.1 The velocity field . . . 125
5.2.2 The bounding of the tectonic force . . . 126
5.3 Convergence analysis and validation with slip-line theory . . . 128
5.3.1 Convergence analysis . . . 128
5.3.2 Validation with the slip-line theory . . . 130
5.4 Results of normal faulting . . . 131
5.4.1 Influence of geometries of the prototype . . . 132
5.4.2 Influence of fluid-retention depth Z_{FRD} and material cohesion . . . 135
5.5 Applications to sedimentary upper crust . . . 135
5.5.1 Faulting in NW Gulf of Mexico . . . 136
5.5.2 Faulting in offshore Niger Delta . . . 138
5.6 Concluding discussions . . . 141

6 Conclusions 144

6.1 Limit Analysis . . . 144
6.1.1 Gravity and tectonic extensional collapses . . . 144
6.1.2 Gravity instability with a resistive toe . . . 145
6.1.3 Formation of low-angle and listric normal fault . . . 145
6.2 Sequential Limit Analysis . . . 146

6.3 Perspectives 146

A Appendix for Chapter 2 **149**

1 Different fluid pressure parametrizations 149

2 Exact critical Coulomb wedge theory (ECCW) 150

B Electronic Supplement to Chapter 2 **155**

1 Theorem of virtual powers with acceleration contribution 155

2 A weak expression of Archimedes theorem 156

3 Derivation of three upper bounds 156

C Electronic Supplement to Chapter 3 **161**

1 Preliminary 161

2 The upper bound forces for three mechanisms in Section 3.3 163

3 Upper bound for a normal fault piercing the cover, Sections 3.4 and 3.5 168

4 Kinematics of hanging-wall deformation 170

5 Cross-sections of Jeanne d'Arc Basin, Section 3.5 171

6 Some results of inverse analysis for Section 3.5 172

D Appendix for Chapter 4 **173**

1 General solution of the kinematic approach of LA 173

1.1 General prototype 174

1.2 Inclined layer 175

1.3 Triangular Wedge 176

E Electronic Supplement to Chapter 4 **178**

1 Different fluid pressure parametrizations 178

2 Analytical collapse length and fault dips for an inclined layer 179

F Appendix for Chapter 5 **182**

1 Geometric relations 182

2 Velocity relations and Limit Analysis 183

Chapter 1

General Introduction

This chapter will develop as following. First, the general geological background in extension is introduced in subsection 1.1. Second, the mechanics of the extensional failure is summarized in subsection 1.2. Then, we will introduce our methodology (subsection 1.3) which was first developed in compressional settings. The final subsection will present the manuscript contents composed of four papers (one published, three in preparation).

1.1 Geology of extensional collapses

1.1.1 Natural examples of gravity and tectonic extensional modes

In this manuscript, we will study two kinds of extensional collapse modes above a weak, frictional detachment in the upper crust. One extensional collapse is gravity-driven failure due to an inclined topography above a weak detachment. This inclination can come from excessive sedimentation as seen from regional gravity shale tectonics system in SW Niger Delta [*Damuth*, 1994; *Corredor et al.*, 2005; *Mourgues et al.*, 2009], Figure 1.1a. Deformation in the overpressured delta results from gravitational thin-skinned instabilities that formed various structural zones in this region. The gravitational collapse where the slip on the detachment is toward the wedge tip is the first mechanism to be studied in the context of fluid-saturated wedges, Figure 1.1a, b. This collapse mode is also found in small-scale landslides such as the Storegga slide in Norway [*Kvalstad et al.*, 2005].

The second extensional collapse mode is the slip of wedge on a low-angle detachment fault driven by lithospheric stresses (or a regional extensional tectonic event) which is opposite to the

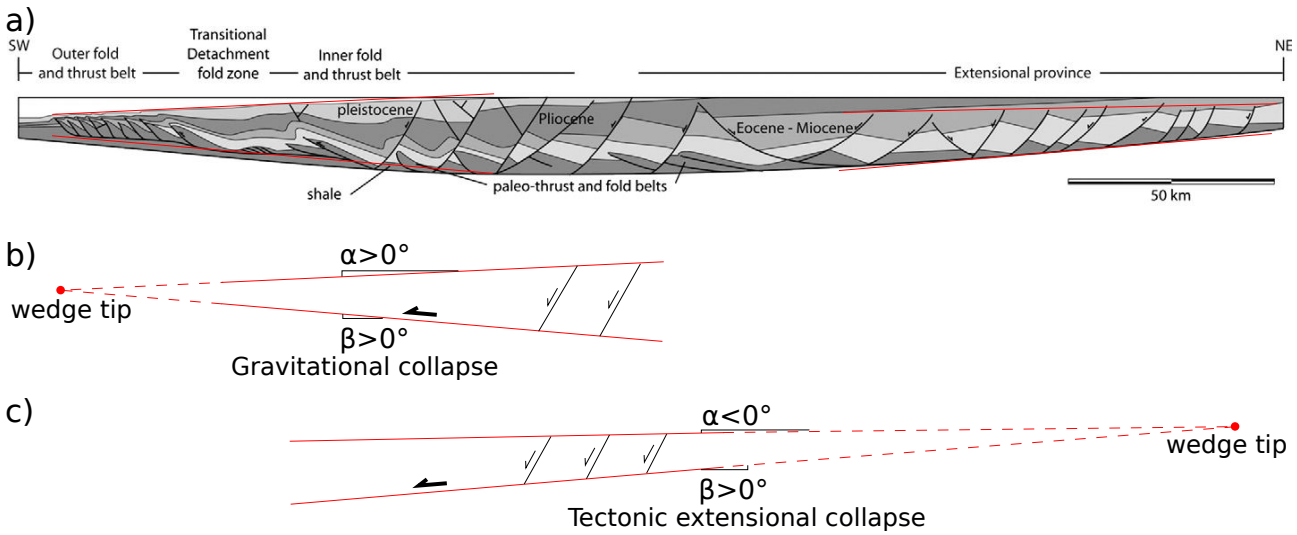


Fig. 1.1: (a) Synthetic cross-section of the regional gravity shale tectonics system in Niger Delta with the main structural zones [*Mourgues et al.*, 2009]. (b,c) Gravity and tectonic extensional collapse modes correspond to the regional tectonics in this region depending on slip direction of detachment relative to the wedge tip.

wedge tip, Figure 1.1a, c. This mode is referred to as a tectonic extensional collapse for many crustal-scale problems including the late phase deformation in the northern part of the Basin and Range province, Nevada and Utah [*Anderson et al.*, 1983], and the extensional province above a gently seaward dipped detachment in NE Niger Delta, Figure 1.1a and 1.1c. *Sorel* [2000] proposed four steps of fault sequences to illustrate the evolution process of the Corinthe rift system on a weak detachment based on seismic section of *Rigo et al.* [1996] (Figure 1.2). More impressively, the structural style in the Albuquerque Basin, New Mexico, also presents various deformation patterns resulting from normal faulting and sedimentation above a low-angle detachment due to the Rio Grande Rift [*Russell and Snelson*, 1994], as seen from cross-sections in Figure 1.3. These observations call for new theoretical developments to capture the failure onset and evolution process resulting from normal faulting and sedimentation through time.

The gravity and tectonic extensional collapses in upper crust are also found in hyper-extended, magma-poor rifted margins [*Nirrengarten et al.*, 2016]. The wedges in the upper and lower plate margins correspond respectively to the hanging wall and footwall of the detachment system, as shown in the cross-section of Porcupine basin (Figure 1.4a) and the same cross-section corrected for post-rift sediment loading and thermal subsidence (Figure 1.4b).

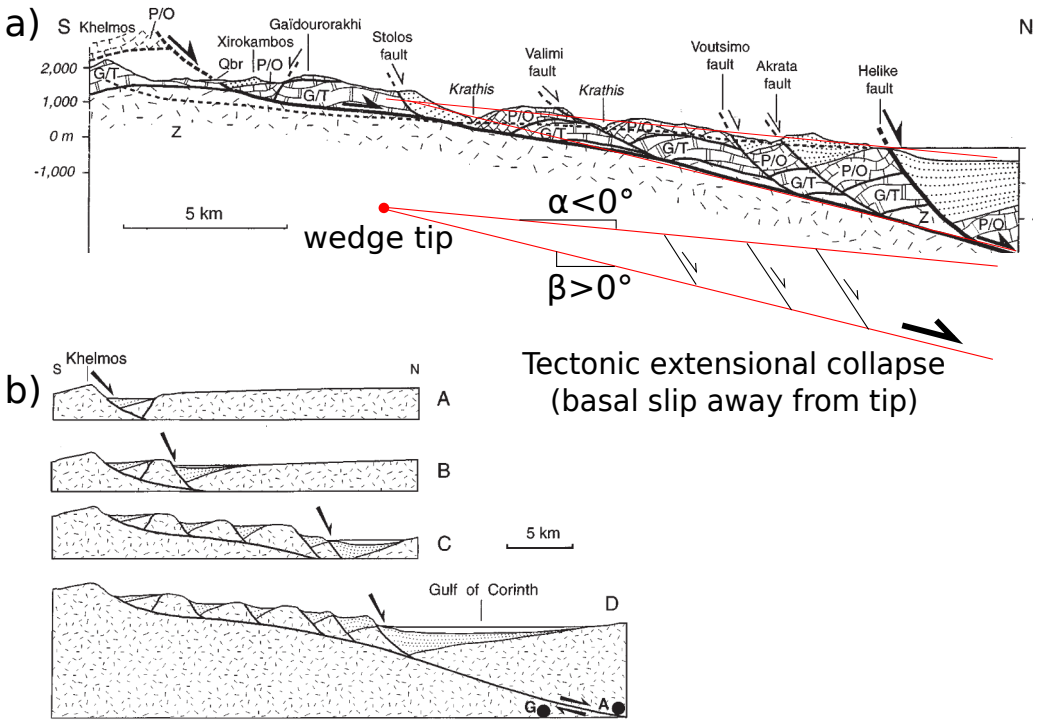


Fig. 1.2: (a) Cross-section of the Corinth-Patras rift along Krathis River, Greece [*Rigo et al.*, 1996; *Sorel*, 2000]. (b) Four step illustrations in development of the Corinth-Patras rift [*Sorel*, 2000].

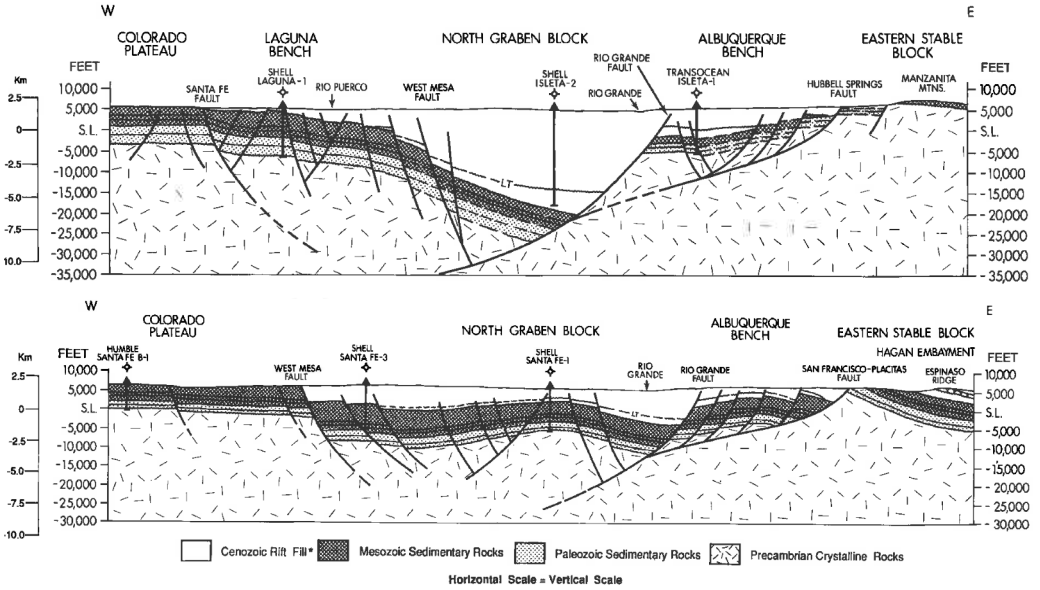


Fig. 1.3: Structural configuration in the Albuquerque Basin segment of the Rio Grande Rift showing the tectonic extensional collapse, New Mexico, USA [*Russell and Snelson*, 1994].

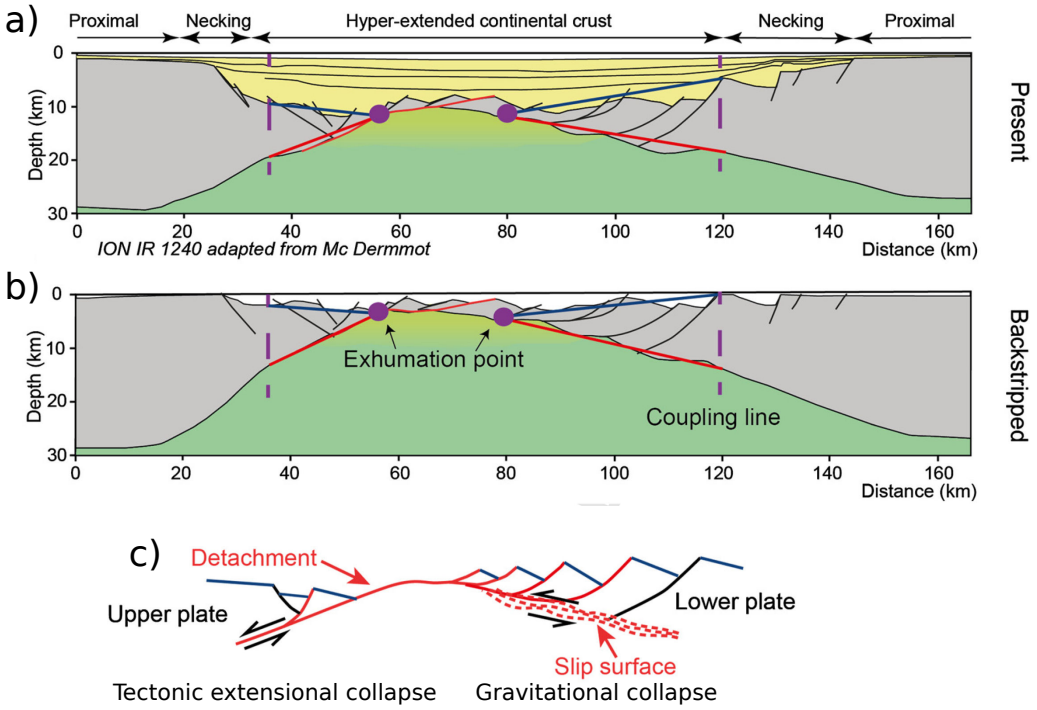


Fig. 1.4: (a) Line drawing of IR1240 cross-section crossing the conjugate margins of the Porcupine basin, extracted from *Nirrengarten et al.* [2016], modified from *McDermott et al.* [2014]. (b) Same cross-section corrected for post-rift sediment loading and thermal subsidence and (c) the simplified schematic diagram showing conjugate hyper-extended margins [*Nirrengarten et al.*, 2016].

The upper plate wedge corresponds to a tectonic extensional wedge, the one in the lower plate matches that of a gravity extensional wedge, as illustrated in Figure 1.4c.

1.1.2 Kinematic model in extension

The kinematic model in extension is referred to as an half-graben. To capture the evolution process of normal faulting, *Groshong* [1989] developed the basic balanced geometrical model for extensional faulting and related bending of the half-graben model, as shown in Figure 1.5. For example, this kinematic model implies the deformation of gravity and tectonic extensional collapses in offshore Niger Delta (Figure 1.1a) and the Rio Grande Rift, New Mexico (Figure 1.3), respectively. In this half-graben kinematics of Figure 1.5, the footwall does not deform or rotate during deformation. It is based on the geometry of a planar normal fault that joins a planar detachment at depth (Figure 1.5a). The hanging wall slides down along the normal fault and is sheared through the conjugated axial surface. As a result of extension, an half-graben

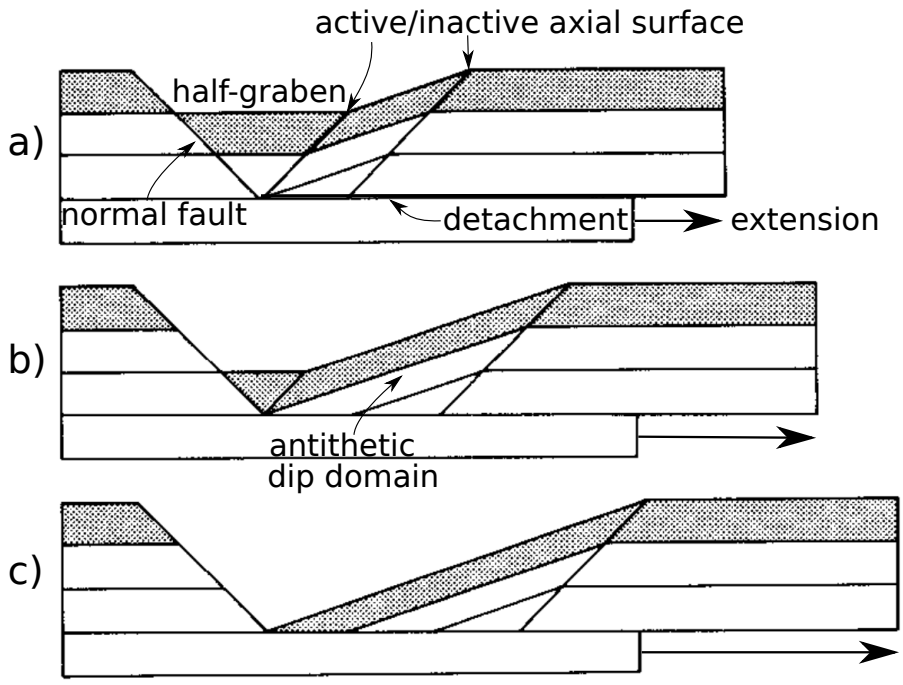


Fig. 1.5: Kinematic model of half-graben above a horizontal detachment in extension, showing the result of increasing displacement, adapted from *Groshong* [1989].

develops, bounded on one side by the normal fault and on the other by the active axial surface, causing the total structure to be asymmetric. As displacement increases on the normal fault (Figure 1.5b and 1.5c), the flat bottom of the half-graben gradually disappears as it drops down and shifts laterally into the domain of antithetic dip. The antithetic dip domain is bounded by two parallel axial surfaces that dip at an angle equal and opposite to that of the normal fault.

The half-graben kinematics in *Groshong* [1989] has considered so far the models involve only preexisting or pregrowth strata. To account for more natural field examples (e.g. Gulf Coast rollovers), *Xiao and Suppe* [1992] updated the half-graben kinematics to account for the bed deposition during deformation, that is, growth strata. Figure 1.6 shows the effect of syntectonic sedimentation on the rollover geometry for a constant fault shape [*Xiao and Suppe*, 1992]. The new features are the deposited beds passing through the active axial surface. The surface that connects the active and inactive axial surfaces is called the growth axial surface in their model. This growth axial surface links the top points of active and inactive axial surfaces, Figure 1.6, and records at each bed the location of the active axial surface on the sea bottom at the time of deposition.

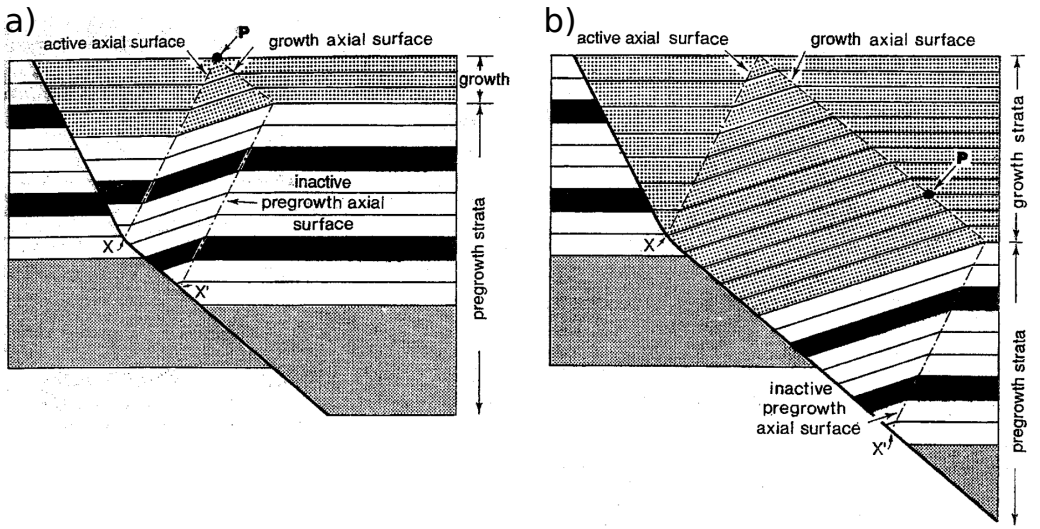


Fig. 1.6: Kinematic model of two stages (a and b) of progressive rollover development with sedimentation during deformation [*Xiao and Suppe*, 1992]. The growth axial surface is the locus of material deposited along the active axial surface during deformation.

For the structural evolution in extension, the kinematics of half-graben proposed by *Groshong* [1989] and *Xiao and Suppe* [1992] resulting from normal faulting and the sedimentation is elegant, but is not mechanically proven. For example, the dips of the normal fault and active axial surface are not constrained. Additionally, the footwall slope in Figure 1.5 might be not sustainable due to the depression of topography during extension. Our mechanical method used in this manuscript requires firstly to choose a failure kinematics, that is the half-graben geometrical model of *Groshong* [1989] in Figure 1.5. The parameters (dips of the normal fault and the axial surface and length of active detachment) will be determined by mechanical optimization.

1.1.3 Analogue modeling

To study the extensional deformations, wet clay is a widely used analogue material in experiments [*Dula*, 1991; *Withjack et al.*, 1995; *Bose and Mitra*, 2009] because of its strong cohesion which easily allows to conduct the extensional tests. The property of volume change and creep of wet clay is often captured by the Cam-Clay model [*Roscoe et al.*, 1958; *Roscoe and Burland*, 1968] which is distinct from Mohr-Coulomb criterion for dry sand materials. Thus, the use of wet clay in experiments to characterize deformation in the brittle crust is controversial. *With-*

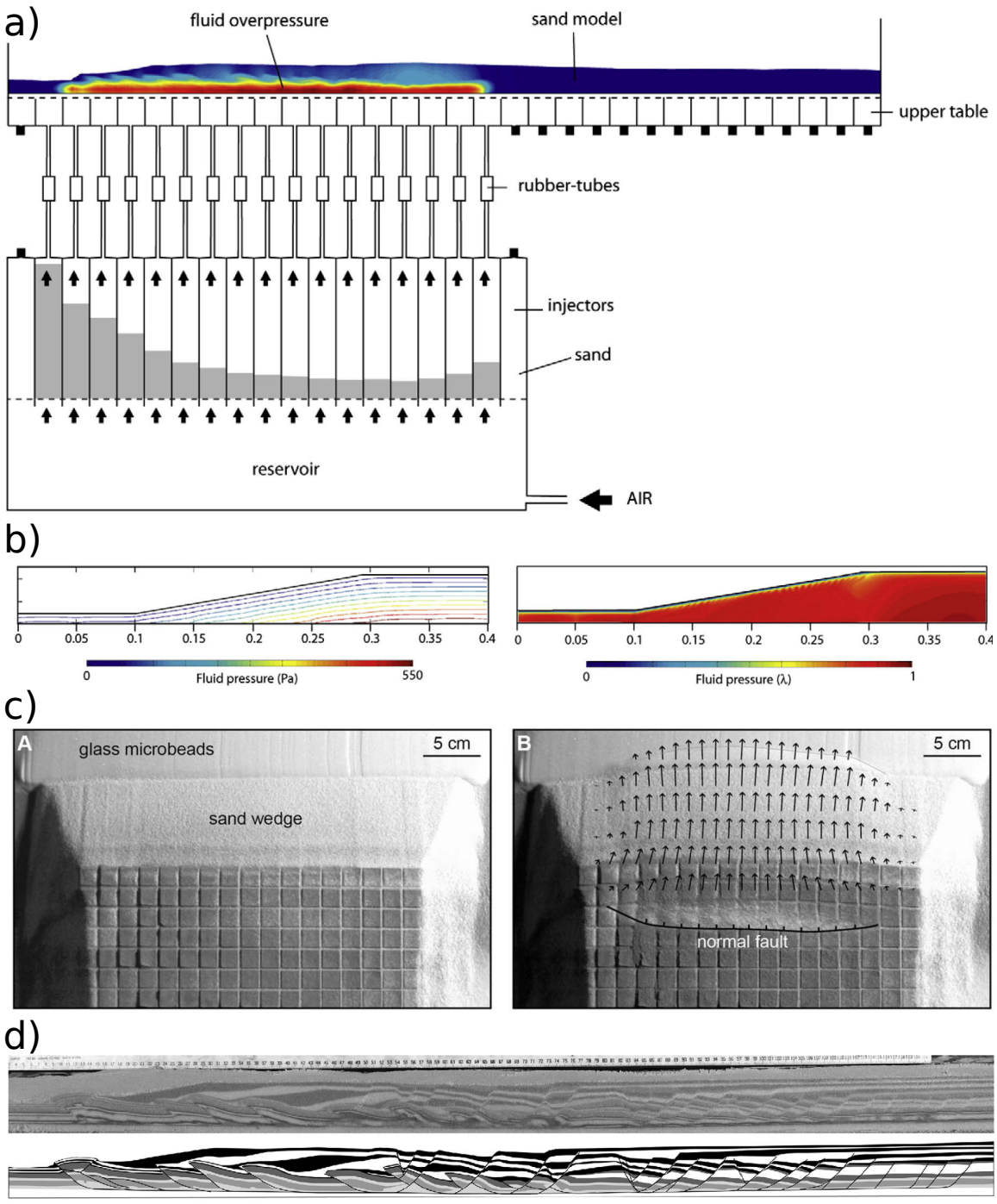


Fig. 1.7: (a) Experimental apparatus allowing to control the distribution of fluid pressure in the sand model [*Mourgues et al.*, 2009]. Each injector is filled with a different thickness of sand to regulate the fluid flow and to control the fluid pressure. (b) Fluid pressure distribution in a sand wedge model obtained by regulating fluid flow within the injectors. λ (fluid pressure parameter) is laterally constant [*Mourgues et al.*, 2009]. (c) Top views of the downslope edge of the model, (a) before and (b) after landslide triggering. Arrows indicate surface displacements [*Mourgues et al.*, 2014]. (d) Cross-sections of analogue experiments showing coupled extension and compression [*Mourgues et al.*, 2009].

jack and Schlische [2006] reported a significant difference of extensional deformation between the materials of dry sand and of wet clay; sand analogue characterises a planar fault whereas clay materials in extension generates listric fault. Additionally, in the clay experiments, the materials sit on a metal plate which is forced to slip as a detachment fault, thus it is questionable whether these simulations can capture the sequences of normal faulting in natural field examples of upper crust. In contrast, the sand analogue experiments have been proposed to study the tectonic extensional collapse at the subduction scale [*Xiao et al.*, 1991] which captures the typical features of migration of half-graben geometries during extension. Thus, the proposed mechanical methodology will use Mohr-Coulomb model which is more suitable to characterise brittle extensional failure of upper crust of interest in this thesis.

On the other hand, viscous materials such as salt and silicone are also used in analogue experiments. To study the gravity-driven failure of offshore deltas, there are the cases with the wedge prototype composed of a progradational dry sand on a viscous silicone substratum considered by *Ge et al.* [1997]; *McClay et al.* [1998]; *Rowan et al.* [2004]; *Vendeville* [2005]. These experiments however do not capture the influence of fluid overpressure which is an important factor in the gravity-driven failure in sedimentary basins and passive margins, such as offshore Niger Delta, Figure 1.1a. Recently, an impressive effort has been conducted to create sand analogue experiments with fluid overpressure by controlling the air flow through the base [*Cobbold and Castro*, 1999; *Mourgues and Cobbold*, 2003; 2006b; *Mourgues et al.*, 2009; *Lacoste et al.*, 2012], such as the setup in Figure 1.7a and 1.7b. The gravitational collapse of an overpressured wedge in Figure 1.7c captures our first failure mode and predicts well the fluid condition to generate the onset instability. Additionally, Figure 1.7d obtains the evolution features of gravity-driven instability resulting from sedimentation progradation. Such developments bring us one step closer to the conditions found in sedimentary basins and passive margins. They call for new theoretical developments to capture the onset and the evolution of failure in overpressured, cohesive and frictional materials. This is an important motivation for the present work, thus it will be the objective in our methodology for the extensional failures.

1.2 Mechanics of extensional collapses

Theoretical works on extensional collapses were proposed since the early mechanical works of *Terzaghi et al.* [1951]; *Hubbert and Rubey* [1959] on effective stress of layers in the presence of

fluid overpressure. *Mandl and Crans* [1981] further investigated the gravity instability linking up-slope extensional to down-slope compressional failures. These analytical solutions are applicable to the failures of prototype with a topography parallel to the planar detachment. The complex topography of many natural field examples will limit the use of these solutions. Our proposed mechanical methodology will not suffer this limitation.

Attractively, the famous Critical Coulomb Wedge (CCW) theory proposed by *Dahlen* [1984]; *Xiao et al.* [1991] can determine the stability of an extensional wedge prototype on a low-angle detachment which is widespread in the brittle crust [*Wernicke*, 1995]. We present the CCW theory herein because this theory is essential throughout the manuscript for the validation of our proposed methodology. The CCW theory is however approximate in the sense that its validity is limited to low topographic slopes and pore fluid pressures. The approximation is acceptable in compressional settings since the taper angle is small but leads to a loss of accuracy in the extensional regime where the taper angle reaches several tens of degrees. It is only recently that the CCW theory was amended by *Wang et al.* [2006] to produce an exact solution that was applied to sandbox experiments [*Mourgues et al.*, 2014]. The fluid pressure is quantitatively expressed by a physical parameter λ in the CCW theory. We thus will present the expression of this fluid parameter before the introduction of CCW theory.

1.2.1 Fluid Pressure

In both accretionary and extensional collapse of wedge structures, pore fluid pressure can be a key parameter having a strong influence on both the strength of the wedge and the fault (detachment) through its control on effective stress [*Hubbert and Rubey*, 1959]. Fluid overpressure is pore pressure above the hydrostatic pressure, indicative of disequilibrium driven by geologic mechanisms such as mechanical loading [*Saffer*, 2003]. The fluid overpressures are widespread in many sedimentary basins, such as in central North Sea, Figure 1.8 [*Hillis*, 2001], offshore Niger Delta [*Cobbold et al.*, 2009], Gulf of Mexico [*Xiao et al.*, 1991].

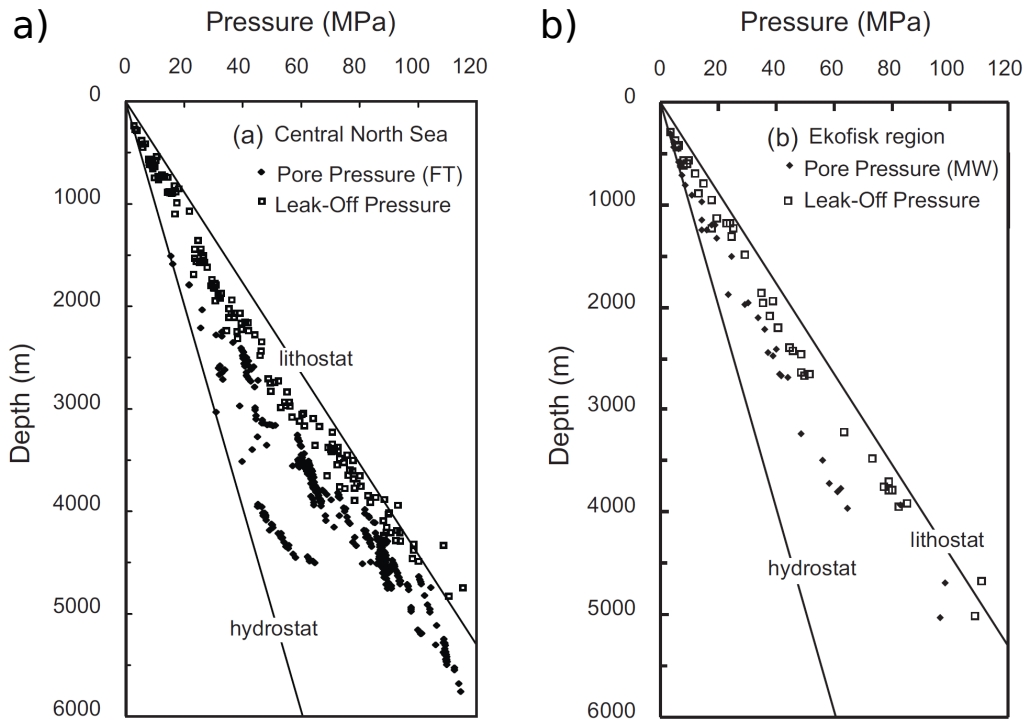


Fig. 1.8: Leak-off and pore fluid pressures from (a) the Central North Sea and (b) Norwegian sector of the North Sea in vicinity of the Ekofisk Field [*Hillis*, 2001].

In many geological problems, the pore fluid pressure, e.g. the point P illustrated in Figure 1.9a, is given in terms of the *Hubbert and Rubey* [1959]'s pressure ratio

$$\lambda = \frac{p_f - \rho_f g D(x)}{\sigma_z - \rho_f g D(x)} = \frac{\bar{p}_f}{\bar{\sigma}_z} \quad \text{with} \quad \sigma_z = \rho g(z - D(x)) + \rho_f g D(x)\,, \tag{1.1}$$

in which, σ_z is the stress corresponding to the pressure resulting from the weight of the column above the point P of interest. The positive scalar $D(x)$ is the height of the fluid column above the saturated rock, Figure 1.9a. The ratio λ varies between ρ_f/ρ and 1 corresponding to the fluid pressure at the hydrostatic and the lithostatic pressure, respectively. Thus, the fluid pressure p_f in terms of the pressure ratio λ is

$$p_f = g[\lambda\,\rho z + (\rho_f - \rho\lambda)D(x)]\,. \tag{1.2}$$

1.2.2 The Critical Coulomb Wedge (CCW) theory

This theory was originally intended for the mechanics of fold-and-thrust belts and accretionary wedges, comparing those geological features with a pile of sand in front of a moving bulldozer

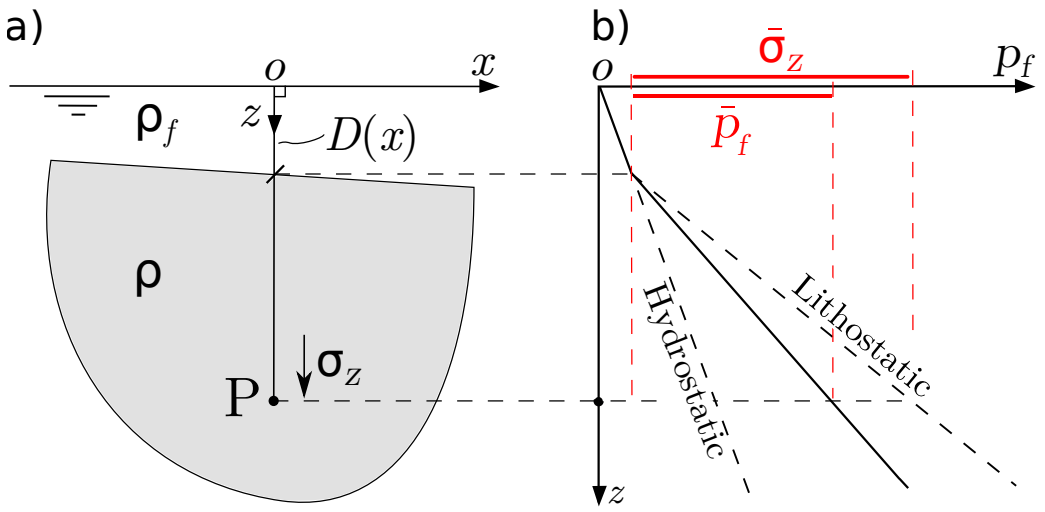


Fig. 1.9: (a) We consider a point P at depth z under the surface of the sea. The height of the water above this point is denoted $D(x)$. (b) Fluid pressure ratio λ is constant along the profile.

[*Davis et al.*, 1983; *Dahlen*, 1984]. The main results of the CCW theory on cohesionless materials are that active accretionary wedges deform until reaching a critical shape, which corresponds to an internal state of stress on the verge of Coulomb failure everywhere [*Dahlen*, 1984]. For the wedge at the critical shape, sliding occurs along the décollement without any deformation within the wedge. The critical angles (surface slope α and detachment dip β, Figure 1.10) of the wedge depend on the internal friction angle of wedge material φ_B, the friction along the detachment φ_D and the fluid pressure ratios λ_B, λ_D within the wedge and on the detachment, respectively. This classic work was extended to establish the mechanical model accounting for a cohesion varying linearly with depth [*Zhao et al.*, 1986; *Dahlen*, 1990]. The CCW theory is also pertinent to the gravitational collapse wedges [*Mourgues et al.*, 2014] of interest for our extensional studies in this manuscript, Figure 1.1b. The stable limit for this gravitational wedge corresponds to the upper envelope of CCW theory [*Dahlen*, 1984] which indicates, when a wedge surface slope is above the critical value that the wedge deforms towards the wedge tip until it returns to a stable state. The CCW theory gives the critical slope α_c as following

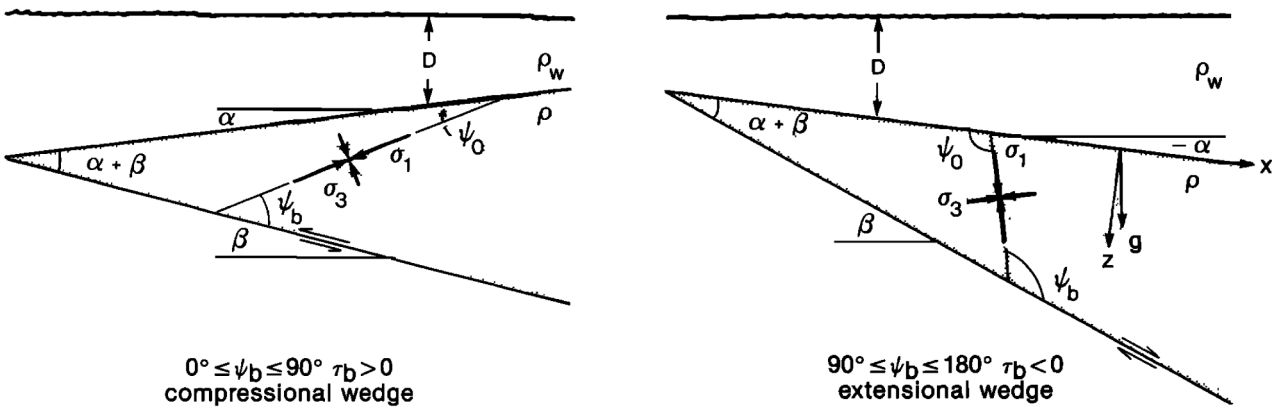


Fig. 1.10: Schematic cross-sections of critically tapered submarine wedges [*Xiao et al.*, 1991]. (a) Compressional wedges have a low-angle thrust (décollement) fault whereas (b) extensional wedges have the low-angle normal (detachment) fault.

relationship

$$\alpha_c + \beta = \Psi_D - \Psi_O \,,$$
$$\Psi_D = \frac{1}{2}\arcsin\left[\frac{\sin(\varphi'_D)}{\sin(\varphi_B)}\right] - \frac{1}{2}\varphi'_D \quad \text{with} \quad \varphi'_D = \arctan\left[\left(\frac{1-\lambda_D}{1-\lambda_B}\right)\tan(\varphi_D)\right], \tag{1.3}$$
$$\Psi_O = \frac{1}{2}\arcsin\left[\frac{\sin(\alpha')}{\sin(\varphi_B)}\right] - \frac{1}{2}\alpha' \quad \text{with} \quad \alpha' = \arctan\left[\left(\frac{1-\rho_f/\rho}{1-\lambda_B}\right)\tan(\alpha_c)\right].$$

in which, Ψ_D is the angle between the maximum principal stress σ_1 and the detachment, and Ψ_O is the angle between σ_1 and the surface, as illustrated in Figure 1.10. Theoretical stability boundaries for this critical compressional tapers are shown in Figure 1.11 for the detachment friction angle $\varphi_D = 10°, 20°$, respectively.

Xiao et al. [1991] extended the CCW theory to the context of active extensional wedges (Figure 1.1b) which are common in zones of upper crustal extension, such as the Basin and Range province of the North American Cordillera, the North Sea, and the Gulf Coast. The extensional wedges that overlie low-angle basal detachment faults are characterized by a tapered cross-section similar to that exhibited by a fold-and-thrust belt, but with an opposite sense of shear on the basal fault. If a compressional wedge is mechanically analogous to a wedge of soil being pushed up an inclined surface by a moving bulldozer, then an extensional wedge is analogous to the same wedge with the bulldozer moving downslope in reverse gear. A wedge whose taper is greater will fail by normal faulting and reduce its taper until it is critical (without internal deformation). The critical slopes of the extensional wedges can be obtained from the

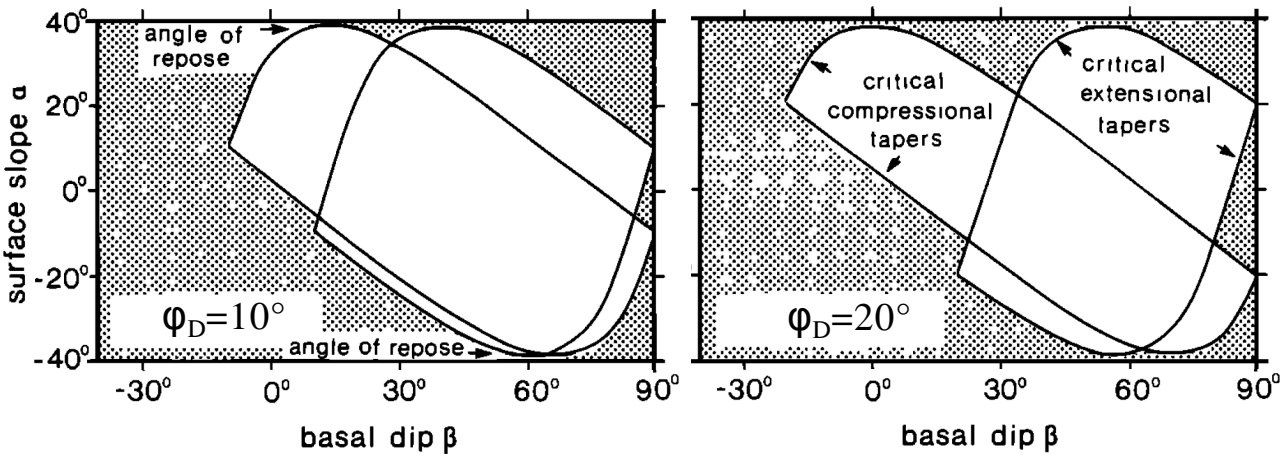


Fig. 1.11: Theoretical stability boundaries for extensional and compressional wedges, showing dependence on the detachment friction angle φ_D [*Xiao et al.*, 1991].

compressional CCW theory by replacing φ_D in equation (1.3) with the value of $-\varphi_D$. The illustration of the tectonic extensional failure is presented in Figure 1.10b. Theoretical stability boundaries for this critical extensional tapers are also shown in Figure 1.11 for the detachment friction angle $\varphi_D = 10°, 20°$, respectively.

The CCW theory has been successfully applied to some extensional collapses, such as in the Gulf of Mexico [*Xiao et al.*, 1991]. *Nirrengarten et al.* [2016] also applied the gravity and tectonic extensional wedges in hyper-extended, magma-poor rifted margins (Figure 1.4b) to fit the results predicted by the CCW theory. The CCW theory is however not applicable to cohesive materials, or an arbitrary topography. This theory also cannot describe more complicated failure structures like the linked extensional-compressional failure modes in many offshore deltas. Additionally, the CCW theory assumes the fault should be planar and in a simple fluid overpressure condition. The normal faulting in the extensional province of Niger Delta (Figure 1.1), however, is characterized by both seaward dipping and landward dipping (counter-regional) listric normal faults. The widespread observation of low-angle normal faults and listric faults are of interest to geologists but are explained by mechanic concepts only for some specific situations.

1.2.3 Numerical modeling

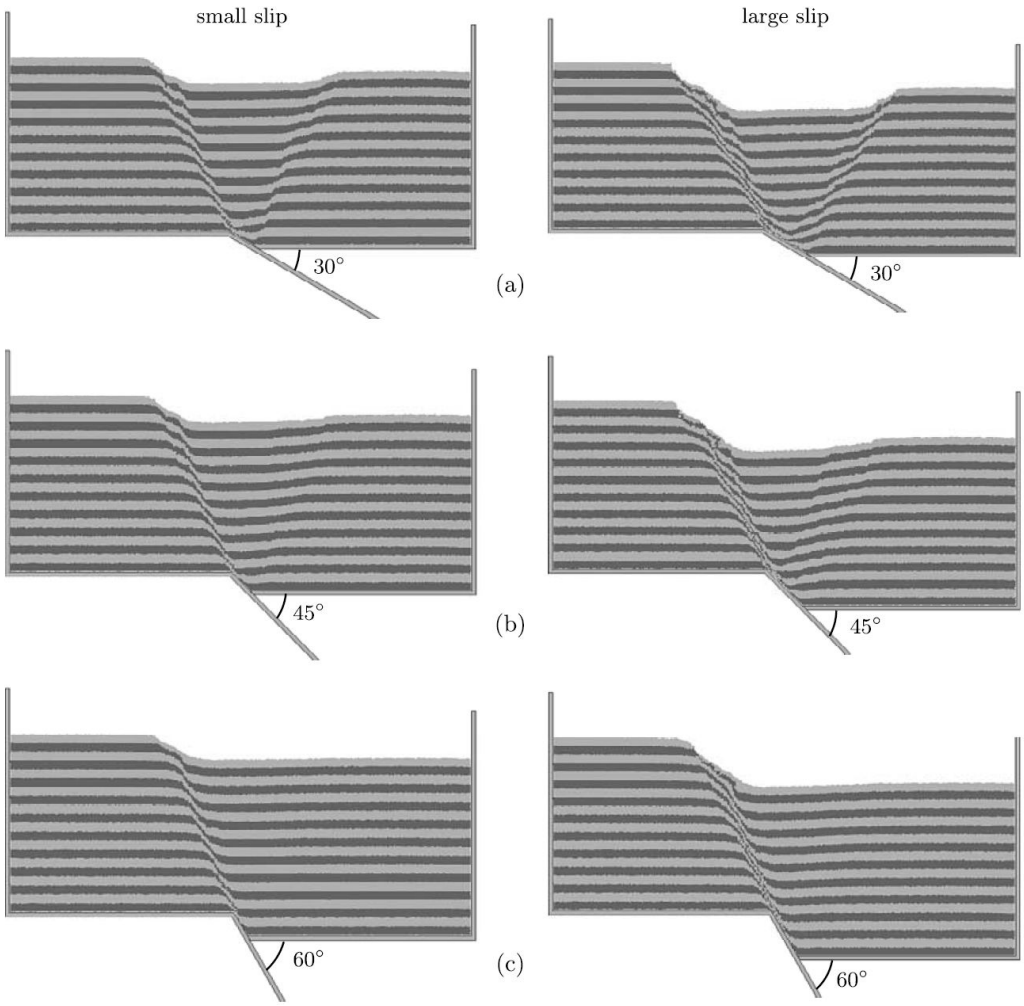


Fig. 1.12: Fault propagation folding DEM simulations with basement fault dip of $30°, 45°$ and $60°$ [*Egholm et al.*, 2007].

Two families of numerical methods, finite-element method (FEM) and distinct-element method (DEM), are classically used to simulate the extensional deformation in structural geology, such as the contributions of *Ortiz et al.* [1987]; *Crook et al.* [2006]; *Nollet et al.* [2012] in FEM, and the DEM works from *Finch et al.* [2004]; *Egholm et al.* [2007]; *Hardy* [2013]. The FEM, enforcing mechanical equilibrium in a weak sense, is complex to implement especially if the strain localization results in displacement discontinuities with large offsets. Additionally, the strain localization requires the introduction of material rheologies (e.g. elastic-plastic constitutive relations) which are poorly known on the geological time and length scales. Our methodol-

ogy proposed in next subsection requires no complex rheology other than Coulomb strength criterion.

The DEM is a family of numerical methods for computing the motion of a large number of small particles. It is effective to capture the small-scale fracturing or the large displacements typical of the extensional regime in several hundreds kilometres. *Egholm et al.* [2007] proposed a numerical method of the DEM family which captures the essential features of the half-graben geometry including the creation of the narrow blocks bounded by normal faults of different dip, Figure 1.12. The DEM, however, cannot address the fluid pressure discussed in subsection 1.2.1. Additionally, the number of particles in DEM simulation, and duration of a simulation is limited by computational power. Thus the DEM lacks of computational efficiency which means that this methodology is not well suited for inverse analysis which requires millions of forward modellings. Our methodology proposed lies between the purely kinematic models of structural geology and the above numerical methods, offering a compromise between the complexity of the physics and the efficiency of calculations.

1.3 Methodology used here : Limit Analysis and Sequential Limit Analysis

In geotechnics, the critical load that deforms a structure is the prime objective. It can be determined by solving the mechanical problem using limit analysis which provides bounds to the critical load with few assumptions on the rheology [*Salençon*, 1974]. The theory of limit analysis has two approaches: the static and kinematic approaches. The statics approach derives a lower bound by constructing possible stress fields which balance the load without exceeding the material strength. The kinematic approach determines an upper bound to the critical load based on possible failure geometries [*Chen*, 1975; *Michalowski*, 1995; *Salençon*, 2002]. The application of statics approach can be referred to *Souloumiac et al.* [2009] for the geometrical models of folds, relevant to fold-and-thrust belts as well as accretionary wedges. The application of kinematic approach to geological structures is the main subject of this thesis. Therefore, only the kinematic approach will be developed herein.

The kinematic approach of limit analysis is applied to extensional structures extending the contributions from *Maillot and Leroy* [2006]; *Cubas et al.* [2008]; *Pons and Leroy* [2012];

Mary et al. [2013a] in compressive setting. This kinematic approach has two steps leading to the determination of the upper bound [*Maillot and Leroy*, 2006]. The first step is actually the result of two theorems: the virtual power theorem, which allows the introduction of the principle of mechanical equilibrium in the chosen kinematics, and the upper bound theorem to determine the bound of the internal power of the chosen kinematics. In this first step, we choose the half-graben kinematics for our extensional failure mechanism, characterized by failure planes or velocity discontinuities created during extensional loading. This extensional loading results in a normal fault, an active axial surface and detachment fault, as illustrated by the classic kinematic half-graben geometry in Figure 1.5 and 1.6. In the second step, we calculate the force needed to create these fault planes based on the chosen kinematics. The mechanical approach calculates an upper bound to this force instead of seeking an exact, unknown, tectonic force. We calculate this upper bound for all kinematically admissible velocity fields and respecting the boundary conditions. Then we will select the dominant failure mode (kinematics) corresponding to the minimum upper bounds. This defines the position of normal fault, the active axial surface and detachment fault. The second step is actually an optimization procedure. This method was validated by many applications in civil engineering, especially for studying slope instability. For example, *Michalowski* [1995] presented a translational failure mechanism of an unstable slope assuming in the form of rigid blocks analogous to slices in traditional slice methods. More impressively, *Utili and Crosta* [2011] modelled retrogressive landsliding evolution of natural slopes subjected to weathering by assuming Mohr-Coulomb material behaviour. This retrogressive evolution occurs with decreasing size of the unstable blocks, following a logarithmic (kinematic) volume relationship.

The kinematic approach is particularly of interests to structural geologists because the geometrical model described by kinematics can be incorporated with mechanics. The friction, cohesion and fluid pressure will be the important physical parameters in the problem. Similar to conditions of the CCW theory, the structure failure being considered is governed by the Mohr-Coulomb criterion and the method is only valid for cohesive and frictional materials. Once the detachment of a structure protrudes significantly beneath the brittle-plastic transition, situated at a depth of 10-15 km, a Coulomb model might not be applicable because the detachment strength is no longer limited by brittle frictional processes. The method is is applicable to Coulomb wedges of all scales, from tens to hundreds of kilometres down to

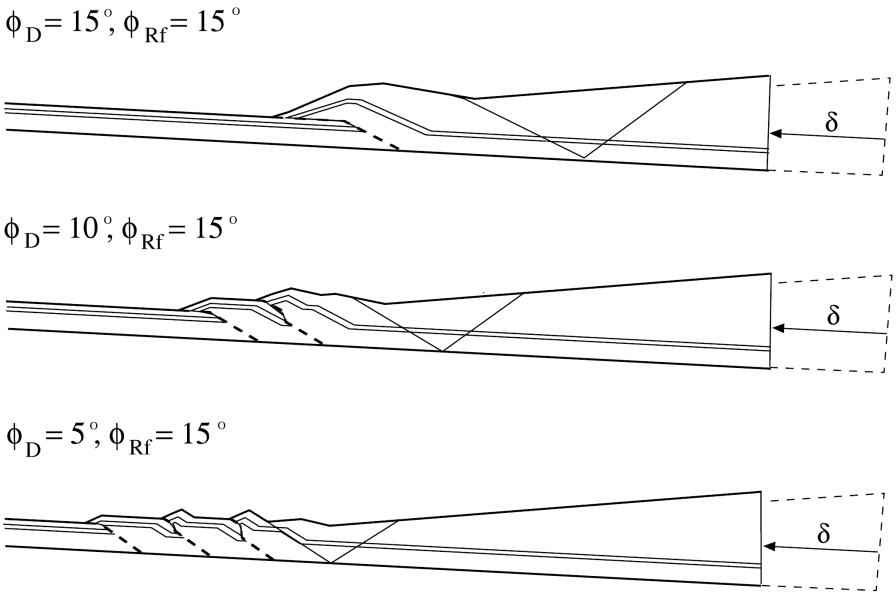


Fig. 1.13: The sequences of thrusting simulated by Sequential Limit Analysis for different values of the friction angles on the detachment and on the ramp fault [*Cubas et al.*, 2008].

laboratory sandbox models. This method will be used throughout of this manuscript to solve many problems associated with the extensional deformation.

In civil engineering, only the onset of failure is studied and the evolution of the failure structure is of little interest. In this work, we propose otherwise to continue to apply the external approach to predict the structure deformation. This approach has already been adopted by *Maillot and Leroy* [2006] for the study of a kink band, and used by *Cubas et al.* [2008] to predict the evolution of the accretionary structure, Figure 1.13. As seen from the deformation structures, the frictions on detachment and ramp fault have much influence on the structural evolution. The evolution is made by a simple translation along faults as well as the active detachment fault determined from this mechanical approach. The force required for this translation is calculated at each step of evolution. At each step, they investigated whether a new fault system in the structure could lead to an upper bound force required to creating terrain, and predicted a sequence overlaps of ramps. We will use the same method to study the deformation pattern of geological structures resulting from normal faulting accounting for the influence of fluid pressure, fault softening and sedimentation.

Compared to the numerical methods discussed in above subsection, our proposed methodology coupling between mechanics and half-graben geometrical constructions has the small

number of degrees of freedom: the dips of the two bounding planes of the half-graben and the position of their common root. This methodology lies between the purely kinematic models of structural geology and the FEM, offering a compromise between the complexity of the physics and the efficiency. Additionally, our methodology is computational efficiency implying that solutions can be obtained within minutes; thus the methodology is well suited for inverse analysis which requires millions of forward modellings, as done by *Cubas et al.* [2013a] in the compressional setting.

1.4 Manuscript content

The manuscript uses limit analysis to investigate extensional collapses in the overpressured frictional upper crust. The main objective is to understand several interesting questions associated with the extensional collapses, such as (1) the roles of fluid overpressures, arbitrary topography, material and fault properties on the stability of extensional structures; (2) the formation of low-angle and listric normal fault; (3) the deformation pattern due to slip on a low-angle fault; and (4) the influence of fault softening and sedimentation processes on this deformation pattern. This manuscript contains four articles during my doctoral studies in France:

- The first article proposes the limit analysis for the two types of extensional deformations. First, gravitational collapse of a wedge of frictional material resting on a low-friction, inclined base (detachment), and second, tectonic extensional collapse triggered by downdip slip on the detachment, following the retreat of a back wall. This article is in forms of a paper published in: Yuan, X.P., Y.M. Leroy, and B. Maillot (2015), Tectonic and gravity extensional collapses in overpressured cohesive and frictional wedges, Journal of Geophysical Research, 120, doi:10.1002/2014JB011612.

- The second article presents the Sequential Limit Analysis being applied in the extensional context to capture the 2-D deformation pattern resulting from normal faulting. This method provides a simple means to combine mechanics and a geometrical construction of the geological structure following the classic kinematic models of hanging-wall deformation in Figure 1.5. The method can be applied to prototype with arbitrary topographic surface, accounting for softening on normal faults, erosion and sedimentation processes and fluid overpressures. This article is in preparation as: Yuan, X.P., B. Maillot, and Y.M. Leroy, Deformation pattern during normal faulting: a sequential limit analysis.

- The third article studies the mechanics of gravity instability in offshore deltas. The failure in the offshore delta is widely recognized by geologists as gravity-driven instability by sedimentation overloading. The frontal thrusts accommodate the upslope extension through a deep detachment fault. However, *Bilotti and Shaw* [2005] and *Suppe* [2007; 2014] studied the stability of Niger Delta by using the CCW theory which is, by default, considering Niger Delta as compressional (or tectonic-driven) failure. This is an important motivation for me to study the linked extensional-compressional failure mechanism using our Limit Analysis approach and reappraise the fluid overpressures in offshore Niger Delta. This article is in preparation as: Yuan, X.P., B. Maillot, and Y.M. Leroy, Reappraisal of gravity instability conditions for offshore wedges: consequences for overpressures in the Niger Delta.

- The fourth article determines the mechanical conditions in terms of rock properties and fluid pressure gradient characteristics conducive to the onset of low-angle and listric normal faults linking a lower detachment to the topography in the brittle, upper crust. These normal faults are characterized by a significant decreasing in fault dip from $\sim 60^\circ$ near the surface down to a low angle (0-20°) in the detachment. The formations of listric fault and low-angle normal fault in the upper crust are of interest for many geologists due to the conflicting with the Andersonian fault mechanics. This article is in preparation as: Yuan, X.P., Y.M. Leroy, and B. Maillot, Role of fluid overpressures on the shape of normal faults in frictional upper crust.

Anther paper as collaboration with others relates to the extensional collapses in hyper-extended, magma-poor rifted margins. Due to detachment faulting, the wedges in the upper and lower plate margins correspond to the tectonic extensional and the gravity extensional collapses, respectively. The use of the CCW theory in these wedges could constrain the overpressured conditions and determine the tectonic activity. The article is published as: Nirrengarten M, Manatschal G, Yuan XP, Kusznir N, Maillot B. Application of the critical Coulomb wedge theory to hyper-extended, magma-poor rifted margins, Earth and Planetary Science Letters, `http://dx.doi.org/10.1016/j.epsl.2016.03.004`.

Chapter 2

Tectonic and gravity extensional collapses in over-pressured cohesive and frictional wedges[1]

Abstract

Two modes of extensional collapse in a cohesive and frictional wedge of arbitrary topography, finite extent, and resting on an inclined weak decollement are examined by analytical means. The first mode consists of the gravitational collapse by the action of a half-graben, rooting on the decollement and pushing seaward the frontal part of the wedge. The second mode results from the tectonics extension at the back-wall with a similar half-graben kinematics and the landwards sliding of the rear part of the wedge. The predictions of the maximum strength theorem (MST), equivalent to the kinematic approach of limit analysis and based on these two collapse mechanisms, not only match exactly the solutions of the critical Coulomb wedge (CCW) theory, once properly amended, but generalises them in several aspects: wedge of finite size, composed of cohesive material and of arbitrary topography. This generalisation is advantageous to progress in our understanding of many laboratory experiments and field cases. For example, it is claimed from analytical results validated by experiments that the stability

[1]Published as: Yuan, XP, Leroy YM, Maillot B. Tectonic and gravity extensional collapses in over-pressured cohesive and frictional wedges, Journal of Geophysical Research - Solid Earth, 2015, 120, doi:10.1002/2014JB011612.

transition for a cohesive, triangular wedge occurs with the activation of the maximum length of the decollement. It is shown that the details of the topography, for the particular example of the Meijilones peninsula (North Chile) is, however, responsible for the selection of a short length scale instability corresponding to a frontal gravitational collapse. This apparent contradiction vanishes once a reasonable amount of cohesion is introduced: the pressures proposed in the literature for that field case are then indeed associated with a stability transition with a long-wavelength mode and not with a dynamically unstable state.

2.1 Introduction

The kinematic approach of limit analysis, also called the maximum strength theorem (MST) [*Maillot and Leroy*, 2006] for compressional deformation in fluid-saturated porous media [*Pons and Leroy*, 2012] is extended to the extensional context. The objective of this work is to propose this simple method to analyze the gravity and tectonic extensional deformation modes occurring in over-pressured frictional wedges extending the stability conditions presented by *Dahlen* [1984] and *Xiao et al.* [1991] to arbitrary-shaped topography and cohesive materials.

Two kinds of collapse modes, combinations of normal faults and axial surfaces, typical of tectonics areas in extension are considered. For example, the Schell Creek range, Nevada, presents a collapse mechanism composed of a normal fault and an axial surface, both rooting on a weak decollement. This asymmetric collapse mode is referred to as a half-graben [*Groshong*, 1989]. This gravitational collapse is a mechanical instability that typically results from excessive sedimentation and/or weakening of a detachment horizon as seen in river deltas [*Mandl and Crans*, 1981] or in the shallow portion of the convergent margin off Antofagasta [*Delouis et al.*, 1998; *von Huene and Ranero*, 2003; *Sallarès and Ranero*, 2005]. This gravitational collapse is the first mechanism to be studied in this contribution in the context of fluid-saturated wedges. The second mode of instability is due to a regional extensional tectonic event (e.g. Brazos Ridge fault, offshore Texas [*Xiao et al.*, 1991; *Withjack et al.*, 1995]). This second mode which is also based on the half-graben kinematics described above is referred to as a tectonic extensional collapse.

Sandbox analogue experiments have been proposed to validate the field interpretation either at the subduction scale [*Xiao and Suppe*, 1992] or on the length scale of the half-graben which could structure a hydrocarbon reservoir [*Patton*, 2005]. Recently, an impressible effort has been

conducted to create analogue experiments with fluid overpressure by controlling the air flow through the base [*Mourgues and Cobbold*, 2003; *Mourgues et al.*, 2009; *Lacoste et al.*, 2012]. Such developments bring us one step closer to the conditions found in sedimentary basins and accretionary wedges. They call for new theoretical developments to capture the onset and the evolution of failure in over-pressured materials, and this is an important motivation of the present work.

An experiment, proposed to validate an interpretation, has to be based on some theoretical background. Most of our theoretical understanding is based on the Critical Coulomb Wedge (CCW) theory [*Davis et al.*, 1983] firstly proposed for compressional wedges. *Dahlen* [1984] introduces extensional conditions which are pertinent to our gravitational collapse mode. The work of *Xiao et al.* [1991] further generalizes the CCW theory by reversing the sense of slip on the decollement which corresponds to our tectonic collapse mode. The solution in the last two references is nevertheless approximate in the sense that its validity is limited to low topographic slopes and pore pressures. It is only recently that the CCW theory was amended by *Wang et al.* [2006] to produce an exact solution (called the Exact Critical Coulomb Wedge - ECCW - theory in this contribution) that was applied to sandbox experiments [*Mourgues et al.*, 2014].

This contribution contents are as follows. Next section is concerned with the general stability conditions for a wedge of arbitrary topography and composed of a cohesive, frictional material. The stability conditions are specialized in section 2.3 for our gravitational instability mode. The special case of a triangular wedge composed of a cohesionless material is then proposed preparing the grounds for the successful comparison with CCW theory. The two challenges of this comparison are first to make sure that our parametrization of the pressure ratio is identical to the one proposed by *Dahlen* [1984] (see Appendix A) and second to complement the modification proposed by *Wang et al.* [2006] to obtain the exact implicit solution (ECCW) (see Appendix B). For the case of cohesive materials and a triangular wedge, it is found that the stability transition is associated with the gravitational collapse along the maximum possible decollement length. This claim is validated by comparing our predictions with the results of a series of experiments with sand and plaster, the proportion of the later material controlling the overall cohesion. Section 2.4 sees the application of the general stability conditions to tectonic collapse. The comparison with the ECCW theory is then presented before the MST is applied to the sand box experiments of *Xiao et al.* [1991]. It is shown that our approach not only captures

the onset of collapse, but also predict the evolution of the deformation style during the retreat of the vertical wall. To show the versatility of our method, section 2.5 is proposed to analyse the stability conditions of the active margin off Antofagasta in North Chile [*von Huene and Ranero*, 2003; *Sallarès and Ranero*, 2005]. It is shown that the pressure conditions proposed in *von Huene and Ranero* [2003] imply a dynamically unstable state involving the maximum decollement length, unless some bulk cohesion is introduced. At 5 MPa bulk cohesion, the wedge is in a stable mode, very near quasi-static instability, still involving the full decollement length. This stability transition is consistent with the quasi-static topographic evolution responsible for the debris flow towards the subduction channel [*Delouis et al.*, 1998].

2.2 Limit analysis for extension

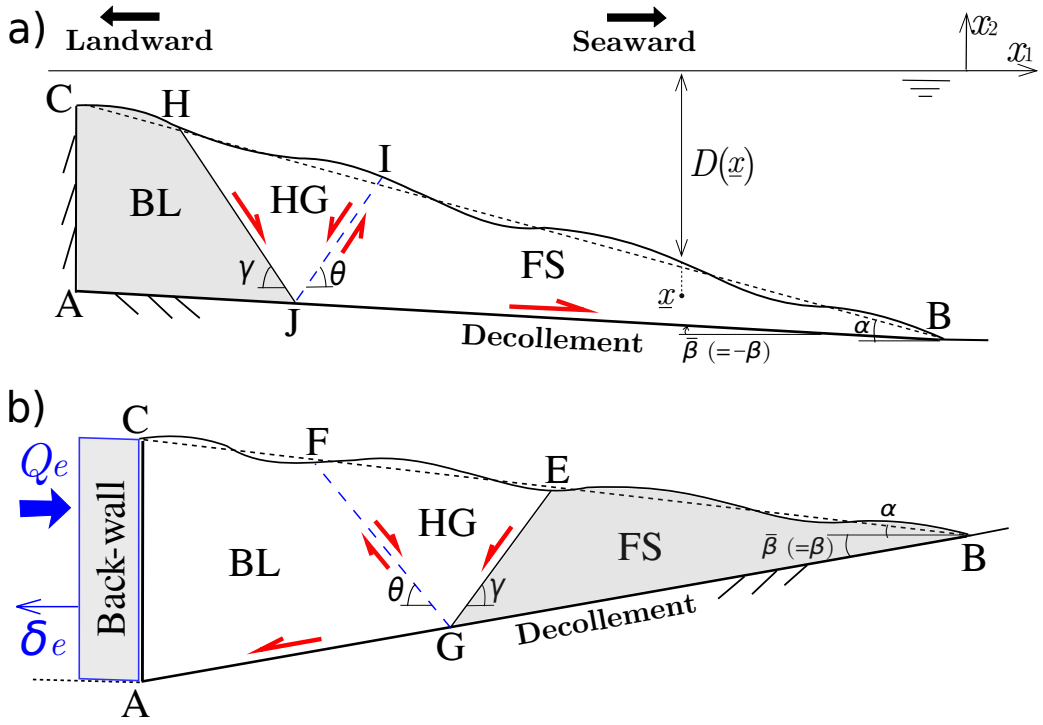


Fig. 2.1: Definition of the two collapse modes: a), the gravity collapse mode relies on a half-graben (HG) with seaward slip of the frontal section (labelled FS for Front & Seaward) on the decollement; b), the tectonic collapse mode has a similar kinematics with slip of the back region (labelled BL for Back & Landward) associated to the landward slip of the HG along the normal fault GE. The distance $D(\underline{x})$ defines the depth of the submerged domain over any material point located by the vector $\underline{x}$.

The objective of this section is to present the theory used throughout this contribution and in particular, to define the concept of collapse mechanism.

2.2.1 Prototype and collapse mechanisms

The geometry of our prototype and of the collapse mechanism is presented in Figure 2.1. It consists of a wedge of arbitrary topography and of a triangular-like shape resting on a straight decollement (AB) inclined at an angle β (positive if dipping landward as in Figure 2.1b; $\bar{\beta}$ is the absolute value of β). The two collapse mechanisms in Figure 2.1a and b consist of a normal fault bounding a half-graben (HG). Material within the HG is sliding on the normal fault (solid segments, JH and GE dipping at γ) and part of this material is crossing the conjugate shear plane (dotted segments, JI and GF, dipping at θ). This material flux results in the push of the frontal section (labelled FS for Frontal & Seaward) seaward or of the back region (labelled BL for Back & Landward) landward, as in Figure 2.1a and b respectively. In the former case, the collapse is purely gravitational and in the latter case it is due to the retreat of the back-wall (AC), boundary of the wedge and the collided plate, because of a tectonic extension. Note that in Figure 2.1b, the large arrow indicates the sense of compression. In the tectonic extension case, the force Q_e will often be compressive, but not necessarily. The sign of Q_e depends on the orientation of the x_1 axis (Figure 2.1a).

The rest of this section presents the theory necessary to decide on the position of the collapse mechanism (points G or J) and the dip of the normal fault and the shear plane. The position of the three points EFG or HIJ define entirely the collapse mechanism referred to as the gravitational (Figure 2.1a) and the tectonic mode (Figure 2.1b), respectively.

2.2.2 Theorem of effective virtual powers

This theorem is the weak form (integral) of the equation of motion and was presented in *Pons and Leroy* [2012] except for the introduction of inertia:

$$\mathcal{P}'_{\text{ext}}(\underline{\hat{U}}) - \mathcal{P}'_{\text{int}}(\underline{\hat{U}}) = \mathcal{P}_{\text{acc}}(\underline{\hat{U}}) \quad \forall \quad \underline{\hat{U}} \; KA\,. \tag{2.1}$$

It states the equality between the acceleration power and the difference between the effective external and internal powers for any kinematically admissible (KA) velocity field denoted $\underline{\hat{U}}$. The set of KA fields does not contain just the exact, unknown velocity field but comprises any

field consistent with the boundary conditions of our problem. It includes also the piecewise uniform velocity fields $\hat{\underline{U}}$ associated to the kinematics of the two collapse mechanisms described above.

The effective external power is defined by

$$\mathcal{P}'_{\text{ext}}(\hat{\underline{U}}) = \int_{\partial\Omega_t^T} \underline{T}^d \cdot \hat{\underline{U}}\, dS + \int_{\Omega_t} \rho \underline{g} \cdot \hat{\underline{U}}\, dV + \int_{\Omega_t} p \,\text{div}(\hat{\underline{U}})\, dV + \int_{\Sigma_U} p_\Sigma \underline{n} \cdot \hat{\underline{J}}\, dS\,. \tag{2.2}$$

The first term is the force density $\underline{T}^d$ applied on $\partial\Omega_t^T$, part of the wedge boundary (for example the sea fluid pressure over the topography BC. The second term is the power of the gravity field (ρ is the fluid-saturated volumetric mass and $\underline{g}$ the gravity acceleration vector) in the domain occupied by the wedge (Ω_t) (Figure 2.1). The last two terms in (2.2) correspond to the power of the velocity field $\hat{\underline{U}}$ on the fluid pressure, seen as an external field, either in the bulk or within any velocity discontinuity ($\hat{\underline{J}}$) along a surface of normal $\underline{n}$. These velocity discontinuities are found across the normal fault, the shear plane, the activated part of the decollement and possibly at the contact with the back-wall. All these surfaces are grouped in the set Σ_U. Note in (2.2) that the pressure p in the bulk could be different from the pressure p_Σ found in the discontinuities. No attempt is made to justify the origins and how such pressure discontinuities are maintained in time.

The effective internal power introduced in (2.1) reads

$$\mathcal{P}'_{\text{int}}(\hat{\underline{U}}) = \int_{\Omega_t} \underline{\underline{\sigma}}' : \hat{\underline{\underline{d}}}\, dV + \int_{\Sigma_U} \underline{T}'_\Sigma \cdot \hat{\underline{J}}\, dS\,, \tag{2.3}$$

and corresponds to the effective stress tensor $\underline{\underline{\sigma}}'$ multiplied by the rate of deformation tensor $\hat{\underline{\underline{d}}}$ (computed from the virtual velocity field $\hat{\underline{U}}$) and to the effective stress vector $\underline{T}'_\Sigma$ times the velocity jump across the surfaces in the set Σ_U. All the velocity fields considered herein will be piecewise continuous so that only discontinuities will contribute to the effective internal power. The acceleration power in (2.1) is

$$\mathcal{P}_{\text{acc}}(\hat{\underline{U}}) = \int_{\Omega_t} \rho \underline{a} \cdot \hat{\underline{U}}\, dV\,, \tag{2.4}$$

with $\underline{a}$ denoting the acceleration field. Note that the sign of this power depends on the orientation of the velocity field with respect to the acceleration.

To complement these definitions, we need to introduce the effective stress carried by the solid phase of our fluid-saturated continuum

$$\underline{\underline{\sigma}}' = \underline{\underline{\sigma}} + p\underline{\underline{\delta}}\,, \tag{2.5}$$

where $\underline{\underline{\delta}}$ is the identity tensor, as well as the effective stress vector on any surface

$$\underline{T}' = \underline{T} + p\underline{n}\,, \tag{2.6}$$

oriented by its normal $\underline{n}$.

The last ingredient required to complete this section is the parametrization of the pressure field. The proposition of *Hubbert and Rubey* [1959] is adopted here with the following fluid pressure ratio:

$$\lambda(\underline{x}) = -\frac{p(\underline{x}) - \rho_f g D(\underline{x})}{\sigma(\underline{x}) + \rho_f g D(\underline{x})} \quad \text{with} \quad \sigma(\underline{x}) = \rho g(x_2 + D(\underline{x})) - \rho_f g D(\underline{x})\,, \tag{2.7}$$

in which ρ_f and $D(\underline{x})$ are the fluid volumetric mass and the thickness of the fluid above the saturated continuum at point $\underline{x}$ (see Figure 2.1a for illustration), respectively. The stress σ in (2.7) is negative and corresponds to the pressure resulting from the weight of the column above the point $\underline{x}$ of interest. The 2-axis is vertical and directed upwards, Figure 2.1a, so that the gravity acceleration vector is $\underline{g} = -g\underline{e}_2$. The scalar λ in (2.7) varies between ρ_f/ρ and 1 corresponding to the range of pressure between hydrostatic and lithostatic. The fluid pressure ratio λ can also be expressed as the sum of the overpressure ratio difference $\Delta\lambda$ and the hydrostatic pressure ratio λ_{hydro}

$$\lambda = \Delta\lambda + \lambda_{hydro} \quad \text{with} \quad \lambda_{hydro} = \rho_f/\rho\,, \tag{2.8}$$

so that $\Delta\lambda$ varies within the range of 0 and $1 - \rho_f/\rho$. The fluid pressure p and its difference from the hydrostatic pressure at any point of the medium are thus expressed as

$$p = g[-\lambda\rho x_2 + (\rho_f - \rho\lambda)D] \quad \text{and} \quad \Delta p = -\Delta\lambda\rho g(x_2 + D)\,. \tag{2.9}$$

Note that the fluid pressure parametrization relies on the vertical axis of our coordinate system and not on the distance to the topography. This difference is crucial to understand some of the discrepancies found in the application of the CCW theory and discussed in what follows.

2.2.3 Maximum strength theorem (MST)

A weak form of the equations of motion has just been introduced. The effective internal and the acceleration powers for our examples are nevertheless unknown since neither the stress vector acting on the discontinuities nor the acceleration are determined. The application of the Maximum Strength Theorem (MST) palliates to this difficulty and provides the dominant

collapse mechanism, a concept to be defined, after a few assumptions on the material strength are discussed.

The effective stress vector acting on a discontinuity of normal $\underline{n}$ and tangent $\underline{t}$, member of Σ_U, is decomposed in a normal σ'_n and a tangential component τ in the right-handed basis $\{\underline{n}, \underline{t}\}$. This vector is within the set

$$G = \{\underline{T}' \,|\, |\tau| + \tan(\varphi)\sigma'_n - C \leq 0\}\,, \tag{2.10}$$

bounded by the Coulomb criterion defined by the friction angle φ and the cohesion C. This set is convex in the space (τ, σ'_n), an essential property for what follows. Consider now the jump in velocity across any discontinuity $\underline{\hat{J}}$ where the effective stress vector $\underline{T}'$ is acting and apply convex analysis [*Salençon*, 2002] to see that there is a maximum to the power $\underline{T}' \cdot \underline{\hat{J}}$ which is called the support function $\pi(\underline{\hat{J}})$. This function depends on the orientation η of $\underline{\hat{J}}$, the angle, counted positive anti-clockwise, with the normal to the plane of discontinuity ($\underline{\hat{J}} \cdot \underline{n} = \hat{J}\cos\eta$). The experience of previous works with this theoretical framework without pressure field [*Cubas et al.*, 2008] or including the fluid phase [*Pons and Leroy*, 2012] is that the velocity jumps have to be selected such that $\eta = \pm(\pi/2 - \varphi)$. This special orientation corresponds to the minimum value of the support function, which is then expressed as

$$\pi(\underline{\hat{J}}) = \hat{J}C\cos\varphi, \;\; \text{with} \;\; \underline{\hat{J}} \cdot \underline{n} = \hat{J}\cos\eta, \;\; \text{and} \;\; \eta = \pm(\pi/2 - \varphi), \tag{2.11}$$

The support function is integrated along the discontinuities constituting the set Σ_U to provide the maximum resisting power

$$\mathcal{P}'_{\text{mr}}(\underline{\hat{U}}) = \int_{\Sigma_U} \pi(\underline{\hat{J}})\, dS \;\geq \mathcal{P}'_{\text{int}}(\underline{\hat{U}})\,, \tag{2.12}$$

which is bounding by above the unknown effective internal power. Combined with the theorem of effective virtual powers in (2.1), this bounding provides

$$\mathcal{P}'_{\text{ext}}(\underline{\hat{U}}) - \mathcal{P}_{\text{acc}}(\underline{\hat{U}}) \leq \mathcal{P}'_{\text{mr}}(\underline{\hat{U}}) \quad \forall \quad \underline{\hat{U}}\, KA\,. \tag{2.13}$$

If the effective external power is smaller than the maximum resisting power for any KA velocity field, the structure is said to be stable under quasi-static conditions (no inertia). It is the condition $\mathcal{P}'_{\text{ext}} = \mathcal{P}'_{\text{mr}}$ for a given velocity field which signals the quasi-static onset of collapse. If the difference $\mathcal{P}'_{\text{ext}} - \mathcal{P}'_{\text{mr}}$ is positive, the structure is said to be dynamically unstable. The collapse mechanism corresponding the maximum value of that difference is said to be dominant and does control the stability conditions, illustrated in Figure 2.2.

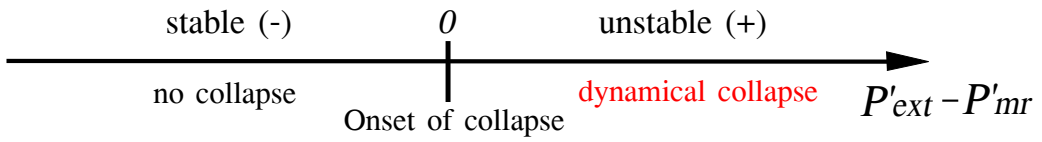


Fig. 2.2: The stability conditions spanned on the axis of the effective, external power and with respect to the maximum resisting power.

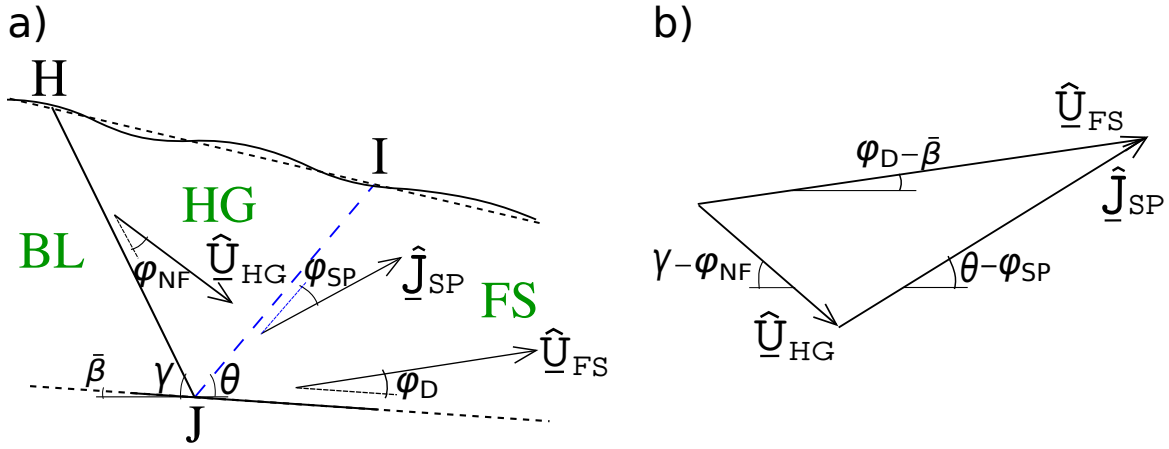


Fig. 2.3: The velocity field for the gravitational collapse, a). The hodogram of the velocity jump across the shear plane JI, b).

2.3 Gravitational collapse

The MST is now applied to the gravitational collapse mode to obtain general stability conditions. These conditions are then specialized to the particular case of cohesionless materials and of a triangular shaped wedge so that the comparison with the classical CCW theory is possible. The role of the length scale set by the cohesion in the stability conditions is then discussed before presenting laboratory experiments to validate the proposed theory.

2.3.1 General stability conditions based on the MST

The KA velocity field for gravitational collapse is uniform over the frontal region (FS), the half-graben (HG) and the back region (BL), Figure 2.3a. The support function in (2.11) guides us in orienting the velocity in each region: the velocity of the FS is inclined by the angle φ_D from the decollement and has for norm $\hat{U}_{FS}$. The HG velocity is inclined by the angle φ_{NF} from the normal fault JH and has the norm $\hat{U}_{HG}$. The BL has a null velocity since the back-wall is

not displaced. The velocity jump at the shear plane JI is the difference $\underline{\hat{U}}_{FS} - \underline{\hat{U}}_{HG}$, a vector of norm $\hat{J}_{SP}$ and oriented by the angle φ_{SP} from JI in Figure 2.3a. The velocity vectors are thus all oriented and we are left with the determination of their norms. The hodogram of the velocity jump across the shear plane which is presented in Figure 2.3b provides that information by application of the law of the sines

$$\frac{\hat{U}_{HG}}{\sin(\theta - \varphi_{SP} - \beta - \varphi_D)} = \frac{\hat{U}_{FS}}{\sin(\theta + \gamma - \varphi_{SP} - \varphi_{NF})} = \frac{\hat{J}_{SP}}{\sin(\gamma + \beta - \varphi_{NF} + \varphi_D)}\,. \tag{2.14}$$

There is nevertheless an indeterminacy in the value of the three ratios in (2.14) which is eliminated by setting one of them arbitrarily equal to 1.

The external effective power defined in (2.2) for this velocity field reads

$$\begin{aligned}\mathcal{P}'_{\text{ext}}(\underline{\hat{U}}) = \rho \underline{g} \cdot (S_{FS}\underline{\hat{U}}_{FS} + S_{HG}\underline{\hat{U}}_{HG}) + \int_J^B p_D \, dS \, \underline{n}_{JB} \cdot \underline{\hat{U}}_{FS} + \int_J^I p_{JI} \, dS \, \underline{n}_{JI} \cdot \underline{\hat{J}}_{SP} \\ + \int_J^H p_{JH} \, dS \, \underline{n}_{JH} \cdot \underline{\hat{U}}_{HG} + \int_H^I p \, dS \, \underline{n}_{HI} \cdot \underline{\hat{U}}_{HG} + \int_I^B p \, dS \, \underline{n}_{IB} \cdot \underline{\hat{U}}_{FS}\,,\end{aligned} \tag{2.15}$$

in which S_{FS} and S_{HG} are the areas of the front and the half-graben, respectively. The first term in the right-hand side of (2.15) corresponds to the power of the velocity field on gravity. The next three integrals are the contribution of the power of the velocity on the pressure field within the decollement (JB), the shear plane (JI) and the normal fault (JH), respectively. The last two terms result from the power of the pressure on the topography. Note that the velocity field being divergence free, there is no contribution to the effective external power of the pressure field within the bulk. Expression (2.15) is now simplified by application of the following weak form of Archimedes' theorem: the power of the velocity field on the hydrostatic part of the pressure is equal to the opposite of the power of the same velocity field on the vertical forces resulting from the weight of the displaced regions, if assumed composed of density ρ_f. The effective external power is then

$$\begin{aligned}\mathcal{P}'_{\text{ext}}(\underline{\hat{U}}) = (\rho - \rho_f)\underline{g} \cdot \left(S_{FS}\underline{\hat{U}}_{FS} + S_{HG}\underline{\hat{U}}_{HG}\right) \\ + \int_J^B \Delta p_D \, dS \, \underline{n}_{JB} \cdot \underline{\hat{U}}_{FS} + \int_J^I \Delta p_{JI} \, dS \, \underline{n}_{JI} \cdot \underline{\hat{J}}_{SP} + \int_J^H \Delta p_{JH} \, dS \, \underline{n}_{JH} \cdot \underline{\hat{U}}_{HG}\,,\end{aligned} \tag{2.16}$$

and is expressed simply in terms of the departure of the pressure from the hydrostatic condition.

The maximum resisting power in (2.12) is now combined with the support function in (2.11) for the proposed velocity field:

$$\mathcal{P}'_{\text{mr}}(\underline{\hat{U}}) = C_D L_{JB} \cos(\varphi_D)\hat{U}_{FS} + C_{NF} L_{JH} \cos(\varphi_{NF})\hat{U}_{HG} + C_{SP} L_{JI} \cos(\varphi_{SP})\hat{J}_{SP}\,. \tag{2.17}$$

It is the sum of the contribution of the decollement segment JB, the normal fault JH and of the shear plane JI.

Application of the MST requires now to maximise the difference $\mathcal{P}'_{\text{ext}} - \mathcal{P}'_{\text{mr}}$ in terms of the dips γ and θ and the length L_{JB}. If that maximum is negative, the system is stable, otherwise there is a quasi-static or a dynamic instability and the optimum triplet of parameters (γ, θ, L_{JB}) define the dominant collapse mechanism.

2.3.2 Comparison with CCW theory

The general solution in (2.16) and (2.17) is now specialized for the case of cohesionless materials. The maximum resisting power is then null and the stability condition reduces to $\mathcal{P}'_{\text{ext}} = 0$. In this instance, and for a triangular wedge, the effective external power (2.16) reduces to

$$\begin{aligned}\mathcal{P}'_{\text{ext}}(\underline{\hat{U}}) = (\rho - \rho_f) g \big[& S_{HG} \hat{U}_{HG} \sin(\gamma - \varphi_{NF}) - S_{FS} \hat{U}_{FS} \sin(\varphi_D + \beta) \big] \\ & + \Delta\lambda_B \rho g \frac{L_{JH}^2 \sin(\gamma - \alpha)}{2 \cos\alpha} \hat{U}_{HG} \sin(\varphi_{NF}) + \Delta\lambda_B \rho g \frac{L_{JI}^2 \sin(\theta + \alpha)}{2 \cos\alpha} \hat{J}_{SP} \sin(\varphi_{SP}) \\ & + \Delta\lambda_D \rho g \frac{L_{JB}^2 \sin(\alpha + \beta)}{2 \cos\alpha} \hat{U}_{FS} \sin(\varphi_D) = 0\end{aligned} \tag{2.18}$$

with

$$S_{HG} = \frac{\sin^2(\alpha + \beta) \sin(\gamma + \theta)}{2 \sin(\gamma - \alpha) \sin(\theta + \alpha)} L_{JB}^2 \,, \quad S_{FS} = \frac{\sin(\alpha + \beta) \sin(\theta - \beta)}{2 \sin(\theta + \alpha)} L_{JB}^2 \,,$$

$$L_{JH} = \frac{\sin(\alpha + \beta)}{\sin(\gamma - \alpha)} L_{JB} \quad \text{and} \quad L_{JI} = \frac{\sin(\alpha + \beta)}{\sin(\theta + \alpha)} L_{JB} \,,$$

in which $\Delta\lambda_B$ and $\Delta\lambda_D$ are the fluid overpressure ratios of the bulk material and the decollement, respectively. To confirm with the assumption of the CCW theory, the fluid ratios and friction angles in the normal fault JH and shear plane JI are set to the bulk ratio $\Delta\lambda_B$ and the bulk friction angle φ_B.

It is necessary to maximise (2.18) with respect to the two angles θ and γ. Stability requires this function to be negative at its maximum. Note from (2.18) that the external power is proportional to the square of the length L_{JB} of the structure. As a consequence, this length is not an outcome of the optimization and remains arbitrary. This indeterminacy is a common feature with the CCW theory. Furthermore, the slope α can be varied in the MST approach as a parameter to find the critical value α_c for which there is a transition from stable to unstable conditions. In that sense, it is intended to prove next that the results of the optimization and the parametric study are identical to those of the CCW theory.

Table 2.1: Geometrical and material parameters and fluid ratios for the wedge analysis. Parameter are for the gravitational collapse (column 3), the tectonic collapse (column 4) and for the field study (column 5). Values are constant or varied within the ranges presented. Notation: $B-$ Bulk, $SP-$ Shear plane, $NF-$ Normal fault, $D-$ Decollement and $BW-$ Back-wall.

Notation	Definition	Value/Range [Gravitational collapse]	Value/Range [Tectonic collapse]	Value/Range [Field example]	Unit
α	topographic slope	$-$30-45	$-$39-39	0-5	deg.
β	decollement angle	$-$10-90	27-90	3.72	deg.
L_{AB}	decollement length	-	-	29.1	km
D_C	depth of the back top (point C)	-	-	3.15	km
φ_a	friction angle ($a = B, SP, NF$)	30	39	27.9	deg.
φ_D	decollement friction angle	10	27	10, 15	deg.
φ_{BW}	back-wall friction angle	-	0-39	-	deg.
C_a	cohesion ($a = B, SP, NF$)	0-0.07$\rho g L_{AB}$	0	(0-10)$\times 10^6$	Pa
C_D	decollement cohesion	0	0	0	Pa
C_{BW}	back-wall cohesion	-	0	-	Pa
ρ_f	fluid phase density	1000	1000	1030	kg/m^3
ρ	saturated rock density	2120	2000	2400	kg/m^3
λ_{hydro}	hydrostatic pressure ratio	0.47	0.5	0.42	-
$\Delta\lambda_B$	bulk overpressure ratio	0-0.53	0-0.5	0-0.58	-
$\Delta\lambda_D$	decollement overpressure ratio	0-0.53	0-0.5	0-0.58	-
g	gravity acceleration	9.81	9.81	9.81	m/s^2

The comparison of the MST and CCW predictions requires to use identical definition of the overpressure ratios and thus of the distance z to the sea floor. This z-axis is vertical in the original work of *Hubbert and Rubey* [1959] as well as in *Pons and Leroy* [2012] and in the present contribution. The z-axis is perpendicular to the decollement in *Davis et al.* [1983] and to the topography in *Dahlen* [1984] and *Lehner* [1986]. This last choice is certainly in line with the classic Rankine assumption that stress varies with distance to the topography and not with the position along it. However it leads to differences in the pressure ratio definition compared to the original definition adopted herein. The differences are presented in details in 1.

There is a further complexity in the comparison of the MST and the CCW predictions due to an approximation introduced by *Dahlen* [1984]. He assumed that the normal stress to the decollement can be approximated by the stress normal to the topography and he obtained

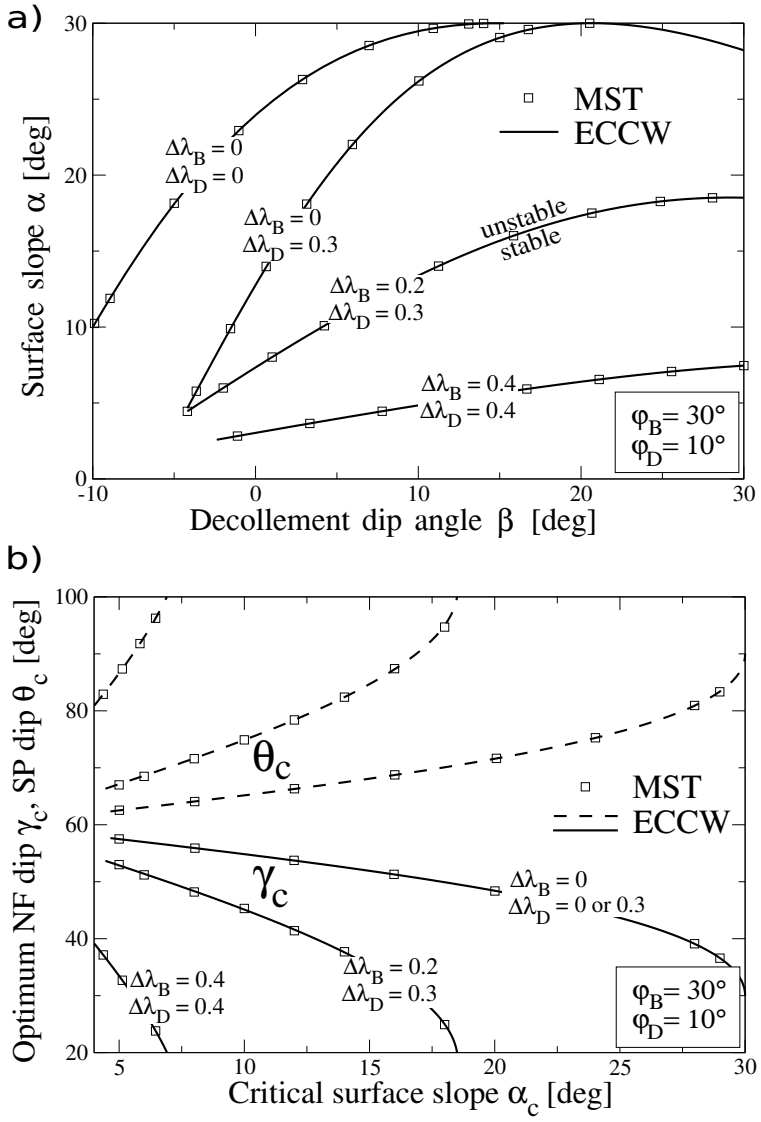


Fig. 2.4: Comparison of MST (symbols) and ECCW predictions (curves) for cohesionless materials, overpressure ratio $\Delta\lambda_D$ in the decollement and bulk fluid overpressure ratio $\Delta\lambda_B$, (a). The optimum dips of the normal fault (NF, γ_c, solid curves) and of the shear plane (SP, θ_c, dashed curves) for the two theories are compared in (b).

an effective friction coefficient in the decollement. The result of this approximation is a simple, albeit implicit expression for the critical taper angle which is widely used today. The approximation is acceptable in compression since the taper angle is small but leads to a loss of accuracy in extensional regime for which the taper angle is worth several tenth of degrees. This shortcoming was recognized and corrected by *Wang et al.* [2006]. This modification of the original work of *Dahlen* [1984] is referred to in what follows as the exact critical Coulomb wedge (ECCW) theory and is presented in 2 to complement the presentation of *Wang et al.* [2006].

Comparison of the MST and ECCW predictions are presented in Figure 2.4, the properties corresponding to the third column of the Table 2.1. The MST predictions obtained as follows: choose a value of β, determine the optimum orientation of the two dips (θ and γ), and check the sign of (2.18). For example, for $\beta = 20°$ and $\Delta\lambda_B = 0.2, \Delta\lambda_D = 0.3$, the function is negative for α less than 17.3°, approximately, and is positive for larger values. The stability transition α_c is thus determined. The critical slope α_c is presented in Figure 2.4a as a function of the decollement dip β. The ECCW and the MST results correspond to the solid curves and to the various symbols, respectively. The two sets of predictions are identical for the four sets of overpressures in the bulk $\Delta\lambda_B$ and decollement $\Delta\lambda_D$. The range in β does not exceed the bulk frictional angle since gravitational collapse mode not using the decollement is expected beyond this value: the maximum α_c is indeed φ_B, seen as the repose angle. Looking at the various sets of pressure considered in this analysis, note that increasing the bulk and decollement pressure ratios decreases the critical slope α_c. Note also that the gravitational instability mode does not require a seaward dipping decollement (β negative). The pressure and frictional properties of the decollement can overcome the difficulty of pushing upslope the sediments in the frontal section during a gravitational collapse. Finally, note that the two theories do predict the same fault dips θ and γ, Figure 2.4b.

2.3.3 The role of cohesion in a triangular wedge

The CCW theory relies on the assumption of cohesionless materials so that the stress state within the wedge scales with the distance z to the topography. The introduction of cohesion ruins this simplicity and the elegance of a potentially analytical solution for the critical stability conditions. The MST approach does not suffer from such limitations.

The characteristic length is chosen as the extent of the decollement L_{AB}, and this leads to the characteristic stress $\rho g L_{AB}$ taken as the reference stress. Dimensionless quantities are noted with a superposed tilde. The stability criterion (2.13) with no inertia is written in a dimensionless form, symbolically, as:

$$\tilde{L}_{JB}\tilde{\mathcal{P}}'_{\text{ext}}(\theta,\gamma) \leq \tilde{C}\,\tilde{\mathcal{P}}'_{\text{mr}}(\theta,\gamma)\,, \tag{2.19}$$

where $\tilde{C} = C/(\rho g L_{AB})$ and using expressions (2.17) and (2.18). The right-hand side is independent of $\tilde{L}_{JB}$ and the left-hand side is proportional to it. As a consequence, the stability condition (equality in 2.19) must be true for any admissible value of $\tilde{L}_{JB}$, in particular with its maximum value. Therefore, the stability transition is associated with the maximum value $\tilde{L}_{JB}$, which is close to one for our collapse mechanism.

The influence of the bulk cohesion on the critical slope α_c is now presented in Figure 2.5a where the activation of the whole decollement is assumed ($\tilde{L}_{JB} = 1$, for sake of simplicity). The physical properties are given in the third column of Table 2.1. The dimensional decollement cohesion $\tilde{C}_D$ is set to zero, the bulk cohesion $\tilde{C}_B$ is varied from zero to 0.07 and the decollement dip β is set to zero. Results are obtained for dry conditions (blue curve), hydrostatic conditions ($\Delta\lambda_B = \Delta\lambda_D = 0$, black curve) and decollement overpressure conditions ($\Delta\lambda_B = 0, \Delta\lambda_D = 0.4$, red curve). The blue (dry) and black (hydrostatic) curves initiate at the same α_c since $\tilde{\mathcal{P}}'_{\text{ext}}$ is proportional to $(\rho - \rho_f)$ (see first line in 2.18). The three curves have the same trend: the larger is $\tilde{C}_B$, the larger is the critical slope. The crossing between the blue and red curves at $\tilde{C}_B = 0.044$ and more generally the fact that the distance between the black and red curves is decreasing with increasing cohesion is more intriguing. This non-linear trend is tentatively explained by considering the dimensionless overpressure in the decollement $\Delta\tilde{p} = -\Delta\lambda\rho g(x_2 + D)/C_B$ where x_2 is the second coordinate of a point in the decollement. Keeping this position constant while increasing C_B results in a decrease of the dimensionless pressure. This pressure term in the external power (2.18) thus decreases and the results for no-overpressure (black curve) and with over-pressure (red curve) should indeed converge for large values of the cohesion.

The influence of the cohesion is also illustrated in Figure 2.5b where the length $\tilde{L}_{JB}$ is presented as a function of the fluid pressure ratio $\Delta\lambda_D$ for $\tilde{C}_B = 0.01$ and 0.02. For $\tilde{C}_B = 0.02$, the system is stable for $\Delta\lambda_D$ less than 0.4. For larger values the system is unstable for the largest slip extent $\tilde{L}_{JB} \simeq 1$. Note that shorter lengths are also unstable for $\Delta\lambda_D > 0.4$. However, the largest length remains the most unstable in the sense defined above that the difference

$\tilde{\mathcal{P}}'_{\rm mr} - \tilde{\mathcal{P}}'_{\rm ext}$ is the largest. Decreasing the cohesion ($\tilde{C}_B = 0.01$) reduces the domain of stability in this fluid pressure ratio-length plane but does not alter the selection of the longest possible length at the onset of collapse.

2.3.4 Experimental validation

Table 2.2: Parameters for gravitational collapse experiments and for the experiments proposed to estimate the frictional and cohesive properties of the sand and plaster mixture. Note that the cohesion is not a monotonically increasing function of the plaster proportion.

Material		Cliff height	Slope dip	Cohesion	Friction angle	Density	Normalized cohesion	Dip measured
Sand	Plaster[wt%]	H_c [cm]	κ [deg]	C_B [Pa]	φ_B [deg]	ρ [g/cm^3]	$\tilde{C}_B$ ($= C_B/\rho g L_{AB}$)	$\bar{\beta}_c$ [deg]
100	0	-	-	0	30-33	1.710	0	17
85	15	3-4	62-68	50-70	35-45	1.515	0.012-0.016	18.7, 20.3, 18.8*, 17.8*
75	25	6-7	62-68	100-120	35-45	1.464	0.023-0.027	18.6, 19.8, 17.8*
50	50	11-12	62-68	180-200	35-45	1.163	0.043-0.047	22, 22, 21.3*
25	75	9-10	62-68	150-170	35-45	0.931	0.035-0.040	21.5

$\star$ Values obtained in tests where glass microbeads were introduced along the side-walls to reduce the friction.

The theory presented above indicates that the first collapse is associated with the maximum length of the decollement ($L_{JB} \simeq L_{AB}$). To provide an experimental validation of this claim, we propose to vary the angle β keeping a constant taper angle $\alpha+\beta$ in a laboratory experiment. This variation is conducted up to first failure to be able to inspect the first collapse mode.

The experimental set-up consists of a rectangular glass box, initially horizontal, in which a wedge of cohesive material is built with a length $L_{AB} = 30$ cm and a maximum height 5 cm, yielding a taper angle of 9.5°, Figure 2.6a and b. It rests on a 2 mm thick glass microbeads layer. At the back, the wedge has a topography parallel to the decollement composed of a sand paper. The experiment consists in lifting the back side of the box to increase the basal slope $\bar{\beta}$ until the wedge collapses by sliding against the fixed base and lateral walls. The basal dip at failure is denoted $\bar{\beta}_c$. Its value depends in particular on the cohesion of the material of the wedge. In most experiments (results indicated with an open circle in Figure 2.7) the material was in direct contact with the vertical lateral walls of the box. To estimate the bias due to this lateral friction, several experiments were conducted inserting a layer of glass microbeads between the wall and the material (results indicated with a black circle in Figure 2.7).

The analogue material production, characterisation and implementation were done as follows. The bulk, cohesive materials are mixtures of CV32 eolian quartz sand (maker: SIFRACO,

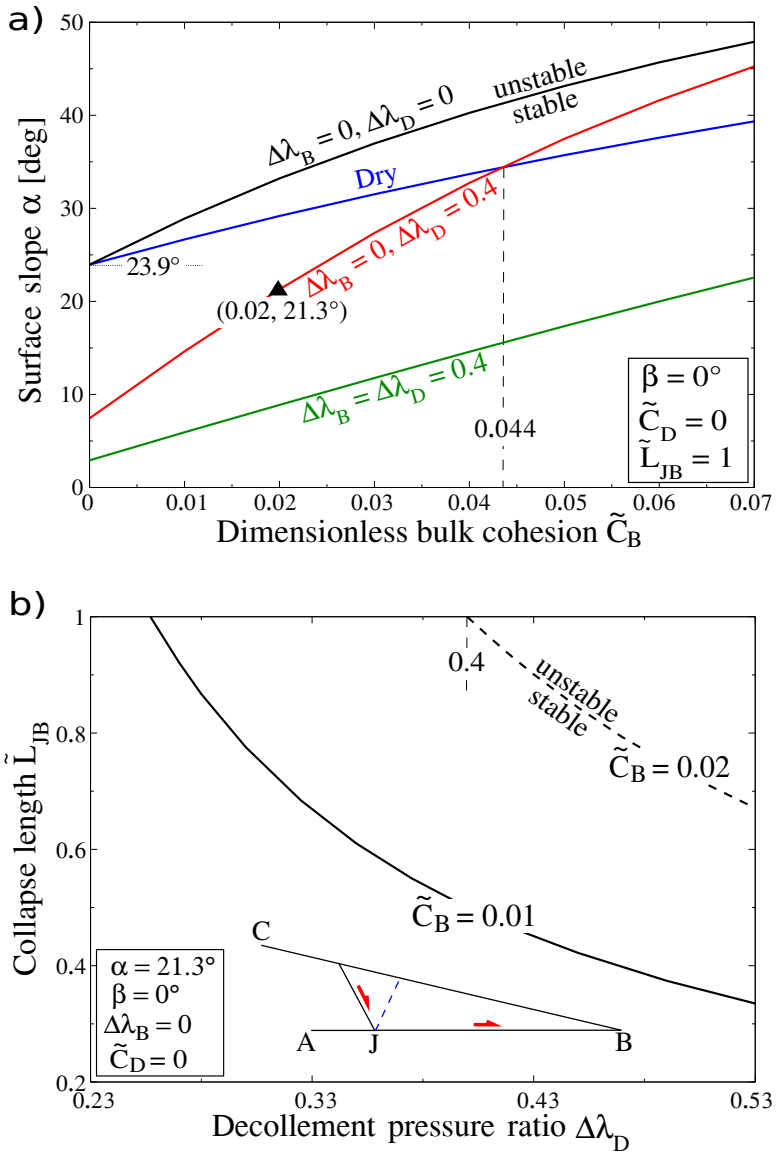


Fig. 2.5: The influence of the bulk cohesion $\tilde{C}_B$ on the critical slope α_c is presented where the value of α_c is computed at a series of values of bulk cohesion $\tilde{C}_B$ for the dry (blue curve), hydrostatic (black curve) and overpressure condition (red curve), respectively, a). The normalized collapse length $\tilde{L}_{JB}$ is shown as the function of the decollement fluid ratio $\Delta\lambda_D$ for bulk cohesion $\tilde{C}_B = 0.01$ and 0.02, respectively, b). The triangular in a), bulk cohesion $\tilde{C}_B$= 0.02 (e.g. C_B= 4.1 MPa with a extent $L_{AB} = 10$ km), shows that the maximum slope of a stable wedge is less than 21.3°.

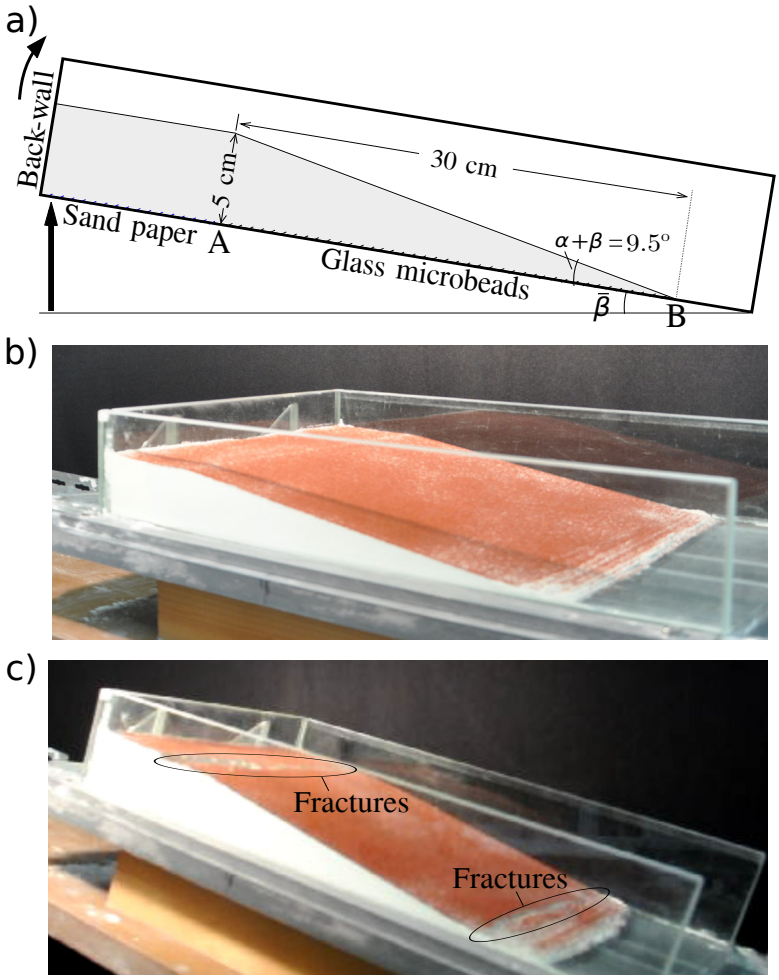


Fig. 2.6: Cross-section of the experimental prototype proposed to check that the stability transition sees the maximum length of the decollement activated, a). The photography in b) presents the initial state. The slope $\bar{\beta}$ is increased by lifting the back of the box (black arrows in a) until the wedge collapses, c).

Sand CV32, 250 μm median grain size) and plaster in various proportions (Table 2.2, column 1 and 2). These materials were sifted to fill the box and the surface was then scraped to obtain the desired wedge shape. During scraping, some compaction of the pack is expected, thus perturbing its density and frictional properties. The use of a Casagrande box to measure the frictional properties of this class of analogue materials is precluded because the normal stress will compact the material and increase very substantially the cohesion beyond the value achieved in our set-up. We nevertheless performed dedicated measurements of these properties. The density was measured using density cups [*Trautmann et al.*, 1985; *Maillot*, 2013], and the frictional properties (bulk cohesion C_B and friction angle φ_B) were estimated by digging a vertical cliff in the bulk material, and increasing its height to its maximum value H_c until collapse. Collapse, at least theoretically, is associated with the sliding of a triangular section replacing the cliff by an inclined ramp. Such collapse mechanism has been considered recently for studying weathering of natural cliffs [*Utili and Crosta*, 2011] and is classical in the civil-engineering literature [*Davis and Selvadurai*, 2005]. It is known that the material properties and the geometrical parameters of the collapse mechanisms are related by

$$H_c = \frac{4C_B}{\rho g}\frac{\cos(\varphi_B)}{1-\sin(\varphi_B)}, \quad \kappa = \pi/4 + \frac{\varphi_B}{2}, \tag{2.20}$$

with the ramp dip κ being the classical fault dip in extension for a Coulomb material. Results with the associated error range are shown in Table 2.2.

The decollement is composed of glass microbeads, a material of different frictional properties than the bulk. Cohesion is disregarded ($C_D = 0$) and the friction angle is estimated by placing a bottomless cup of material on the glass microbeads and tilting the glass base until the cup slides. The basal friction is estimated to be $\varphi_D = 17 \pm 1^{\circ}$.

Experimental and theoretical results are presented in Figure 2.6c, 2.7, and Table 2.2 (last two columns). The first observation (Figure 2.6c) is that the collapse involves the activation of the whole length L_{AB} of the weak decollement. The frontal deformation observed at the tip of the wedge (Figure 2.6c) is due to imperfections of the surface slope towards the tip which are ignored in the present analysis.

The second observation is that $\bar{\beta}_c$ fluctuates by one or two degrees when repeating experiments. Therefore, its increase with cohesion from an average of 17° to 22° is meaningful. It is in good agreement with the 5° increase predicted with the MST for three values of φ_B (35°, 40° and 45°). However, the value of $\bar{\beta}_c$ for the experiments with lateral friction (open circles)

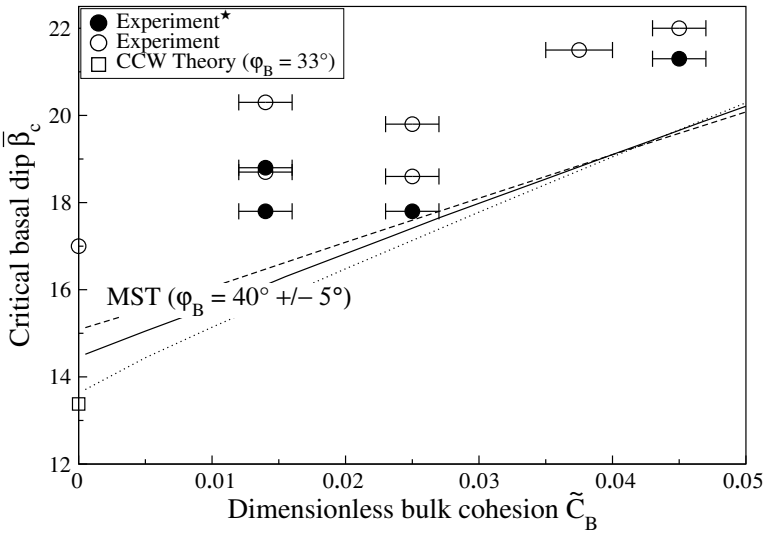


Fig. 2.7: The critical basal dip $\bar{\beta}_c$ (taper angle constant, 9.5°) at the onset of gravitational collapse (Figure 2.6) as function of the cohesion of the wedge material. The open circle are experimental results with relatively high friction on the side wall of the box, the black circle are obtained with lower lateral friction (glass microbeads between side wall and bulk material, friction around $17 \pm 1^{\circ}$). The dotted, solid and dashed curve are the theoretical results of bulk friction angle $\varphi_B = 35^{\circ}$, 40° and 45°, respectively.

is systematically larger by 2° or 3°, than predicted, either with the MST or the CCW theory ($\varphi_B = 33^{\circ}$, the square in Figure 2.7) for cohesionless materials. We attribute this difference to spurious friction on the lateral walls [*Souloumiac et al.*, 2012], which are not taken into account in both 2D theoretical descriptions (MST and CCW). Indeed, experiments with reduced lateral friction (black circles) present a lower discrepancy, while keeping the same trend in the variation of $\bar{\beta}_c$ with $\tilde{C}_B$.

The main conclusions of that series of ten experiments is that the collapse onset occurs for the largest possible slip extent and that the critical wedge angle is well predicted by the MST accounting for cohesion. The experimental uncertainties are coming mainly from the difficulty in (i) constructing homogeneous and reproducible packs, and (ii) estimating the frictional properties of these packs at very low stress levels. In that respect, *Galland et al.* [2006] and *van Gent et al.* [2010] have proposed useful devices and protocols to characterize the friction, the cohesion and the tensile strength, accounting for the initial compaction (or void ratio) of the powder.

2.4 Tectonic extensional collapse

The tectonic extensional collapse induced by the retreat of the vertical back-wall is now discussed, Figure 2.1b. The upper bound to the force Q_u is calculated for the three different collapse mechanisms presented in Figure 2.8. The first mechanism is typical of a super-critical wedge sliding on its decollement as a rigid block. The second mechanism concerns a sub-critical wedge and the internal deformation is close to the back-wall. The third mechanism is valid for both sub-critical and super-critical wedges depending on the length L_{AG} of the activated decollement, measured from the back-wall to the root (point G) of the normal fault (GE) and shear plane (GF). The two regions, BL and HG, have uniform velocities. The three mechanisms share the same velocity of the back-wall $\hat{\underline{U}}_{BW}$, which is directed horizontally and of norm $\hat{U}_{BW}$ set to one. Note that for the three cases, slip between the bulk material and the back-wall is accounted for. The derivation of the bounds is presented in the Electronic Supplement and only the final results are provided here.

2.4.1 Mechanism (1): decollement fully activated

The first collapse mechanism corresponds to the rigid translation of the wedge on the fully activated decollement at the uniform velocity of norm $\hat{U}_D$, a vector oriented by the angle φ_D from the decollement, see Figure 2.8(1). The velocity jump at the back-wall is the difference $\hat{\underline{U}}_{BW} - \hat{\underline{U}}_D$, a vector of norm $\hat{J}_{BW}$ and oriented by the angle φ_{BW} from the vertical direction. The application of the MST provides the tectonic upper bound Q_{u1}

$$\begin{aligned} Q_{u1} = {} & C_D L_{AB} \cos(\varphi_D) \hat{U}_D + C_{BW} L_{AC} \cos(\varphi_{BW}) \hat{J}_{BW} - (\rho - \rho_f) g S_{ABC} \hat{U}_D \sin(\beta - \varphi_D) \\ & - \Delta\lambda_D \rho g S_{ABC} \hat{U}_D \frac{\sin(\varphi_D)}{\cos\beta} + \frac{1}{2} \Delta\lambda_B \rho g L_{AC}^2 \hat{U}_D \cos(\beta - \varphi_D) - \frac{p(A) + p(C)}{2} L_{AC} \,, \end{aligned} \tag{2.21}$$

where C_{BW}, C_D and S_{ABC} are the back-wall interface cohesion, the decollement cohesion and the wedge area, respectively. Pressure at any point M is denoted $p(M)$. The wedge velocity and the back-wall jump are related by

$$\hat{U}_D = \frac{\cos(\varphi_{BW})}{\cos(\varphi_{BW} - \beta + \varphi_D)} \,, \quad \hat{J}_{BW} = \frac{\sin(\beta - \varphi_D)}{\cos(\varphi_{BW} - \beta + \varphi_D)} \,. \tag{2.22}$$

according to the hodogram in Figure 2.8(1).

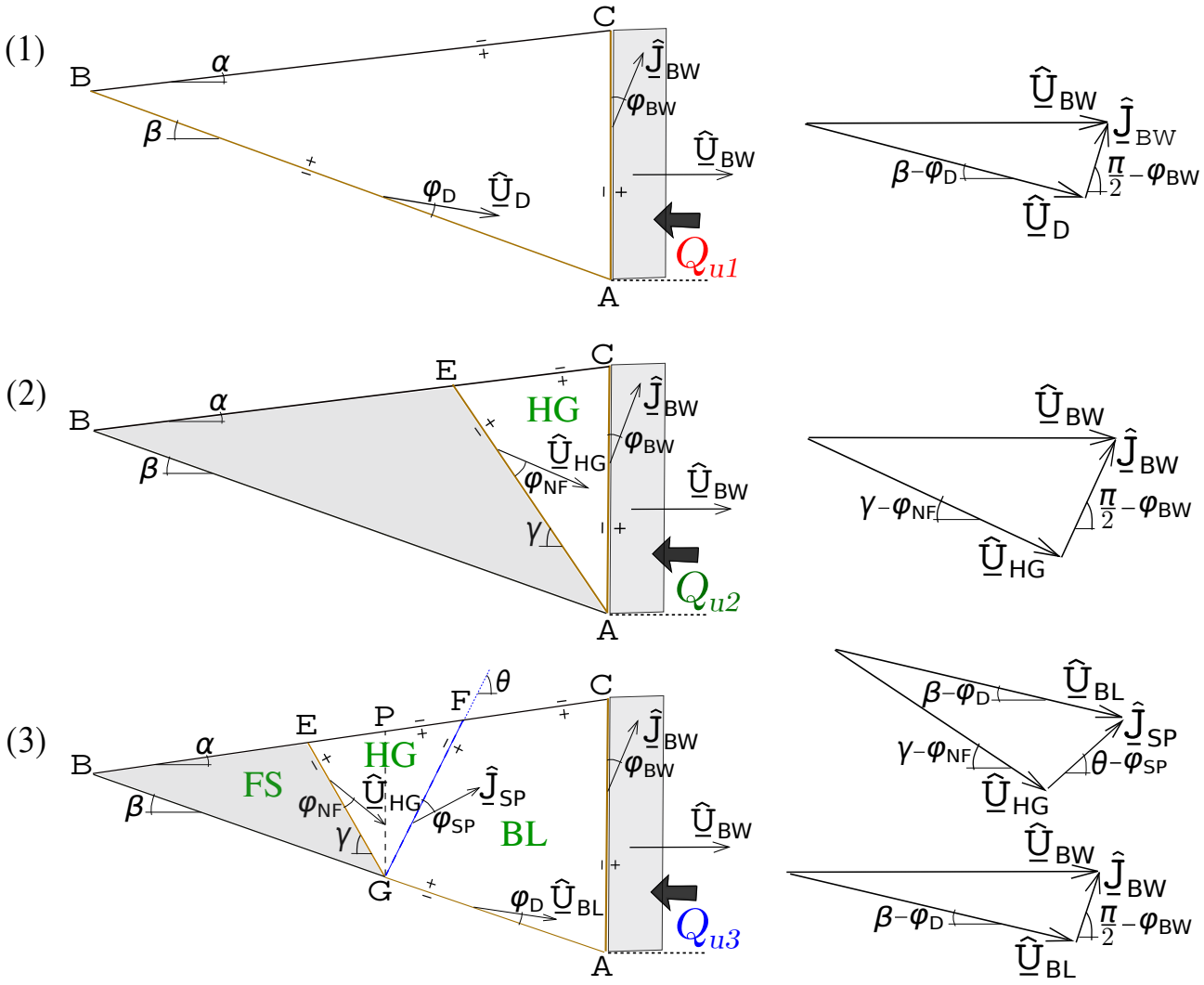


Fig. 2.8: The tectonic extensional collapse is examined with three mechanisms corresponding to the full activation of the decollement in (1), the activation of a normal fault (AE) rooting at the back-wall in (2) and the partial activation of the decollement, of a normal fault (GE) and of a shear plane (GF) in (3). The hodogram of the velocities are also presented for each mechanism.

2.4.2 Mechanism (2): a normal fault rooting at the back-wall

The second collapse mechanism consists of a normal fault rooting at the base of the back-wall and dipping at γ, Figure 2.8(2). There is no activation of the decollement. The half-graben has the uniform velocity field of norm $\hat{U}_{HG}$, which is oriented by the angle φ_{NF} from the normal fault, Figure 2.8(2). The jump in velocity across the back-wall interface is $\underline{\hat{J}}_{BW} = \underline{\hat{U}}_{BW} - \underline{\hat{U}}_{HG}$ and is oriented with the angle φ_{BW} from back-wall. The MST pleads to the following expression for the tectonic upper bound Q_{u2}

$$\begin{aligned} Q_{u2} = {} & C_{NF} L_{AE} \cos(\varphi_{NF}) \hat{U}_{HG} + C_{BW} L_{AC} \cos(\varphi_{BW}) \hat{J}_{BW} - (\rho - \rho_f) g S_{HG} \hat{U}_{HG} \sin(\gamma - \varphi_{NF}) \\ & - \Delta\lambda_B \rho g S_{HG} \hat{U}_{HG} \frac{\sin(\varphi_{NF})}{\cos\gamma} + \frac{1}{2} \Delta\lambda_B \rho g L_{AC}^2 \hat{U}_{HG} \cos(\gamma - \varphi_{NF}) - \frac{p(A) + p(C)}{2} L_{AC} \,, \end{aligned} \tag{2.23}$$

in which C_{NF} and S_{HG} are the normal-fault cohesion and the surface of the half-graben. The velocities associated to this second collapse mechanism

$$\hat{U}_{HG} = \frac{\cos(\varphi_{BW})}{\cos(\varphi_{BW} - \gamma + \varphi_{NF})} \,, \quad \hat{J}_{BW} = \frac{\sin(\gamma - \varphi_{NF})}{\cos(\varphi_{BW} - \gamma + \varphi_{NF})} \,. \tag{2.24}$$

are deduced from the hodogram in Figure 2.8(2).

2.4.3 Mechanism (3): a normal fault and a shear plane rooting on the decollement

The third mechanism consists of the normal fault GE dipping at γ and the shear plane GF dipping at θ, Figure 2.8(3). The two planes root at point G on the decollement which is activated from point A to G. The geometry of this third mechanism is thus described with three parameters: γ, θ and the distance L_{AG}. The velocities of BL and HG are uniform and denoted $\underline{\hat{U}}_{BL}$ and $\underline{\hat{U}}_{HG}$. These velocities are oriented by the angles φ_D and φ_{NF} from the corresponding plane, see Figure 2.8(3). There are two velocity discontinuities corresponding to the shear plane ($\underline{\hat{J}}_{SP} = \underline{\hat{U}}_{BL} - \underline{\hat{U}}_{HG}$) and to the interface with the back-wall ($\underline{\hat{J}}_{BW} = \underline{\hat{U}}_{BW} - \underline{\hat{U}}_{BL}$). These two jumps are oriented by the angles φ_{SP} and φ_{BW} from the shear plane and to the back-wall,

respectively. The tectonic upper bound is

$$
\begin{aligned}
Q_{u3} &= C_{NF}L_{GE}\cos(\varphi_{NF})\hat{U}_{HG} + C_{SP}L_{GF}\cos(\varphi_{SP})\hat{J}_{SP} + C_D L_{AG}\cos(\varphi_D)\hat{U}_{BL} \\
&+ C_{BW}L_{AC}\cos(\varphi_{BW})\hat{J}_{BW} - (\rho-\rho_f)gS_{HG}\hat{U}_{HG}\sin(\gamma-\varphi_{NF}) - (\rho-\rho_f)gS_{BL}\hat{U}_{BL}\sin(\beta-\varphi_D) \\
&- \Delta\lambda_D\rho g S_{AGPC}\hat{U}_{BL}\frac{\sin(\varphi_D)}{\cos\beta} - \Delta\lambda_B\rho g S_{GEP}\hat{U}_{HG}\frac{\sin(\varphi_{NF})}{\cos\gamma} - \Delta\lambda_B\rho g S_{GFP}\hat{J}_{SP}\frac{\sin(\varphi_{SP})}{\cos\theta} \\
&+ \frac{1}{2}\Delta\lambda_B\rho g L_{AC}^2\hat{U}_{BL}\cos(\beta-\varphi_D) - \frac{p(A)+p(C)}{2}L_{AC}\,.
\end{aligned}
\tag{2.25}
$$

The velocity jumps over the shear plane and at the back-wall are presented in two hodograms in Figure 2.8(3). The application of the law of sines provides

$$
\begin{aligned}
\hat{U}_{BL} &= \frac{\cos(\varphi_{BW})}{\cos(\varphi_{BW}-\beta+\varphi_D)}\,, \qquad \hat{J}_{BW} = \frac{\sin(\beta-\varphi_D)}{\cos(\varphi_{BW}-\beta+\varphi_D)}\,, \\
\hat{J}_{SP} &= \hat{U}_{BL}\frac{\sin(\varphi_D-\beta+\gamma-\varphi_{NF})}{\sin(\theta-\varphi_{SP}+\gamma-\varphi_{NF})}\,, \quad \hat{U}_{HG} = \hat{U}_{BL}\frac{\sin(\theta-\varphi_{SP}-\varphi_D+\beta)}{\sin(\theta-\varphi_{SP}+\gamma-\varphi_{NF})}\,.
\end{aligned}
\tag{2.26}
$$

2.4.4 Comparison with CCW theory for extensional collapse

The objective is to compare our predictions with the CCW theory for extensional collapse for dry, cohesionless materials [*Xiao et al.*, 1991]. These authors presented the CCW theory for extensional wedges and their results are illustrated in Figure 2.9a with the dotted, closed curve. Results are obtained for the material properties summarized in the fourth column of Table 2.1. The wedge is said to be super-critical within the region bounded by this curve: the whole decollement is activated. Outside this domain, we expect only the rear part of the decollement to be activated, next to the retreating wall.

It is proposed to compare the MST with the CCW theory in the following manner. Consider the two segments AA' and BB' in Figure 2.9a corresponding to a variation of the surface slope and the decollement dip, respectively. Along these segments, we compute the three upper bounds (2.21)-(2.26). The least of the three upper bounds is the closest to the exact, unknown tectonic force and the corresponding mechanism is considered to be dominant.

Consider first the segment AA' in Figure 2.9a along which $\beta = 32^\circ$ and α varies within $[-26^\circ; 30^\circ]$. The three upper bounds, normalized by $\rho g S_{ABC}$, along this transect are presented in Figure 2.9b. The collapse mechanism (1) (decollement fully activated) is dominant between point A and point A_{13} on the CCW stability curve (-14.7°). For larger values of α, it is mechanism (3) which is dominant up to point A_{23}. Mechanism (2) is dominant for the rest of

the segment. These transitions from mechanism (1) to (3) and then (3) to (2) are illustrated in Figure 2.9c where the length of the activated decollement, normalized by L_{AB}, is presented. The value is 1 between A and A_{13}; it drops to a small value between A_{13} and A_{23} and finally drops to zero between A_{23} and A'. The MST has thus captured exactly the CCW predictions which is seen here as a transition between modes (1) and (3).

Consider now segment BB' in Figure 2.9a along which $\alpha = 0^o$ and β varies within $[20^o; 45^o]$. From point B to B_{23}, it is mode (2) (no decollement activation) which is dominant. This last point marks the transition to mode (3) which dominates up to point B_{13} at the crossing of the CCW stability limit (36.7^o). Within the super-critical domain, mode (1) dominates of course. The three upper bounds along this segment BB' at the basis of this interpretation are presented in Figure 2.9d.

This method for probing the CCW stability boundary is repeated between point C and C' to come to the conclusion that MST and CCW theories are in agreement.

The new information is the role of the back-wall, not accounted for in the CCW theory, which controls the collapse mechanism away from the stability boundary in the sub-critical domain. The limit between mechanism (2) and (3) as function of β is presented by the dashed curve in Figure 2.9a. This limit is dependent on the back-wall interface friction angle φ_{BW} (assumed equal to the bulk friction in this section). This finding is of course more relevant for the interpretation of experimental than field studies.

2.4.5 Experimental validation

The concept of tectonic collapse mechanism is now validated by applying the MST to the interpretation of the sand-box experiment done by *Xiao et al.* [1991]. The sand box is resting on an inclined ramp with a Mylar sheet acting as a decollement. The initial set-up as well as the first mode of collapse are presented in Figure 2.10a. The left section of the sand body is sticking to the Mylar sheet while slip occurs along a short segment of the decollement close to the back-wall. A normal fault roots at the left end of this segment and partitions the sand body into two regions, a graben being observed on the right of the box. Note from the inclined markers at the back-wall the presence of a vertical zone of intense shear. The geometry of the sand box ($\beta = 32°$, $\alpha = 0$), the sand friction angle ($\varphi_B = 39°$) as well as the friction on the decollement ($\varphi_D = 27°$) are provided by the authors. The missing information is the friction

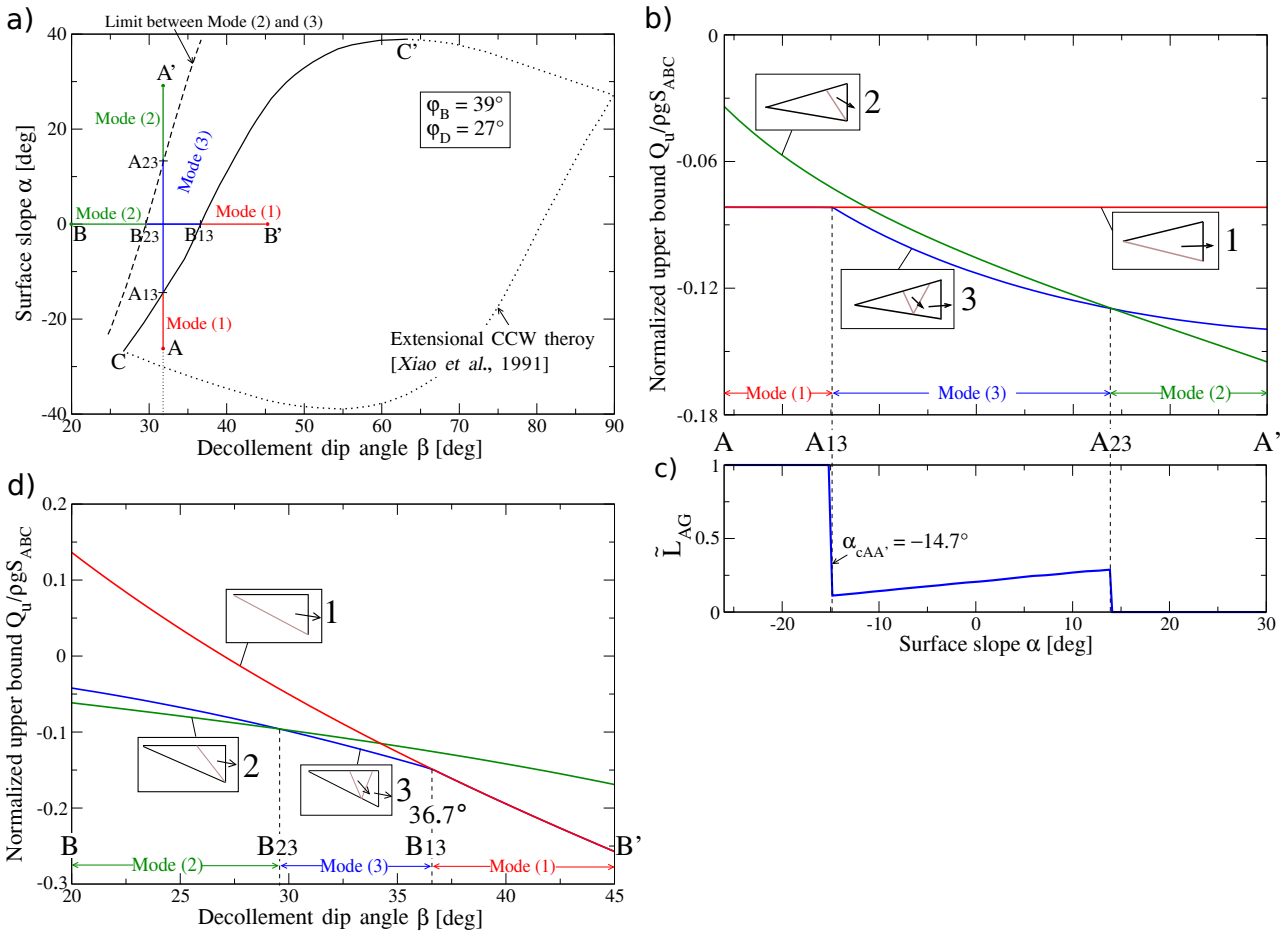


Fig. 2.9: The extensional CCW stability boundary [*Xiao et al.*, 1991] in a), between points C and C' is shown to correspond to the transition between mode (1) (decollement fully activated) and mode (3) (partial activation). This finding is obtained by comparing the least upper bounds for the three modes along segment AA' and BB', b) and d), respectively. The extent of the activated decollement along segment AA' is presented in c).

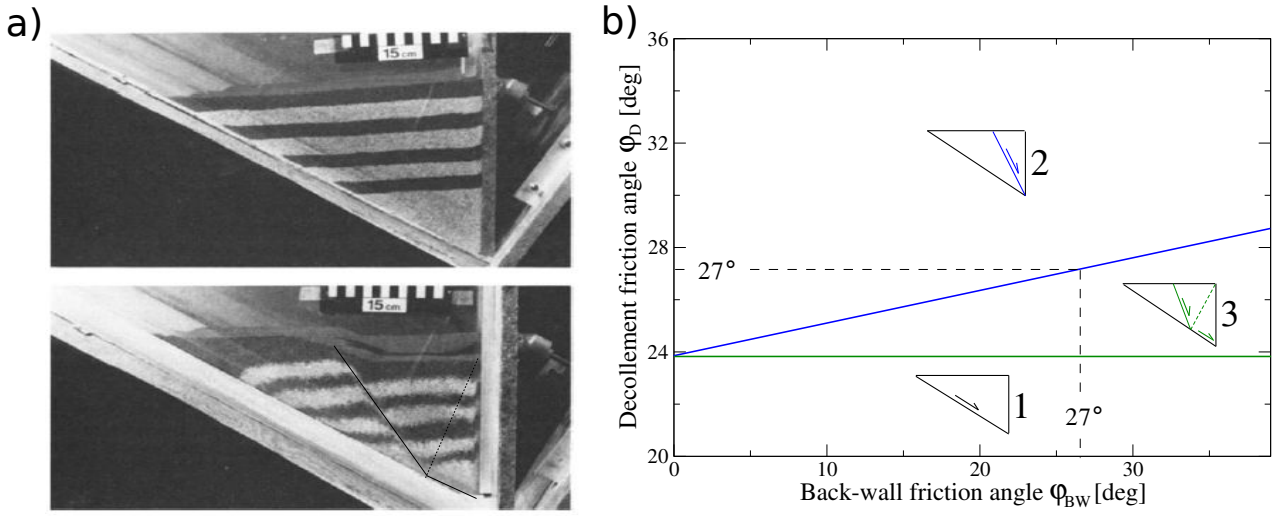


Fig. 2.10: Two photographs of the experiments of *Xiao et al.* [1991] showing the initial set-up and the first collapse mechanism, a). The map of dominant failure mechanism in the space spanned by the back-wall and the decollement friction angles, b).

angle along the back-wall.

The application of the MST is done in two steps. First, the nature of the first collapse mechanism is used to infer the frictional properties along the back-wall. Second, the MST is applied on a modified topography to capture the jump in position of the collapse mechanism from the back-wall region to the left of the sand box, Figure 2.11a.

To capture the missing material property, the three potential collapse mechanisms discussed in section 2.4 are considered. They do apply to this set-up because the upward motion of the Mylar sheet is equivalent to the downward movement of the back-wall. The first collapse mechanism corresponds to super-critical conditions. The second mechanism is sub-critical and assumed that the slip occurs on the back-wall and the onset of a normal fault rooting at its base. The dip of this fault is optimized. The third collapse mechanism assumes that the lower part of the decollement is activated with a half-graben mechanism within the sand body. The dips of the two faults and the position of their common root on the decollement is found by optimization.

The dominance of these three mechanisms is now presented in a map spanned by the friction angle along the back-wall (φ_{BW}) and the decollement friction angle (φ_D), Figure 2.10b. Material and interfaces are assumed cohesionless. It is seen that for decollement friction angle

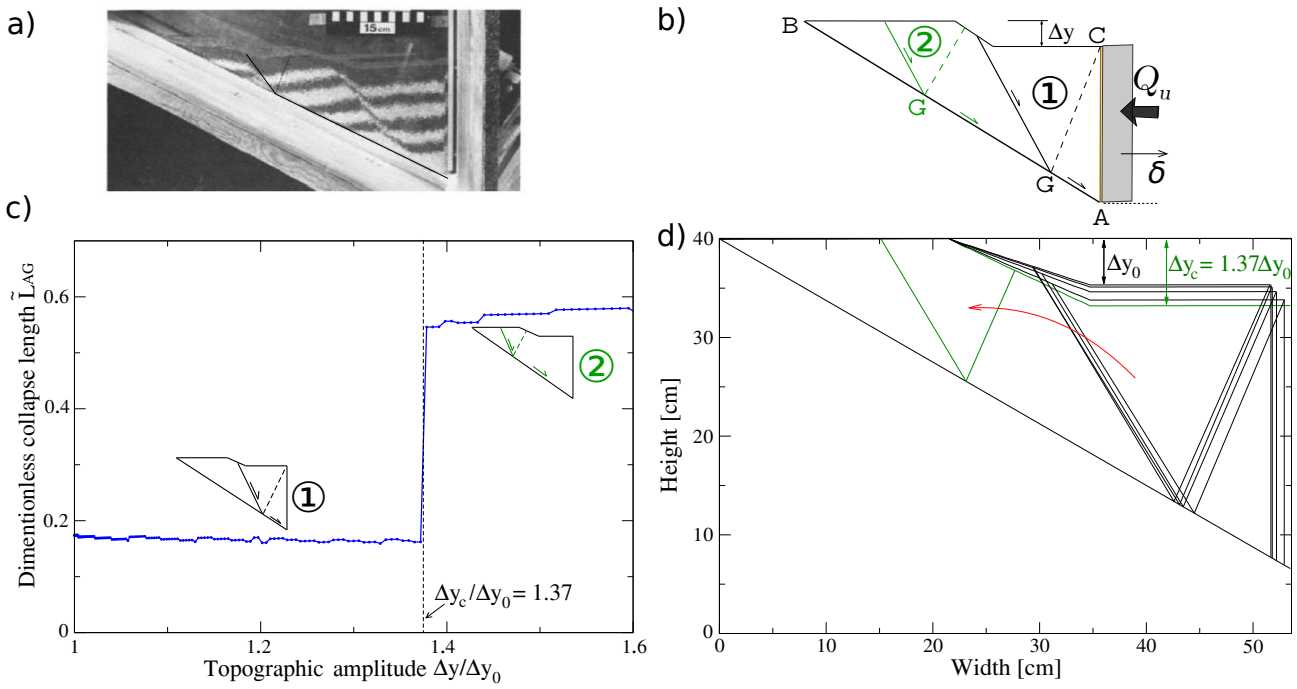


Fig. 2.11: The photograph in a) taken from *Xiao et al.* [1991] shows the development of two collapse mechanisms, the first at the back-wall contact and the second on the left of the sand box. The parametrization of the topographic evolution due to the development of the first collapse mechanism as well as the position of the second mechanism are illustrated in b). The length of the activated decollement for the dominant mechanism as a function of the topographic step amplitude, c). The idealised evolution of the geometry, the successive position of the frontal collapse mechanisms during topographic up to the transition to the second collapse mechanism (green), d).

below 23.8°, the whole decollement is activated, regardless of the back-wall friction. For larger decollement friction values, the dominance is divided between collapse mechanism (2) and (3), the boundary between the two being the blue straight line in Figure 2.10b. The mechanism (2) with a normal fault rooting at the base of the retreating wall is dominant for the larger values of the decollement friction and the mechanism (3) is important in the intermediate range present in the triangular region of Figure 2.10b. Note that within this triangular domain, the shear plane conjugate to the normal fault is always outcropping at the top of the back-wall. The first collapse noticed from the experiment of *Xiao et al.* [1991] is in this intermediate domain. The value $\varphi_D = 27°$ indicates further that the friction coefficient along the wall must thus be greater than 27°. The equality of these two friction angles is coincidental since there is no Mylar sheet between the back-wall and the sand body. A friction angle φ_{BW} of 30° satisfy this condition for mechanism (3) to be dominant and is chosen for sake of illustration in the rest of this analysis.

Our interpretation of the experimental findings of *Xiao et al.* [1991] is that collapse mechanisms (3) is activated and its development results in a step in the topography. This mechanism is nevertheless abandoned after a while for a new half-graben collapse more to the left, as seen in Figure 2.11a and illustrated in Figure 2.11b. It is proposed to capture this transition by modifying incrementally the geometry of our prototype and by repeating the application of the MST. For that purpose, the topography seen in Figure 2.10a prior to the transition of the collapse mechanism to the left is approximated by three segments. The segment to the left, unaltered by the deformation, being Δy above the segment to the right. The central segment has a linear slope between the two other horizontal segments. The vertical displacement Δy is starting from $\Delta y_0 = 4.6$ cm corresponding to the estimate made from the lower photograph in Figure 2.10a. The position of the retreating wall is computed by assuming that the area of sand seen through the glass wall is preserved during the experiment (a proxy for mass conservation).

The normalized collapse length $\tilde{L}_{AG}$ $(= L_{AG}/L_{AB})$ function of $\Delta y/\Delta y_0$ is shown in Figure 2.11c. The activity is occurring at the back of the wedge and four successive positions of the collapse mechanisms are presented in Figure 2.11d. The position of the root of the half-graben is displaced to the right following the wall displacement and the dips of the normal fault and shear plane seems to be unaltered. There is a critical $\Delta y_c = 1.37\,\Delta y_0$ at which the extent of the activated segment of the decollement changes drastically. The new collapse mechanisms (in green in Figure 2.11d) is then to the left. The new shear plane is outcropping within the

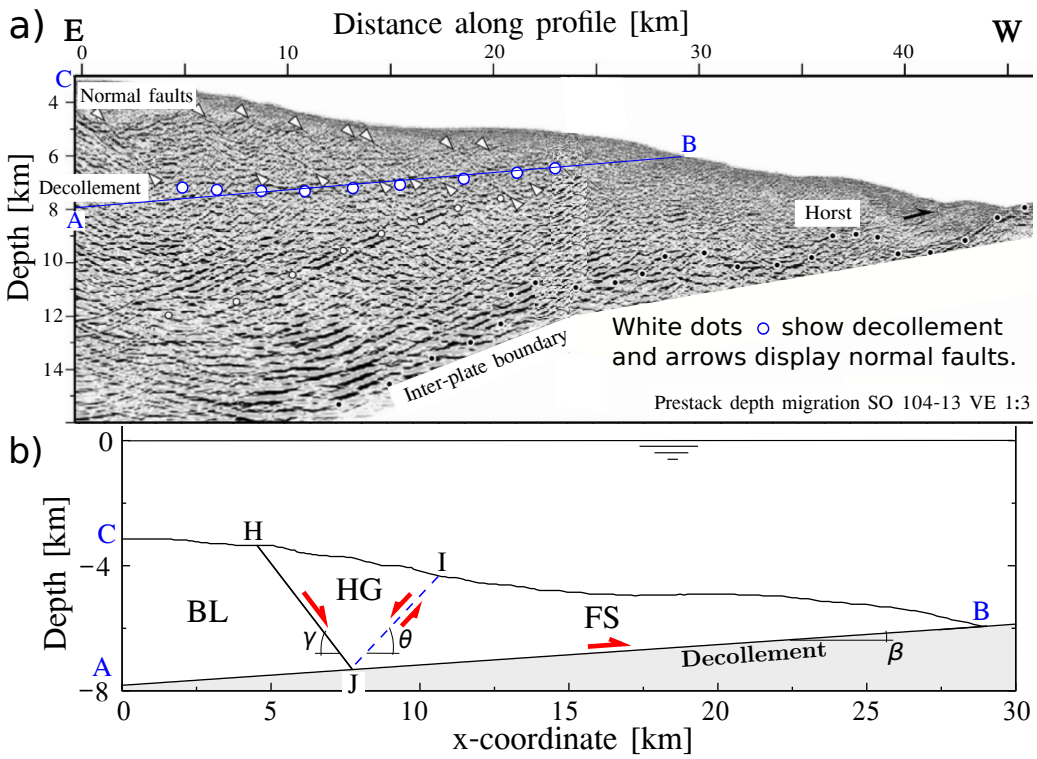


Fig. 2.12: Interpretation of the seismic section oriented East to West at the convergent margin off Antofagasta, North Chile, modified from *von Huene and Ranero* [2003]; *Sallarès and Ranero* [2005] (a). White dots show the detachment and arrows display the normal faults existing in the wedge. The optimized collapse mode is rooting in the region of overpressures idealized as a straight surface, b).

transition zone of the topography. We shall not try to validate the value of Δy_c from the experimental results which may, incidentally, suffer from side-wall friction bias that would displace the new shear plane up-dip of the decollement [*Souloumiac et al.*, 2012]. Nevertheless, this exercise shows the versatility of the MST in capturing the essential features of the structural evolution. A dedicated experiment would certainly shed light on the qualitative merits of our predictions.

2.5 Application to North Chile

Having validated the collapse modes in extension, it is now proposed to apply the MST at the field scale accounting for potential over-pressures, disregarded so far. The example of the North-Chile margin in the area of the Mejillones peninsula [*Delouis et al.*, 1998] is proposed for that purpose. The subduction is taking place with erosion of the subducted plate where

the continental debris moved to the wedge toe are partly entering the subduction channel. This region has been recognised to be in extension above a weak detachment which is not the subduction interface but a sub-horizontal fluid barrier within the continental plate [*von Huene and Ranero*, 2003; *Sallarès and Ranero*, 2005]. Normal faults are rooting in the detachment and participate to the extensive deformation resulting ultimately in erosion of the subducted plate. Our objective is to determine the position of the active normal faulting, associated to our gravitational collapse mechanisms, as a function of the overpressure ratios within the detachment as well as in the bulk material.

The geometry of our prototype is constructed from the seismic section presented in Figure 9b of *Sallarès and Ranero* [2005] and shown here as Figure 2.12a from Est to West. Of interest is the region above the inter-plate boundary which is approximated by the blue segment AB dipping at $\beta = 3.72^{\circ}$ on average and of a total length of 29.1 km. It constitutes the decollement considered in all previous examples. The topography is discretized by a set of 236 points and the optimization of the gravitational collapse mechanism presented in Figure 2.12b consists in finding the maximum difference $\mathcal{P}'_{\text{ext}} - \mathcal{P}'_{\text{mr}}$ for all triplet (H, I, J), as done in *Cubas et al.* [2008]. Note that the gravitational collapse activates the section JB of the decollement resulting in an upward motion of the frontal part of the wedge. The material property values or ranges are summarized in the fifth column of Table 2.1. The bulk friction angle φ_B is 27.9° ($\tan\varphi_B = 0.51$ in *von Huene and Ranero* [2003]) and is equal to the friction angle of the normal fault and shear plane ($\varphi_{NF} = \varphi_{SP} = \varphi_B$). These equalities would be typical of faults at their onset prior to the development of any damage. The decollement friction angles is set to either 10° or 15°. The decollement cohesion is assumed to be zero and the bulk cohesion is set to 0, 5 or 10 MPa. The material and fluid volumetric masses are 2400 and 1030 kg/m^3, respectively [*Adam and Reuther*, 2000; *Sallarès and Ranero*, 2005].

Results are presented in Figure 2.13a in a plane spanned by the fluid overpressure ratios in the decollement and in the bulk material. Material and interfaces are assumed cohesionless. The resulting stability map has three regions. The first region, for low values of both pressure ratios, correspond to stable conditions. The collapse mechanism cannot be activated. The second region is central within the stability map and is bounded on top by the grey curve. An instability mode occurs for these pressure conditions resulting in a gravitational collapse which is found at the front of the wedge. The third region corresponds to large values of the two

pressure ratios. The mode of instability is then found more to the back of the structure.

von Huene and Ranero [2003] employed the CCW theory to study this erosional margin assuming the average friction coefficient and pore fluid pressure proposed by *Lallemand et al.* [1994]. We deduce from their data using the relation $\mu_D^\star = \mu_D(1-\lambda_D)/(1-\lambda_B) = 0.24$, assuming $\varphi_D = 10°$, that the pressure ratios are $\lambda_D = 0.837$ and $\lambda_{hydro} = \rho_f/\rho = 0.447$ in our analysis. Consequently, the pressure ratio differences should be $\Delta\lambda_D = 0.39$ and $\Delta\lambda_B = 0.433$. These pressure conditions correspond to the blue triangle in our stability map in Figure 2.13a which is in the dynamically unstable domain with a dominant collapse at the back.

The position of the dominant collapse mechanism as well as the lower bound to the acceleration power provided by the maximum difference in $\mathcal{P}'_{\text{ext}} - \mathcal{P}'_{\text{mr}}$ are now discussed to illustrate the transition between the three stability regions defined above, Figure 2.13b. For sake of simplicity, the horizontal axis corresponds to the diagonal $ABCD$ in the pressure map of Figure 2.13a. The normalized length is defined between points B and D only since the segment AB is stable. The normalized, activated decollement length is small compared to one between B and C and large between C and D, the two main jumps corresponding to the stability transitions discussed above. The minor jumps between B and C and between C and D are controlled by the local accidents in the topography and are reminiscent of the findings of *Pons and Leroy* [2012]. More interesting is the variation in the lower bound to the acceleration power. This bound is negative between A and B (stable conditions) and increases approximately linearly between C and D independently of the jumps in position of the collapse mechanism. Consequently, it appears that the pressure conditions of *von Huene and Ranero* [2003] correspond to a dynamically unstable mode which is not sustainable. The pressure conditions and the material properties should be such that the blue triangle in Figure 2.13a is close to point B at the critical stability threshold.

To assess the role of the material properties in setting these stability predictions, it is now proposed to vary the bulk cohesion and the decollement friction angle, Figure 2.13c. The stability transitions are presented as solid curves and a dashed curves for φ_D equal to 10° and 15°, respectively. Three sets of these two curves are presented corresponding to a cohesion of 0, 5 and 10 MPa. Increasing those two material properties reduces the domain of instability in that map. Furthermore, we observe that the set ($\varphi_D = 10°, C_B = 5$ MPa) leads to a stability transition close to the field conditions considered by *von Huene and Ranero* [2003].

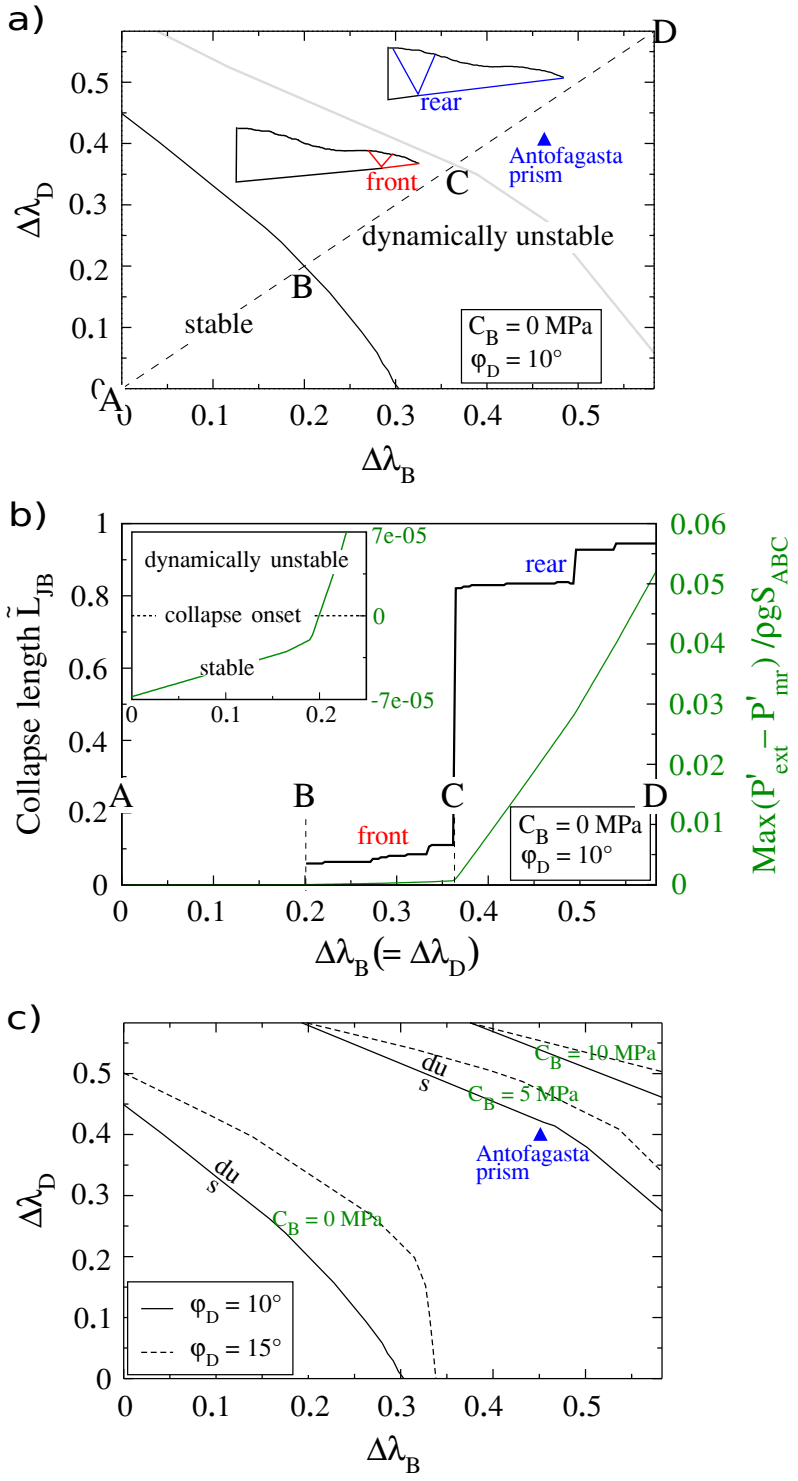


Fig. 2.13: The stability conditions map for the Antofagasta prism in the space spanned by the bulk and decollement pressure ratios, a). The position of the root of the dominant mechanism for equal pressure ratios and the lower bound to the acceleration power, b). The sensitivity of the stability transition (s = stable, du = dynamically unstable) to the bulk cohesion and to the decollement friction angle, c).

2.6 Conclusion

This contribution proposes a mechanical analysis of two types of extensional deformations. First, gravitational collapse of a wedge of frictional material resting on a low friction inclined base (decollement), and second, tectonic collapse triggered by down dip slip on the decollement, following the retreat of the back-wall. In the CCW theory the first case corresponds to compressive wedges at their maximum taper, i.e. on the verge of failure by instability of the topography, while the second case corresponds to extensional wedges, also at their maximum taper. The perfect match observed between the Limit Analysis and the CCW solutions, once properly amended, for various over-pressures and friction angles completes the validation of our approach that was started in the classical compressive tectonic setting, without over-pressures [*Cubas et al.*, 2008] and with over-pressures [*Pons and Leroy*, 2012]. In all cases, the kinematic approach of limit analysis (referred to here as the Maximum Strength theorem) generalises the results of the CCW theory by including a wedge of finite size, limited by a back-wall, and material with cohesion, thus providing a length scale in the solution. It also includes two important features for application to real experimental or natural cases: an arbitrary topography and pre-existing faults as true discontinuities. The method remains however semi-analytical, requiring only a discretisation of the topography and moderate numerical implementation.

The study of the gravitational collapse for a triangular wedge of finite extent has lead to the conclusion that the maximum possible length of decollement is activated at the stability transition despite the introduction of a characteristic length in the problem via the material cohesion. The conclusion is not the same once the same gravitational mode is applied at the field scale for the North-Chile margin considering the over-pressured detachment studied by *von Huene and Ranero* [2003]; *Sallarès and Ranero* [2005]. The stability transition if the bulk and decollement pressure ratios were equal and increased is marked by a frontal collapse and this particular position is controlled by the specifics of the topography. It is only for large values of these pressure ratios, corresponding to dynamically unstable equilibrium states, that the collapse activates the maximum possible detachment length. These results obtained for zero cohesion indicates that the pressure conditions proposed by *von Huene and Ranero* [2003] would correspond to dynamic conditions. The introduction of bulk cohesion (order of 5 MPa) is found to be sufficient to reconcile our stability transition predictions with the proposed pressure conditions. The gravitational collapse is then frontal, consistent with the idea that

erosion above the detachment is bringing material to the wedge toe.

The proposed methodology is now ready for use for field cases. It could be used, for example, to test the idea that the Tohoku-Oki earthquake corresponds indeed to a gravitational collapse of the wedge front up dip the decollement [*Cubas et al.*, 2013b]. The analysis could be semi-analytical as proposed here or rely on numerical implementation of the MST [*OptumG2*, 2014] as proposed in *Cubas et al.* [2013c] to capture the activation of major splay faults in the Maule earthquake area. The advantage of the numerical approach is that a stress field can be obtained, either as a dual field to the velocity field for the MST or as a statically admissible field if the static approach of limit analysis is considered.

There are several potential extensions to the present work. The analysis of *Xiao et al.* [1991] with the tectonic collapse mode gave a glimpse at one of them. In this analysis, the geometry of the sand body was modified once the collapse mechanism was optimized based on simple rules close to the ones adopted by *Groshong* [1989]. After each geometry modification a new search for the collapse mechanism is conducted until a rear collapse is detected. This staggered scheme, optimisation followed by geometrical evolution is at the basis of the sequential limit analysis considered for kink folds by *Maillot and Leroy* [2006]; *Kampfer and Leroy* [2009; 2012] and for accretionary wedges on the large scale by *Cubas et al.* [2008] for a single sequence of fault-related folds and by *Mary* [2012]; *Mary et al.* [2013a;b] for an arbitrary number of sequences resulting in a large amount of shortening. It is clear that such evolution could also be constructed for extensional collapse. Furthermore, one could imagine to combine the frontal, compressional and the rear extensional collapses to produce the deformation styles of many sedimentary basins as the Niger Delta [*Kostenko et al.*, 2008] while accounting for over-pressures.

Some theoretical questions specific to gravitational collapse remain however to be clarified before proceeding. The present approach does not allow us to determine the power of acceleration, and therefore we have no time scale to follow the evolution of a gravitational collapse. A proposition could be to use the lower bound to the acceleration powers and to use a classical Newmark's scheme following the geometry evolution which defines the displacement field. Any tentative algorithm will need to be compared to a full numerical solution for a sand body undertaking arbitrary large deformation and the recent developments of the particle finite-element method [*Zhang et al.*, 2013] is certainly a good candidate.

Chapter 3

Deformation pattern during normal faulting: a sequential limit analysis

Abstract

Sequential Limit Analysis combines mechanical equilibrium and the geometrical construction of half-grabens to predict extensional deformation resulting from faulting and sedimentation. This two-dimensional (2-D) methodology is validated for a wedge extension in dry and fluid overpressured cases, and the final surface slopes of stable wedges are well predicted by the critical Coulomb wedge (CCW) theory. The first application concerns the deformation branching out from a lower, inclined detachment. It is shown how the normal fault and the associated axial surface (bounding plane) of the half-graben are rotating because of topographic subsidence. The continuous rotation of the normal fault means that material in the footwall is sheared upon entering the hanging wall creating a region called the Foot-to-Hanging Wall region (FHW). Friction reduction along the normal fault renders the rotations discontinuous and as a result, the FHW contains blocks of intact material separated by shear bands. Sedimentation, on the other hand, compensates the topographic subsidence of the half-graben and tends to slow down the rotations and thus to reduce the size of the FHW and its number of blocks. These two processes, fault softening and sedimentation, are essential to recreate the final geometry resulting from the interpretation of a seismic line though the Southern Jeanne d'Arc Basin, offshore Newfoundland. A simple sedimentation history with a slow sedimentation rate in the Lower Jurassic followed by an increasing rate up to present time is proposed to obtain a single

block in the FHW region bounded by two faults. The positions of the two bounding faults, activation timings and relative slip displacement are well predicted by the inverse analysis.

3.1 Introduction

Slip on low-angle detachment faults is widely recognized to be a dominant tectonic process in zones of active crustal extension [*Wernicke*, 1995]. This contribution proposes a two dimensional (2-D) methodology to predict the deformation pattern above the low-angle detachment in the brittle crust resulting from normal faulting. Such methodology is based on the maximum strength theorem in *Yuan et al.* [2015] to render half-graben geometrical constructions mechanically balanced.

The widespread existence of the crustal extension includes the Gulf of Mexico [*Xiao et al.*, 1991] and the late phase deformation in the northern part of the Basin and Range province, Nevada and Utah [*Anderson et al.*, 1983]. The seismic section below the Corinthe rift system [*Rigo et al.*, 1996] also shows that the low-angle shear zone at 10 km depth acts as a weak detachment. These extensional deformations are controlled by normal fault and conjugate axial surface bounding an half-graben. The half-graben geometrical model proposed by *Groshong* [1989] illustrates well the evolution process of a single half-graben geometry. In this geometrical model, the hanging wall slides down along the normal fault and becomes sheared as it passes through the conjugate axial surface. *Xiao and Suppe* [1992] improved the half-graben kinematics accounting for sedimentation process during deformation for the natural field examples, such as the Gulf of Mexico [*Xiao et al.*, 1991] and the Albuquerque Basin [*Russell and Snelson*, 1994]. However, these half-graben geometrical models are not mechanically proven, such as the dips of normal fault and the axial surface. Additionally, as observed from the above field examples, it is not understood the pattern of half-graben migration in space during extension. This is an important motivation for the present work to combine the mechanical equilibrium and the half-graben geometries to predict the extensional deformation.

Sandbox analogue experiments [*Xiao et al.*, 1991; *Exadaktylos et al.*, 2003] have been proposed to validate the above field interpretations, especially the features of half-graben migration during extension. Additionally, the experiment in *Dahl* [1987] captures the essential features of the half-graben geometry including the creation of the Foot-to-Hanging Wall region (FHW). The FHW characterizes the material originally in footwall sheared upon entering hanging wall

because of the rotation of the normal fault during extension. The formation process and mechanism for such FHW region are not understood. Two processes, fault softening and sedimentation, are recognized to have substantial influence on the development of such fault networks, as shown by the deformation pattern using the same methodology in compressional settings [*Mary et al.*, 2013a]. Thus, these two important processes should be captured in our new developments to predict the extensional deformation resulting from normal faulting.

Most of our theoretical understanding of wedge stability on the weak detachment is based on the extensional Critical Coulomb Wedge (CCW) theory [*Xiao et al.*, 1991; *Yuan et al.*, 2015] which require the wedge of a planar topography. However, the evolution process cannot be captured by the extensional CCW theory because the internal deformation is controlled by the regional fault softening, sedimentation process resulting in arbitrary topography. On the other hand, the numerical method, Distinct Element Method (DEM), is adapted to capture the small-scale fracturing and the large displacements typical of the extensional regime in several hundreds kilometers. *Egholm et al.* [2007] proposed a numerical method of the DEM family which managed to capture the essential features of the half-graben geometry including the creation of the narrow blocks bounded by normal faults of different dip. Furthermore, heterogeneous cohesive properties can be accounted for such as in layered systems and the block region is found to be of a lense shape with a complex internal structure [*Schöpfer et al.*, 2007]. *Abe et al.* [2011] included a separation mechanism at the fine scale capturing the opening of the normal fault close to the top surface, as exemplified by analogue experiments [*Holland et al.*, 2006].

Compared to the above numerical models, our proposed methodology coupling between mechanics and half-graben geometrical constructions has the small number of degrees of freedom: the dips of the two bounding planes of the half-graben and the position of their common root. Furthermore, our methodology is computational efficiency implying that solutions can be obtained within minutes; thus the methodology is well suited for inverse analysis which requires millions of forward modelings, as done by *Cubas et al.* [2013a] in the compressional setting. Additionally, our methodology accounts for softening on normal faults, and includes erosion or sedimentation processes and fluid overpressures which are widespread in sedimentary basins and are essential in the extensional failures.

This contribution contents are as follows. Next section presents the prototype of wedge in

extension used for validation purpose. The incremental update of the half-graben geometry is used for the evolution of the wedge structures. The dips of the normal fault and axial surface are found by optimization of maximum strength theorem to obtain the minimum boundary force as explained by *Yuan et al.* [2015]. Section 3 pertains to the study of the wedge evolution and its purpose is to validate the methodology. We will see that two modes of deformation, gravitational collapse and tectonic extensional collapse, are well captured and compared with the theoretical results of the CCW theory [*Dahlen*, 1984; *Xiao et al.*, 1991]. Section 4 introduces the important effects of fault softening and sedimentation; these effects control the size of the foot-to-hanging wall regions and the number of blocks it contains. Finally, we perform the restoration of a seismic line though the Southern Jeanne d'Arc Basin, Grand Banks, offshore Newfoundland by *Withjack and Callaway* [2000]. We conclude the key to capture the single block in the hanging wall is to propose a small sedimentation rate during the early phase of rifting. Note that all the technical details of the calculations as well as a review of limit analysis are found in the Electronic Supplement associated to this contribution.

3.2 Sequential Limit Analysis of a Homogenous Wedge under Extension

Here we shall apply the sequential limit analysis to understand the deformation of the simplest case of a wedge being strained on one of its lateral boundaries.

The wedge (Figure 3.1a) is composed of a uniform and cohesive frictional Mohr-Coulomb material (friction angle φ_B and cohesion C_B) with an arbitrary topography. It is resting on an inclined, planar detachment (line AB with friction angle φ_D and dip β). The back wall is vertical (AC) and its contact with the materials is characterized by the friction angle φ_{BW}. A constant extensional displacement δ of the back wall parallel to the detachment results in one of the three following expected collapse mechanisms (Figure 3.1a). The first mechanism is the sliding of the wedge along the entire length L_{AB} of the detachment as a rigid block. The second mechanism concerns with the deformation at the back wall (Figure 3.1b) in which case the detachment remains inactive and accommodates no displacement. In addition to these two limiting cases, we consider a third mechanism in which a segment of the detachment is activated by retreating the back wall (Figure 3.1c). In this Figure, L_{AG} is the activated detachment, the

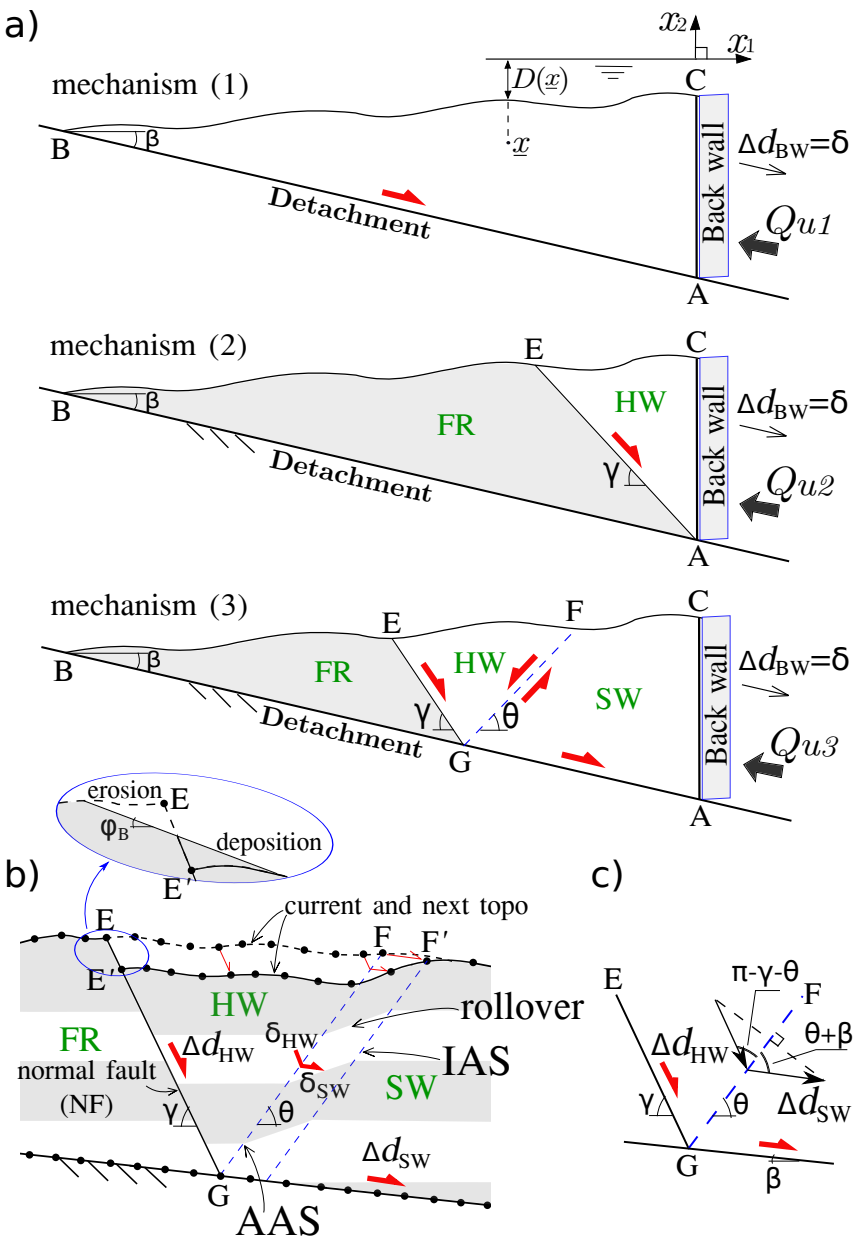


Fig. 3.1: The prototype is a wedge with (a) the three expected collapse mechanisms, corresponding to (1) the full activation of the detachment, (2) the activation of a normal fault AE rooting at the back wall, and (3) the partial activation of the detachment, of a normal fault GE and of an active axial surface (AAS) GF. In (a), HW, SW and FR are labelled for Hanging Wall, Sliding Wall and Frontal Region, respectively. (b) Illustration of the geometric evolution after an increment of slip for mechanism (3) based on the half-graben geometry, and illustration of erasing the fault scarp EE', replaced by a slope with material friction angle φ_B. In (b), rollover region is bounded by active axial surface and inactive axial surface (IAS). Grey stripes are passive markers. (c) The displacement relations between hanging wall and sliding wall.

point G is the root of half-graben, and the line segment GE is the normal fault. The surface GF is called active axial surface [*Xiao and Suppe*, 1992]. The wedge is divided by GE and GF into frontal region, hanging wall, and sliding wall, respectively. The thick arrows represent the tectonic force, which opposes the sliding of the back wall in Figure 3.1a.

The first step of the sequential limit analysis consists in applying the maximum strength theorem to determine which collapse mechanism should be preferred. The details of the method are presented in *Yuan et al.* [2015] and its Electronic Supplement. The three upper bound forces at the back wall, Q_{ui}, associated to the three collapse mechanisms ($i = 1, 2, 3$) in Figure 3.1a are determined by using of the maximum strength theorem. The analytical expressions including fluid pressure contributions are given in section S2 of the Electronic Supplement. Then we select the minimum force of the three possible tractions Q_{ui} acting on the back wall and the corresponding mechanism is considered to be the most efficient to deform the system. Note that the search for the least force requires us to minimize upper bound forces in terms of the geometric parameters of the corresponding mechanism: none for mechanism 1, γ for mechanism 2, γ, θ and L_{AG} for mechanism 3. Angles (dips) and the length are defined in Figure 3.1a. The minimization of upper bound forces is conducted following the method proposed by *Cubas et al.* [2008]. The detachment and the topography are discretized by two sets of points, as illustrated in Figure 3.1b. Upper bound forces are then calculated for all discrete positions of point E (defining the dip of AE, γ for mechanism 2), or points E, F, G (defining the dips θ and γ and the length L_{AG} for mechanism 3) with expressions in section S2 of the Electronic Supplement.

The second step of the sequential limit analysis is to update the topography resulting from the displacement δ of the back wall, parallel to the detachment. For mechanism 1, the material is translated by the same value as a rigid block. We adopt the incremental update of the geometry shown in Figure 3.1b [*Groshong*, 1989; *Xiao and Suppe*, 1992; *Pashin and Groshong*, 1998] for mechanism 2 ($\theta = 90°$) and mechanism 3. The sliding wall and the back wall are translated by $\Delta d_{SW} = \Delta d_{BW} = \delta$, the hanging wall slips along the normal fault GE by Δd_{HW}, and the frontal region is assumed to be stationary. To ensure mass conservation, the vertical component of the displacements in hanging wall and sliding wall crossing the GF should be same, i.e., (Figure 3.1c)

$$\Delta d_{HW} \sin(\gamma + \theta) = \Delta d_{SW} \sin(\theta + \beta)\,. \tag{3.1}$$

This geometrical update implies that some material points of the hanging wall will cross GF, as illustrated in Figure 3.1b. Their movement is therefore a combination of hanging-wall and sliding-wall displacements, δ_{HW} and δ_{SW}. Again, from mass conservation, these two displacements must satisfy the following relation

$$\frac{\delta_{HW}}{\Delta d_{HW}} + \frac{\delta_{SW}}{\Delta d_{SW}} = 1\,. \tag{3.2}$$

After displacement, these points lie between the active axial surface and the inactive axial surface, as illustrated in Figure 3.1b. Note that the wedge weight $\rho g S_{ABC}$, where ρ, g, S_{ABC} are the material density, gravity acceleration and the wedge area, respectively, will be used to normalize the upper bound force at the back wall. This weight is constant in the absence of erosion or sedimentation. The two steps of the sequential limit analysis described above are applied at every increment of extension: (i) optimize to select the dominant collapse mechanism; (ii) update the geometries based on this collapse mechanism.

If the topography created in the vicinity of point E (where the normal fault intersects the topography) has a dip γ greater than the material repose angle, φ_B. Then, a potential instability of the topography might develop causing surficial mass redistribution as is illustrated in Figure 3.1b. They are two ways to proceed: we may first assume that the material has enough cohesion to sustain a steep slope and avoid surficial sliding and we thus proceed without further treatment. Second, and more consistently with sand analogues of interest here, we replace the excessively steep slope by a slope at the repose angle φ_B (Figure 3.1b), positioned such that mass conservation is ensured [*Mary et al.*, 2013a;b]. The second procedure is adopted in the Section 3 because we consider cohesionless materials.

The last ingredient required to complete this section is the definition of fluid pressure $p(\underline{x})$ and fluid pressure ratio $\lambda(\underline{x})$. We follow *Pons and Leroy* [2012] and *Yuan et al.* [2015] on this point:

$$\lambda(\underline{x}) = -\frac{p(\underline{x}) - \rho_f g D(\underline{x})}{\sigma(\underline{x}) + \rho_f g D(\underline{x})} \quad \text{with} \quad \sigma(\underline{x}) = \rho g(x_2 + D(\underline{x})) - \rho_f g D(\underline{x})\,, \tag{3.3}$$

where ρ_f and $D(\underline{x})$ are the fluid density and the thickness of the fluid above the saturated continuum at point $\underline{x}$ (see Figure 3.1a for illustration), respectively. The scalar λ in (3.3) varies between λ_{hydro} $(= \rho_f/\rho)$ and 1, corresponding to the range from hydrostatic to lithostatic pressure. The definition of λ is crucial for the comparison with the CCW theory [*Dahlen*, 1984; *Xiao et al.*, 1991] in fluid overpressured wedges (Section 3.3). This has been discussed at

length in *Yuan et al.* [2015] where the fluid pressure influence is analyzed with the help of the overpressure ratio $\Delta\lambda = \lambda - \lambda_{hydro}$.

3.3 Simulation Results and Interpretation by the CCW Theory

The first application of the wedge prototype in Figure 3.1a simulates the experimental work of *Xiao et al.* [1991] for cohesionless material and initial flat topography ($\alpha = 0°$). All material and geometrical parameters are given in Table 3.1 and are consistent with the experimental parameters in *Xiao et al.* [1991]. Note, as discussed in the Electronic Supplement, that the normalized upper bound forces are independent of the initial detachment length for the cohesionless materials considered here. Consequently, the final shape of the structure is independent of this characteristic length. The initial detachment and topography are discretized with 1 000 points. The extension is applied in an incremental dimensionless step $\Delta\tilde{\delta} = \Delta\delta/L_{AB}$ of $5{\times}10^{-5}$. This displacement is applied until a stable wedge is obtained in which case further extension can only induce a rigid slip over the whole detachment but no internal deformation. At every step of this extension, a comparison between the various upper bound forces is made to select the dominant collapse mechanism which corresponds to the minimum force at the back wall. This selection discussion is postponed to the Electronic Supplement for sake of conciseness.

3.3.1 Numerical Results for the Case of a Dry Wedge

The evolution process is illustrated for two cases in Figure 3.2a and 3.2b corresponding to the detachment dip $\beta > \varphi_D$ and $\beta < \varphi_D$, respectively. The first case for $\beta = 32° > \varphi_D$ is based on the experimental setup of *Xiao et al.* [1991]. For $\beta > \varphi_D$ in Figure 3.2a, extension first triggers deformation near the back wall (mechanism 2 at $\tilde{\delta} = 0.07$), which then extends to the central and frontal parts of the wedge by means of mechanism 3 (at $\tilde{\delta} = 0.14$ and 0.26). The simulation results match well those of *Xiao et al.* [1991]; in both models deformation is initially observed at the back wall. Then a new half-graben sequence to the direction of wedge tip is found with the further extension. Once the wedge is sufficiently thinned, our simulation in Figure 3.2a, it slides rigidly by mechanism 1 (at $\tilde{\delta} = 0.37$), no further deformation is registered and the calculations are stopped. The overall deformation corresponds to a tectonic extensional collapse mode, defined in *Yuan et al.* [2015] as the whole topography is modified to attain a

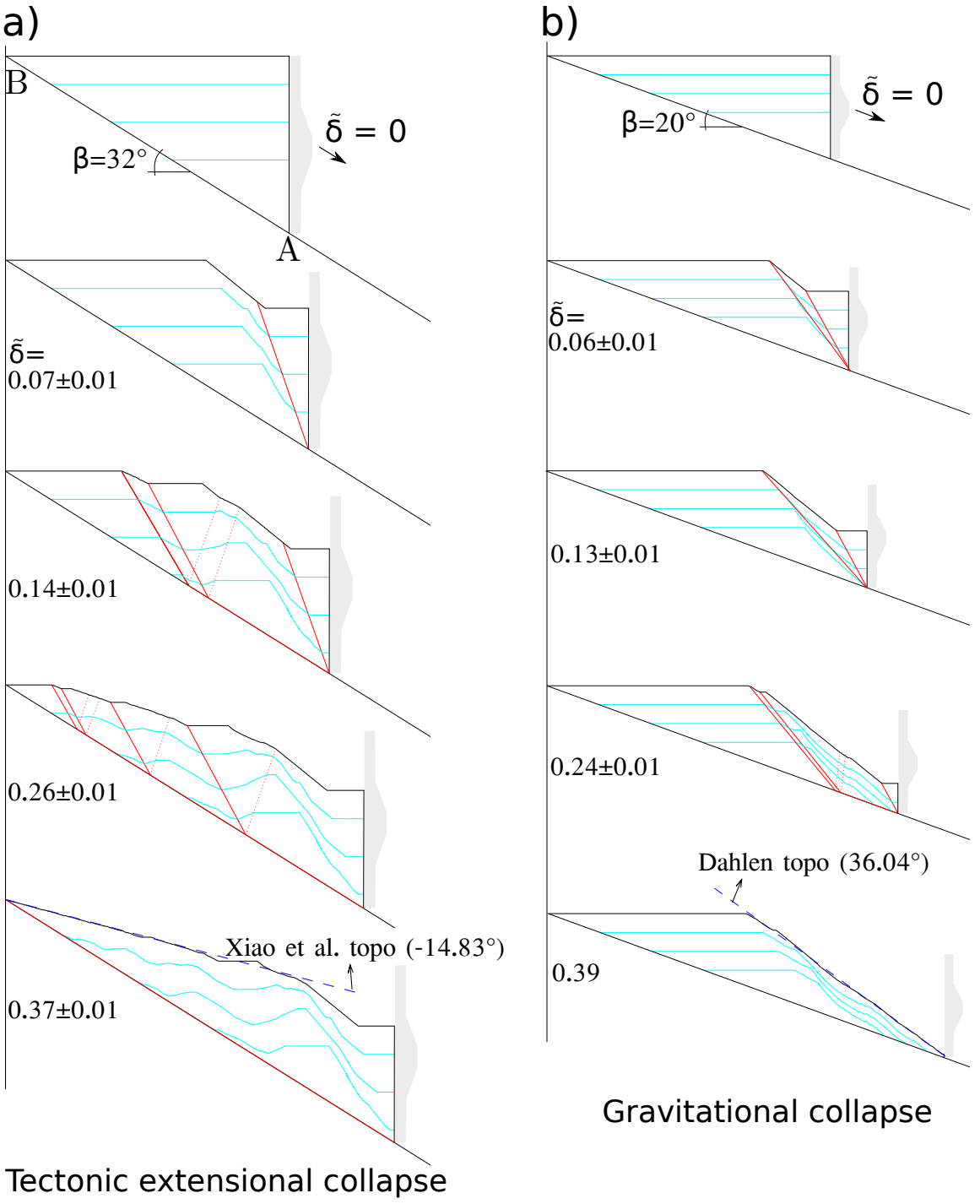


Fig. 3.2: The extension results in either a tectonic extensional collapse, (a) $\beta = 32° > \varphi_D$, or in a gravitational collapse for (b) $\beta = 20° < \varphi_D$. Solid and dotted red lines represent normal fault and active axial surface, respectively. These lines show the active collapse mechanisms during the past three displacement steps around the displacement value $\tilde{\delta}$ indicated in each plot. Cyan lines are passive markers revealing internal deformation. Dry conditions are considered. The vertical and horizontal scales are equal.

Table 3.1: Geometrical and material parameters for the simulations on wedge prototype (Section 3).

Notation	Definition	Values	Unit
α	initial topographic slope	0	deg.
β	detachment dip	20, 32	deg.
d_C	sea bed depth (Point C)	0	m
φ_a	friction angle ($a = B, AAS, NF$)	39	deg.
φ_{BW}	friction angle on back wall	30	deg.
φ_D	detachment friction angle	27	deg.
C_a	cohesion ($a = B, AAS, NF, D$)	0	Pa
ρ	saturated sand density	2000	kg/m^3
ρ_f	fluid phase density	1000	kg/m^3
λ_{hydro}	hydrostatic pressure ratio	0.5	-
$\Delta\lambda_B$	bulk overpressure ratio	0	-
$\Delta\lambda_D$	detachment overpressure ratio	[0.0; 0.2]	-

Notation: $B-$ Bulk, $AAS-$ Active axial surface, $NF-$ Normal fault, $BW-$ Back wall and $D-$ Detachment. Values are constant or varied within the ranges presented.

new critical shape. The critical topographic slope of *Xiao et al.* [1991] is $-14.83°$ and indeed it matches much of the frontal part of the wedge (see the dashed line in Figure 3.2a). The surface is no longer planar in the back half of the wedge because of the influence of the rigid back wall. The cyan markers show undulations that correspond to preferred zones of activation of mechanism 3 which will be analysed later in the paper (see section 3.3.2).

For the case of a detachment dip $\beta < \varphi_D$ (Figure 3.2b), extension results essentially in a gravitational collapse of material near the back wall with a dominance of mechanism 2, some activation of mechanism 3 (at $\tilde{\delta} = 0.24$), and no occurrence of mechanism 1. The terminology used in *Yuan et al.* [2015] presents the gravitational collapse similar to a landslide. The calculation stopped when no material was remained against the back wall. At this stage ($\tilde{\delta} = 0.39$), the landward-dipping topographic slope matches the critical surface slope of 36.04° of the CCW theory [*Dahlen*, 1984] for the gravitational collapse case. As seen from the topography and cyan markers in Figures 3.2, the sequential limit analysis also predicts the internal deformation leading the wedge towards stable state. We next examine the development of this internal deformation pattern.

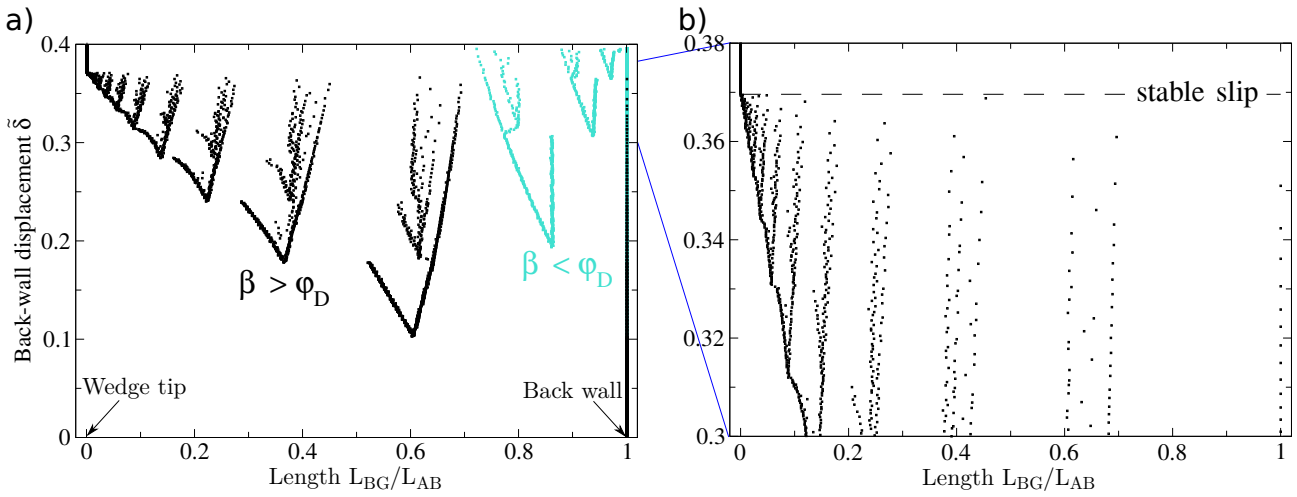


Fig. 3.3: The G-gram presents the position of the common root to the normal fault and the active axial surface for increasing back-wall dimensionless displacement (vertical axis), a). Black dots ($\beta > \varphi_D$) and cyan dots ($\beta < \varphi_D$) correspond to the evolution processes in Figure 3.2a and 3.2b, respectively. In (b), a close up on the G-gram for the case $\beta > \varphi_D$ only, showing the gradual transfer of internal deformation towards the wedge tip for $\tilde{\delta} \leq 0.369$ and the switch to stable sliding ($L_{BG}/L_{AB} = 0$) for $\tilde{\delta} > 0.369$.

3.3.2 Internal Deformation Pattern for the Case of a Dry Wedge

The evolution of the internal deformation can be better understood in terms of a G-gram [*Mary et al.*, 2013a]: a graph showing the successive relative position of point G, the common root to the normal fault and the active axial surface, with respect to the wedge tip. The dimensionless distance $\tilde{L}_{BG} = L_{BG}/L_{AB}$, where L_{AB} is the detachment length, is shown as a coloured dot at the corresponding value of the extension $\tilde{\delta}$ (Figure 3.3). Black dots and cyan dots correspond to the relative position of point G in Figure 3.2a and 3.2b, respectively. There are approximately five thousand steps. To help reading this G-gram, note that $\tilde{L}_{BG} = 0$ corresponds to mechanism 1 (sliding over the whole detachment), $\tilde{L}_{BG} = 1$, to mechanism 2 (back wall sliding), and $0 < \tilde{L}_{BG} < 1$ is associated with the activation of mechanism 3 (internal deformation). For the case $\beta > \varphi_D$ (black dots), mechanism 2 is active alone up to $\tilde{\delta} = 0.1$ and the dots are forming a vertical line at the right of plot. For larger displacements, mechanism 3 starts to dominate occasionally, and both mechanisms 2 and 3 are active, up to $\tilde{\delta} = 0.369$. Stable slip with mechanism 1 finally takes over for $\tilde{\delta} \geq 0.369$ (Figure 3.3b). During extension with mechanism 3, the G points are organized in a series of eight V's developing towards the wedge tip. The spacing between the various V's is such that the active axial surface of a given

half-graben intersects the topography close to where the normal fault of the neighbouring half-graben does. There is also some minor activity, with similar V structure but more diffuse, inside the main eight V's. This G-gram structure is reminiscent of the one found in compressional settings by *Mary et al.* [2013a;b] where fore-thrusts are grouped along the detachment such that the topography tends towards a straight line at the critical slope. Here, at least eight V's develop over the detachment ensuring thinning of the wedge with the final critical surface slope. This distribution of V's results in a non-uniform deformation, with relatively undeformed regions separated by highly sheared zones as is observed in the undulations of the markers in Figure 3.2. The V's are triggered from back wall to wedge tip, and ceases their activity also from the back wall to front tip, as seen from the decreasing density of points in each V as the wedge is getting closer to stable slip (Figure 3.3b).

In contrast, for case $\beta < \varphi_D$ (cyan dots), mechanism 2 is active throughout extension, but is combined with mechanism 3 for $\tilde{\delta} \geq 0.2$. Mechanism 3 develops three similar (but with a mirror symmetry) V-patterns in the G-gram, with a reverse spatial evolution, from wedge tip to the back wall.

3.3.3 Numerical Results for the Case of an Overpressured Wedge

We now illustrate how detachment overpressure may change the mode of extension from gravitational to tectonic collapse. The fluid overpressure ratio $\Delta\lambda_D$ in the detachment is varied within the interval $[0.0; 0.2]$, and hydrostatic conditions are considered in the bulk material ($\Delta\lambda_B = 0$). Only final geometries obtained for $\beta = 20^\circ \ < \varphi_D$ are presented in Figure 3.4. For no detachment overpressure, the final geometry is that of Figure 3.2b. For increasing $\Delta\lambda_D$ up to 0.1, the gravitational collapse mode still dominates but the final topography slope decreases because the overpressure reduces the mechanical strength of the detachment. The change in mode of deformation from gravitational to tectonic extensional collapse occurs for $\Delta\lambda_D$ between 0.10 and 0.15. For the increase of $\Delta\lambda_D$ in tectonic extensional collapse, visible at $\Delta\lambda_D = 0.15, 0.20$ in Figure 3.4, the extensional displacement required to finalize the internal deformation decreases. This is a consequence of the decrease in the CCW topographic slope with increasing $\Delta\lambda_D$ in the tectonic extension mode. Note also that all final geometries presented here exhibit a topographic slope matching quite well the critical slopes of the CCW theory, once properly amended (and called the Exact CCW theory in *Yuan et al.* [2015]).

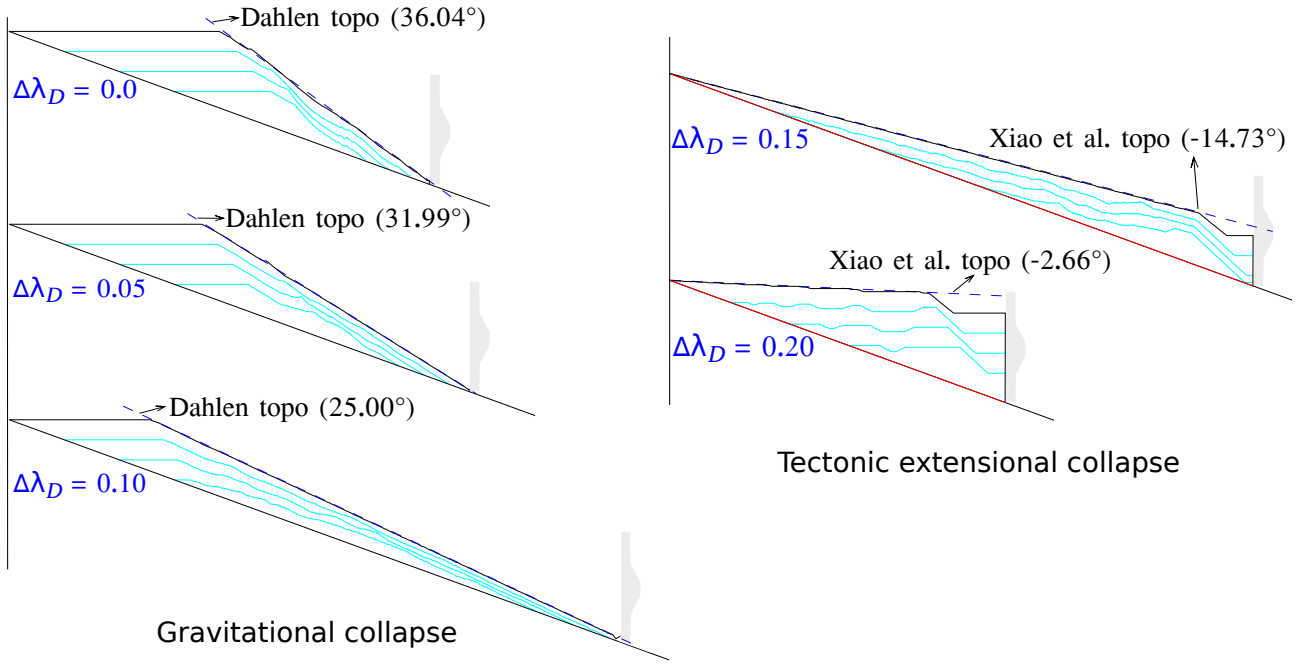


Fig. 3.4: Stable wedges resulting for $\beta = 20°$ and various detachment overpressure ratios $\Delta\lambda_D$. See Table 3.1 for other parameters. In all cases, back-wall friction angle $\varphi_{BW} = 30°$. The blue dashed line in the seven stable state images correspond to the critical slopes calculated from *Dahlen* [1984] and *Xiao et al.* [1991]. The vertical and horizontal scales are equal.

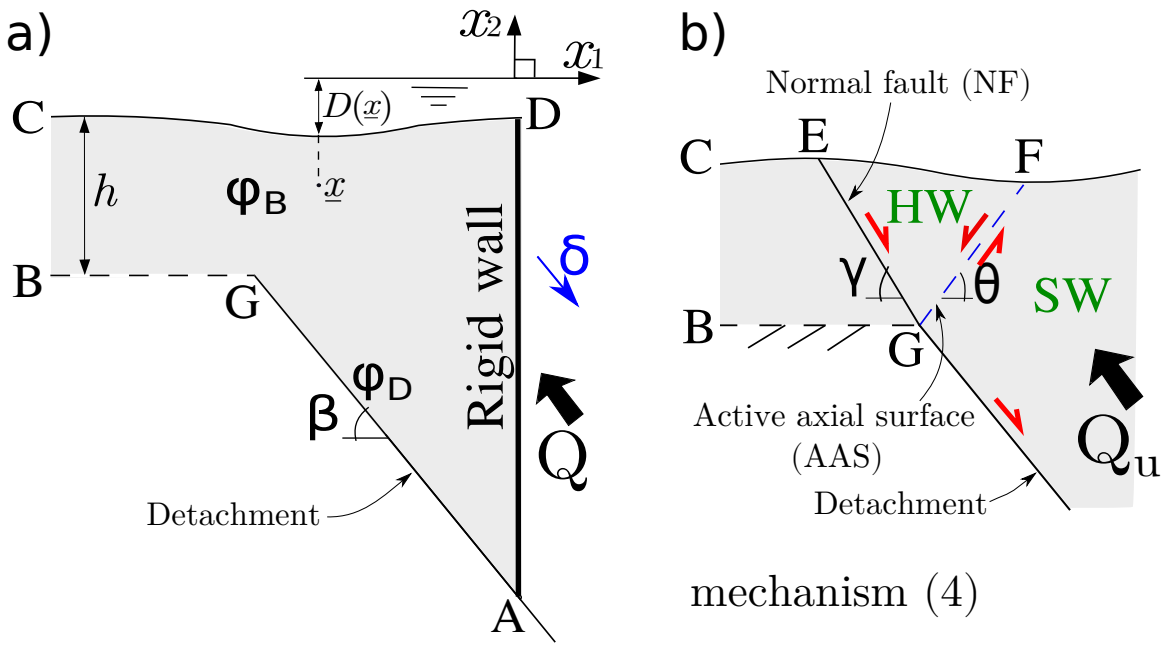


Fig. 3.5: (a) The prototype considered in Sections 3.4 and 3.5 consists of a detachment fault AG and an initially flat cover. (b) The collapse mechanism 4 composes normal fault and active axial surface rooting at point G, and is identical to mechanism 3 defined in Figure 3.1a.

The match between the computed wedge topography and the critical slope of topography predicted by the CCW theory in the various cases constitutes a validation of the sequential limit analysis and of our choice of collapse mechanisms (Figure 3.1a). It constitutes also a non trivial verification of our numerical implementation.

3.4 Roles of Fault Softening and of Sedimentation

The objective is now to concentrate on the hanging-wall deformation of a normal fault and to study the effects of sedimentation and fault softening. The prototype of Figure 3.1a is modified in Section 3.4 to describe a lower normal fault (segment AG not extending to the surface) playing the role of detachment fault, Figure 3.5a. This detachment is buried at a depth h beneath the initial flat topography. The cover deformation is studied here with the activation of mechanism 4, Figure 3.5b, which includes slip along the normal fault rooting at the upper end of the detachment (point G). Apart from this specific location of the root, this mechanism is identical to mechanism 3 presented in Figure 3.1a.

In the mechanism 4, the normal fault GE dipping at γ has specific material properties.

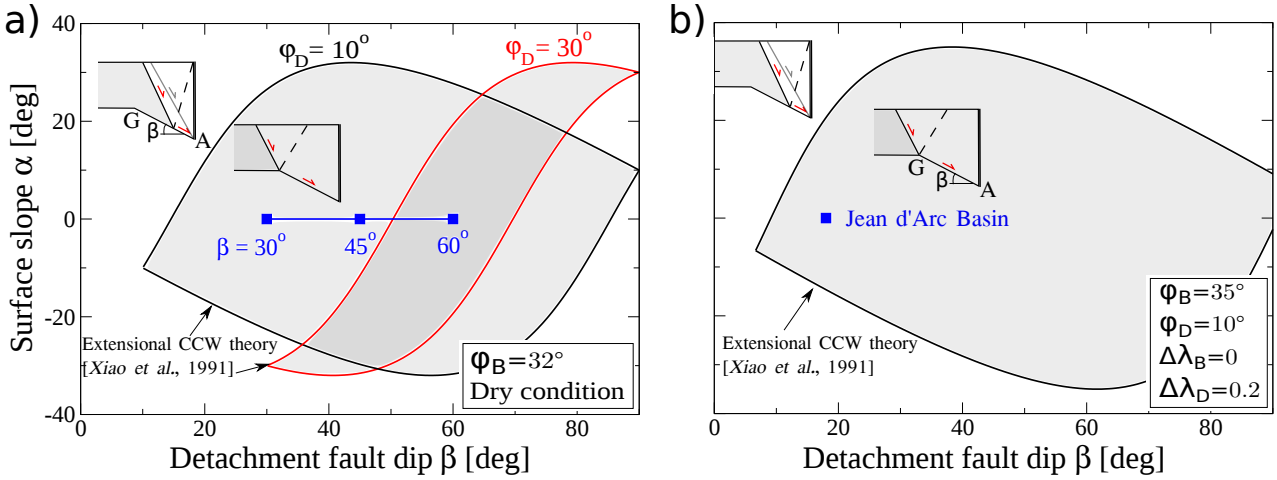


Fig. 3.6: The stability domain of the extensional CCW theory [*Xiao et al.*, 1991] are used to examine the deformed positions (a) for the simulations in Section 3.4 and (b) the application in Section 3.5. The geometries (β, α) of the cover within the stability domain are characterized by deformation along detachment AG. Extension of a normal fault in our simulation through the cover requires conditions preventing the deformation to occur near the back wall.

The active axial surface GF rooting at point G is dipping at θ. These two dips γ and θ are optimized according to the maximum strength theorem, and the hanging-wall deformation results from these two angles during extension following the same kinematics discussed in Section 2. The expression of upper bound force at the back wall is given in section S3 of the Electronic Supplement. Material parameters are given in Table 3.2, column 3. Fault softening along the normal fault GE is implemented as follows: the friction angle of normal fault is set to the bulk friction φ_B if that fault has not been activated at the previous step. If this fault was activated, we use a decreased value φ_{NFS} (NFS: Normal Fault with Softening) to compute the associated upper bound force. This is a simplified version of the linear softening law considered in *Cubas et al.* [2008].

In order to ensure the deformation occurs by activation of the detachment fault, we use again the extensional CCW theory [*Xiao et al.*, 1991] to analyse the failure mechanism, Figure 3.6a. The stability domain of the extensional CCW theory is plotted for two values of detachment friction angles $\varphi_D = 10°, 30°$. The geometries (β, α) of the prototype outside this stability domain are characterized by the deformation near the back wall (e.g. the mechanism 2 in Figure 3.1a). For the initial topography being flat ($\alpha = 0°$), the detachment faults dipped at

Table 3.2: Geometrical and material parameters for the simulations of the hanging-wall deformation in Section 4 and 5.

Notation	Definition	Values		Unit
		[Section 3.4]	[Section 3.5]	
α	initial topographic slope	0	0	deg.
β	detachment dip	30, 45, 60	18	deg.
h	cover thickness	10	12×10^3	m
d_D	sea bed depth (Point D)	-	0	m
φ_a	friction angle ($a = B, AAS$)	32	35	deg.
φ_{NFS}	NF friction angle with softening	25, 30, 32	[20; 34]	deg.
φ_D	detachment friction angle	10, 30	10	deg.
C_a	cohesion ($a = B, AAS, NF, D$)	0	0	Pa
r_S	sedimentation ratio	[0.0; 1.4]	variable	-
ρ	saturated rock density	2000	2500	kg/m^3
ρ_f	fluid density	-	1000	kg/m^3
λ_{hydro}	hydrostatic pressure ratio	-	0.4	-
$\Delta\lambda_B$	bulk overpressure ratio	-	0	-
$\Delta\lambda_D$	detachment overpressure ratio	-	0.2	-

Notation: $B-$ Bulk, $AAS-$ Active axial surface, $NF-$ Normal fault, and $D-$ Detachment.

$30°, 45°, 60°$ correspond to the three squares in Figure 3.6a. The case of $\beta = 60°$ is within the two stability domains and thus the whole detachment fault is activated. The same conclusion applies for the dip of 30° and 45° if the friction angle φ_D is 10°. If that friction angle is set to 30°, deformation near the back wall, illustrated in Figure 3.6a, is required prior to the extension of the detachment fault through the cover. This transition from the back wall to the wedge tip of the deformation activity was discussed in detail in the previous section and will be disregarded in what follows if such conditions prevail.

3.4.1 Reference Simulations

As a reference, we first present in Figure 3.7 six simulations conducted with neither fault softening nor sedimentation, setting β either to $30°, 45°$ or 60° and φ_D to 10° or 30°, and imposing a small back-wall displacement $\tilde{\delta} = 0.2$ parallel to the detachment (displacement is normalized by the thickness h of the initial cover). Note from Figure 3.7 that the normal fault dip $\gamma > \beta$ so the complete normal fault is concave, except for case f) where $\gamma \approx \beta$. Hanging-wall

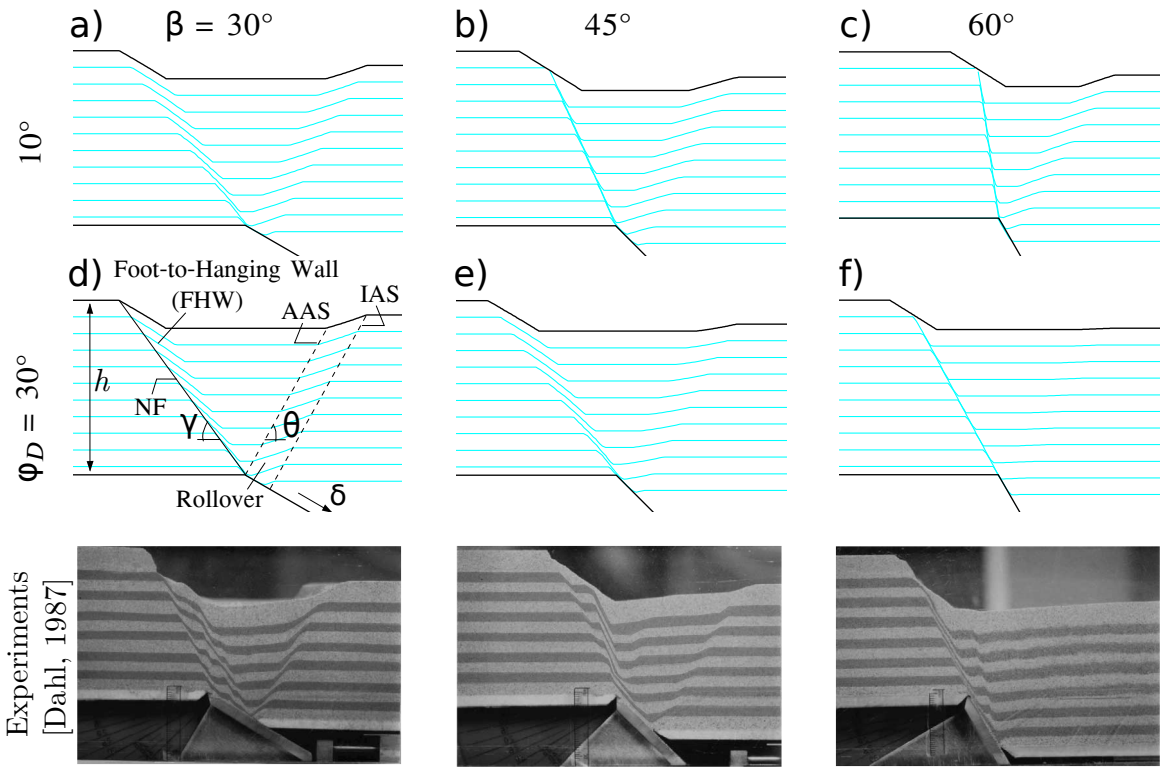


Fig. 3.7: The deformation in the hanging wall with neither softening nor sedimentation. The detachment dips are at 30°, 45° or 60° (first to third column), and the associated friction angle φ_D is set to 10° or 30° (first and second row). The third row shows analogue experiments from *Dahl* [1987] and *Egholm et al.* [2007] with $\beta = 30°, 45°$ and 60°. In d), the oblique solid line indicates the current active normal fault (NF), while the dashed lines represent the active axial surface (AAS) and the inactive axial surface (IAS). The vertical and horizontal scales are equal.

material is sheared when crossing active axial surface to enter into the rollover domain between this surface and inactive axial surfaces. That inactive axial surfaces was the first active axial surface and has been converted by the downwards displacement, Figure 3.7d. Material in the rollover is thinned and has an antithetic dip. Rollovers are commonly observed in the field and were described with geometrical models [*Xiao and Suppe*, 1992]. We find here a mechanical justification and a quantitative link between the geometrical models to the frictional properties. In case f), the detachment has a friction $\varphi_D = 30°$ close to the bulk friction $\varphi_B = 32°$ and a dip $\beta = 60°$ near the Andersonian dip $\pi/2 - (\pi/4 - \varphi_B/2) = 61°$. The sequential limit analysis optimization then yields $\gamma \approx \beta$ as expected from Anderson's theory, and there is no rollover because the axial surface does not play the role of a velocity discontinuity between hanging

wall and sliding wall.

The sequential limit analysis can include another effect that is generally not addressed in geometrical models: the change of dip of the normal fault as the hanging wall subsides. For a large detachment friction angle φ_D (cases d, e) and for a low detachment dip (case a) in Figure 3.7, the dip γ decreases approximately 10° with displacement. This produces a triangular region where the material sustains intense shear. This region will be referred to as the Foot-to-Hanging Wall (FHW) shear zone, because its material was originally in the footwall below the normal fault, and now is in the hanging wall of the normal fault.

A number of features predicted by our model including the creation of the FHW region are clearly observed in the sandbox experiments [*Dahl*, 1987; *Egholm et al.*, 2007] shown in the third row of Figure 3.7. Similar to our simulation results, the sandbox experiments have the rollovers in $\beta = 30°, 45°$ cases but not in $\beta = 60°$ case. The analysis without fault softening produces a continual migration of the fault surface into footwall material. This motivates how the introduction of fault softening will provide episodic migration of the fault surface to produce discreet fault blocks observed in the experiment.

3.4.2 Fault Softening

The numerical solution for $\beta = 30°$ and $\varphi_D = 30°$ are selected in this sub-section because they provide with a rather large FHW region (Figure 3.7d). This configuration is ideal to introduce a further complexity in the model: fault softening. Fault softening is by means of a sudden drop in the friction angle on the normal fault GE after it has sustained the first increment of displacement. Any new orientation of the normal fault has the bulk friction φ_B, and the softening friction angle φ_{NFS} (Normal Fault with Softening) is assigned to the normal fault if its dip is preserved.

The effect of fault softening is illustrated for the case in which φ_{NFS} equals the value of φ_B (no fault softening) in Figure 3.8a. Figures 3.8b and 3.8c illustrate the effects of a drop in friction angle of 2° and 7°, respectively. The plots in the left column are the continuation of the case in Figure 3.7d for a larger displacement. These series of plots show normal fault rotates further anti-clockwise towards a dip close to β. This evolution as well as the dip change of active axial surface are presented in Figure 3.9. As can be appreciated, the variation of γ is gradual, increasing the area of the FHW region. Note that the total volume of the cross-sections

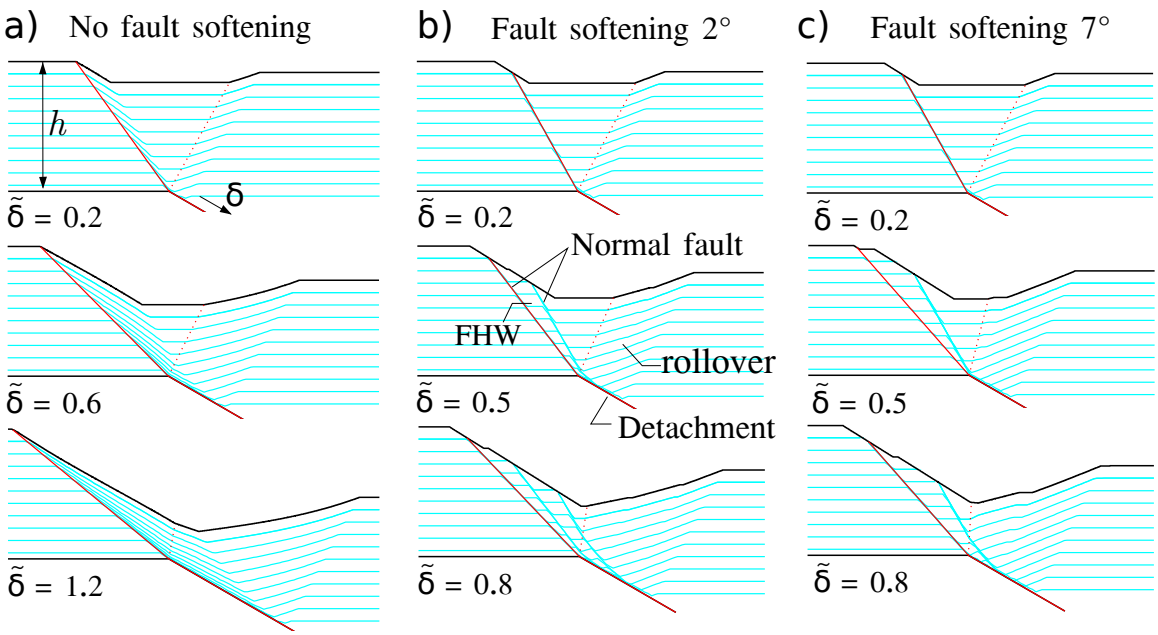


Fig. 3.8: Effect of softening on the normal fault. The evolution process for (a) no fault softening, (b) 2° and (c) 7° drop of the normal-fault friction angle, for various values of $\tilde{\delta} = \delta/h$ (Slip on the detachment over the cover thickness). In column (b) and (c), surface is deflected across the faults but not offset because of surface process (erosion and deposition), illustrated in Figure 3.1b. The vertical and horizontal scales are equal.

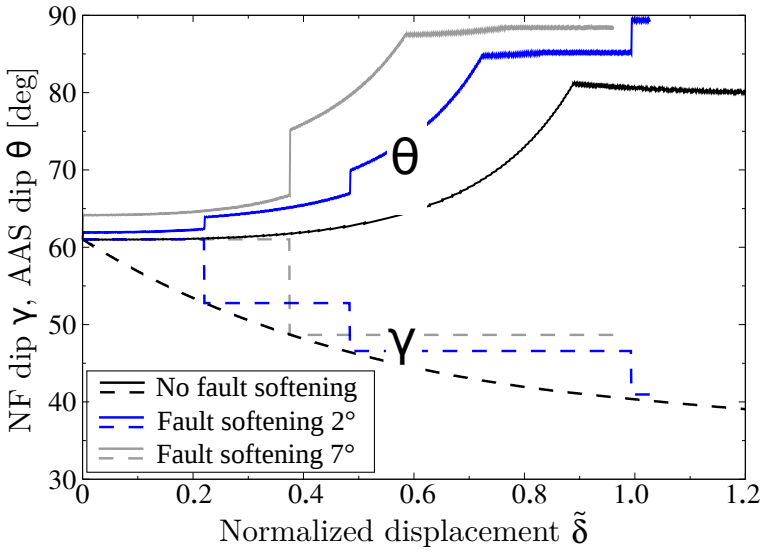


Fig. 3.9: Variation of the dip of normal fault (γ, dashed curves) and the dip of active axial surface (θ, solid curves) with displacement $\tilde{\delta}$ for the three fault softening cases in Figure 3.8.

is conserved because there is no external sedimentation. At the same time, the active axial surface also rotates anti-clockwise up to approximately 80°, solid black curve (θ) in Figure 3.9, producing a slight curvature in the rollover beds (Figure 3.8a). The dip θ of active axial surface reaches a roughly constant value when all the flat beds initially in the hanging wall have passed through the active axial surface (Figure 3.9 for $\tilde{\delta}$ larger than 0.86, approximately).

In Figure 3.8a ($\tilde{\delta} = 1.2$), note that material of the FHW region passed through the active axial surface keeps a synthetic dip, and the material separated from the rollover region is the trace of the first active normal fault. The softening cases (Figure 3.8b and 3.8c) show the same trends in terms of the rotation of both normal fault and active axial surface, but the rotation is not smooth but stepwise (Figure 3.9, blue and grey lines). The sudden softening on the active normal fault means more mechanical work is done and thus the possibility to remain active during a finite period of extension. Note that the dip of active axial surface is varying during such period according to the optimization. The resulting finite deformation is markedly different from the no fault softening case, with the FHW region being dissected by several fault-bound blocks instead of a continuous shear zone. Note also that the larger softening produces a single block whereas the smaller softening results in two blocks (Figure 3.8b and 3.8c at $\tilde{\delta} = 0.8$). In the rollover region, the jumps in the dip of active axial surface resulted in a kink band (Figure 3.8c, visible at $\tilde{\delta} = 0.5$ and 0.8).

With this new insight we can look again at the experiments in Figure 7 in which the FHW regions are composed of one or several fault-bound blocks. Our model results indicate that softening of sand analogue materials [*Panien et al.*, 2006; *Maillot*, 2013] seems a reasonable explanation to the development of these structural features. Moreover, a slight fault softening produces many jumps which are not distinguishable from the continuous rotation. It is only for two degrees of fault softening that the number of blocks become observable. For even larger fault softening values, the number of jumps in dips decreases and the number of block formation is reduced for the same extension. We will see next how the sedimentation stabilizes the migration of the normal fault and of the active axial surface, and affects the number of blocks in the FHW.

3.4.3 Sedimentation and No Fault Softening

Sedimentation is modelled by filling the topographic depression formed in the hanging wall with material of the same physical properties as the pre-growth section. The compaction of sediments is not considered. The thickness Δh_S of sedimentation is calculated such that the sedimentation ratio of *Xiao and Suppe* [1992], $r_S = \Delta h_S/(\Delta d_{HW} \sin\gamma)$, a constant defined as the sedimentation increment to the hanging-wall subsidence increment. Note that the rotation of the normal fault leads to the variation in $\sin\gamma$ during extension and thus Δh_S is not a constant. A hanging-wall depression is formed when the sedimentation ratio r_S is smaller than one. For a ratio $r_S = 1$, the original flat topography is preserved with the initial height during extension. A ratio $r_S > 1$ means that the height of the flat topography is increasing during extension.

The simulation with no fault softening of Figure 3.8a is now repeated with a constant sedimentation ratio for each simulation. This ratio r_S varies from zero to 1.4 and the final extensional displacement is $\tilde{\delta}_f = 1.1$. Results are presented in Figure 3.10 and the growth strata is represented by four black markers (one every $\tilde{\delta}_f/4$). The first obvious conclusion is that sedimentation rate increase reduces the anti-clockwise rotation of the normal fault and its associated active axial surface. This is simply because sedimentation lessens the formation of topographic gradients. As a consequence, the FHW region contracts with increasing in sedimentation ratio. This effect is clearly seen for $r_S \geq 1$, in which the simulation results match exactly the geometrical models of *Xiao and Suppe* [1992]: the dips of the normal fault and of

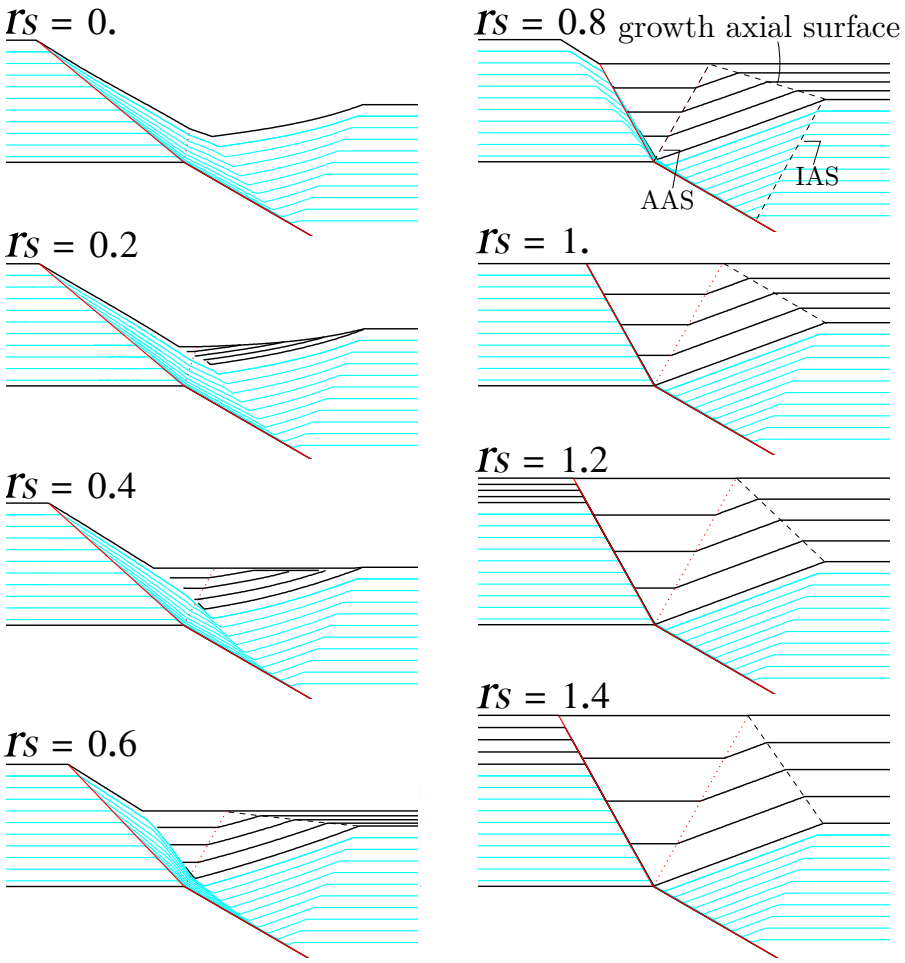


Fig. 3.10: Influence of an increase in the sedimentation ratio r_S on the hanging-wall deformation pattern. The conditions are those resulting in Figure 3.8a (no fault softening). The cyan markers are pre-growth strata, whereas the black markers correspond to the growth strata. The final displacement for all calculations is $\tilde{\delta}_f = 1.1$. The vertical and horizontal scales are equal.

the active axial surface are constant, see Figure S5 in the Electronic Supplement. Animations of the numerical experiments for $r_S = 0.0, 0.6, 1.4$ are presented in the Electronic Supplement that accompanies this paper.

Our simulation results develop some structures similar to those models of *Xiao and Suppe* [1992]. The thickness of the sedimentation markers are different on the footwall, the hanging wall and the right part of the section, Figure S5(a-d). The rollover is now composed of two triangular regions (needs $r_S > 0.6$) for the final extensional displacement of $\tilde{\delta}_f = 1.1$. The lower triangle is composed of the original material and the upper triangle is composed of new sediment material. The right boundary of the upper triangle is called the growth axial surface [*Xiao and Suppe*, 1992], labelled in Figure 3.10. It separates sediments which have and have not been sheared through the axial surfaces. This growth axial surface starts at the active axial surface on the topography and ends at upper point of the inactive axial surface. Its dip increases with the imposed sedimentation ratio.

3.4.4 Combined Effects of Sedimentation and Fault Softening

The objective of this section is to combine the effects of fault softening and sedimentation to shed light on the hanging-wall deformation pattern. A ratio r_S less than one is considered since for $r_S \geq 1$ the deformation pattern is relatively simple with, in particular, no rotation of the normal fault and the associated active axial surface. An additional effect is considered, the role of a surficial mass redistribution. The sediment mass is redistributed such that the topographic slope never exceeds the repose angle (equal to the bulk friction angle). On the other hand, the sediments could be cohesive enough to preserve the fault.

Results presented in the left column of Figure 3.11 are for 2° fault softening with surficial mass transport, whereas those in the right column ignore the effects of mass redistribution. We observe that sedimentation stabilizes efficiently the rotation of the normal fault and of the active axial surface in the presence of softening (compare the results for $r_S = 0.8$ in Figures 3.10 and 3.11). Increasing the sedimentation rate reduces the number of blocks in the FHW region. There are two for $r_S \leq 0.4$ and only one for $r_S = 0.6$ for 2° fault softening case. A comparison of the two columns of Figure 3.11 shows that the surface process has similar effects to those of sedimentation: it reduces the rotation of normal fault and active axial surface and tends to reduce the number of blocks within the FHW region. There is only one for $r_S = 0.4$ whereas

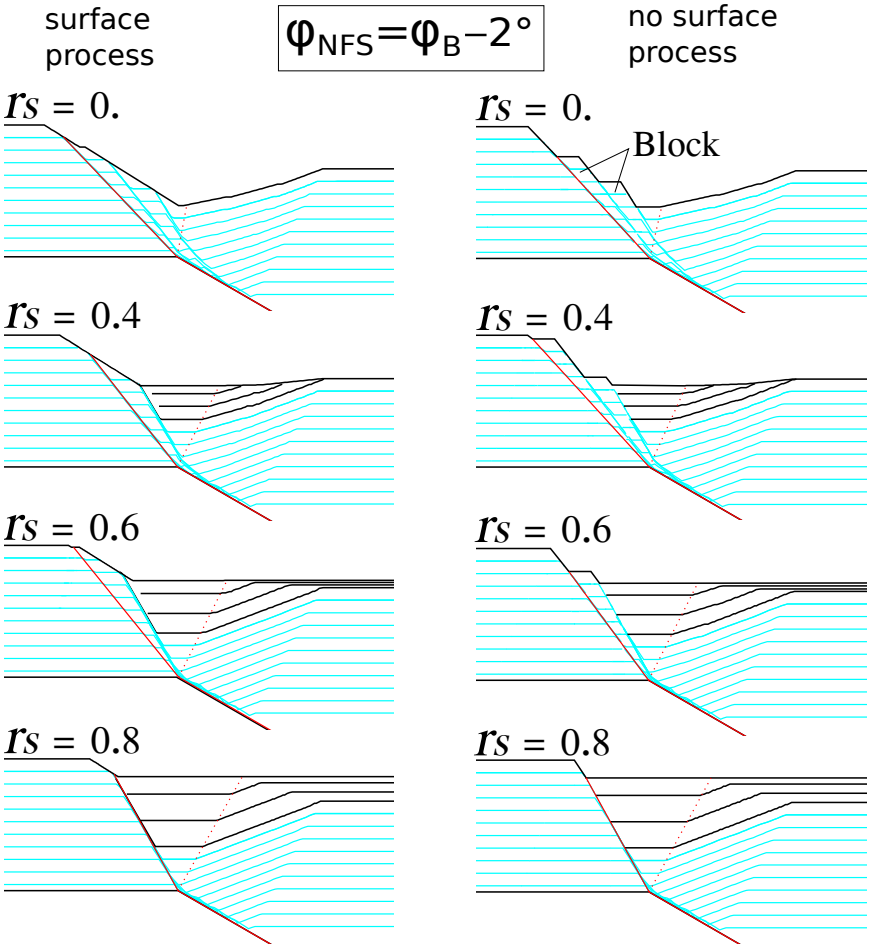


Fig. 3.11: Combined effects of sedimentation and 2° fault softening on the hanging-wall deformation pattern. In the left column, surface process indicates the over-steepened surface fails, essentially by landsliding, erasing the fault scarp. The slope cannot exceeds repose angle for cohesionless materials. In the right column, no surface process shows the fault scarp persevered as it formed. The final displacement for all calculations is $\tilde{\delta}_f = 0.8$. The vertical and horizontal scales are equal.

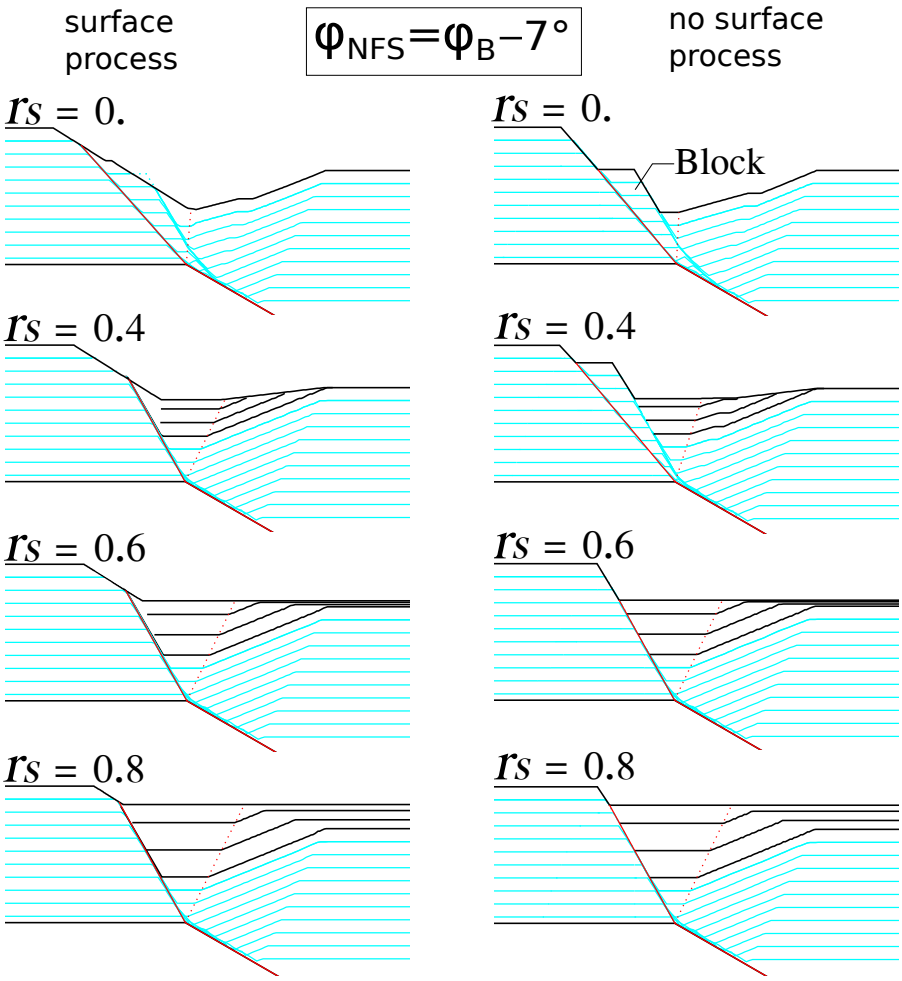


Fig. 3.12: Combined effects of sedimentation and 7° fault softening on the hanging-wall deformation pattern. The left column contains results with surface process (slope cannot exceed repose angle) for cohesionless materials. Results in the right column do not have surface process. The final displacement for all calculations is $\tilde{\delta}_f = 0.8$. The vertical and horizontal scales are equal.

there are two blocks for the case of no mass redistribution.

Consider now the case of 7° fault softening shown in Figure 3.12 and compare with the case of 2° fault softening. For larger softening, the sedimentation effect on the rotation of faults is even stronger and is now effective for $r_S \geq 0.6$ instead of 0.8 previously. The earlier observation that large softening reduces the number of blocks in the FHW region is confirmed in the presence of sedimentation ($r_S \geq 0.4$). Comparing now the two columns of Figure 3.12, it is observed as before that the surface process is important for intermediate sedimentation ratio around 0.4.

In summary, the collapse mechanism 4 (Figure 3.5b) using the sequential limit analysis links the dips (γ, θ) of the geometrical models of *Xiao and Suppe* [1992] to material frictional properties, and to the topographic evolution due either to sedimentation or surficial mass redistribution. In some cases, the classically assumed constant dips are confirmed by the optimization (strong softening and/or sedimentation) at the Andersonian dip 61° ($\pi/4+\varphi_B/2$). In the other cases, γ and θ evolve substantially, producing important differences such as the creation of a FHW region with or without fault-bound blocks, or smaller differences, such as perturbations in the dips found in the rollover region. We now apply this new insight to simulate the formation of a sedimentary basin.

3.5 Application to Jeanne d'Arc Basin, Grand Banks, Newfoundland

This section is devoted to a parametric study on the mechanical properties and the field conditions (sedimentation ratio r_S) which could have prevailed during the development of a natural half-graben. This application is based on the deep seismic reflection profile 85-4A [*Withjack and Callaway*, 2000], presented by *Keen et al.* [1987]. The plane of the profile strikes NW-SE through the Jeanne d'Arc Basin, Grand Banks, South-East of Newfoundland, Figures 3.13a3. This region is of economical interest owing to the two billions barrels of recoverable reserves [*Tankard et al.*, 1989].

This seismic section is selected for two reasons which justify our 2-D mechanical approach. First, the main bounding fault strikes roughly perpendicular to the seismic line, as seen on the map presented by *Enachescu* [1987; 1988; 1992] and summarized in Figure S6 of the Electronic

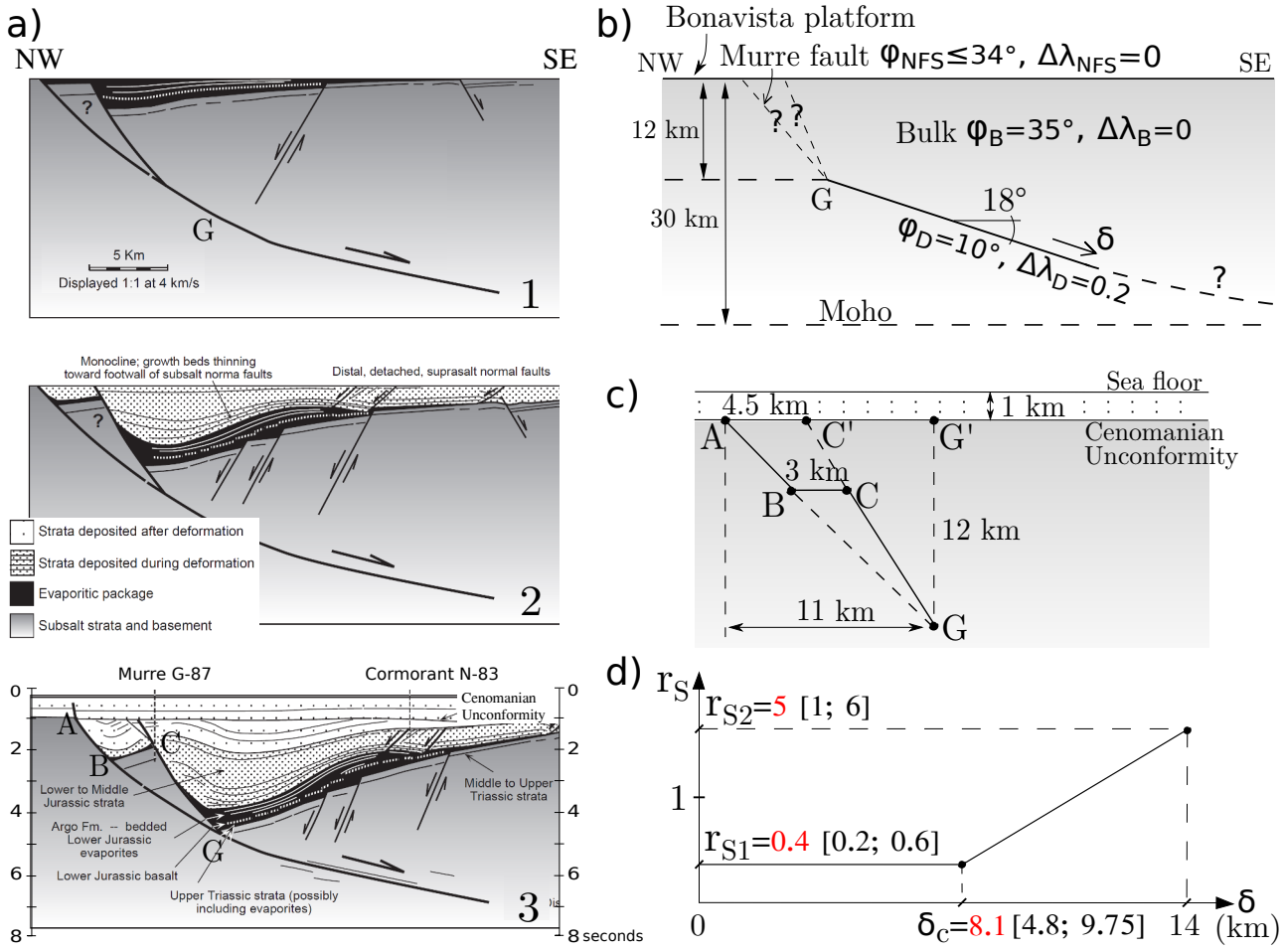


Fig. 3.13: Cross-section through the Southern Jeanne d'Arc Basin, Grand Banks, offshore Newfoundland [*Withjack and Callaway*, 2000]. In (a), the restorations to the Lower and Middle Jurassic and the interpretation of seismic section 85-4A. (b) and (c), the geometric idealization used by optimization. Properties of the bulk material, the detachment and the normal fault with softening are characterized by the pressure ratio λ_a and the friction angle φ_a (with $a = B, D, NFS$, respectively). (d) The proposed sedimentation ratio r_S is function of the fault displacement δ. The optimized value is in red and the interval of search is between brackets.

Supplement. In this region across 200 km long, several cross-sections display similar fault structures across the basin, typically the presence of a single block in the hanging wall. These cross-sections are far from the the fault ends. The second reason, also shown in Figure S6, is that the fault trace is approximately straight in the vicinity of the seismic line.

The recent synthesis of *Withjack and Schlische* [2005] describes the tectonic events that characterize the rifting between North America and Africa including the formation of Jeanne d'Arc Basin. We will not summarize such synthesis, instead we concentrate on the restorations proposed by *Withjack and Callaway* [2000]. Their two stages of restoration corresponding to the Lower and to the Middle Jurassic are found in Figures 3.13a1 and 3.13a2. Our objective is to apply sequential limit analysis approach with the simple conditions necessary for such plane strain interpretation and assuming a single, continuous, extensional tectonic event. It is hoped that our mechanical methodology could be used with additional tectonic complexity to simulate the evolution process and to validate the proposed scenario.

The main feature of the interpretation in Figure 3.13a3 is the Murre fault, bounding the basin to the NW. This fault roots in the Moho at 30 km depth according to *Keen et al.* [1987]. It is approximated by a piecewise fault trace in our prototype, Figure 3.13b, with the lower part dipping 18°. This angle was estimated from the migrated reflection image of *Deemer et al.* [2009], their Figure 2, a nearby seismic line to the 85-4A line of interest. The dip of normal fault is an outcome of our mechanical study as in the previous section. The dip of the segment CG is approximately 62° based on the seismic data. The missing information is the depth at which we approximate the piecewise fault. This transition is chosen at the base of the tilted block seen in Figure 3.13a3 at 4.6 s. The corresponding depth is estimated to be approximately 13 km below the current sea bed based on the data of *Deemer et al.* [2009]. This point G is the root of the FHW structure that is presented in Figure 3.13c. The Murre fault AG is considered to be planar and intersects the Cenomanian unconformity at 11 km from the apex of the G point (distance between A and G'). The initial position of the normal fault corresponds to segment AC and its position with respect to the Murre fault is based on a 4.5 km estimate of the segment AC' length. Segment BC is assumed to be horizontal because we do not account for rotation. This segment length is 3 km. The total displacement which takes place on the upper fault is then the sum of the fault offsets (AB and CG) and is 14 km.

Material properties for this prototype are summarized in column 4 of Table 3.2. The bulk

friction angle is set to a constant value of 35°, a typical value for crustal rocks. The softening on the normal faults is assumed in the range of 1° to 15°, a range sufficiently large to capture the tilted block thickness, according to the parametric studies presented earlier. No fluid overpressure is considered in the structure except for the lower part of the Murre fault where this overpressure ratio is set to 0.2 and the friction is set to 10°. Note that these two values were selected such that the deformation occurs in the upper part of the Murre fault and not by a major normal fault cutting the whole crust from the Moho in the SE (equivalent to collapse mechanism 2 in Figure 3.1a). The justification of this is presented with the extensional CCW theory in Figure 3.6b. A further assumption in our prototype is the history of the ratio r_S of sedimentation rate to extension rate. We assume here, for simplicity, that it is constant (r_{S1}) for an extension up to δ_c and then it increases linearly to reach r_{S2} at the final extension $\delta = 14$ km, see Figure 3.13d. We expect $r_{S1} < 1$ to create a topography depression responsible for the formation of the FHW region, and $r_{S2} > 1$ to fill up the basin at present time. These three parameters r_{S1}, r_{S2} and δ_c are unknowns.

The sequential limit analysis method provides a forward scenario for any given set of parameters. The optimal simulation result should reproduce four features of the cross-section presented by *Withjack and Callaway* [2000]. First, the activation order of the normal fault bounding the tilted block should be captured: the Murre fault being the first one, and the fault to the NW being the second. Second feature, the amount of fault rotation should be captured by segment BC of 3 km-length (Figure 3.13c), the distance between the Murre fault and the SE bounding fault. Third, the relative amount of offset on faults AB and CG, two thirds and one third, should be respected respectively (Figure 3.13a3). Lastly, the dip of the NW bounding fault should be such that it intersects the surface where the Murre faults intersects the Cenomanian unconformity, approximately 11 km to the apex of point G.

Our model contains some approximations and the following list is certainly far from being complete. The sediments are considered to be frictional, not compacted and not viscous despite the presence of evaporites in the deformed region and of salt in the footwall. The deformation responsible for the Cormorant anticline is thus not captured. Furthermore, the antithetic faults most likely controlling the position of this reservoir are not accounted for since their offset is not part of our collapse mechanism. They are replaced at best by axial surfaces with zero offset by definition. Additionally, the model is not considered the block rotation due to the presence

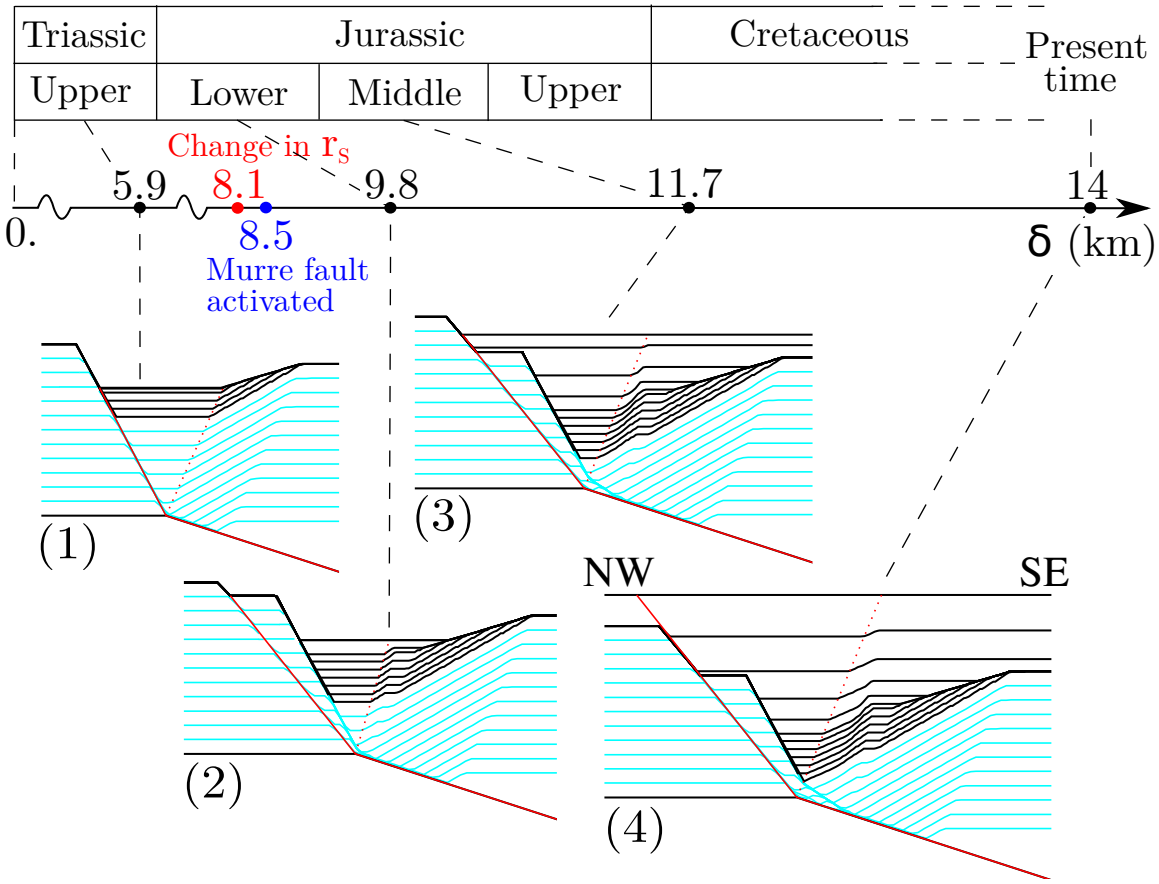


Fig. 3.14: Four steps of the simulation that best fit the four requirements: the order of activation of the bounding faults, the dip of the NW bounding fault, the thickness of the tilted block, and the ratio of offsets on the two bounding faults. The vertical and horizontal scales are equal.

of the listric fault. Finally, the history of the sedimentation rate ratio will not be justified. The choice made above for this ratio was consistent to have a low value first to create a topography responsible for the genesis of the two bounding faults, and then a large value to fill up the basin as seen in present day.

The parametric study is to be conducted in a space of four dimensions: r_{S1}, r_{S2}, δ_c and the fault friction angle φ_{NFS}. The intervals of search for these parameters are: $[0.2; 0.6]$, $[1.0; 6.0]$, $[4.8; 9.8]$ and $[20°; 34°]$, respectively. The number of simulations is $5{\times}6{\times}4{\times}15$, respectively, or a total of 1800. Some simulation results are presented in Electronic Supplement from Figure S7 to Figure S12. In most of the cases (95%), the final sedimentation rate is not sufficient to fill up the basin. Among the 90 remaining cases, we further eliminated the cases with a number of tilted block exceeding one. The four features of the cross-section discussed above lead to

the selection of a single optimal simulation which is presented in Figure 3.14. The best fit is obtained for $r_{S1} = 0.4, r_{S2} = 5.0, \delta_c = 8.1$ km and $\varphi_{NFS} = 25°$.

Our simulation results (numbered 1 to 4 in Figure 3.14 and denoted YML1 to YML4) and the three sketches in Figure 3.13 denoted WiCa1 to WiCa3 are now tentatively compared. The initial extension occurs most likely in the Upper Triassic and the normal fault has not yet rotated after a displacement of 5.9 km. The sedimentation rate then starts to increase after a displacement of 8.1 km before the Murre bounding fault is activated at a displacement of 8.5 km, Figure 3.14. This activation should occur in the Lower Jurassic such that YML2 corresponds to WiCa1. In the Middle Jurassic, the sedimentation is above the FHW region as seen on YML3 and WiCa2. The sedimentation ratio continues to increase and the results in YML4 resembles the interpretation in WiCa3, and this is the objective of the whole exercise.

One point deserves some comments. The WaCa2 sketch is not entirely consistent with YML2 predictions: a subsidence topography is required to change the activation from the SE of the Murre bounding fault whereas the proposed restoration WiCa2 considers a filled basin at this time. Our proposed subsidence on the topography in YML2 is in the order of 2.5 km. It is mechanically possible for a material with a cohesion in the order of 10 MPa. The introduction of surface process (surface erosion) presented in the previous section will not change the main predictions and thus we keep with a more probable sea floor geometry at that time. However, the fault offset is preserved in WiCa2 because of the sedimentation and thus this surface process is most unlikely to occur. To reconcile the two findings in WaCa2 and YML2, one would need a complex history of the dimensionless ratio r_S to have an alternated activation of the two bounding faults. Another possibility is that the 2-D setting is restrictive as one could imagine from the transpressional events discussed by *Sinclair* [1995].

3.6 Conclusions

The sequential limit analysis has been applied in the extensional context to capture the 2-D deformation associated with normal faulting. This method provides a simple means to combine mechanics and a geometrical construction of the geological structure following the seminal work of *Suppe* [1983]. The geometrical model considered here is the half-graben proposed by *Groshong* [1989] and it defines a collapse mechanism. The method consists of a two-step scheme at each extensional increment. First, the main features of the collapse mechanism

(dips of normal fault and axial surface and position of their common root) are determined according to the maximum strength theorem [*Yuan et al.*, 2015]. Second, the geometry of the structure is updated according to the half-graben kinematics in *Xiao and Suppe* [1992]. The method can be applied to 2-D topographies of arbitrary shape, accounts for softening on normal faults, can include erosion or sedimentation processes and fluid overpressures. The calculations are semi-analytical, requiring only a discretization of the topography and moderate numerical implementation.

The sequential limit analysis approach was applied to a simple wedge geometry with a initial flat topography and a planar inclined detachment. The retreat of the back wall leads to two possible types of deformation, called tectonic extensional collapse and gravitational collapse in *Yuan et al.* [2015]. During tectonic collapse, the whole topography is modified to attain a new critical shape well predicted by the Critical Coulomb Wedge (CCW) theory [*Xiao et al.*, 1991]. During gravitational collapse, the back wall separates from the wedge, which develops a secondary landward, straight slope well predicted by *Dahlen* [1984]. Increasing the detachment overpressure ratio leads to a transition from gravitational collapse to tectonic extensional collapse. The slopes of the stable wedge with detachment overpressures is well predicted with the Exact CCW theory discussed at length in *Yuan et al.* [2015]. The internal deformation leading the wedge to the new stable state is organized in a series of half-grabens. The positions of the half-graben roots on the detachment as well as their number change during extension is modifying the topography in a pattern reminiscent of the findings of *Mary et al.* [2013a;b].

We considered next the deformation of cover above a detachment fault during extension. The normal fault and the associated active axial surface rotate because of topography subsidence of the hanging wall. The continuous rotation of the normal fault creates a zone of intense shear of material which passes from the footwall to the hanging wall (FHW region). The rotation of the active axial surface perturbs the folding in the rollover. Fault softening renders the discontinuous rotation of normal fault and active axial surface, and the FHW regions are now containing blocks composed of undeformed material. The formation of FHW regions and their blocky internal structure is observed, at least in analogue experiments using sand [*Dahl*, 1987; *Egholm et al.*, 2007]. Sedimentation effect is considered by compensating the topography subsidence. This effect reduces the rotations of the normal fault and of the active axial surface.

There is thus a competition between softening and sedimentation effects in terms of numbers of blocks found in the FHW regions. The sedimentation ratio (defined as the sedimentation rate divided by the vertical component of the slip rate on the normal fault) has to be smaller than 0.6 for the FHW to be observed and the frictional softening should not exceed 2° to find at least two blocks in the FHW.

The field application concerns the Southern Jeanne d'Arc Basin, Grand Banks, offshore Newfoundland and is based primarily on the interpretation of *Withjack and Callaway* [2000] of the seismic line 85-4A and their proposed restoration. The complexity of the tectonic history renders the mechanical modelling rather difficult and some simplifications are proposed in this first attempt. The main feature of the interpretation is the presence of a single block in the FHW which requires fault softening and topographic subsidence in the early part of the rifting. Sedimentation is clearly observed and accounted for by increasing linearly the sedimentation ratio after an early period at a small constant value. Fault friction and sedimentation parameters are optimized after multiple sequential limit analysis calculations for the objective of matching several features: the timing of the FHW bounding faults, their relative distance and position, and finally the ratio of displacement on the two bounding faults. The final geometry is thus reproduced although a deep graben is required in the Lower Jurassic which could be argued by sedimentologists.

Future sequential limit analysis applied to the regions of normal faulting could be improved in at least three ways. First, normal faults are commonly listric and they were approximated as bi-linear here. The listric fault results either from a deformation of the footwall [*Martel*, 2004; *Grasemann et al.*, 2005], a gradual growth during sedimentation or a change with depth of the pressure conditions [*Mandl and Crans*, 1981]. This listric fault is captured by the collapse mechanism proposed by *Chen* [1975] for civil engineering applications. Second, the half-graben geometry has to be complemented to capture the antithetic faults which are important for oil-industry applications as in the example of Jeanne d'Arc Basin. Finally, the ductile response of shales and evaporite should be accounted for, as indicated by laboratory experiments [*Withjack et al.*, 1995; *Withjack and Callaway*, 2000].

Chapter 4

Reappraisal of gravity instability conditions for offshore wedges: consequences for overpressures in the Niger Delta

Abstract

The gravity instability in the overpressured sedimentary offshore deltas often results in three structural domains in interaction by the weak detachment plane: an upslope extensional province with normal faults, a transitional domain sliding seaward, and a downslope compressive region with thrust ramps to the surface. We provide the fluid pressure conditions for the gravity instabilities due to the interaction of these three structural domains. For that purpose, we apply the kinematic approach of Limit Analysis (LA) which relies on the mechanical equilibrium and the assumption that the onset of the instability is indeed triggered by the motion of the three domains as described above if a Coulomb criterion is enforced on all slipping surfaces. The LA provides the detachment activation length and the normal and thrust fault dips accounting for the detailed topography. The approach is validated by showing that our predictions match well the experimental results on normal faulting triggered by air overpressure in sand analogues. For offshore wedges, the stabilizing effect of the frontal thrusting and of the transitional zone requires large overpressures to reduce friction within the detachment and sed-

iment built-up upslope to trigger the instability. As a consequence, the topographic slope there is found to be several degree larger than predicted with the Critical Coulomb Wedge (CCW) theory, depending on the ratio of the detachment length to the sediment thickness downslope, the cohesion and the overpressures. Fitting our prototype to the offshore Niger Delta and estimating the above length ratio from cross-sections to be in the range 30 to 70, it is found that, for cohesionless materials, the effective friction coefficient $\mu'_B \leq 0.3$ within the bulk material and $\mu'_D \leq 0.02$ on the detachment at the onset of the gravity instability. These values are much lower than those previously determined ($\mu'_B = 0.5 - 0.9$, $\mu'_D = 0. - 0.2$) by considering only the compressive fold-and-thrust belt at the distal end of the delta and the CCW theory. Theses new values correspond to a pore-fluid pressure in the range of 80 to 90 % of the lithostatic pressure within the bulk material (Hubbert-Rubey fluid-pressure ratio $0.8 - 0.9$), and in the range 97 to 99% of the lithostatic pressure within the detachment.

4.1 Introduction

Regional seismic studies across the Amazon Fan [*Silva et al.*, 1998; *Cobbold et al.*, 2004], the offshore Niger Delta [*Weber and Daukoru*, 1975; *Hooper et al.*, 2002; *Maloney et al.*, 2010], and the offshore Brunei wedge [*Tingay et al.*, 2009; *King et al.*, 2010] show normal faulting in the thick, coastal part on the shelf and simultaneous thrusting in the thin, deep parts, with all faults rooted on a common detachment level. These structures are thus typically characterized by three distinct domains above the weak detachment: the upslope extensional province, the non-deformed transitional sliding domain at mid-slope and the downslope compressive province. They are interpreted as the result of gravity-driven mechanical instabilities triggered by the sediment load and the associated high fluid pressures at depth [*Damuth*, 1994]. The objective of the present study is to propose a methodology, to capture the fluid pressure conditions at the onset of these gravity instabilities, accounting for the interaction of the three structural domains. This methodology relies on a strong assumption, shared with the classical Critical Coulomb Wedge theory (CCW), that the detachment, composed here of shales, is frictional and cohesive.

The link between extensional and compressional provinces during gravity instability was demonstrated experimentally. The wedge prototype composed of a progradational dry sand on a viscous silicone substratum considered by *Ge et al.* [1997]; *McClay et al.* [1998]; *Rowan*

et al. [2004]; *Vendeville* [2005] results in the synchronously delta-top graben system and delta-toe fold-and-thrust belt. These experiments however do not capture the influence of the fluid overpressures. It is only recently that analogue experiments with air flow through sand has been proposed [*Mourgues and Cobbold*, 2003; 2006b] to simulate the onset and the evolution of overpressured, gravity-driven shale deltas.

The interaction between the three structural provinces was also questioned on theoretical grounds. *Crans et al.* [1980] proposed an exact, analytical solution based on the slip line theory to capture listric faults for frictional, overpressured materials considering an inclined layer. Their approach applies to the extensive and compressive domains. The difference in forces parallel to the slope in these two regions is then balanced assuming a frictional detachment providing the extent of the intermediate region. The main difference with the CCW theory of *Dahlen* [1984] is that the later approach applies to a wedge. It generalized the concept of slope instability well known in civil engineering to the length scale of sedimentary, saturated wedges. It applies to the extensive upslope (active) and to the compressive downslope (passive) domains but does not propose any connection between the two. The orientation of faults composing these two domains is well captured by the now classical geometrical method relying on the Mohr construction, of *Lehner* [1986]. Note that the solution *Dahlen* [1984] was corrected by *Wang et al.* [2006], as discussed in *Yuan et al.* [2015], referred to as paper 1 in what follows. The correction is minor for compressive wedges but becomes substantial for extension. The extent of the intermediate region within the wedge can also be constructed following the same argument of *Crans et al.* [1980], despite the difference in geometry, as presented in *Mourgues et al.* [2009]

Among the numerous applications of the CCW theory to fold-and-thrust belts and fluid-saturated wedges, there has been some recent work by *Bilotti and Shaw* [2005] and *Suppe* [2007; 2014] on the Niger Delta, assuming a fully frictional behaviour of the sediments and the detachment. The CCW theory was applied to the geometries of frontal compressive wedge to infer fluid overpressures. The pore-fluid pressure within the detachment was 90% of the lithostatic pressure (Hubbert-Rubey fluid-pressure ratio $\lambda \sim 0.9$).

Our objective is to propose a methodology for capturing the interaction between the three domains of the collapsing wedges assuming arbitrary geometry and cohesive materials. It is a 2-D analytical application of the kinematic approach of Limit Analysis [*Chen*, 1975; *Salençon*,

2002] as presented by *Maillot and Leroy* [2006] for dry frictional materials and by *Pons and Leroy* [2012] and in paper 1 for fluid-saturated media. The application of Limit Analysis to the offshore Niger Delta allows us to re-evaluate the fluid pressures to even larger levels than those already inferred by *Bilotti and Shaw* [2005].

This contribution contents are as follows. Section 4.2 and Appendix A concerns the presentation of the Limit Analysis for the collapse with three domains, typical of offshore deltas. Section 4.3 validates this method by comparing the predictions with analytical [*Hubbert and Rubey*, 1959; *Lacoste et al.*, 2012] and experimental [*Mourgues and Cobbold*, 2006a] estimations of the collapse length and fault dips for an inclined layer. The new method is then applied to the offshore Niger Delta to constrain the fluid pressures necessary to produce the current activation of the three structural domains. The Electronic Supplement to this contribution proposes a comparison of the various fluid overpressure parametrizations found in the literature as well as the complete derivation of the solution of *Lacoste et al.* [2012] for sake of completeness.

4.2 Gravity instabilities with Limit Analysis

The concept of gravity-driven collapse discussed above is now developed into a prototype amenable to a theoretical analysis. The Limit Analysis is then presented for the general case of a wedge with an arbitrary topography and fluid overpressures.

4.2.1 General prototype

Geometry and material The geometry of our prototype and the gravity-driven collapse mechanism are presented in Figure 4.1. The domain is composed of a uniform, fluid saturated material and has an arbitrary topography. It rests on a planar detachment (AB) inclined at an angle β (positive if dipping landward). The detachment and the bulk material are frictional with distinct cohesions and friction angles, noted C_D, φ_D and C_B, φ_B, respectively. The gravity instability results from the activation of the normal fault and a thrust ramp (JH and GE in Figure 4.1). These faults could have different properties from the bulk material and they are denoted C_{NF}, φ_{NF} and C_R, φ_R. The normal and the reverse faults have conjugate shear discontinuities or axial surfaces denoted JI and GF and dipping at θ_a and θ_p, respectively. The subscript a and p means active and passive, a classical terminology in geotechnics for defining

the regions collapsing in extension and compression, respectively. Density of the bulk material is ρ and that of the fluid, ρ_f.

We have thus defined the three structural regions. It is the half-graben (HG) defined by the region HIJ which is the driver for the instability. It presses the resisting sliding block (SB) seaward up to the compressive domain where thrusting occurs with the hanging wall (HW) defined by the region EFG. This motion is with respect to the immobile frontal seaward region (FS) and the back, landward region (BL). The mechanical approach presented in the last part of this section will provide the means to compute the position of the six points E, F, G and H, I, J.

Pore fluid pressure The material is submerged and any point $\underline{x}$ within the wedge has above it a sea bed at the depth $D(\underline{x})$, Figure 4.1. The vertical coordinate x_2 points upward with an origin at the sea surface. The fluid pressure p at $\underline{x}$ and the corresponding fluid overpressure Δp, difference with the hydrostatic pressure, are

$$p = g[-\lambda\,\rho x_2 + (\rho_f - \rho\lambda)D] \quad \text{and} \quad \Delta p = -\Delta\lambda\,\rho g(x_2 + D)\,. \tag{4.1}$$

The two scalars λ and $\Delta\lambda$ are the fluid pressure ratio and the overpressure ratio defined by *Hubbert and Rubey* [1959]

$$\Delta\lambda = \lambda - \lambda_{hydro}\,, \quad \text{with} \quad \lambda_{hydro} = \rho_f/\rho \quad \text{and} \quad \Delta\lambda_{Max} = 1 - \rho_f/\rho, \tag{4.2}$$

The maximum value $\Delta\lambda_{Max}$ being introduced for further reference. The value of the pressure ratios could differ in the bulk material, in the detachment as well as in the normal and reverse faults so that the notations λ_B, λ_D, λ_{NF} and λ_R are proposed for these specific regions. The history and present-day conditions which could explain these differences are not discussed in this contribution.

It should be stressed that there are different definitions of λ in the literature due to the selection of various coordinate systems. These different parametrizations lead to difficulties for comparing the various predictions. Some definitions have been discussed at length in the appendix of paper 1 and two new definitions are presented in the Electronic Supplement of this contribution.

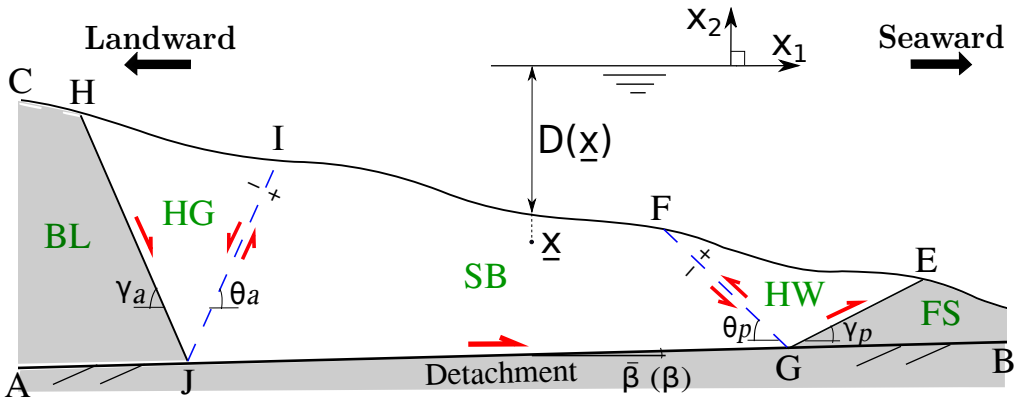


Fig. 4.1: The general prototype and the collapse mechanism for gravitational instabilities. The half-graben (HG) collapse drives the sliding of the central region (sliding block SB) up to the thrusting at point G with the hanging wall (HW) (red semi-arrows along the faults JH, GE and the active detachment JG and double semi-arrows across the axial surfaces JI and GF).

4.2.2 Application of Limit Analysis

The first step of the kinematic approach of Limit Analysis [*Chen*, 1975; *Salençon*, 2002] consists in the definition of the virtual velocity field associated to the collapse mechanisms just described. This velocity is virtual since it may not be the exact one and corresponds, as in our particular case, to a simplification proposed to obtain an analytical solution.

The proposed virtual velocity field is uniform in each of the three structural domains and denoted $\underline{\hat{U}}_{HG}$, $\underline{\hat{U}}_{SB}$ and $\underline{\hat{U}}_{HW}$. The superposed hat is to remind the reader of the virtual character of the piecewise uniform field. This last property implies that there are discontinuities across the two axial surfaces (JI and GF) and of course across the detachment (JG) and the two faults (JH and GE). The set of these discontinuities is denoted Σ. The difference between the velocity on the two sides of a discontinuity in Σ is the velocity jump denoted $\underline{\hat{J}}$ (the positive and negative sides on each discontinuity is defined in Figure 4.1).

One further property is required for this velocity field: all velocity jumps are not parallel to the corresponding discontinuity but are oriented at the angle φ corresponding to the discontinuity friction angle. The theoretical reasons for this choice, which are counter-intuitive for a naturalist, were discussed at length in *Maillot and Leroy* [2006]; *Yuan et al.* [2015]. The immediate consequence of this orientation selection is the introduction of a set of constraints which enforce that the sense of shear on the axial surfaces and the faults are indeed the ones

presented in Figure 4.1

$$\begin{aligned}
&\varphi_B + \varphi_D + \beta < \theta_a < \pi\,, \quad \varphi_{NF} - \varphi_D - \beta < \gamma_a < \pi,\\
&\varphi_B + \varphi_{NF} < \gamma_a + \theta_a < \pi\,, \quad -\beta < \theta_p < \pi - \varphi_B - \beta - \varphi_D,\\
&\beta < \gamma_p < \pi + \beta - \varphi_R + \varphi_D\,, \quad 0 < \gamma_p + \theta_p < \pi - \varphi_B - \varphi_R\,,
\end{aligned} \tag{4.3}$$

as it is demonstrated in 1.1 with two hodograh constructions.

The second step in Limit Analysis is the application of an integral expression (weak form) of mechanical equilibrium. Following *Pons and Leroy* [2012], it states the equality between the effective external power and the effective internal work

$$\mathcal{P}'_{\text{ext}}(\hat{\underline{U}}) = \mathcal{P}'_{\text{int}}(\hat{\underline{U}})\,,\ \forall\, \hat{\underline{U}} \tag{4.4}$$

for any virtual velocity field having the properties described above. The effective external power is

$$\mathcal{P}'_{\text{ext}}(\hat{\underline{U}}) = \int_{\Omega_t} \rho \underline{g} \cdot \hat{\underline{U}}\, dV + \int_{\Sigma} p_{\Sigma} \underline{n} \cdot \hat{\underline{J}}\, dS\,, \tag{4.5}$$

and has two contributions. The first contribution is the power of the gravity field on the virtual velocity, with $\underline{g}$ denoting the vertical gravity acceleration. The second contribution corresponds to the power of the velocity discontinuities (normal component, with the normal vector denoted $\underline{n}$ and pointing towards the positive side) on the fluid pressure, considered as an external field, for the set Σ defined above. The calculation of $\mathcal{P}'_{\text{ext}}(\hat{\underline{U}})$ is technical and this exercise is postponed to 1.1 where the general expression (D.3) is finally proposed.

The internal effective power $\mathcal{P}'_{\text{int}}$ in (4.4) results in our particular case from the power of the effective stress vectors on the velocity jumps of the set Σ. Since the exact stress field and consequently the stress vectors are unknowns, it is proposed in the kinematic approach of Limit Analysis to construct an upper bound to this internal power. It is defined as the maximum resisting power and is obtained by integration along the discontinuities of Σ

$$\mathcal{P}'_{\text{mr}}(\hat{\underline{U}}) = \int_{\Sigma_U} \hat{J} C \cos\varphi\, dS\,, \tag{4.6}$$

where C and φ are the cohesion and friction angle of the discontinuity. Again, the detailed expression for this quantity is found in 1.1 in equation (D.4).

Combine now (4.4) and the fact that (4.6) is a bound to the internal power to obtain the inequality

$$\mathcal{P}'_{\text{ext}}(\hat{\underline{U}}) - \mathcal{P}'_{\text{mr}}(\hat{\underline{U}}) \leq 0\,. \tag{4.7}$$

The stability conditions controlling the onset of the gravity instability are as follows. If this inequality is strictly enforced for all choices of velocity field, there is no gravity instability. If there are collapse mechanisms for which effective external power and maximum resisting power are identical, they define the conditions for the onset of a gravity instability. If the effective external power is found to be greater than the maximum resisting power, the corresponding collapse mechanisms represents a dynamic instability. Note that the kinematic approach of Limit Analysis does not warrant a unique collapse mechanism at the onset of instability.

For all practical purposes, the procedure to determine the collapse mechanism describing an instability consists of maximising the difference in the left hand-side of (4.7). The mechanism associated with this maximum is considered to be dominant, since it is the closest to the instability condition. This maximum is found by varying the dips γ_a, θ_a, γ_p, θ_p and the positions of points J and G or, equivalently, the positions of the six points E, F, G and H, I, J.

4.3 Validation for an inclined layer

The arbitrary topography of our general prototype is now a planar topographic surface parallel to the detachment ($\alpha = \bar{\beta} = -\beta$), forming an inclined layer of thickness h (Figure 4.2a). All materials are considered to be cohesionless so that the resisting power in (4.6) is zero. The friction angles and fluid pressure ratios in the normal fault and thrust ramp are assumed to have the some values as the bulk materials, $\varphi_{NF} = \varphi_R = \varphi_B$, $\lambda_{NF} = \lambda_R = \lambda_B$. The solution of Limit Analysis for this simplified problem is now presented and compared with known results and with experimental data for granular materials.

The general expression (D.3) in the 1.1 for $\mathcal{P}'_{\text{ext}}$ simplified greatly for this prototype and the stability condition (4.7) reads

$$
\begin{aligned}
\tilde{\mathcal{P}}'_{\text{ext}} &= \mathcal{A}\,\tilde{L}_{JG} + \mathcal{B} \leq 0\,, \\
\text{with} \quad \mathcal{A} &= \big[-\Delta\lambda_{Max}\sin(\beta+\varphi_D) + \Delta\lambda_D \sin(\varphi_D)/\cos\beta \big]\,, \\
\text{and} \quad \mathcal{B} &= \frac{1}{2}\Delta\lambda_{Max}\Big[\big[\cot(\gamma_a+\beta)+\cot(\theta_a-\beta)\big]\sin(\gamma_a-\varphi_B)\tilde{U}_{HG} \\
&\quad - \big[\cot(\theta_p+\beta)+\cot(\gamma_p-\beta)\big]\sin(\gamma_p+\varphi_B)\tilde{U}_{HW} \\
&\quad + \big[\cot(\theta_a-\beta)+\cot(\theta_p+\beta)\big]\sin(\beta+\varphi_D)\Big] \\
&\quad + \frac{1}{2}\Delta\lambda_B\frac{\sin(\varphi_B)}{\cos\beta}\Big[\frac{\tilde{U}_{HG}}{\sin(\gamma_a+\beta)} + \frac{\tilde{J}_{JI}}{\sin(\theta_a-\beta)} + \frac{\tilde{U}_{HW}}{\sin(\gamma_p-\beta)} + \frac{\tilde{J}_{GF}}{\sin(\theta_p+\beta)}\Big]\,.
\end{aligned}
\tag{4.8}
$$

The superposed tilde identifies dimensionless quantities obtained by division of physical quantities with reference values, $\rho g h$ for stresses, h for lengths. The virtual velocities are normalized by the sliding block velocity $\hat{U}_{SB}$ and the superposed tilde marks this division. The relation between the various velocity is constructed in 1.1 and the final result is

$$\begin{aligned} \frac{\tilde{U}_{HG}}{\sin(\theta_a - \varphi_B - \beta - \varphi_D)} &= \frac{1}{\sin(\theta_a + \gamma_a - \varphi_{NF} - \varphi_B)} = \frac{\tilde{J}_{JI}}{\sin(\gamma_a + \beta - \varphi_{NF} + \varphi_D)}\,, \\ \frac{\tilde{U}_{HW}}{\sin(\theta_p + \varphi_B + \beta + \varphi_D)} &= \frac{1}{\sin(\theta_p + \gamma_p + \varphi_R + \varphi_B)} = \frac{\tilde{J}_{GF}}{\sin(\gamma_p - \beta + \varphi_R - \varphi_D)}\,. \end{aligned} \tag{4.9}$$

It should be noted that the sea depth does not influence the stability condition in (4.8). It is only the pressure ratios which matters for the fluid contribution. The same remark applies in the next section.

The term $\mathcal{A}\,\tilde{L}_{JG}$ in (4.8) is independent of the fault dips and is interpreted as the contribution of the sliding block region to the effective, external work. The term $\mathcal{B}$ is independent of the sliding block extent and corresponds to the contributions of the upslope half-graben and the downslope hanging wall.

The zero cohesions implies that the maximum resisting power $\mathcal{P}'_{\rm mr}$ in (4.6) is also zero and, according to the stability condition (4.7), that the onset of static instability is defined by

$$Max\big[\tilde{\mathcal{P}}'_{\rm ext}(\beta, \gamma_a, \theta_a, \gamma_p, \theta_p, \tilde{L}_{JG})\big] = 0\,, \tag{4.10}$$

having limited the list of arguments to the geometrical variables. The relation for $\tilde{\mathcal{P}}'_{\rm ext}$ in (4.8) is affine and the sign of the scalar $\mathcal{A}$ is determinant to find the optimum geometrical variables maximising (4.10). If $\mathcal{A}$ is positive, the optimum length $\tilde{L}_{JG}$ is infinite. If $\mathcal{A}$ is negative, there is an optimum length $-\mathcal{B}/\mathcal{A}$ if $\mathcal{B}$ is positive. A negative maximum $\mathcal{B}$ would mean stability. The sign of $\mathcal{A}$ is conveniently examined by introducing the critical β_c for which it is zero:

$$\beta_c = -\frac{1}{2}\sin^{-1}\left[\Big(1 - 2\frac{\Delta\lambda_D}{\Delta\lambda_{Max}}\Big)\sin(\varphi_D)\right] + \frac{1}{2}\varphi_D\,. \tag{4.11}$$

The layer dip is negative and if β is less than β_c (larger in absolute value), the scalar $\mathcal{A}$ is positive. The maximum $\tilde{\mathcal{P}}'_{\rm ext}$ is then associated to an infinitely long layer. For such values of β, the system is dynamically unstable. Of more interest here are the cases for which β is greater than β_c (smaller in absolute value). The maximum in (4.10) is then evaluated as follows: *(i)* maximise $\mathcal{B}$ with respect to $\gamma_a, \theta_a, \gamma_p$ and θ_p subjected to the constraints (4.3), and thus

Table 4.1: Geometrical, material parameters and fluid pressure ratios for the stability analyses (validation and application to the Niger Delta).

Notation	Definition	Value/Range [Section 3, 4.1]	Value/Range [Section 4.2]	Unit
α	topographic slope	variable	1^{b}	deg.
β	detachment dip	variable	1.5^{b}	deg.
h	reference height	1	3^{b}	km
L_{JGc}	collapse length	variable	$100 - 200$	km
φ_a	friction angle ($a = B, AS, NF, R$)[a]	30	30^{c}	deg.
φ_D	detachment friction angle	10	10^{c}	deg.
C_a	cohesion ($a = B, AS, NF, R$)[c]	$(0, 0.1)\cdot\rho g h$	$(0 - 7) \cdot 10^6$	Pa
C_D	detachment cohesion	0	0	Pa
ρ_f	fluid phase density	1000	1030	kg/m^3
ρ	saturated rock density	2000	2400^{b}	kg/m^3
λ_{hydro}	hydrostatic pressure ratio ($= \rho_f/\rho$)	0.5	0.42	-
$\Delta\lambda_B$	bulk overpressure ratio	$0.0 - 0.2$	$0.3 - 0.5$	-
$\Delta\lambda_D$	detachment overpressure ratio	$0.1 - 0.3$	$0.5 - 0.57$	-

[a]Notation: $B-$ Bulk, $AS-$ Axial surface, $NF-$ Normal fault and $R-$ Ramp. [b]Parameters are from *Bilotti and Shaw* [2005]. [c]Parameters are from *Krueger and Grant* [2011] and *Suppe* [2014].

determine the optimum dips of the half-graben and hanging wall; *(ii)* calculate the collapse length $\tilde{L}_{JG}$ which ensures the instability condition (4.10) if the maximum $\mathcal{B}$ is positive.

The new result here is that the length of the sliding block is determined by the ratio of two scalars. The denominator is only function of the detachment dip and friction and of the overpressure. The numerator is function of the geometry, the frictional properties and the overpressures in the half-graben and in the hanging wall. The change in sign (negative to positive) of the numerator signals a dynamic instability starting with the longest wave-length mode possible. This change could be due to a variation in the detachment overpressure, friction properties or a rotation of the detachment, for example.

4.3.1 Comparison with other analytical results

Hubbert and Rubey [1959] considered the classic stability analysis of an infinite frictional, cohesionless layer above a fluid overpressured base and determined the critical slope, their equation (117)

$$\bar{\beta}_c = \tan^{-1}\left[(1 - \lambda_D^{(L)})\tan(\varphi_D)\right], \tag{4.12}$$

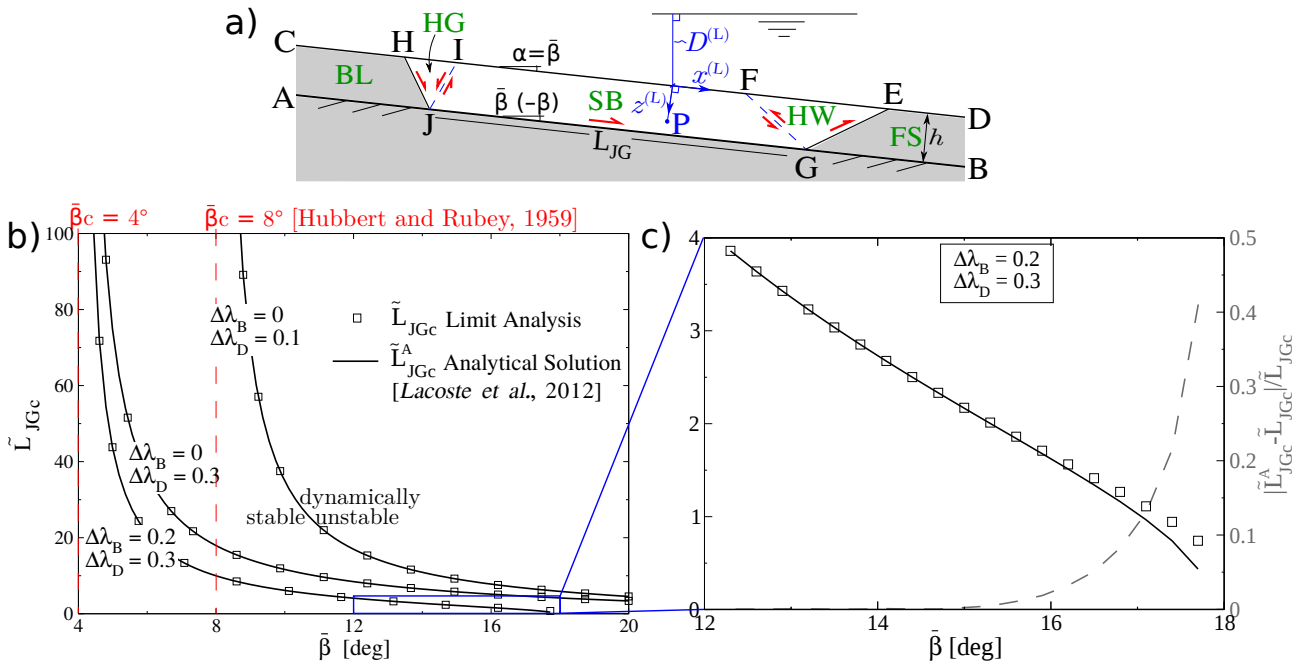


Fig. 4.2: (a) Illustration of the inclined layer ($\alpha = \bar{\beta}$) of thickness h. (b) Comparison of the collapse extent $\tilde{L}_{JGc}$ from predictions of Limit Analysis (symbols) and the approximately analytical results (curves) [*Lacoste et al.*, 2012], the red dashed lines present the critical dips for the infinite collapse mode. (c) The relative difference ratio (grey dashed curve) between the collapse length in Limit Analysis and approximately analytical solution [*Lacoste et al.*, 2012] when the value of $\tilde{L}_{JGc}$ is small.

which is expressed here in terms of the overpressure ratio $\lambda_D^{(L)}$ defined in *Lacoste et al.* [2012]

$$\lambda^{(L)} = \frac{p_f^{(L)} - \rho_f g(D^{(L)} + z^{(L)} \cos\alpha)}{(\rho - \rho_f) g z^{(L)} \cos\alpha} \,. \tag{4.13}$$

The distance $D^{(L)}$ and the coordinate $z^{(L)}$ are defined in Figure 4.2a. Further information on the fluid pressure ratios are found in the Electronic Supplement. This solution (4.12) coincides exactly with our solution (4.11). This can be verified by incorporating into (4.12) the definition of $\lambda_D^{(L)}$ in terms of λ_D, equation (E.2), rearrange the trigonometric functions and finally use (4.2) to obtain (4.11).

The collapse extent $\tilde{L}_{JGc}$ is now compared with the approximate solution of *Lacoste et al.* [2012] (their equation (9)) which is presented in details in the Electronic Supplement. For that purpose, the values of $\bar{\beta}_c = 4°, 8°$ corresponding to $\Delta\lambda_D = 0.3$ and 0.1 are selected. They associated critical lengths are the red dashed lines in Figure 4.2b for $\tilde{L}_{JGc} \to \infty$. The other material property values for the examples in that figure are summarized in the third column of

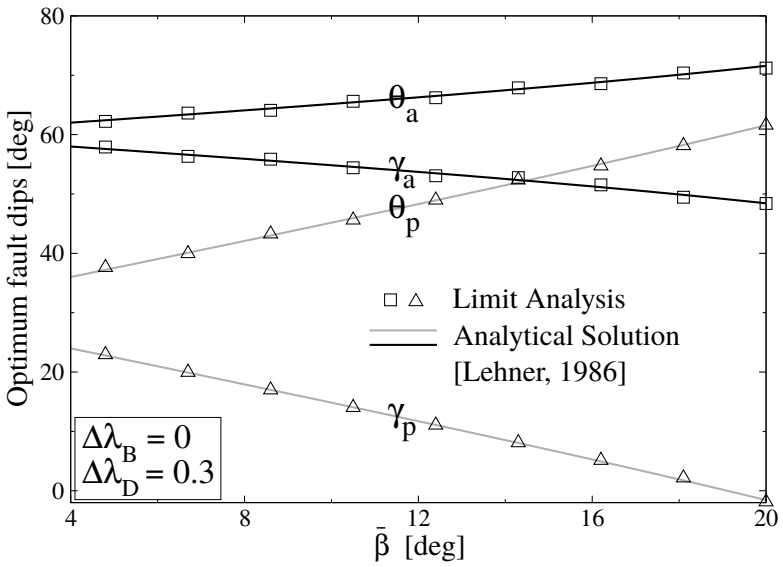


Fig. 4.3: Comparison of fault dips ($\gamma_{ac}, \theta_a, \gamma_c$ and θ_p) for the active (or updip, extensional) and passive (or down dip, compressional) collapses. The solid lines are the theoretical dips in the 2.

Table 4.1.

The comparison of the Limit Analysis (symbols) and analytical results (curves) are presented in Figure 4.2b and 4.2c. Our predictions and the approximately analytical results are very close for the three sets of detachment and bulk overpressure ratios. Differences become important at low values of $\tilde{L}_{JGc}$, corresponding to high slopes ($\bar{\beta} \geq 16°$) as shown by the relative difference $|\tilde{L}^A_{JGc} - \tilde{L}_{JGc}|/\tilde{L}_{JGc}$ (grey dashed curve) in Figure 4.2c. Note that, as expected, the range of critical detachment dips $\bar{\beta}$ for the finite collapse length is always greater than the critical dip $\bar{\beta}_c$ for the infinite collapse length. These curves also demonstrate that if an experiment is performed by increasing the dip $\bar{\beta}$ until collapse occurs, then collapse will occur at the lowest $\bar{\beta}$, corresponding to the longest length available for slip. If the experiment is simulated by increasing $\Delta\lambda_D$, keeping constant dip $\bar{\beta}$, then the onset collapse will use the longest length available.

The validation of fault dips ($\gamma_{ac}, \theta_a, \gamma_c$ and θ_p) according the two approaches is presented in Figure 4.3, for bulk pressure ratio $\Delta\lambda_B = 0$ and detachment pressure ratio $\Delta\lambda_D = 0.3$. The theoretical dips in 2 are provided by the method of the geometrical construction of Mohr's circles [*Lehner*, 1986] for the active and passive Rankine stress states. The two sets of predictions coincide very well. Note that the sum of active faults $\gamma_{ac} + \theta_a = 60° \, (= \pi/2 - \varphi_B)$ and passive dips $\gamma_c + \theta_p = 120° \, (= \pi/2 + \varphi_B)$.

4.3.2 Validation with sandbox experiments in fluid overpressured conditions

The dips of the active faults are now validated by the application of Limit Analysis to the sandbox experiments of *Mourgues and Cobbold* [2003] in which fluid overpressured are obtained with compressed air. The experimental setup consists of a rectangular glass box in which flat sand packs were built with a length of 40 cm, a width of 20 cm, a height of 4 cm and inclined at a slope $\bar{\beta} = 6.7°$. The sand density $\rho_s = 1700$ kg/m^3, the internal friction coefficient $\mu = 1.18$ ($\varphi_B = 50°$) and the bulk cohesion ($C_B = 12 - 72$ Pa). The sand pack rests on two overlapping sieves. Beneath the sieves a pressure chamber provides a uniform air pressure (p_b) at the base of the sand body. The top is maintained at the atmospheric pressure p_{at} so that air flows through the sand in a direction perpendicular to the slope. With this setup, the pressure ratios on the detachment and in the sand are the same $\lambda_B^{(M)} = \lambda_D^{(M)}$ [*Mourgues and Cobbold*, 2003; 2006b; *Lacoste et al.*, 2012; *Pons and Mourgues*, 2012]. Definition of $\lambda^{(M)}$ in terms of λ is given, again, in the 1. By slowly moving one of the sieves in extension, a velocity discontinuity is created at the base and conjugate normal faults form, meeting at the discontinuity (Figure 4.4a). For each of the four experiments, the corresponding value of λ is given in Figure 4.4a. The dips of these faults is measured and plotted in Figure 4.4b (symbols) for increasing basal pressures.

Limit analysis on our prototype provide not only the active faults orientations but also the passive faults dips as well the intermediate domain length. However, since the latter data was not published, the comparison is limited to the active faults dips. Futhermore, to complete our data set, we assume that the detachment has zero cohesion and we choose $\varphi_D = 10°$ to obtain indeed slip on the imposed slope at 6.7°.

The experimental results and our predictions using the Limit Analysis are presented in Figure 4.4b where the fault dips are as function of fluid pressure ratio $\lambda_D\,(= \lambda_B)$. The experimental results show that the normal fault dips γ_a (triangle symbols) decrease and the shear plane dip θ_a (square symbols) increase with the fluid pressure ratio. The theoretical results (γ_a, θ_a, black curves) present the same trend. We conclude that the series of four experiments are well captured by the Limit Analysis. Another interesting observation is that the dips (γ_c, θ_p, grey curves in Figure 4.4b) of the passive faults are not varying much until the fluid pressure ratio is close to 0.9. The discrepancies between limit analysis predictions and experimental observations are probably due to the side-wall frictions in experiments.

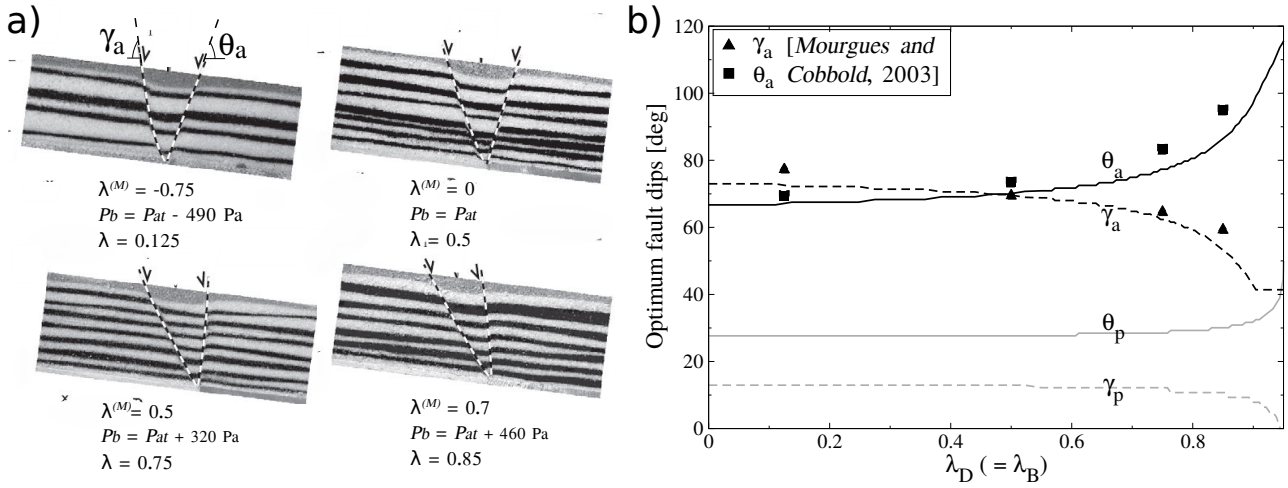


Fig. 4.4: The validation of dips of active faults from the sandbox experiments. (a) The extensional faults formed by different air pressure through the sand packs, modified after *Mourgues and Cobbold* [2003]. (b) The comparison of extensional fault dips (γ_a, θ_a) from experiments (symbols) and predictions from the Limit Analysis (solid and dashed curves) as function of fluid pressure ratio.

4.4 Application to the offshore Niger Delta

The prototype is now wedge shaped to approximate the cross-section of the offshore Niger Delta. The collapse mechanism is identical to the one previously considered. The fluid overpressures are determined by requiring that the observed surface and detachment dips, α and β, correspond to conditions for the onset of instability. The large differences between the predicted fluid overpressures and the ones previously determined [*Bilotti and Shaw*, 2005] are finally discussed.

4.4.1 Stability conditions

The stability condition (4.7) is based on the difference between the effective external power and the maximum resisting power which read

$$\begin{aligned}\tilde{\mathcal{P}}'_{\text{ext}}(\underline{\tilde{U}}) = \Delta\lambda_{Max}\big[&\tilde{S}_{HG}\tilde{U}_{HG}\sin(\gamma_a-\varphi_{NF}) - \tilde{S}_{SB}\sin(\beta+\varphi_D) - \tilde{S}_{HW}\tilde{U}_{HW}\sin(\gamma_p+\varphi_R)\big] \\ &+ \Delta\lambda_{NF}\,\tilde{S}_{JJ'H}\tilde{U}_{HG}\frac{\sin(\varphi_{NF})}{\cos(\gamma_a)} + \Delta\lambda_B\,\tilde{S}_{JJ'I}\tilde{J}_{JI}\frac{\sin(\varphi_B)}{\cos(\theta_a)} + \Delta\lambda_B\,\tilde{S}_{GG'F}\tilde{J}_{GF}\frac{\sin(\varphi_B)}{\cos(\theta_p)} \\ &+ \Delta\lambda_R\,\tilde{S}_{GG'E}\tilde{U}_{HW}\frac{\sin(\varphi_R)}{\cos(\gamma_p)} + \Delta\lambda_D\,\tilde{S}_{JJ'G'G}\frac{\sin(\varphi_D)}{\cos\beta}\,,\end{aligned} \tag{4.14}$$

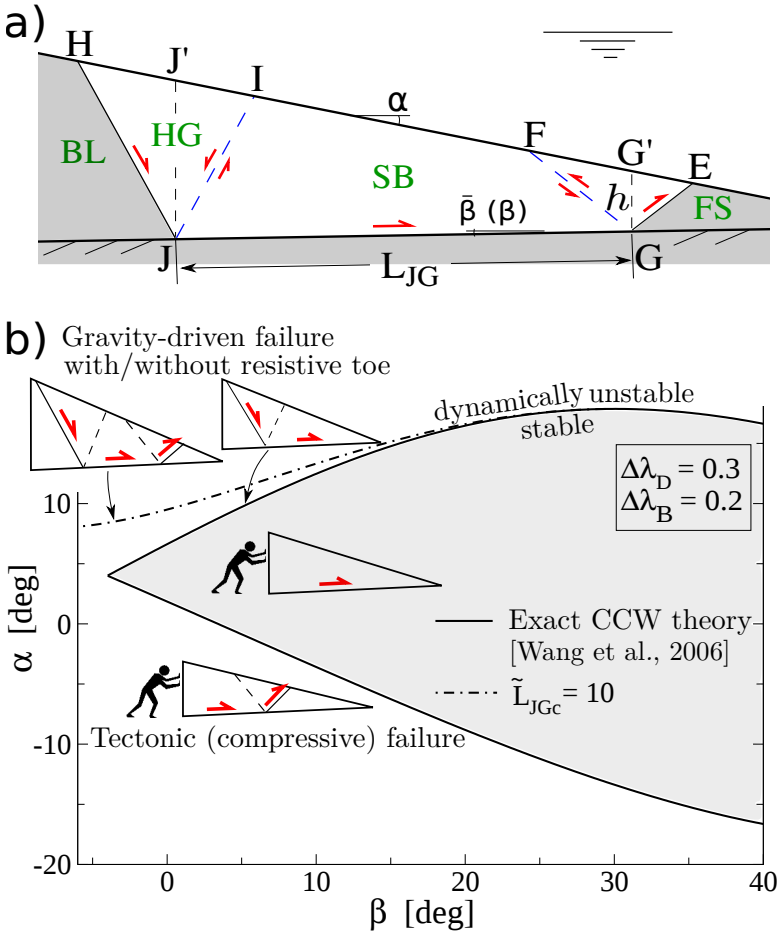


Fig. 4.5: (a) Combined extensional-compressional collapse mechanism in a wedge prototype with a resistive toe (height h). (b) The critical surface slope as function of detachment dip (dash-dot curve) for collapse length $\tilde{L}_{JGc} = L_{JGc}/h = 10$, the solid curves bound the stability domain of the CCW theory, once properly amended by *Wang et al.* [2006].

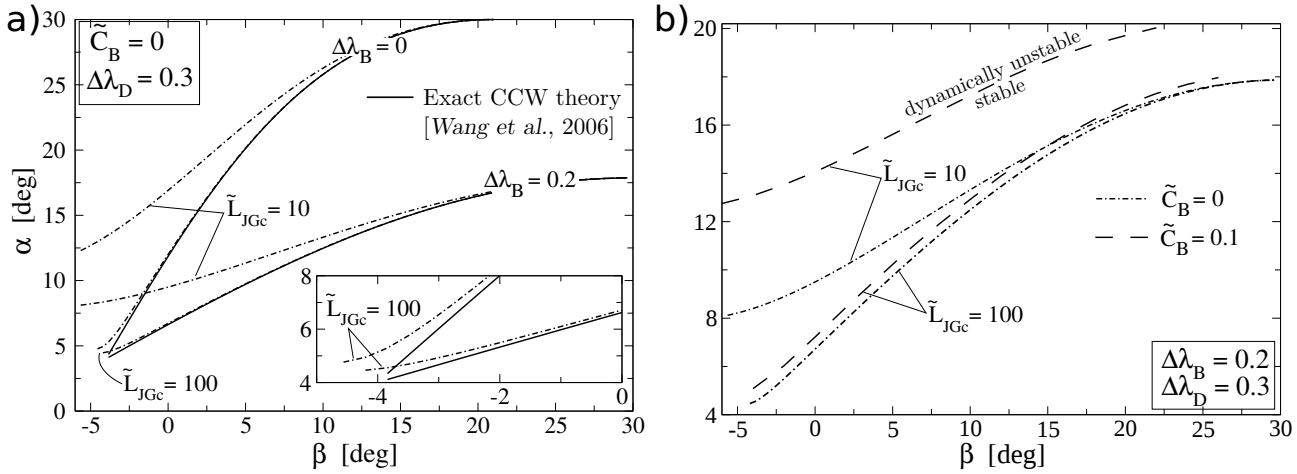


Fig. 4.6: (a) The critical surface slope for collapse length $\tilde{L}_{JGc} = 10,\ 100$ at the bulk overpressure ratio $\Delta\lambda_B = 0,\ 0.2$ (dotted-dashed curves), setting dimensionless bulk cohesion $\tilde{C}_B = 0$. The solid curves are the upper stability limits of the Exact CCW theory corresponding to $\tilde{L}_{JGc} \to \infty$. (b) The critical surface slope for cohesive materials, $\tilde{C}_B = 0.1$ (dashed curves).

and

$$\begin{aligned}\tilde{\mathcal{P}}'_{\rm mr}(\underline{\tilde{U}}) = \tilde{C}_D\tilde{L}_{JG}\cos(\varphi_D) + \tilde{C}_{NF}\tilde{L}_{JH}\cos(\varphi_{NF})\tilde{U}_{HG} + \tilde{C}_B\tilde{L}_{JI}\cos(\varphi_B)\tilde{J}_{JI} \\ + \tilde{C}_R\tilde{L}_{GE}\cos(\varphi_R)\tilde{U}_{HW} + \tilde{C}_B\tilde{L}_{GF}\cos(\varphi_B)\tilde{J}_{GF}\,.\end{aligned} \tag{4.15}$$

These two equations correspond to a normalized and a dimensionless version of (D.3) and (D.4) in the 1.1. These normalization and dimensional analysis are done as in the previous section except for the reference length which is now h, the thickness of the sediment above point G, Figure 4.5a. The surfaces $S_{JJ'H}$, $S_{JJ'I}$, $S_{GG'F}$, $S_{GG'E}$ and $S_{JJ'G'G}$ are the triangular surfaces based on the points G' and J' found on the topography at the apex of points G and J, respectively. Expression for these surfaces are provided in the 1.3 for sake of completeness. The normal fault JH and the thrust ramp GE have the same pressure and material properties as the bulk material. The relations between the various virtual velocity provided in (4.9) still apply.

The collapse mechanism position with respect to sea depth is immaterial, since the external power is only function of the pressure ratios, as discussed in the previous section. The collapse mechanism is characterised by the dimensionless length $\tilde{L}_{JG} = L_{JG}/h$, ratio of the central block length to the thickness of the resisting toe measured above point G.

It is proposed to built a a stability map in the (α, β) plane based on the stability condition

(4.7) for given value of the pressure ratios and the sliding block length. The following procedure is conducted for every set (α, β) to decide if the corresponding wedge is stable or not. We first maximize the difference in (4.7) with respect to the four dips γ_a, θ_a, γ_p and θ_p, respecting the constraints in (4.3). Second, if the maximum difference is negative, the wedge is said stable, otherwise unstable. Note that a positive difference marks a dynamic instability. The end result is the dash-dot curve in Figure 4.5b) obtained for the data corresponding to the third column in Table 4.1 and to $\tilde{L}_{JGc} = L_{JGc}/h = 10$.

The stability conditions due to the Exact CCW theory for cohesionless materials (grey area) has also been plotted in this Figure 4.5b). Within the grey area, the wedge slides along the whole detachment without internal deformation either by its self weight or by tectonic compression. The lower boundary of this domain corresponds to the stability limit of accretionary wedges in the compressive regime. Of more interest here is he upper boundary of the grey domain corresponding to gravity instability [*Wang et al.*, 2006]. This upper limit is very close to our predictions (dot-dashed curve) for β larger than 25°. The difference between our prediction and the ECCW theory is more apparent for small values of β with a maximum of 5°.

The stability of our prototype is further explored with the help of Figure 4.6a, presenting the critical curves of the Exact CCW theory and those obtained for $\tilde{L}_{JGc} = 10, 100$, at the bulk overpressure ratio $\Delta\lambda_B = 0, 0.2$. As $\tilde{L}_{JGc}$ changes from 10 to 100, a lower value of the critical surface slope α_c is predicted, very close to that of the Exact CCW theory, which corresponds to the limit $\tilde{L}_{JGc} \to \infty$. Increasing the bulk overpressure ratio from 0 to 0.2 reduces much the critical surface slopes, and reduces the effect of $\tilde{L}_{JGc}$. Introducing bulk cohesion, on the contrary, amplifies the effect of $\tilde{L}_{JGc}$ (Figure 4.6b). Recall that $C_B = \tilde{C}_B \rho g h = 2$ MPa for a reference thickness $h = 1$ km (Table 4.1, third column).

In summary, the frontal thrust introduced in the collapse mechanism of the gravity instability increases the stability domain of the wedge to higher surface slopes. This effect is greater for cohesive materials and at low fluid pressures. For scaling reasons, it vanishes for $\tilde{L}_{JGc} \to \infty$ (in practice, ≥ 100). The qualitative physical explanation is that the additional frontal thrust offers an additional resistance to the instability, which is therefore triggered at a higher surface slope (thus the term "resistive toe" in Figure 4.5b). The modulations of this stabilizing effect by the relative detachment length ($\tilde{L}_{JG}$), the cohesion and the bulk fluid pressure, can all be interpreted by their contribution to the resistance to thrusting at the toe .

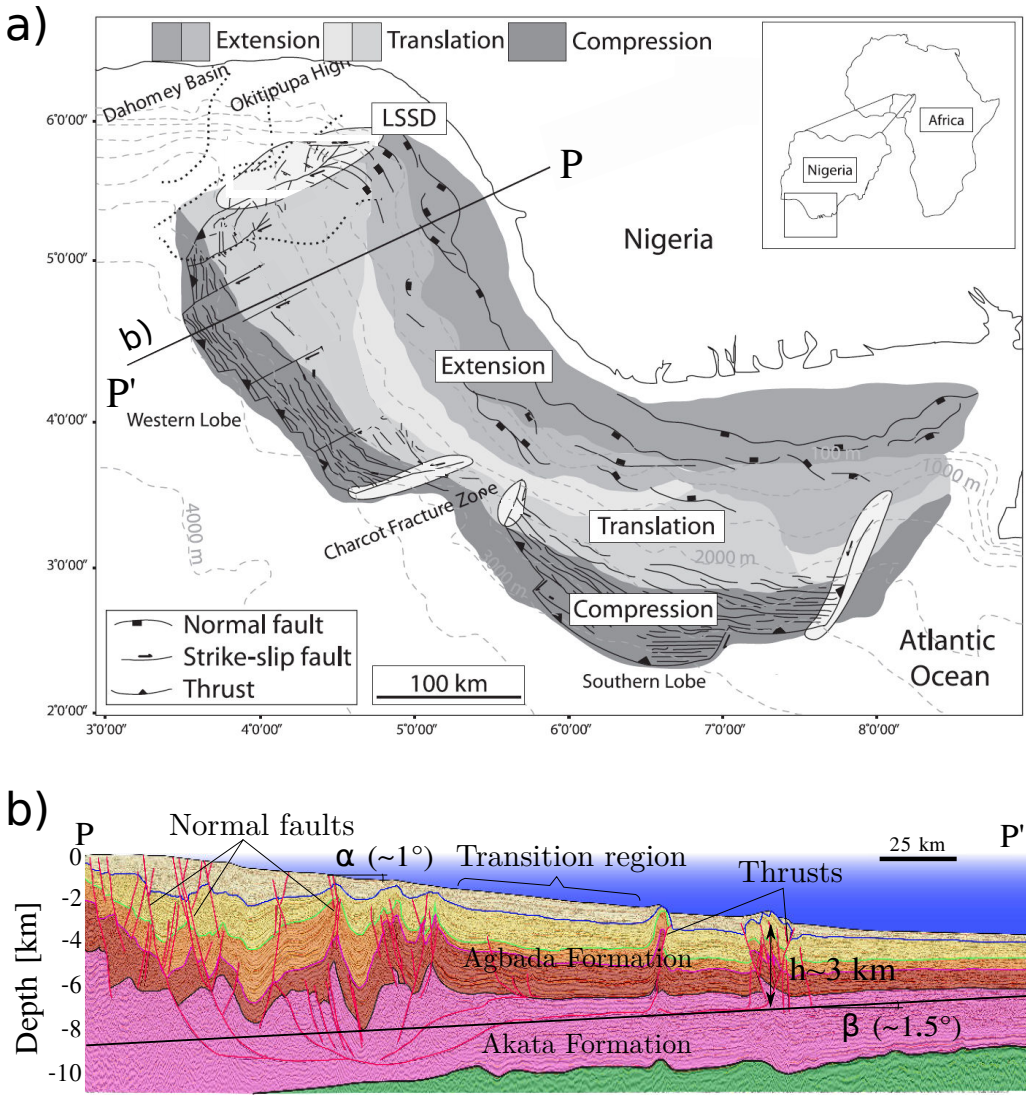


Fig. 4.7: (a) Overview of offshore Niger Delta structural domains, modified from *Leduc et al.* [2012]. (b) The section PP' with the three structural domains and the position of the assumed detachment surface in the Akata formation (from *Morgan* [2006], redrawn by Rob. Butler for the Virtual Seismic Atlas).

4.4.2 Stability Analysis of Niger Delta

The structure of the Niger Delta is characterised by normal faulting in the thickest part near the coast, and by a fold-and-thrust belt in the deepest, thinnest parts, 100 to 200 km further offshore (Figure 4.7a). The normal faults and thrusts are connected by a detachment fault (Figure 4.7b). This is broadly interpreted as a seaward gravity instability of the sedimentary basin (Agbada Formation) above a substratum of overpressured shale (Akata Formation) [*Wu and Bally*, 2000]. An analysis of ten regional sections of the compressive toe by *Bilotti and Shaw* [2005] concluded on an average taper of 2.5°, with an average surface slope α ∼1° and an average detachment dip β ∼1.5° (Figure 4.7b). The length L_{JGc} is estimated in the range $100-200$ km from the works of *Corredor et al.* [2005] and *Leduc et al.* [2012] (Figure 4.7a), and the height h of sediments at the front of the thrust belt is about 3 km. Thus the dimensionless length $\tilde{L}_{JGc}$ lies roughly between 30 and 70.

For overpressured and relatively unconsolidated shale and shale gouge within a fault zone, the friction coefficient $\mu_D \sim 0.4$ (φ_D ∼20°) [*Krueger and Grant*, 2011; *Kohli and Zoback*, 2013], and the wedge friction angle $\mu_B \sim 0.6$ (φ_B ∼30°). We adopt here the values chosen by *Suppe* [2014] to study the stability of the offshore Niger Delta: $\mu_B \sim 0.6$ and $\mu_D \sim 0.2$ (φ_D ∼10°). We assume that the detachment cohesion is null and the bulk cohesion is set to zero or 7 MPa, because in the context of gravity instabilities, the material cohesion is an influential factor [*Yuan et al.*, 2015]. For some well data, the fluid pressure is hydrostatic ($\Delta\lambda_B = 0$) at depths down to 2.3 km (fluid-retention depth) from the sea bed, and the pressure increases closely to lithostatic pressure ($\Delta\lambda_B \leq 0.58$) when the depth is beyond 3 km [*Krueger and Grant*, 2011]. The increase in λ_B below the upper hydrostatic zone makes the above rigorously inapplicable in our Limit Analysis method because, as the CCW theory applied to wedges in the Gulf of Mexico [*Xiao et al.*, 1991] and to offshore Niger Delta [*Bilotti and Shaw*, 2005], we assumes that λ_B is constant within the wedge. Accordingly, we set $\Delta\lambda_B$ in the range $0.3-0.5$ and $\Delta\lambda_D$ in $0.5-0.57$. All parameters are summarized in Table 4.1 (fourth column).

To explore the stability conditions, we first use the effective friction coefficients. Using the definition in *Hubbert and Rubey* [1959]: $\mu'_i = \tan(\varphi_i)(1-\lambda_i^{(L)})$, with the definition of $\lambda^{(L)}$ in (E.2) and the approximation $\cos^2\alpha \sim 1$, justified by the very low surface slope of the Niger

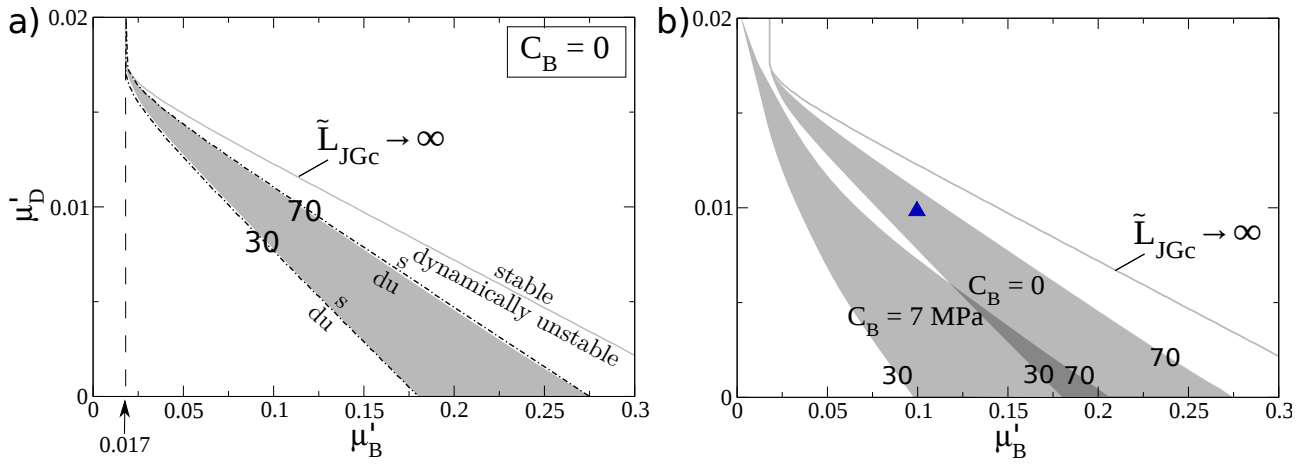


Fig. 4.8: (a) The stability maps for the offshore Niger Delta in the space spanned by the bulk and detachment effective friction coefficient μ'_B, μ'_D assuming the wedge prototype ($\alpha = 1°, \beta = 1.5°$) is at critical state. The grey shaded domain presents the uncertainty of the collapse length $\tilde{L}_{JGc} = 30 - 70$. The hashed area shows the domain of effective friction coefficient predicted by CCW theory from *Bilotti and Shaw* [2005]. (b) The sensitivity of the stability transition due to the bulk cohesion C_B and the collapse length $\tilde{L}_{JGc}$.

Delta, we obtain the effective friction coefficients

$$\mu'_i = \tan(\varphi_i)(1 - \frac{\Delta\lambda_i}{\Delta\lambda_{Max}}), \quad i = \mathrm{B}, \mathrm{D}, \tag{4.16}$$

of the bulk material ($i = B$) and of the detachment ($i = D$). The relation between μ'_B and μ'_D is determined such that the observed surface slope $\alpha \sim 1°$ and dip $\beta \sim 1.5°$ of the detachment produce a wedge at critical state for $\tilde{L}_{JGc} = 30, 70$ and $\tilde{L}_{JGc} \to \infty$ (Figure 4.8a). For any values of μ'_i above or to the right of the grey shaded area, the wedge is stable if it is limited to a collapse such that $\tilde{L}_{JG} \leq 70$. In comparison, the CCW theory (i.e., $\tilde{L}_{JGc} \to \infty$) predicts a smaller stability domain. The map also shows that for $\mu'_B \leq 0.017$, the wedge is unstable regardless of the value of μ'_D. This value can also be determined from *Lehner* [1986], equation (E.7). The bulk material is then so weak that the collapse occurs without activation of the detachment. The hashed region in Figure 4.8a is discussed in the next section. The stability domain expands for a cohesive material ($C_B = 7$ MPa, Figure 4.8b). For example, for $\tilde{L}_{JGc} = 70$ and $C_B = 0$ MPa, the conditions $\mu'_B = 0.1, \mu'_D = 0.01$ (triangle symbol) become stable when $C_B = 7$ MPa. In the case $\tilde{L}_{JGc} \to \infty$, the stability curve for $C_B = 7$ MPa is the same as for $C_B = 0$ MPa.

The overpressures responsible for these very low values of the friction coefficients are now

examined in the (α, β) space (Figure 4.9). The ten cross-sections (α, β) considered by *Bilotti and Shaw* [2005] are shown as black squares, and the red square corresponds to the average values. The grey shaded regions are the stability domains based on the range $\tilde{L}_{JGc} = 30 - 70$ for $\Delta\lambda_B = 0.3, 0.4, 0.5$, corresponding to $\mu'_B = 0.28, 0.18, 0.08$, respectively. Some curves for $\tilde{L}_{JGc} \to \infty$ are also shown for reference. In both cases $\Delta\lambda_D = 0.55$ (Figure 4.9a) and $\Delta\lambda_D = 0.57$ (Figure 4.9b), the red square is below the $\Delta\lambda_B = 0.3$ curve, and is therefore stable. Again for $\Delta\lambda_D = 0.55$, the average cross-section is stable for $\Delta\lambda_B = 0.4$ and is dynamically unstable for $\Delta\lambda_B = 0.5$. For $\tilde{L}_{JGc} \to \infty$ at $\Delta\lambda_B = 0.4$, however, the average cross-section is critical because the grey curve is crossing the red square. For $\Delta\lambda_D = 0.57$, the average cross-section is dynamically unstable for $\Delta\lambda_B = 0.5$ and is critical for $\Delta\lambda_B = 0.4$. If the cohesion is increased to 7 MPa, for $\Delta\lambda_D = 0.55$ (Figure 4.9c) and $\Delta\lambda_D = 0.57$ (Figure 4.9d), $\Delta\lambda_B = 0.5$ will ensure the average cross-section is critical.

To conclude with Figure 4.8 and Figure 4.9, a critical state of gravity instability according to our prototype implies that the effective friction coefficients must be in the range $\mu'_D \leq 0.017 \leq \mu'_B \leq 0.27$, in the absence of cohesion. The corresponding fluid overpressure ratio $\Delta\lambda_B$ is between 0.4 and 0.5, and $\Delta\lambda_D \geq 0.51$ (with a maximum value at 0.57). If the bulk material has a cohesion of 7 MPa, then the range is $\mu'_D \leq 0.02$ ($\Delta\lambda_D > 0.5$) and $\mu'_B \leq 0.2$ ($\Delta\lambda_B \geq 0.37$).

4.5 Concluding discussions

The collapse in the offshore Niger Delta is widely recognized as a gravity instability driven by sedimentation and the associated fluid overpressures. The frontal thrusts accommodate the upslope extension through a deep detachment fault. In contrast, *Bilotti and Shaw* [2005] and *Suppe* [2007; 2014] used the Critical Coulomb Wedge (CCW) theory to infer the overpressures focusing on the frontal compressive part of the Niger Delta, illustrated as domain A in Figure 4.10a. The corresponding point A in Figure 4.10b indicates a tectonic-driven collapse mechanism typical of fold-and-thrust belts and accretionary wedges generated by a far-field tectonic force. The domain A applied to Niger Delta conflicts with the widely recognized gravity instability driven by overloading sedimentation in this region. In gravity-driven failure mechanism, the force producing the frontal thrusts is resulting from the upslope extensional failure, and thus this force is less than the far-field force from compressional (or tectonic-driven) failure. For the gravity instability of wedge structure, one could have fitted the CCW theory to the

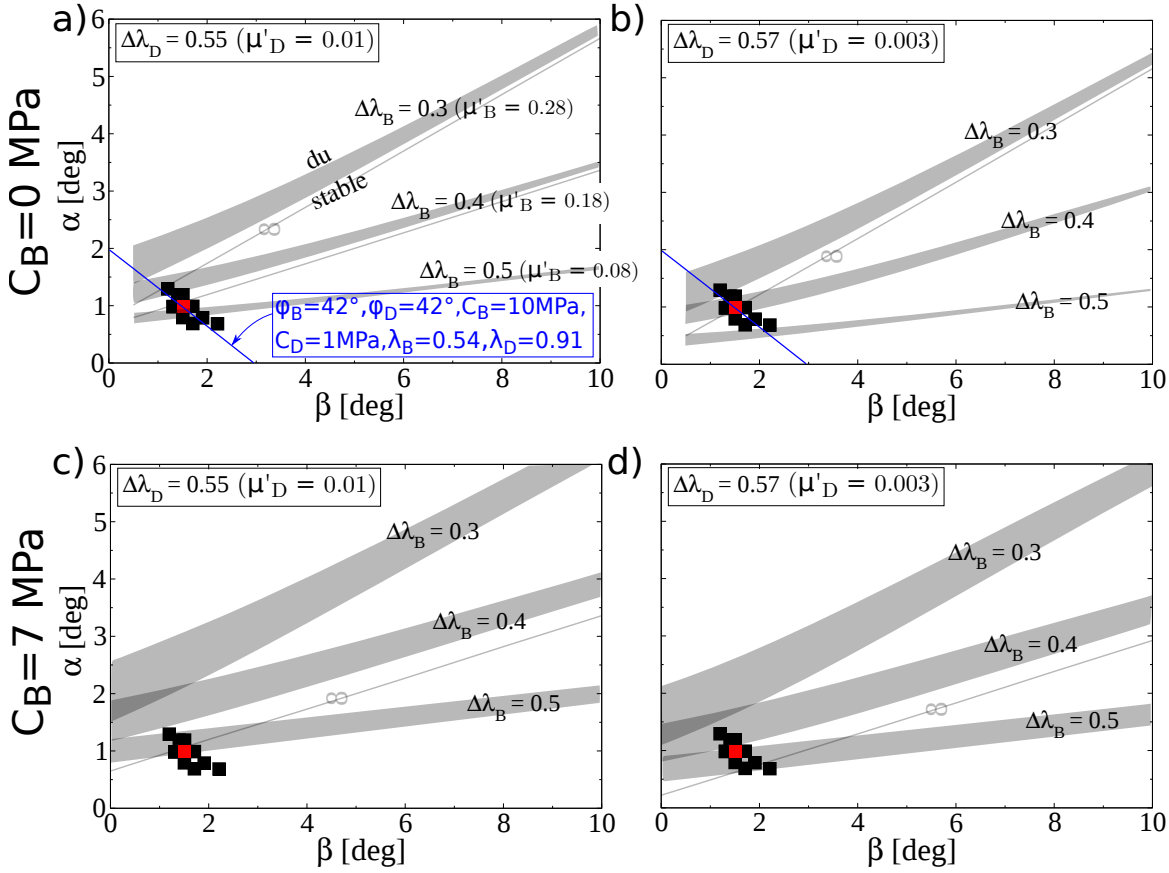


Fig. 4.9: The critical surface slope as function of detachment dip for detachment friction angle $\varphi_D = 10°$ and fluid overpressure ratio $\Delta\lambda_D = 0.55, 0.57$, setting the bulk cohesion $C_B = 0$, 7 MPa. The values of $\mu'_D = 0.01$ and 0.003 are corresponding to (a,c) and (b,d), respectively. The black squares present 10 surface slopes versus detachment dips in the offshore Niger Delta [*Bilotti and Shaw*, 2005]. The grey shaded domains present the uncertainty of the collapse length $\tilde{L}_{JGc} = 30 - 70$. The blue curve is determined from CCW theory assuming the cross-sections are at criticality of compressive collapse [*Bilotti and Shaw*, 2005].

extensional part of the Niger Delta (illustrated as domain B in Figure 4.10a), neglecting the frontal, compressional part. The combined extensional-compressional gravity-driven collapse system implies roughly domain C in Figure 4.10a since the additional frontal thrust offers an additional resistance to the instability, which is therefore triggered at a higher surface slope. The differences in terms of critical slope are substantial between the above three mechanisms . For example, for $\beta = 0°$, the three collapse mechanisms predict respectively the critical surface slopes $2°, 7°$ and $9°$ (Figure 4.5b).

This contribution develops Limit Analysis for the gravity instability of offshore deltas characterized by the linking of upslope extensional and downslope compressional collapses on a planar weak detachment. The mechanical approach is validated by showing that our predictions of an inclined layer match well the experimental results on normal faulting triggered by air overpressure in sand analogues. For offshore wedges, the stability condition of this gravity-driven collapse is depending on the geometrics of wedge and the collapse length (the distance between the extensional and compressional domains). We then apply this failure mechanism to the offshore Niger Delta and constrain the fluid pressures that necessary to determine the critical state of the structures (surface slope 1°, detachment dip 1.5° and dimensionless collapse length $30 - 70$). The Limit Analysis predicts the substantially high fluid overpressures in both bulk materials and on the detachment. For example, for cohesionless materials, it shows that the pore-fluid pressure within bulk materials is 80-90% of the lithostatic pressure (Hubbert-Rubey fluid-pressure ratio $\lambda_B = 0.8 - 0.9$), and the detachment is 97-99% of the lithostatic pressure.

On the contrary, *Bilotti and Shaw* [2005] focused on the compressive region of the offshore Niger Delta and accordingly assumed that the measured α, β angles should lie on the compressive limit of the CCW theory. Choosing $\varphi_B = \varphi_D = 42° \, (\mu = 0.91)$, $C_B = 10$ MPa, $C_D = 1$ MPa, the fluid pressure ratio $\lambda_B = 0.54$ ($\Delta\lambda_B = 0.12$, $\mu'_B = 0.71$), and $\lambda_D = 0.91$ ($\Delta\lambda_D = 0.49$, $\mu'_D = 0.14$), they were able to fit a critical curve of compressive collapse through the data points (blue line, Figure 4.9a). Including some uncertainty ranges, *Bilotti and Shaw* [2005] inferred the corresponding effective friction coefficients $\mu'_B = 0.5 - 0.9$ and $\mu'_D = 0. - 0.2$. Consequently, their predictions locate in the stable domain of our stability map, Figure 4.8. We can conclude that *Bilotti and Shaw* [2005] overestimated the value of μ'_B and did not constrained well on μ'_D. Furthermore, reducing the high values of friction and cohesion chosen by *Bilotti and Shaw* [2005] for the appropriate properties of sedimentary shale in that region, physical parameters

adopted from *Krueger and Grant* [2011] and *Suppe* [2014], one would obtain even higher effective friction coefficients from the CCW theory. Therefore, even when allowing for uncertainties in the parameters, the inferred fluid overpresssures are much lower than the values we found. Additionally, the low range of $\lambda_B = 0.39 - 0.69$ in *Bilotti and Shaw* [2005] were possibly due to the measured fluid pressures from the shallow wells. The drilling-hole data shows that the fluid pressure are dependent much on the depth [*Krueger and Grant*, 2011; *Suppe*, 2014] and highly overpressured in the faults (e.g. thrust belts) [*Cobbold et al.*, 2009] in that region.

The very high fluid pressures that we inferred are confirmed by the observation of the activation of a ∼15 km long flat detachment below a flat topography [*Corredor et al.*, 2005, Fig. 4], and by the low effective friction coefficient ($\mu'_D \sim 0.009$) used in numerical modelling [*Albertz et al.*, 2010]. In fact, the overpressures are such that some mobile shales of the Akata formation intruded above into the upper Agbada Formation and even to the surface [*Corredor et al.*, 2005]. Although our prototype does not account for the large scale shale movements, the very high overpressures found, implying very low effective friction coefficients, are equivalent to a thick viscous flow in the detachment, in terms of mechanical resistance.

The stability conditions depend much on the collapse length L_{JG}. Normally, the simultaneous normal fault and thrust triggered by sediment progradation are occurring respectively on the shelf-edge and bottom slope-edge, suggesting for an easy guess. The collapse length however is controlled by the details of the topography and the material heterogeneities (for example by weakening after faulting). To account for an irregular topographic surface, the lengths and surface areas must be computed numerically instead of using (D.7) and (D.8). The critical ratio $\tilde{L}_{JGc}$ and the exact position of the normal and thrust faults would be outcomes of the optimisation. Such a refinement of the prototype is certainly desirable, but only in conjunction with an in depth analysis of the geological data to extract kinematic constraints for the mechanical analysis.

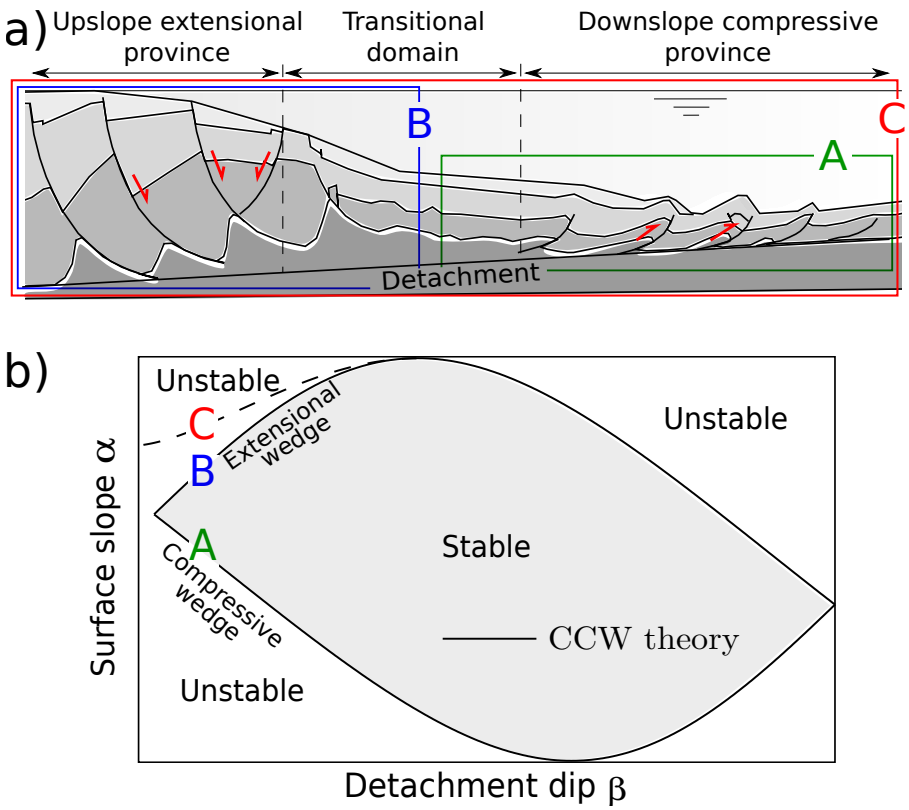


Fig. 4.10: (a) Schematic illustration of gravity-driven collapse of offshore deltas, modified from *King et al.* [2010]. (b) The stability boundary for the stable wedge illustrated by the critical Coulomb wedge (CCW) theory [*Dahlen*, 1984].

Beyond the direct applications presented here, there are some obvious perspectives for the present work. The proposed methodology is now ready for use for other field cases. It could be used, for example, to test the stability condition in NW Borneo Margin to generate the Brunei toe-thrust systems [*Morley*, 2003; *Morley et al.*, 2008; *Sapin et al.*, 2009] where many geologists confused the tectonic- and gravity-driven collapse mechanisms. Additionally, the study of the stability condition could be improved by accounting for more realistic structures in offshore delta, e.g. the consideration of listric fault generation in the Niger Delta [*Corredor et al.*, 2005; *Kostenko et al.*, 2008], the fluid overpressures linked to sedimentation and compaction [*Tingay et al.*, 2009]. More impressively, *Gemmer et al.* [2004; 2005] incorporated a sedimentary progradation a numerical prototype using the finite-element method to study the evolution of instability above a ductile detachment. The present contribution allow us to develop sequential Limit Analysis to study the deformation process of structures in offshore

Niger Delta driven by the progradation of overpressured sedimentation. The Sequential Limit Analysis is a method of kinematic increment of the above mechanical approach, based on the development of frontal thrusting in accretionary wedges [*Cubas et al.*, 2008] and large wedge growth [*Mary et al.*, 2013a;b]. The kinematic increments on extensional faulting inspired from the half-graben geometry [*Groshong*, 1989; *Xiao and Suppe*, 1992] could be combined with the frontal, compressional collapses to produce the extensional-compressional styles.

Chapter 5

Role of fluid overpressures on the shape of normal faults in brittle, upper crust

abstract

A two-dimensional (2-D) kinematic approach of Limit Analysis is proposed to study the shape of normal fault that links topography to a low, weak detachment fault in overpressured, cohesive and frictional sedimentary upper crust. The curved normal fault is treated as though composed of a number of segmented planar faults. Hanging-wall region above these segmented faults is discretized into blocks of the same number by active axial surfaces. The dips of normal fault and axial surface are optimized to obtain the least boundary force which corresponds to the most efficient way to deform the structure. The results of Limit Analysis show that the low-angle normal fault and the listric fault can be achieved in a gently dipped slope where fluid pressures are hydrostatic above a fluid-retention depth Z_{FRD} and overpressured below this depth. Two fluid overpressured cases are considered: Case 1 is the fluid overpressure increasing parallel to the lithostatic gradient, and Case 2 is the fluid overpressure increasing linearly to lithostatic pressure at the detachment depth Z_D. Simplify to the prototype of surface slope parallel to the detachment in Case 1, the good match between our simulation results and the slip-line solutions essentially validates our methodology. The parametric studies show that the prototype with a flat topographic surface cannot generate the listric fault, the increasing of detachment dip and

material cohesion reduce substantially the curvature of normal fault. Our methodology applied to Gulf of Mexico shows the fault shape depends much on the dip of detachment fault. For example, the detachment dipped at 5° results in the large curved normal faults and the 17° dipped detachment generates bi-linear fault when the Z_{FRD} line is deep. The normal fault in offshore Niger Delta is resulted from the shallow depth of Z_{FRD} ($\leq 0.1 Z_D$) in fluid pressure of Case 1. Fluid pressure in Case 2 will generate often a low-angle, planar normal fault which is not the case from the observations in Niger Delta.

5.1 Introduction

Listric faults are commonly observed in many extensional contexts from large-scale continental rifting [*Withjack and Peterson*, 1993; *Withjack et al.*, 1995], passive margins [*Morley et al.*, 2011] to small-scale problems, such as retaining wall and slope stability in civil engineering [*Chen*, 1975]. The listric faults are characterized by a significant decreasing in fault dip from $\sim 60°$ near the topographic surface down to a low-angle ($0 - 20°$) normal fault or detachment fault. The objective of this manuscript is to determine the mechanical conditions in terms of cohesive, frictional rock properties and fluid pressure gradient characteristics conducive to the onset of a normal fault linking a lower detachment to the topography.

Andersonian theory predicts that a planar normal fault dipped at $\sim 60°$ will form in an extensional context [*Anderson*, 1951]. The decreasing of friction angle with depth will not result in a large curvature of fault because the Andersonian theory cannot allow a fault dip lower than 45°. One argument is that the listric fault and low-angle normal fault are only likely at the brittle-ductile transition areas [*Jackson and McKenzie*, 1983; *Jackson and White*, 1989]. However, geological reconstructions and seismic reflection profiles reinforce the view that active low-angle normal faulting in the brittle crust is widespread [*Wernicke*, 1995]. For example, the clear seismic images in offshore Niger Delta [*Shaw et al.*, 2004; *Corredor et al.*, 2005] show that a number of listric, low-angle normal faults form in upper crust ($\leq$10 km) as gravity instability due to overloading sedimentation. It is still unclear to what failure mechanism would be used to explain the large curved and low-angle normal faults similar to this region.

Analogue experiments is an alternative way to study the shape of normal fault, wet clay is a widely used material [*Dula*, 1991; *Withjack et al.*, 1995; *Bose and Mitra*, 2009] because its property of strong cohesion which easily allows to conduct the extensional tests. However, the

use of wet clay in experiments to characterize deformation in brittle crust is controversial due to the properties of volume change and creep captured by the Cam-Clay model [*Roscoe et al.*, 1958; *Roscoe and Burland*, 1968]. *Withjack and Schlische* [2006] reported a significant fault difference between the material of dry sand and of wet clay in extensional fault-bend folding experiments. In their study, normal faults are planar and dipped at $\sim 60^\circ$ in sand models whereas, in clay models, fault is curved and dipped from $\sim 60^\circ$ at surface down to $\sim 30^\circ$ at sliding base. Alternatively, *Holland et al.* [2006; 2011] captured a tension fault near the surface connected with a deep, slightly curved fault by using cohesive hemihydrate powder. This fault mode transition from tensile to shear was explained by a modified Mohr-Coulomb criterion accounting for a cut-off or a tensile strength of analogue material [*Kettermann and Urai*, 2015]. The question raised from the above literatures is whether the curved fault can be formed in a cohesive and frictional (classic Mohr-Coulomb) material.

Numerical methods were often used to study the extensional deformation on a variety of inherited low-angle and listric faults [*Van Wees et al.*, 1996; *Erickson et al.*, 2001; *Resor and Pollard*, 2012]. The boundary conditions in these cases are different from the generation of listric fault. There are also some profound analytical works explaining the listric fault formation in a cohesive, frictional overpressured slope. *Mandl and Crans* [1981] determined an active fault shape by using the slip-line theory in a gently-dipped slope where the stress field is simple and thus the determination of slip-line field is possible. Their conclusion is that the fault shape is planar when the fluid pressure is hydrostatic, and is curved in overpressured condition. However, a weak detachment, prototype with finite size, arbitrarily fluid pressure profile and material cohesion will ruin the simplicity of the stress field, and thus the slip-line field and fault shape cannot be determined.

The kinematic approach of Limit Analysis [*Chen*, 1975], also called the maximum strength theorem in *Salençon* [2002], could provide a mechanical way to study the fault shape accounting for the above limitations. In civil engineering, the geometry of prototype is critical factor to generate the curved fault and this method used in slope stability shows that the curved (log-spiral) fault mechanism is often better than planar fault mechanism [*Chen*, 1975; *Michalowski*, 1995; *Utili and Crosta*, 2011]. For example, the study of the cliff stability proves that the critical cliff height for log-spiral failure mechanism is about 4% less than that of planar fault mechanism [*Chen*, 1975]. We will use this methodology in this contribution and check if listric fault is due to

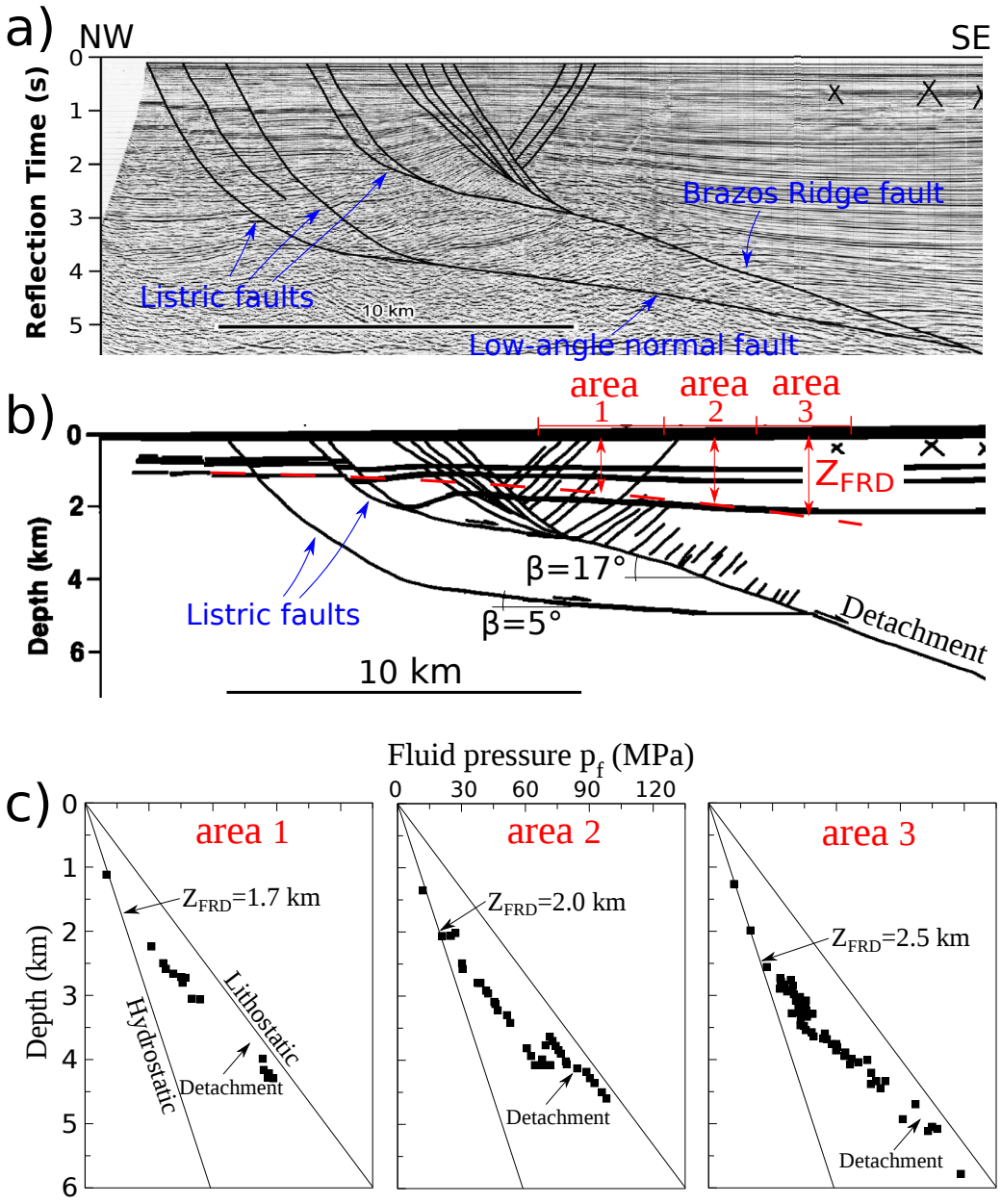


Fig. 5.1: (a,b) Seismic profiles in NW Gulf of Mexico from *Xiao et al.* [1991] and *Suppe* [2014]. (c) Measured fluid pressure in this region, derived from Hubbert-Rubey fluid pressure ratio λ in *Xiao et al.* [1991]. The fault dip in (a,b) decreases with depth from sea floor down to the detachment fault. The red dashed curve in (b) indicates the fluid-retention depth Z_{FRD}.

or can be achieved (1) without sedimentation and compaction process (no growth fault during sedimentation) [*Xiao and Suppe*, 1989], (2) without geometries (no topography effect), just using a straight inclined sea floor and a dipped detachment, (3) without a complex mechanical response, only using Coulomb criterion, (4) without a bi-linear overpressure gradient and (5) without footwall deformation during extension which happens often in the prototype of a brittle overburden above a ductile substrate [*Salisbury and Keen*, 1993].

This contribution contents are as follows: In Section 5.2 and Appendix, we develop the Limit Analysis for the failure prototype in two *leaky* fluid overpressured conditions. Section 5.3.2 conducts the convergence analysis of our proposed method, and some simulation results are compared with the solutions of slip-line theory for the validation of our method. In Section 5.4, we study the influence of some parameters on the failure mode, such as prototype geometry, fluid-retention depth, physical properties of material and the detachment. In Section 5.5, the method is applied to NW Gulf of Mexico and offshore Niger Delta where the typical listric faults can be clearly observed from seismic profiles.

5.2 The prototype

The first part of the prototype geometry is part of the data and consists in a straight sea-floor topography and a weak planar detachment DE_1, dipping at α and β, respectively, Figure 5.2a. The properties of the bulk material and the detachment are cohesive and frictional with cohesion C_B, C_D and friction angle φ_B, φ_D. The subscripts B and D denote the bulk and the detachment, respectively.

The second part of the geometry of this prototype is an outcome of the mechanical predictions and could also be constructed from Figure 5.1a. The normal fault between point E_1 and point E_{n+1} are composed of n segmented planar faults which generate an apparent listric fault, inspired from hanging-wall kinematics proposed by *Xiao and Suppe* [1992]. The n segmented straight faults lie in the n layers of an equal thickness. The hanging wall is partitioned into n block regions by the active axial surfaces, as illustrated by black dashed lines in Figure 5.2a. In the i^{th} block, the segment fault E_iE_{i+1} dipped at γ_i has the length $L_{E_iE_{i+1}}$. The active axial surface E_iF_i for each block is dipped at θ_i. The bock area, $E_iF_iF_{i+1}E_{i+1}$, is denoted ΔA_i. The relations defining these geometrical parameters are based on simple geometrical rules and is postponed to 1. The hanging wall is complemented by a sliding block region bounded by the

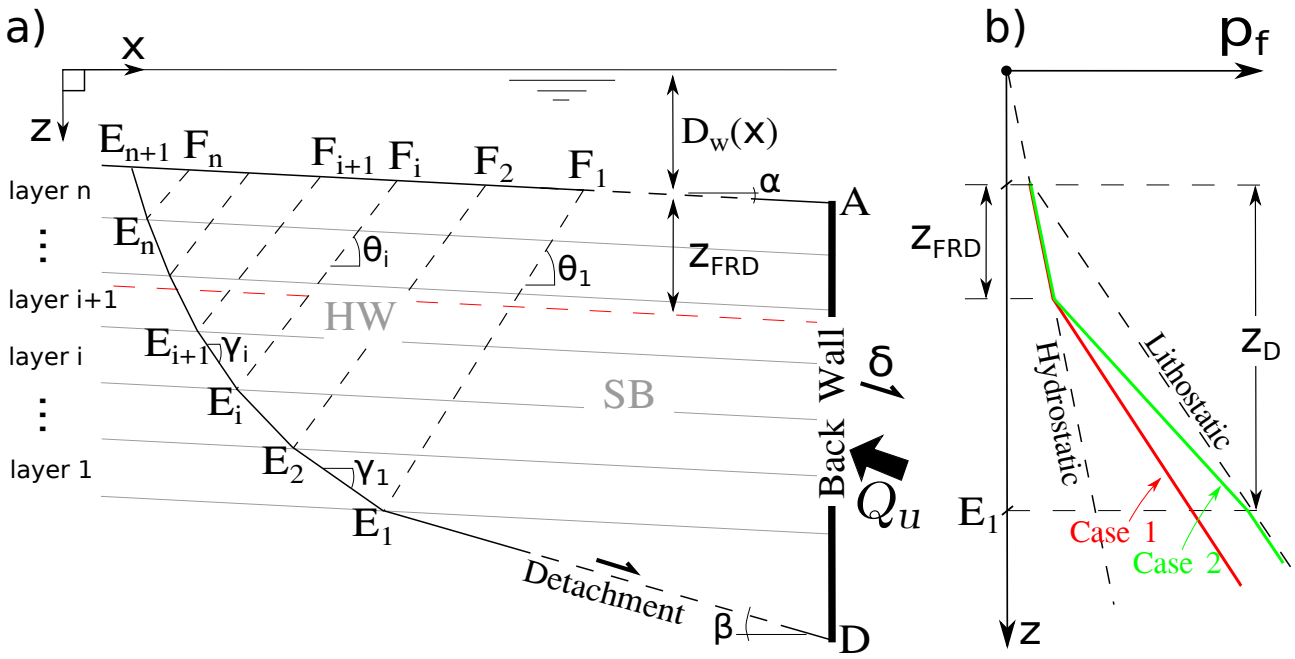


Fig. 5.2: (a) The prototype geometry has two regions, the Sliding Block (SB), ADE_1F_1, is translated rigidly and the Hanging Wall (HW) is divided into n rigid blocks sliding above the segmented faults from point E_1 to point E_{n+1}. (b) The fluid pressure is hydrostatic up to the depth Z_{FRD} below which the pressure gradient is either lithostatic (Case 1 in red) or such that the pressure is lithostatic at the depth of point E_1 (Case 2 in green).

segment E_1F_1 to the right and an imaginary back wall (AD) to the left, at a remote, unspecified distance. The velocity in the blocks of hanging wall and sliding block are uniform, dictated first by the dip of the segmented faults and detachment and second by their uniform frictional properties.

The prototype is now complemented by the fluid pressure distribution, presented in Figure 5.2b. The central idea is that there is a depth below which the fluid is retained resulting in overpressure build-up. This fluid-retention depth is denoted Z_{FRD} [*Suppe*, 2014] and the region above that depth is hydrostatic. This region is always found above the tip of the detachment fault in our analysis. Below Z_{FRD}, the overpressure increases with depth and two gradients are proposed based on the literature (e.g. *Kooi* [1997]; *Hillis* [2003]; *Yue and Suppe* [2014]). For Case 1, the pressure increases with depth with a lithostatic gradient until the depth of point E_1 where a jump occurs to reach the lithostatic pressure which prevails below. The pressure is thus parametrized by

$$p_f = \begin{cases} \rho_f g z\,, & z \leq Z_{FRD} + D_w(x) \\ \rho g z - (\rho - \rho_f) g (Z_{FRD} + D_w)\,, & Z_{FRD} + D_w(x) < z \leq z_{E_1} \\ \rho g z - (\rho - \rho_f) g D_w\,, & z > z_{E_1} \end{cases}, \tag{5.1}$$

in which, ρ and ρ_f are the saturated rock and the fluid density, respectively. z_{E_1} is the z-coordinate of point E_1 measured from the sea surface. $D_w(x)$ is the sea floor depth above the point of interest of coordinate (x, z). In Case 2, there is no jump at the depth of point E_1 and the gradient in the retention zone is linear so that the pressure is parametrized by

$$p_f = \begin{cases} \rho_f g z\,, & z \leq Z_{FRD} + D_w(x) \\ \rho_f g (D_w + Z_{FRD}) + \dfrac{(\rho g Z_D - \rho_f g Z_{FRD})}{(Z_D - Z_{FRD})} (z - D_w - Z_{FRD})\,, & Z_{FRD} + D_w(x) < z \leq z_{E_1} \\ \rho g z - (\rho - \rho_f) g D_w\,, & z > z_{E_1} \end{cases}, \tag{5.2}$$

in which, $Z_D\,(= z_{E_1} - D_w)$ is the depth of point E_1 below sea floor, Figure 5.2b. Note that in what follows, the overpressure Δp_f is often considered and is defined as the difference $(p_f - \rho_f g z)$.

The rest of this section is now devoted to the introduction of our mechanical approach. The objective is to predict the two series of angles $(\gamma_1, \gamma_2, ..., \gamma_n)$ and $(\theta_1, \theta_2, ..., \theta_n)$. The difference $(\gamma_n - \gamma_1)$ is called the fault rotation angle, Figure 5.3a. If the fault rotation angle is zero, there is no listric segment and segmented faults have the same dip as considered by *Yuan*

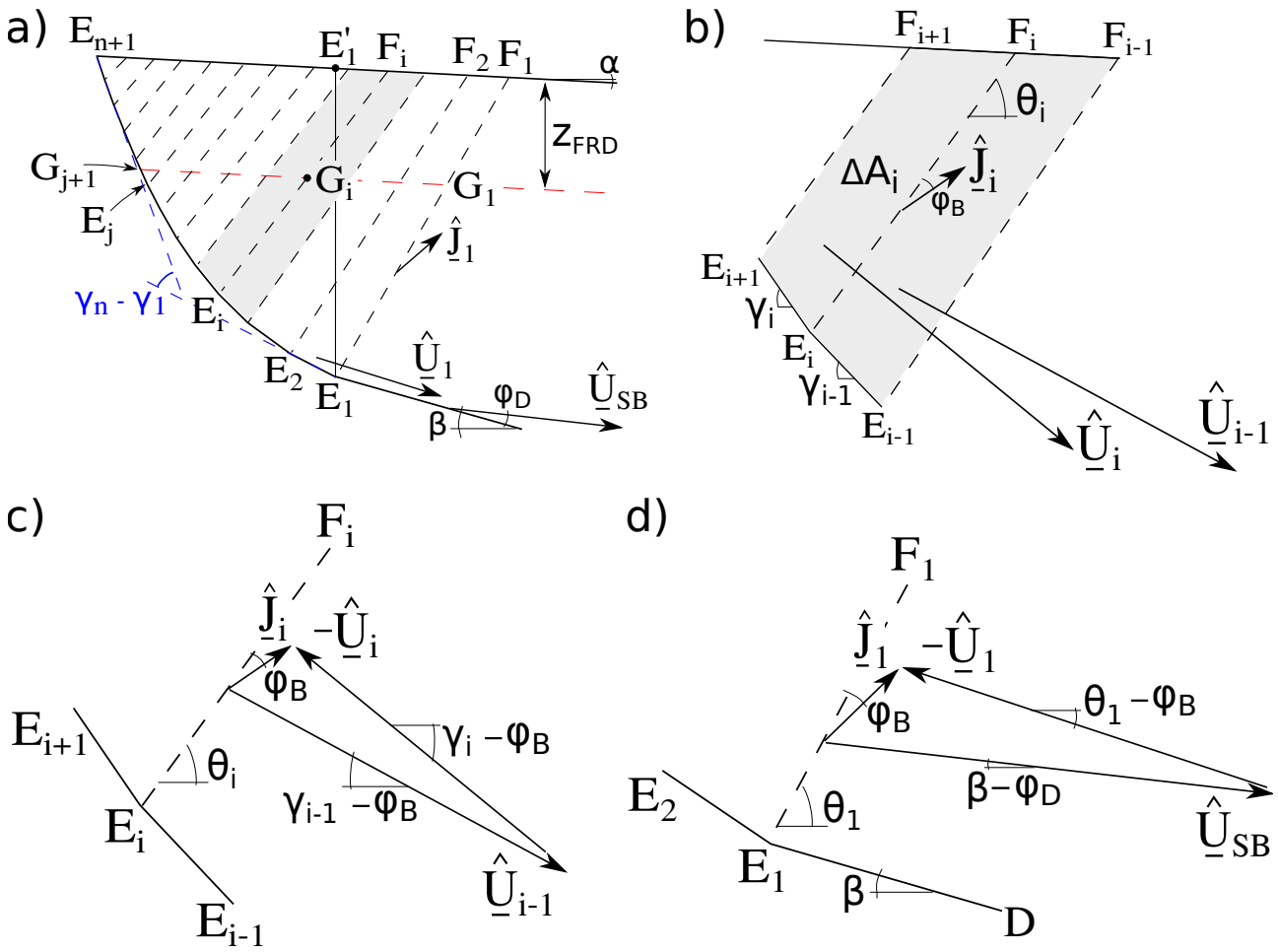


Fig. 5.3: (a) The close up of the hanging wall which is divided into a number of blocks. (b) The velocities in the block $E_iF_iF_{i+1}E_{i+1}$ and $E_iF_iF_{i-1}E_{i-1}$, and (c) the velocity jump $\hat{J}_i$ on the active axial surface E_iF_i between them. (d) The hodograph of velocity jump across the surface E_1F_1.

et al. [2015]. This angle defines the importance of the listric fault character and its relation to material properties, the dips of the topography and the detachment as well as the overpressure characteristic will be studied in Section 4. The reader unfamiliar with mechanics is encouraged to continue directly there.

5.2.1 The velocity field

We construct a velocity by making sure that this velocity field, which is not the exact velocity field, is kinematically admissible and pertinent. These concepts have been presented in *Salençon* [2002] and in *Maillot and Leroy* [2006]. It suffices to the reader to know that the velocity of

each block should be such that the velocity jumps across two blocks or along the segmented fault is always making an angle equal to the friction angle φ_B. This requirement is illustrated in Figure 5.3b for two successive blocks. The velocity of the i^{th} block is denoted $\hat{\underline{U}}_i$ and the jump vector $\hat{\underline{J}}_i = \hat{\underline{U}}_{i-1} - \hat{\underline{U}}_i$ across E_iF_i is illustrated with the hodograph in Figure 5.3c. The law of sine applied to this triangular construction provides relations between the norm of the jump and of the two successive block regions. This velocity field should be complemented by the velocity of the sliding block region $\hat{\underline{U}}_{SB}$ dipping at $\beta - \varphi_D$, Figure 5.3d. The sliding block region has the same velocity as the retreating, remote back wall. The relations characterising this complete velocity field are provided in 2.

5.2.2 The bounding of the tectonic force

The general framework considered here has been presented in *Pons and Leroy* [2012] and in *Yuan et al.* [2015]. It consists of the application of the Limit Analysis extended to saturated, porous media. It provides an upper bound to the unknown tectonic force which enters the effective virtual power

$$\mathcal{P}'_{\text{ext}}(\hat{\underline{U}}) = \int_{\Omega_t} (\rho - \rho_f)\underline{g} \cdot \hat{\underline{U}}\, dV + \int_{\Sigma} \Delta p_f\, \underline{n} \cdot \hat{\underline{J}}\, dS + Q\hat{U}_{SB} \cos(\varphi_D)\,. \tag{5.3}$$

The first term on the right-hand side is the power of the gravity field on the velocity field and the domain Ω_t is composed on the two regions, hanging wall and sliding block. The second term corresponds to the power of fluid overpressure along all the discontinuities, a set Σ composed of the segmented faults, the active axial surfaces and the detachment. The third term is the power of the tectonic force of norm Q at the back wall acting on its velocity of norm $\hat{U}_{SB}$, having set to one ($\hat{U}_{SB} = 1$) in what follows.

This external work is bounded by above, according to the kinematic approach of limit analysis, with the maximum resisting power

$$\mathcal{P}'_{\text{ext}}(\hat{\underline{U}}) \leq \mathcal{P}'_{\text{mr}}(\hat{\underline{U}})\,, \tag{5.4}$$

the later being defined by integrating the support function $\pi(\hat{\underline{J}})$ in *Salençon* [2002] as

$$\mathcal{P}'_{\text{mr}}(\hat{\underline{U}}) = \int_{\Sigma_U} \pi(\hat{\underline{J}})\, dS, \;\; \text{with} \;\; \pi(\hat{\underline{J}}) = \hat{J}C\cos\varphi\,. \tag{5.5}$$

It sums up the maximum dissipation which occurs on the discontinuities in the Σ_U. Each term is proportional to the cohesion C, the velocity jump $\hat{\underline{J}}$, the length of the discontinuity and the

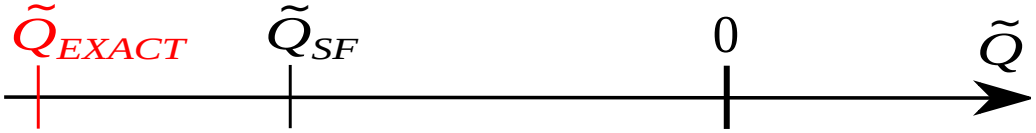


Fig. 5.4: The dominant failure mechanisms are defined along the axis set by the normalized upper bound force $\tilde{Q}$. $\tilde{Q}_{EXACT}$ is the unknown, exact solution of force. The segmented-fault mechanism with the minimum force $\tilde{Q}_{SF}$ corresponds to the most efficient mechanism to deform the system. The negative tectonic forces indicate the compressive forces at the back wall.

trigonometric coefficient φ is a consequence of an optimization (see *Maillot and Leroy* [2006] for a discussion). The explicit expression for the maximum resisting power can be found in (F.12) of 2.

Combining the (F.11) and (F.12), we obtain the explicit expression of upper bound force at the back wall for segmented-fault mechanism as

$$\begin{aligned} Q_{SF} = \Bigg[& \sum_{i=1}^{n} C_B L_{E_i E_{i+1}} \hat{U}_i \cos(\varphi_B) + \sum_{i=1}^{n} C_B L_{E_i F_i} \hat{J}_i \cos(\varphi_B) + C_D L_{DE_1} \cos(\varphi_D) \\ & - (\rho - \rho_f) g \Big[\sum_{i=1}^{n} \Delta A_i \hat{U}_i \sin(\gamma_i - \varphi_B) + S_{SB} \sin(\beta - \varphi_D) \Big] \\ & - \Big[\sum_{i=1}^{j-1} (\Delta p_{E_i} + \Delta p_{E_{i+1}}) L_{E_i E_{i+1}} \hat{U}_i + \Delta p_{E_j} L_{E_j G_{j+1}} \hat{U}_j + \sum_{i=1}^{j} \Delta p_{E_i} L_{E_i G_i} \hat{J}_i \Big] \sin(\varphi_B)/2 \\ & - (\Delta p_D + \Delta p_{E_1}) L_{DE_1} \sin(\varphi_D)/2 \Bigg] \Big/ \cos(\varphi_D) \,, \end{aligned} \tag{5.6}$$

in which, L_{XY} denotes the length size between point X and point Y. Δp_X indicates the fluid overpressure at point X. S_{SB} corresponds to the size of the sliding block region. In (5.6), the term of $(\Delta p_D + \Delta p_{E_1}) L_{DE_1} \sin(\varphi_D)/2$, indicating the power of fluid overpressure on the detachment DE_1, is the same for the each mechanism, so we replace with a null for all the calculations.

The angles $(\gamma_1, \gamma_2, ..., \gamma_n)$ and $(\theta_1, \theta_2, ..., \theta_n)$ are independent and will be optimized to get the least upper bound Q_{SF} which is the one closest to the unknown, exact force Q_{EXACT}, Figure 5.4. Thus the proposed failure mechanism with the minimum force corresponds to the most efficient mechanism to deform the system. Note that the segmented-fault mechanism can be a planar-fault mechanism when the optimized fault dips $(\gamma_1, \gamma_2, ..., \gamma_n)$ are at the same value.

Table 5.1: Geometrical and physical parameters used for convergence analysis and validation in section 5.3.

Notation	Definition	Values		Unit
		Convergence Analysis [Section 5.3.1]	Validation[a] [Section 5.3.2]	
α	surface slope	1	2	deg.
β	detachment dip	10	2	deg.
Z_{FRD}	fluid-retention depth	$0.2Z_D$	$0.1Z_D$, $0.3Z_D$	km
φ_B	bulk friction angle	30	20	deg.
φ_D	detachment friction angle	10	20	deg.
C_B	bulk cohesion	0	2000	Pa
C_D	detachment cohesion	0	2000	Pa
ρ	density of saturated materials	2500	1430	kg/m^3

[a]The values are from *Crans et al.* [1980]; *Crans and Mandl* [1980].

5.3 Convergence analysis and validation with slip-line theory

Our analytical results are depending much on the number of segment faults (n). In this section, we will test the convergence of our methodology by increasing the value of n and check the upper bound force at the back wall. And then, the simulation results are compared with the solutions of slip-line theory in a simple prototype for the validation of our method.

5.3.1 Convergence analysis

The upper bound force at the back wall as function of the value n is presented by the black curve in Figure 5.5a. All the geometrical and physical parameters are shown in the column 3 of Table 5.1 for fluid pressure in Case 2. The force decreases fast with the increasing number n to 5, and is almost constant when $n \geq 20$ and thus the convergence is reached. Our convergence analysis is tested by comparing with another two failure modes. The forces of planar-fault (2 degrees of freedom, γ_1, θ_1) and two-segmented fault (5 degrees of freedom, $\gamma_1, \theta_1, \gamma_2, \theta_2, z_{E_2}$) failure modes are presented by two red lines in Figure 5.5a. For the planar-fault failure mode, our proposed segmented-fault mechanism captures it when the number of segments (n) equals to one. The two-segmented fault failure mode is better than the segmented-fault mechanism at $n = 2$ since this mode has one more degree of freedom, the hinge (point E_2) between two segmented faults. This failure mode however loses the competition with the segmented-fault

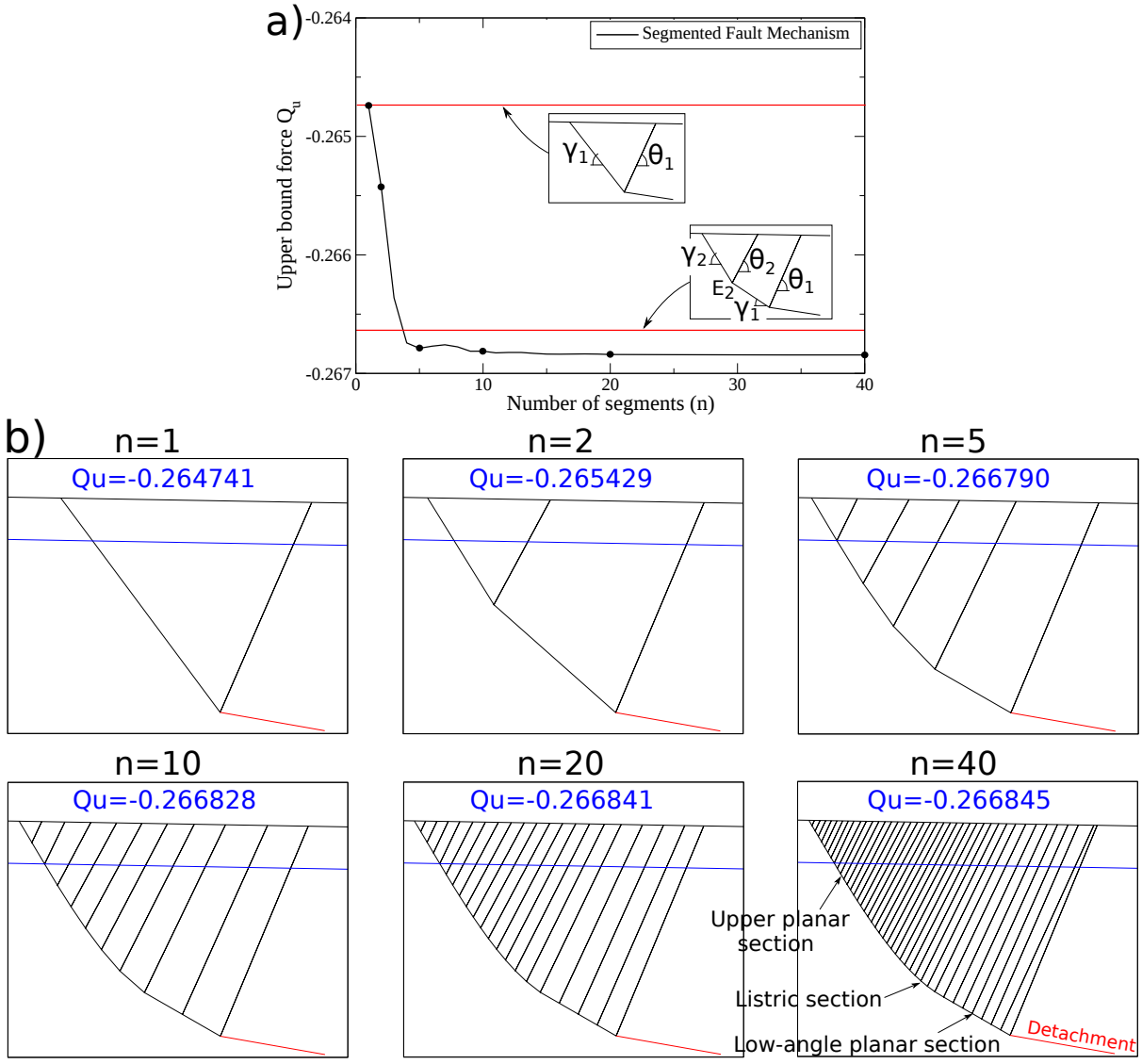


Fig. 5.5: Convergence analysis with the number of segmented faults (n) in fluid pressure of Case 2. (a) Normalized upper bound forces of the failure mechanism as function of the value n. (b) Failure modes with the increasing number of segments from $n = 1$ to 40. The vertical and horizontal scales are equal. $C_B = 0, \alpha = 1°, \beta = 10°, \varphi_D = 10°, Z_{FRD} = 0.2Z_D$.

mechanism when $n \geq 4$ due to the lower forces optimized. We will choose the number of segmented faults $n = 20$ for the following calculations due to the convergence reached from the above analysis.

The failure modes are clearly observed in Figure 5.5b, six cases ($n = 1 - 40$) are chosen for the comparisons. We can see the segmented faults close to the detachment flattens with the increasing number of segments, visible from $n = 1, 2, 5$ in Figure 5.5b. A further increasing n renders the segmented fault smooth. The comparison of $n = 5, 10, 20, 40$ reaches this conclusion. The normal fault composes three sections: low-angle planar and upper planar sections, and the listric part between the other two sections, as indicated at $n = 40$ in Figure 5.5b. The upper planar fault has a dip of $\pi/4 + \varphi_B/2$ from the topographic surface, this is also confirmed by the solution of the slip-line theory in *Crans et al.* [1980]. The hanging wall above the low-angle planar section have the same virtual velocity as the sliding block so that the dip of the low-angle planar section is at $\varphi_B + \beta - \varphi_D = 30°$.

5.3.2 Validation with the slip-line theory

The slip lines of delta slopes in fluid overpressure of Case 1 are served for the validation. This fluid overpressure is essential in normal faulting in many cases of gravity instabilities, it not only permits the formation of slope-parallel detachment ($\beta = \alpha$), but also determines the listric shape of normal fault [*Crans et al.*, 1980; *Crans and Mandl*, 1980; *Mandl and Crans*, 1981]. The generated detachment thus has the same friction properties as the delta bulk material ($\varphi_B = \varphi_D$). In the prototype with a gentle delta slope ($\alpha = 2°$), they obtained the stress field and then calculated two slip lines to be positive angle $\pi/4 - \varphi_B/2$ ($\varphi_B = 20°$) with the direction of the first principal stress. The material cohesion C_B is 2×10^3 Pa and thus the dimensionless cohesion $\tilde{C}_B$ ($= C_B/\rho g h$) is 3×10^{-5} for our simulations. The value of λ_{hydro} ($= \rho_f/\rho = 0.7$) are derived from the value of submerged specific weight $\rho - \rho_f$ ($= 4.3 \times 10^2$ kg/m^2) in *Crans and Mandl* [1980]. The geometrical and physical parameters are summarized in the column 4 of Table 5.1. The slip-line 1 and 2, playing as active axial surface and normal fault, respectively, are presented by the black curves [*Crans et al.*, 1980] in Figure 5.6 for the cases of $Z_{FRD} = 0.1Z_D, 0.3Z_D$ with $Z_D = 5$ km. The red curves are our simulation results for these two cases. Although their slip-line 1 is curved according to the slip-line field, the assumption of planar axial surface in our method has enough precision to capture the listric

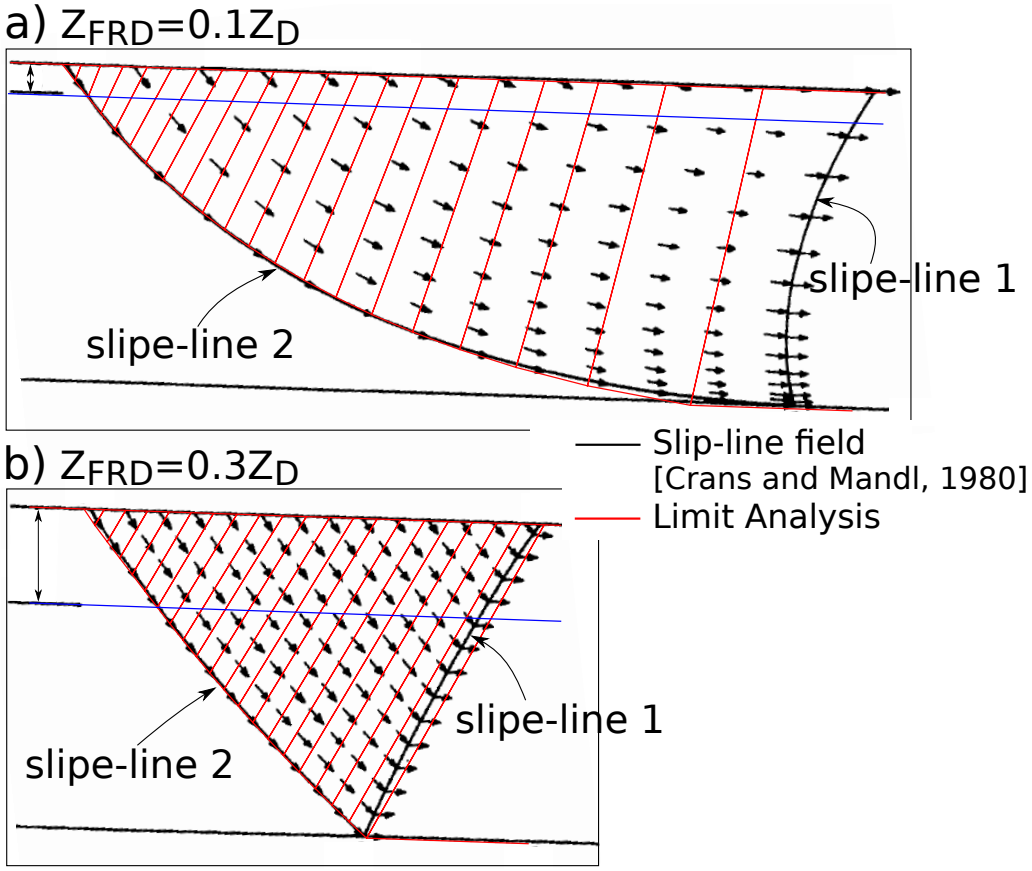


Fig. 5.6: Compare with the solutions of the slip-line theory (black curves and symbols) in *Crans et al.* [1980] for $Z_{FRD} = 0.1Z_D, 0.3Z_D$ (fluid pressure of Case 1). The red curves are the simulation results of limit analysis, and the blue lines indicates the depth of Z_{FRD}. The vertical and horizontal scales are equal.

shape of normal fault (slip-line 2). In Figure 5.6a, the value of Z_{FRD} varies between $0.096Z_D$ and $0.1Z_D$ [*Crans et al.*, 1980] and our results are matching well the results of slip-line field. The above comparisons essentially validate our methodology when the geometry of prototype is simple.

5.4 Results of normal faulting

The slip-line theory in *Crans et al.* [1980] is relying on the simple stress field, thus it has several limitations which are not for our Limit Analysis approach, such as the existence of a weak detachment ($\varphi_D < \varphi_B$), the prototype with finite size and cohesive material. From the most field observations, however, the weak detachment is existing and the surface slope is not parallel

Table 5.2: Geometrical and physical parameters used for Section 5.4 and 5.5.

Notation	Definition	Values/Ranges			Unit
		Parametric Studies [Section 5.4]	Gulf of Mexico [Section 5.5.1]	Niger Delta [Section 5.5.2]	
α	surface slope	$0-4$	1	2	deg.
β	detachment dip	$0-50$	5, 17	0	deg.
Z_D	depth of detachment	-	6	10	km
Z_{FRD}	fluid-retention depth	$(0.2, 0.5)\cdot Z_D$	$(0.2-0.5)\cdot Z_D$	$(0.1-0.5)\cdot Z_D$	km
φ_B	bulk friction angle	30	20	20, 30	deg.
φ_D	detachment friction angle	10	20	10	deg.
C_B	bulk cohesion	$(0, 0.04)\cdot \rho g Z_D$	0	0	Pa
C_D	detachment cohesion	0	0	0	Pa
ρ	density of saturated rocks	2500	2300	2500	kg/m^3

to the weak detachment. Thus the parametric studies next are mostly concerning the influence of geometries of prototypes, physical properties of material and the detachment.

5.4.1 Influence of geometries of the prototype

The geometries of the prototype have substantial effect on the failure mode of normal faulting. The studies of surface slope α and detachment dip β are presented in Figure 5.7 for the fluid pressure in Case 2. The geometrical and physical parameters are shown in the column 3 of the Table 5.2.

For the flat topography ($\alpha = 0°$) in fluid pressure of Case 2, according to Rankine assumption on the verge of Coulomb extensional failure, the effective stress field is

$$\begin{aligned} \sigma'_{zz} &= (\rho - \rho_f) g z\,, \quad \text{for} \quad 0 \le z \le Z_{FRD} \\ \sigma'_{zz} &= (\rho - \rho_f) g \frac{(Z_D - z) Z_{FRD}}{Z_D - Z_{FRD}}\,, \quad \text{for} \quad Z_{FRD} < z \le Z_D \end{aligned} \tag{5.7}$$

and $\sigma'_{xx} = \sigma'_{zz}(1-\sin\varphi_B)/(1+\sin\varphi_B)\,, \sigma_{xz} = 0$ for $0 \le z \le Z_D$. Thus the σ'_{xx} and σ'_{zz} correspond to minimum and maximum principal stresses σ'_3, σ'_1, respectively. Fresh fractures in a material on the verge of Coulomb failure are oriented at $\pm(\pi/4 - \varphi_B/2)$ with respect to the axis of the σ'_1, thus the dip of such fractures with $\alpha = 0°$ should be $60°\,(= \pi/4 + \varphi_B/2)$. Therefore, the flat topography is not sufficient to introduce the change of fault orientation, and

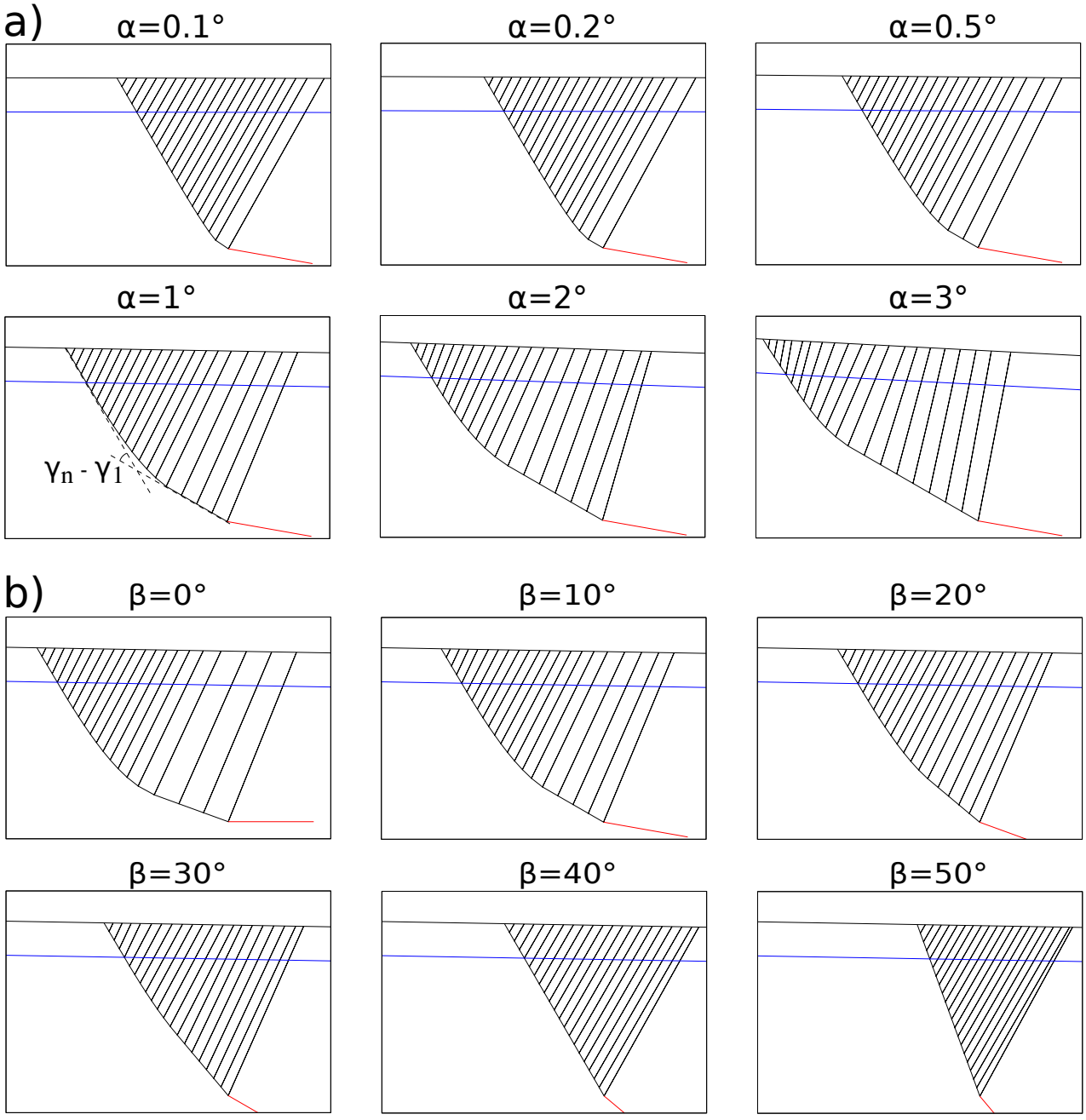


Fig. 5.7: (a) Failure modes with the increasing of surface slope α keeping the detachment dip $\beta = 10°$. (b) Failure modes with the increasing of detachment dip β keeping the surface slope $\alpha = 1°$. The vertical and horizontal scales are equal. $C_B = 0, \varphi_D = 10°, Z_{FRD} = 0.2Z_D$.

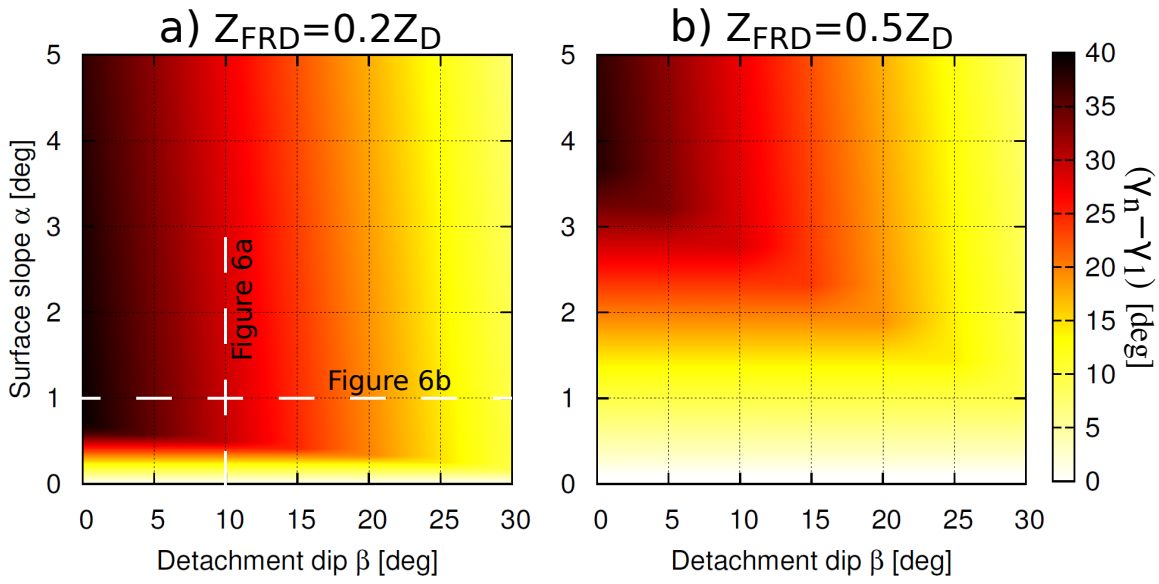


Fig. 5.8: Fault rotation angle $(\gamma_n - \gamma_1)$ as function of detachment dip β and surface slope α for fluid-retention depth (a) $Z_{FRD} = 0.2Z_D$ and (b) $Z_{FRD} = 0.5Z_D$. Two white dashed lines in (a) shows the fault rotation of failure modes in Figure 5.7. $C_B = 0, \varphi_D = 10°$.

the fault should be planar with the depth. This dip of 60° is Andersonian dip which is also captured by our prediction when the surface is flat.

Figure 5.8a presents the failure modes for several surface slopes keeping 10° detachment dip. When the surface is at 0.1°, 0.2° and 0.5°, the listric section generates at the bottom of the normal fault and is close to the detachment, Figure 5.8a. This listric section moves up with a increasing of surface slope $(1 - 3°)$. Simultaneously, the low-angle planar section forms linking the listric section to the detachment, and this length increases with the increasing of surface slope. Note that the dip of this low-angle planar fault is at $\varphi_B + \beta - \varphi_D = 30°$.

The study of the influence of detachment dip β is shown in Figure 5.8b keeping 1° surface slope. The lower planar section is at a low dip when detachment dip is at 0° and 10°. The increasing of detachment dip increases also the height of listric section, the same effect as the influence of surface slope. The listric section, however, becomes blurring when the dip β increases to $20°, 30°$. This listric section disappears when this dip is at $40°, 50°$ and the fault renders a velocity in the hanging wall same as the sliding block region. The fault dip γ for the cases of $\beta = 40°, 50°$ is at $60°, 70°$, respectively.

The shape of listric section can be characterized by the fault rotation angle $\gamma_n - \gamma_1$, the dip

difference between the last and the first segmented fault, as indicated in Figure 5.7a. Fault rotation angle as function of detachment dip β and surface slope α is presented in Figure 5.8. The color indicates the amount of this fault rotation, and the more darker the more rotating. Note that this (α, β) plane does not capture the position of the listric section. For the fluid-retention depth $Z_{FRD} = 0.2Z_D$, Figure 5.8a, the fault rotation increases substantially for the increasing of surface slope from 0° to 0.5°. The directed failure modes are observed in Figure 5.7a corresponding to the vertical dashed line in Figure 5.8a keeping detachment dip $\beta = 10^\circ$. The fault rotation is roughly constant for surface slope greater than 0.5°, however, the listric section moves up with the increasing α, observed from Figure 5.7a. The increasing of detachment dip results in the decreasing of fault rotation, as seen from horizontal dashed line ($\alpha = 1^\circ$). The fault rotation decreases from 40° to 10° for the increasing of β from 0° to 30°. The influence of fluid-retention depth can be observed from the increasing of Z_{FRD} to $0.5Z_D$ in Figure 5.8b. Compared to the case of $0.2Z_D$, the fault rotation for case of $0.5Z_D$ increases gradually with the increasing of surface slope.

5.4.2 Influence of fluid-retention depth Z_{FRD} and material cohesion

The influence of Z_{FRD} on the failure mode is studied for cohesive material $\tilde{C}_B = 0.04$ in Figure 5.9. A comparison of $\alpha = 1 - 3^\circ$ for the case of $\tilde{C}_B = 0$ (the second row of Figure 5.7a) and the case of $\tilde{C}_B = 0.04$ (the first row of Figure 5.9) reaches a conclusion that the cohesion reduces substantially the activation length of normal fault. The longer length of normal fault means less mechanical work due to material cohesion and thus the less possibility to remain active. The comparison of the first and the second row in Figure 5.9 shows the increasing of Z_{FRD} lowers down the listric section.

5.5 Applications to sedimentary upper crust

To obtain well constrained quantitative results, the method is best applied to an extensional normal faulting where the pore-fluid pressure distribution is reasonably well known from drilling or other data, and the typical listric faults can be clearly observed from the seismic profiles. The NW Gulf of Mexico [*Xiao et al.*, 1991] and offshore Niger Delta [*Shaw et al.*, 2004; *Corredor et al.*, 2005] are certainly ideal field examples for our applications.

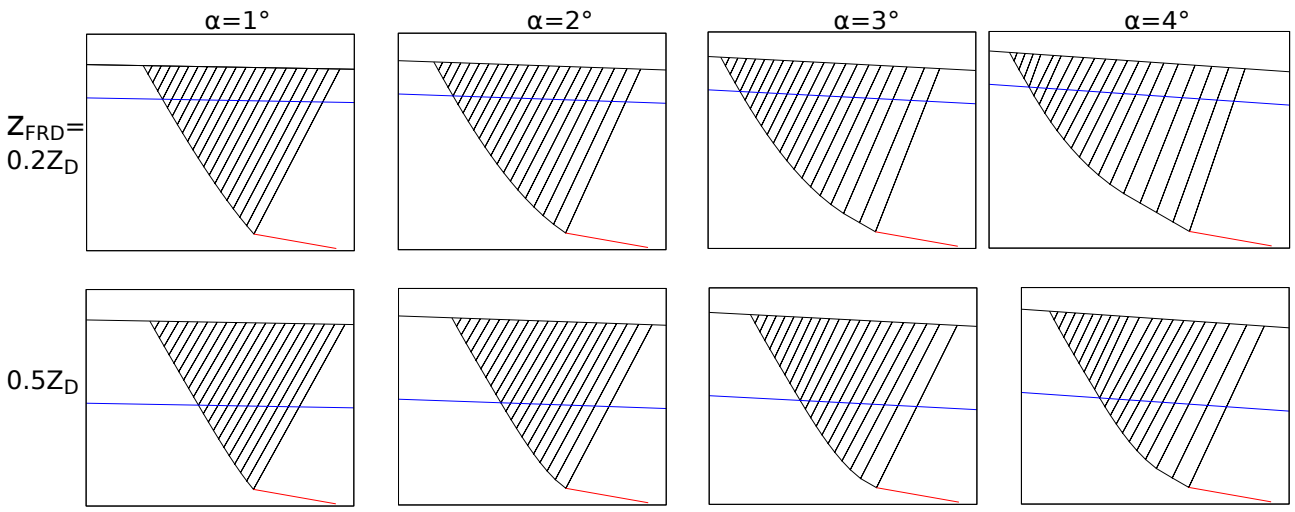


Fig. 5.9: Failure modes for different fluid-retention depth Z_{FRD} ($= 0.2Z_D, 0.5Z_D$, two rows) and the surface slope α ($1-4°$, four columns). The vertical and horizontal scales are equal. Material cohesion $\tilde{C}_B = 0.04$ ($C_B = \tilde{C}_B \rho g h = 10$ MPa for depth of 10 km), $\beta = 10°, \varphi_D = 10°$.

5.5.1 Faulting in NW Gulf of Mexico

Slip at depth of 6 km in the Gulf of Mexico [*Xiao et al.*, 1991] splays into two low-angle normal faults, as shown in Figure 5.1a. One of the two faults, Brazos Ridge fault dipped at $\beta = 17°$, results in several bi-lineal normal faults connecting to the topography. A moderately dipped detachment ($\beta = 5°$) NW to the Brazes Ridge fault results in three curved normal faults linking this detachment to the topography. The surface trace of the Brazos Ridge fault runs roughly parallel to the coast of Texas about 50 km offshore. A series of seismic cross-sections in *Xiao et al.* [1991] show that there is little variation in the structure along strike.

The extensional hanging wall overlying the low-angle normal faults has an essentially flat topographic surface at the present time. Note that the flat topographic surface at the present time is due to the delta progradation, and the listric faults were formed at the time when the topography was gently dipped. The gentle surface dip of sedimentary delta is $1 - 1.3°$, ~ 30 km SE to the current cross-section, Figure 5.1a. The relative stratigraphic thickening in the hanging wall indicates that the Brazes Ridge fault is presently active, although the maximum rate of slip was in the middle Miocene ($15-11$ Ma) [*Vogler and Robison*, 1987]. We can deduce the surface slope above the Brazos Ridge fault was gently dipped in the middle Miocene if the average progradating rate is around 2 km/Ma. As discussed in above section, surface slope is

an important factor to generate the listric fault and is set to 1° in our calculations. As discussed above, the detachment dips β are set to 5° and 17° for our simulations.

Pore-fluid pressure in this region can be determined using data from several wells in the contribution of *Xiao et al.* [1991]. The wells close to the seismic cross-section are divided into three groups (area 1, area 2, area 3) as shown in Figure 5.1b. *Xiao et al.* [1991] converted to Hubbert-Rubey fluid pressure ratio λ from the measured fluid pressure $p_f = \lambda\rho gz$ which are shown in Figure 5.1c. In general, fluid pressures are hydrostatic ($\lambda = 0.4$) from the sea floor to the depth of $Z_{FRD} = 1.7 - 2.5$ km for the three areas, Figure 5.1c, then increases roughly linearly to the detachment fault ($\lambda \sim 0.95$). The fluid-retention depths Z_{FRD} measured from three areas are shown roughly as the red line in Figure 5.1b. This depth can be shallow to 1 km above the zone of listric faults, as indicated by the red dashed curve in Figure 5.1b. The fluid pressure profiles in Figure 5.1c are similar to the fluid pressure in Case 2, and in our simulations, we assume the Z_{FRD} varies from 1.0 km to 2.5 km and is parallel to the topographic surface. The detachment depth Z_D is assumed at 6 km from the observations in Figure 5.1a and 5.1b. Thus the dimensionless value of $\tilde{Z}_{FRD}$ varies within $0.16 - 0.4$.

The stability analysis of this region using the critical Coulomb wedge theory [*Xiao et al.*, 1991] assumes the bulk material and detachment properties are uniform, frictional and cohesive. We have the same assumptions for the application of our method in this region. The two remaining parameters required to use our method are the friction angles φ_B and φ_D. These can be constrained significantly by the available in-situ observations. For the gentle surface slope and the calculations in above section, the theoretical normal-fault dip near the topography is approximately $\pi/4 + \varphi_B/2$. The observed normal-fault dips near the sea floor, Figure 5.1b, lie between 40° and 55°, the low dip of 40° could be caused by compaction of initially steeper faults [*Xiao and Suppe*, 1989]. We choose the friction angle $\varphi_B = 20°$ to be consistent to the fault dip 55°. From the calculations in above section, the friction angle φ_D is set to the value of φ_B to generate the same dip of low-angle normal fault as the detachment.

The simulation results are presented in Figure 5.10 for the detachment dip $\beta = 5°$ and 17°, respectively. All the geometrical and physical parameters are summarized in the column 4 of the Table 5.2. For the $\beta = 5°$ in Figure 5.10a, the listric faults are rooting at a low-angle normal fault, dipped at 5°. These features are similar to the observations in Figure 5.1a where the detachment dip $\beta = 5°$ results in a low-angle normal fault and series of listric faults branching

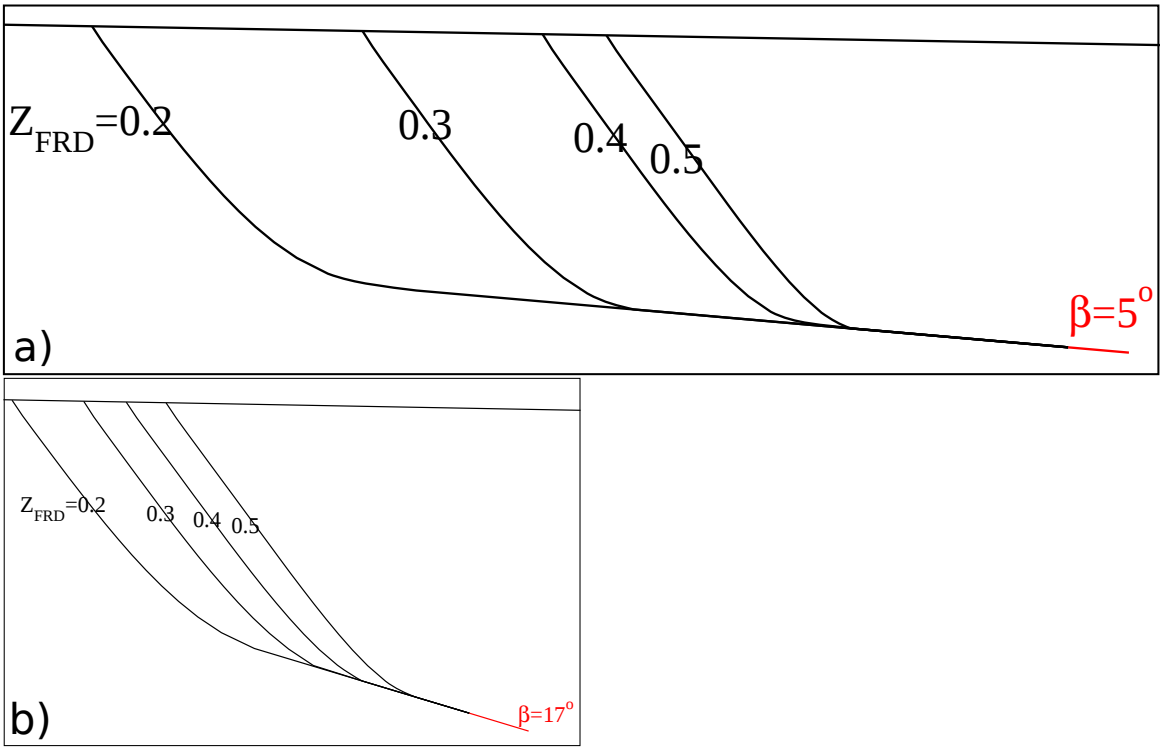


Fig. 5.10: Simulations of normal faulting in Gulf of Mexico varying $\tilde{Z}_{FRD} = 0.2-0.5$ (Case 2) for the detachment dip (a) $\beta = 5°$ and (b) $\beta = 17°$. The vertical and horizontal scales are equal.

out from this normal fault. Increasing $\tilde{Z}_{FRD}$ reduces substantially the stretch of the listric faults. The simulation results show that $\tilde{Z}_{FRD}$ is within $0.2 - 0.3$ for the fit with the stretch size based on the observations in Figure 5.1b. For the case of detachment dip $\beta = 17°$, Figure 5.10b shows several listric faults branch out from a normal fault dipped at 17°, and the stretch length of this normal fault is substantially shorter than that of $\beta = 5°$. For example, in the case of $\tilde{Z}_{FRD} = 0.2$, the stretch length of low-angle normal fault for $\beta = 17°$ is around $0.7Z_D$ whereas this length is $2.2Z_D$ for $\beta = 5°$. A longer fault immersed in high fluid overpressure means more mechanical work. Thus a lower dipped detachment will result in a longer normal fault immersing in overpressured region.

5.5.2 Faulting in offshore Niger Delta

The objective of this section is to apply again our method to the offshore Niger Delta and to predict the formation of the structures in extension, typically the listric normal fault. Regional seismic studies (Figure 5.11a) across the offshore Niger Delta show a seaward gravity instability

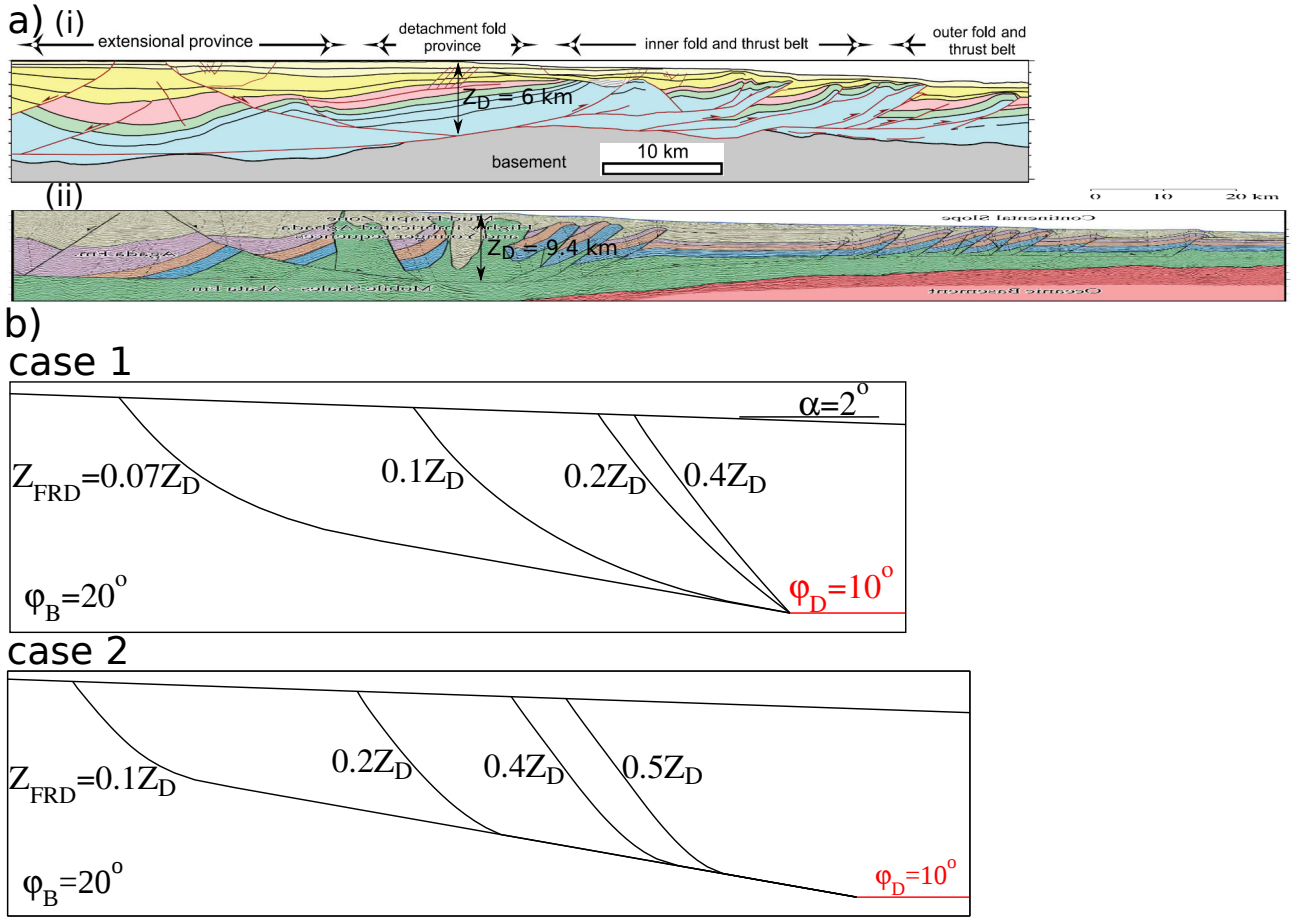


Fig. 5.11: Interpreted regional seismic profiles across the Niger Delta showing the listric faults in the extensional province on the shelf [*Shaw et al.*, 2004; *Corredor et al.*, 2005]. Simulations of normal faulting in offshore Niger Delta for fluid pressure in Case 1 and Case 2, respectively. The vertical and horizontal scales are equal.

of the large sedimentary delta (Agbada Formation) above a substratum of overpressured shale (Akata Formation) [*Shaw et al.*, 2004; *Corredor et al.*, 2005]. The normal faulting in the thick, coastal part on the shelf and simultaneous thrusting in the thin, deep parts, root on a common detachment level. The listric fault in the extensional province characterizes a low dip and curved fault which extends 30 km to the landward, see in Figure 5.11a. We will study the required conditions (fluid overpressures and material properties) in this region that would produce the observed structures according to our method.

Our method contains same approximations as the above application. We assume the bulk material and detachment properties are uniform, frictional and cohesive. The friction angle φ_B of bulk material can be estimated from the observed dips of regional thrusts, $32-40°$ from Figure 5.11a. For a gentle surface slope, the theoretical thrust dip is approximately $\pi/4-\varphi_B/2$. Thus,

the friction angle φ_B is in a range of $10-26^\circ$ and it is assumed at 20°. The weak detachment fault should have a friction φ_D lower than bulk materials, thus we assume here 10° for the simulations. The detachment dip β is assumed to be 0° from the observation of cross-sections in Figure 5.11a. Note that the normal faulting formed at the time when the topography was gently dipped during the sedimentation progradation. We assume the topography surface is straight and the surface dip is $1-2^\circ$ from the current observations in offshore Niger Delta. The fluid-retention depth Z_{FRD} is assumed to be parallel to the topography surface. Fluid pressure tests in frontal toe system [*Cobbold et al.*, 2004; *Krueger and Grant*, 2011] show the value of Z_{FRD} is around 2 km. The drilling tests in translational province [*Goodwyne*, 2012] indicate a wide range of Z_{FRD} between 700 m and 1800 m. The lack of measurements in the upslope extensional region limits the application of our method. For the simplicity, we assume herein the value of Z_{FRD} in upslope region has the same range as the tests in translational province [*Goodwyne*, 2012]. The two profiles in Figure 5.11a show the detachment depths Z_D are 6 and 9.4 km. Thus we have the dimensionless fluid-retention depth $\tilde{Z}_{FRD} = 0.12-0.3$ for profile (i) in Figure 5.11a, and $0.07-0.19$ for profile (ii). We will use a wide range of $\tilde{Z}_{FRD} = 0.07-0.5$ for the following simulations.

The simulation results are presented in Figure 5.11b for the fluid pressure of the Case 1 and Case 2. All the geometrical and physical parameters are summarized in the column 5 of the Table 5.2. For the Case 1, we can observe the substantial influence of Z_{FRD} on the fault shape. For example, for the case of $\tilde{Z}_{FRD} = 0.07$ in Case 1, a low-angle and curved fault forms similar to the observation in offshore Niger Delta, Figure 5.11a. $\tilde{Z}_{FRD} = 0.1$ results in a listric fault similar to the slip-line solution in Figure 5.6a. However, increasing $\tilde{Z}_{FRD}$ reduces the extension of the listric fault substantially, visible at $\tilde{Z}_{FRD} = 0.2, 0.4$ in Figure 5.11b. The increasing of friction angle φ_B to 30° has the same effect, as seen from the blue curve in Case 1. Note that listric faults are not always observed in offshore Niger Delta, some normal faults, characterising as planar shape [*Wu and Bally*, 2000; *Hooper et al.*, 2002; *Rouby et al.*, 2011], are more close to our simulations at $\tilde{Z}_{FRD} \geq 0.2$.

For the Case 2, the first observation is that the fluid pressure has an important impact on the fault shape. The $\tilde{Z}_{FRD} = 0.1$ in Case 2 results in a long, low-angle normal fault and a listric fault linking it to the topography. Increasing $\tilde{Z}_{FRD}$ reduces the length of low-angle normal fault but the listric fault are rooting at the same fault.

5.6 Concluding discussions

This contribution propose an analytical method to study the shape of normal fault that links the topography to the lower detachment fault in overpressured, cohesive and frictional sedimentary upper crust. This analytical method is a 2-D kinematic approach of limit analysis [*Chen*, 1975], also called the maximum strength theorem in *Salençon* [2002]. The continuously normal fault is treated as though composed of a number of segmented planar faults inspired from the hanging-wall kinematics proposed by *Xiao and Suppe* [1992]. The hanging-wall region above these segmented faults is discretized into blocks of the same number by active axial surfaces. We construct kinematically admissible and pertinent velocity in each block and velocity jump between them. The shape of segmented fault is optimized with the steepest descent method to obtain the least upper bound force at back wall which corresponds to the most efficient way to deform the system.

The analysis results show that the low-angle normal fault and the listric fault can be achieved (1) without sedimentation and compaction process (no growth fault during sedimentation) [*Xiao and Suppe*, 1989], (2) without geometries (no topography effect), just using straight, gently inclined sea floor and dipped detachment, (3) without a complex mechanical response, only using Coulomb criterion; (4) without a bi-linear overpressure gradient and (5) without a complex prototype and footwall deformation, such as a brittle overburden above a thick ductile substrate. The proposed fluid overpressures widespread in sedimentary upper crust are essential in gravitational faulting, it not only generates the low-angle normal fault, but also determines the shape of listric fault. Simplify to the prototype of surface slope parallel to the detachment in Case 1, the good match between our simulation results and the slip-line solutions [*Crans et al.*, 1980] essentially validates our methodology.

The results of parametric studies show that the surface slope is essential for the formation of the listric fault, even when the surface slope is gently dipped ($\leq 3^\circ$). A planar fault will form for the prototype with a flat topography. Compared to the fluid pressure in Case 1, the normal faulting in Case 2 usually results in a low-angle, planar fault under the listric fault connecting to the topography. For the fluid pressure in Case 2, the listric fault forms near the bottom to the detachment when the surface is at a small value ($\leq 1^\circ$). Increasing the surface slope, this listric fault moves up and length of low-angle planar fault increases. Parametric studies also show the increasing of detachment dip and material cohesion reduce substantially

the curvature of normal fault and its activation length, for example, the normal fault is planar when the detachment dip is greater than 40°.

The study of normal faulting in NW Gulf of Mexico [*Xiao et al.*, 1991] shows the shape of normal fault depends much on the detachment dip. For example, the detachment dipped at 5° results in the large curved normal faults and the 17° dipped detachment generates bi-linear fault when the Z_{FRD} line is low. In offshore Niger Delta, the long extending of normal fault could be resulted from the shallow depth of Z_{FRD} ($\leq 0.1Z_D$) in fluid pressure of Case 1, similar to one solution of slip-line theory in *Crans et al.* [1980]. Fluid pressure in Case 2 will generate often a low-angle, planar normal fault which is not the case from the observations in this region.

Although Case 2 is the typical shale pressure in offshore deltas [Krueger and Grant, report], the real fluid pressure in offshore deltas could be complicated and different from our two cases. The fluid pressure could reach the lithostatic pressure at a depth above the detachment fault, and keep the listhostatic pressure with the depth until to the detachment. Thus the shape of fault resulted from this fluid pressure would be slightly different from our simulation results above. Another important hypothesis in these applications is that the Z_{FRD} line is assumed to be parallel to the topography. The real profile of the top of fluid overpressure, however, is quite complicated, such as in Gulf of Mexico (Figure 5.1c) and in Brunei delta extensional province [*Morley et al.*, 2008]. Additionally, the ductile properties of the substrate (salt) in northern Gulf of Mexico [*Trudgill et al.*, 1999; *Morley et al.*, 2011] could result in the listric fault due to the footwall deformation. The fault forms initially planar and rotates during extension. This formation of listric fault is confirmed by many analogue experiments in the prototype with a ductile substrate and brittle overburden, or the prototype of clay material [*Dula*, 1991; *Withjack et al.*, 1995; *Bose and Mitra*, 2009].

Beyond the direct applications presented here, there are some obvious perspectives for the present work. Firstly, numerical methods (e.g. finite element and finite difference methods) could be used to validate our method accounting for the fluid pressures instead of considering the effective friction derived from fluid overpressure and friction coefficient. The effective friction is not sufficient to have large curved fault, also it changes the virtual velocities in our Limit Analysis method. Additionally, the analytical method in this contribution could be improved accounting for the arbitrary topography, the fluid-retention depth not parallel to the topography. For example, for a prototype with flat topography, a gently dipped fluid-retention depth

could also generate the listric fault. Last but not least, the field applications according to Limit Analysis could take account the 3-D complexity against more natural examples. The precise analysis depends on various parameters, such as the change of physical parameters (rock friction, porosity and permeability) with depth, precise fluid profiles with depth, sediment loading and compaction, as well as a thorough understanding of the processes in a given system.

Chapter 6

Conclusions

6.1 Limit Analysis

The manuscript studies widespread extensional failures in the brittle, upper crust using a two-dimensional kinematic approach of Limit Analysis, called maximum strength theorem [*Salençon*, 2002]. This mechanical approach applied to extensional failures extends the contributions of *Maillot and Leroy* [2006], *Cubas et al.* [2008] and *Pons and Leroy* [2012] for compressive settings. The application of Limit Analysis is to calculate the upper bound of external forces on a geological structure. The search for this upper bound force uses the kinematic approach based on fields of virtual velocities. With this method, it is possible to determine the upper bound force accommodating the failure mechanism (the position of normal fault and active detachment). The main advantages of this theory is that only few mechanical parameters are required beforehand. For example, in the case of material described by the Coulomb criterion, only cohesion and friction angle of the materials and on discontinuities (faults) are the physical parameters.

6.1.1 Gravity and tectonic extensional collapses

We firstly use the Limit Analysis to examine the gravity and tectonic extensional collapses (**Chapter 2**) of wedge structures resting on an inclined weak detachment. The predictions of Limit Analysis not only match exactly the solutions of the critical Coulomb wedge (CCW) theory, but also generalises the CCW theory in several aspects: wedge of finite size and of complex topography.

For the gravity extensional collapse, Limit Analysis shows that the stability transition for a cohesive wedge occurs with the maximum length of the detachment. It is shown that details of the topography, for the particular example of the Meijilones peninsula (Northern Chile) are, however, responsible for a short-length scale instability corresponding to a frontal gravitational collapse. A reasonable amount of cohesion (5 MPa) will result in a stability transition with a long-wavelength mode.

For the tectonic extensional collapse, Limit Analysis permits investigation of a wedge of finite size and of arbitrary topography, which are not applicable for the CCW theory. The mechanical approach captures essentially the feature of structural deformation close to the back wall. It also predicts the jump in position of the collapse mechanism from the back-wall region to the frontal wedge by modifying the topographic surface.

6.1.2 Gravity instability with a resistive toe

In **Chapter 4**, the Limit Analysis approach is also applied to the gravity instability linking up-slope extensional failure to downslope compressional resistive toe. The Limit Analysis extends the development of gravity extensional collapses in the Chapter 2 accounting for the stabilizing effect of the frontal thrusting. Fitting our prototype to the taper observed in the offshore Niger Delta, we predict a pore-fluid pressure in the range of 80 to 90% of the lithostatic pressure within the bulk material (Hubbert-Rubey fluid-pressure ratio $0.8 - 0.9$), and in the range 97 to 99% of the lithostatic pressure within the detachment. On the contrary, the stability of frontal Niger Delta examined with the CCW theory [*Bilotti and Shaw*, 2005; *Suppe*, 2007; 2014] implies the fault-thrust belts in this region are compressional (or tectonic-driven) collapses. However, the gravity instability in Niger Delta is resulting from the sedimentation overloading, and the fault-thrust belts are linked to the up-slope extension. Our predictions of fluid pressures are much higher than the determinations from the CCW theory.

6.1.3 Formation of low-angle and listric normal fault

The Limit Analysis approach is also used to study the shape of normal fault which links topography to a low detachment fault (**Chapter 5**). The analysis results show that low-angle normal faults and listric faults can be achieved in prototypes with a gently dipping surface slope where fluid pressures are hydrostatic above the fluid-retention depth and overpressured

below this depth. The parametric studies show that the prototype with a flat topographic surface cannot generate listric faults. Increasing detachment dip and material cohesion reduces substantially the curvature of normal fault. The field study in Gulf of Mexico shows that the fault shape depends much on the dip of detachment fault. For example, the detachment dipped at 5° results in the large curved normal faults and the 17° dipped detachment generates bi-linear fault when the fluid-retention depth is deep. The application to Niger Delta reveals that the formation of low-angle and listric faults result from a shallow fluid-retention depth.

6.2 Sequential Limit Analysis

There is a sequential version of the above mechanical method, called Sequential Limit Analysis, that allows us to follow the evolution of deformation resulting from normal faulting through time (**Chapter 3**). Due to its efficiency, we can perform several thousand forward simulations of a cross-section and thus optimize the fit with seismic sections.

The methodology is validated for a wedge extension in dry and fluid overpressured cases, and the final surface slopes of stable wedges are well predicted by the CCW theory. The application to the deformation above a lower normal fault shows how the normal fault and the associated axial surface of the half-graben rotates because of topographic subsidence, which proves mechanically the improper use of half-graben kinematics proposed by *Groshong* [1989] and *Xiao and Suppe* [1992] when the sedimentation rate is low. The continuous rotation of the normal fault means that material in the footwall is sheared upon entering the hanging wall creating a region called the Foot-to-Hanging Wall region (FHW). The creation of the FHW region is illustrated by sandbox experiments and field examples. Friction reduction along the normal fault renders the rotations discontinuous and as a result, the FHW contains internal blocks. Sedimentation tends to slow down the rotations and thus to reduce the size of the FHW.

6.3 Perspectives

There are many prospectives based on the mechanical studies in **Chapter 2**. For example, the failure criterion throughout this manuscript is Mohr-Coulomb criterion, a more complex failure criterion accounting for tension cut-off [*Paul*, 1961] could be implemented to capture the

tension fault in the shallow depth [*Holland et al.*, 2006; 2011]. Additionally, compared to the CCW theory, our mechanical methodology can consider the stability of a wedge structure with an inherited, weak normal fault. In our current manuscript, the planar normal fault rooting at the back wall is used as the second failure mechanism during extension. The studies of active retaining wall in civil engineering [*Chen*, 1975] reached a conclusion that the normal fault near the back wall implies a listric (log-spiral) shape.

For the perspectives of Sequential Limit Analysis in **Chapter 3** applied to the extensional deformation pattern, future approach could be improved in at least three ways. Firstly, the fault is softening for a certain extension, but this fault softening will be forgotten once a new normal fault is activated. Fault remembering is a good direction to improve our Sequential Limit Analysis. Secondly, the Sequential Limit Analysis could be used to capture the deformation pattern of wedge extension in Albuquerque Basin of the Rio Grande Rift (Figure 1.3) [*Russell and Snelson*, 1994] and Corinth-Patras Rift along Krathis River (Figure 1.2) [*Rigo et al.*, 1996] accounting for the fault softening and sedimentation. Finally, the numerical methods such as finite element and distinct element methods could be used to simulate the deformation process above a low-angle detachment accounting for fault softening and sedimentation processes.

There is one perspective for the further study of the extensional-compressional failure modes of offshore deltas in **Chapter 4**. The extensional province on land and in shallow water of Niger Delta (Figure 1.1) is characterized by both seaward dipping and landward dipping (counter-regional) listric normal growth faults. The listric shape of normal fault on the stability is certainly a good candidate for the improvement of our mechanical approach.

The future work based in **Chapter 5** could be improved from the following aspects. First, the failure mode can be improved accounting for more realistic fluid pressure of sedimentary basins which could be different from the proposed two simple cases. For example, the *in situ* fluid pressure could reach the lithostatic pressure at a depth above the detachment fault, and keep the listhostatic pressure with the depth until to the detachment. In many cases, the real profile of the top of fluid overpressure is often not parallel to the topography and is quite complicated, such as in Gulf of Mexico [*Xiao et al.*, 1991] and in Brunei delta extensional province [*Morley et al.*, 2008]. Second, the formation of listric fault and low-angle normal fault due to the footwall deformation are exemplified by many analogue experiments in the prototype with a brittle overburden and ductile substrate, or the prototype with the clay material [*Dula*,

1991; *Withjack et al.*, 1995; *Bose and Mitra*, 2009]. The ductile substrate will response to isostasy that deforms and rotates the detachment. In the applications of Limit Analysis, we assume a planar, immobile detachment which could influence our results. The future Limit Analysis approach is hoped to apply to these prototypes.

Appendix A

Appendix for Chapter 2

1 Different fluid pressure parametrizations

The definition of the pressure ratio, introduced by *Hubbert and Rubey* [1959], requires a parametrization of the path from the free surface to the point of interest. Various authors have introduced their parametrizations leading to different definitions of the fluid pressure ratio. These differences are minor in compression because the taper angle remains small. However, in extension, this angle is sufficiently large to exacerbate these differences and the stability verdict becomes sensitive to the exact definition. The objective of this appendix is to compare the various parametrizations found in the literature.

The parametrization of *Hubbert and Rubey* [1959] for $\lambda^{(H)}$ (the first author name will be attached in upperscript to the ratio) relies on a vertical path from the free surface to the point of interest. This path corresponds to the black line in Figure A.1 and was used also by *Pons and Leroy* [2012] since it is the most natural parametrization for an irregular topography. *Davis et al.* [1983] and *Dahlen* [1984] used different parametrization corresponding to the red $\lambda^{(D1)}$ and blue path $\lambda^{(D2)}$, respectively, in Figure A.1. The method to derive the relation between these different pressure ratios is that the pressure at any point P in the bulk should be uniquely defined.

The three definitions introduced so far and applied at the same point P are

$$\begin{aligned}
\lambda^{(H)} &= -\frac{p_f^{(H)} - \rho_f g D^{(H)}}{\sigma_z^{(H)} + \rho_f g D^{(H)}} \quad \text{with} \quad \sigma_z^{(H)} = -\rho g (z^{(H)} - D^{(H)}) - \rho_f g D^{(H)} \,, \\
\lambda^{(D1)} &= \frac{p_f^{(D1)} - \rho_f g D^{(D1)}}{\sigma_z^{(D1)} - \rho_f g D^{(D1)}} \quad \text{with} \quad \sigma_z^{(D1)} = \rho_f g D^{(D1)} + \rho g (H^{(D1)} - z^{(D1)}) \,, \\
\lambda^{(D2)} &= -\frac{p_f^{(D2)} - \rho_f g D^{(D2)}}{\sigma_z^{(D2)} + \rho_f g D^{(D2)}} \quad \text{with} \quad \sigma_z^{(D2)} = -\rho g z^{(D2)} \cos\alpha - \rho_f g D^{(D2)} \,,
\end{aligned} \tag{A.1}$$

complemented by the following geometric relations

$$\begin{aligned}
D^{(D2)} - D^{(D1)} &= (H^{(D1)} - z^{(D1)}) \sin(\alpha + \beta) \sin\alpha \,, \\
D^{(D2)} - D^{(H)} &= (z^{(H)} - D^{(H)}) \sin^2\alpha \,, \\
z^{(D2)} &= (H^{(D1)} - z^{(D1)}) \cos(\alpha + \beta) \,, \\
z^{(D2)} &= (z^{(H)} - D^{(H)}) \cos\alpha \,.
\end{aligned} \tag{A.2}$$

The system of three equations in (A.1)-(A.2) has four unknowns, the pressure ratios and the actual pressure at point P: $p_f^{(H)} = p_f^{(D1)} = p_f^{(D2)}$. Eliminate the latter and obtain

$$\begin{aligned}
\lambda^{(D1)} &= \lambda^{(D2)} \cos(\alpha + \beta) \cos\alpha + \frac{\rho_f}{\rho} \sin(\alpha + \beta) \sin\alpha \,, \\
\lambda^{(H)} &= \lambda^{(D2)} \cos^2\alpha + \frac{\rho_f}{\rho} \sin^2\alpha \,.
\end{aligned} \tag{A.3}$$

The trigonometric dependence is such that $\lambda^{(H)}$ and $\lambda^{(D2)}$ are rather different if the topographic slop α is large, as for the gravitational collapses of interest here.

2 Exact critical Coulomb wedge theory (ECCW)

The classical CCW theory is now modified to account properly for the overpressure within the decollement. It complements the derivation found in *Wang et al.* [2006] and *Mourgues et al.* [2014], by providing the complete expression of the implicit solution in terms of the critical taper $\alpha + \beta$ as function of the fluid over pressures and friction angles. This expression is valid for any permissible value of the slopes α and β, thus the proposed name ECCW. We furthermore calculate and illustrate the solution in both gravitational and tectonic extensional cases. This ECCW theory is derived following exactly the steps of *Dahlen* [1984] and *Lehner* [1986] up to the condition of the decollement slip activation.

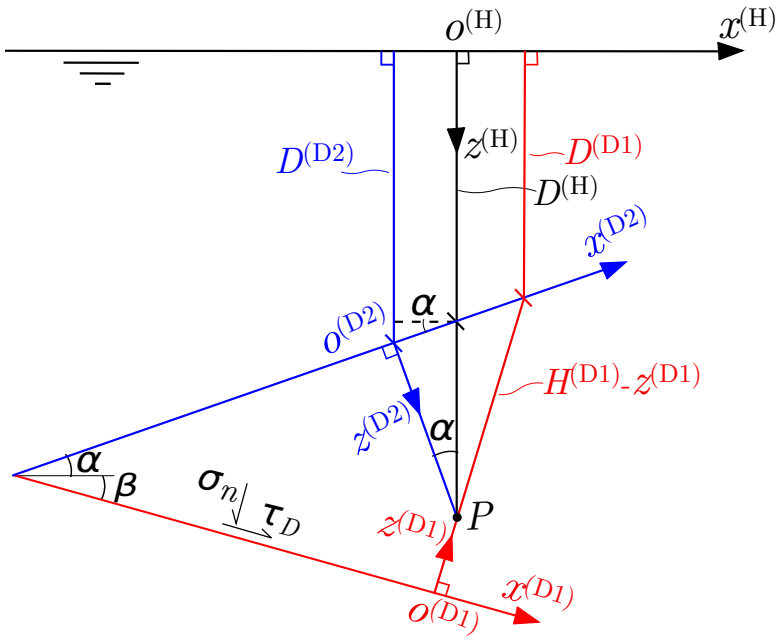


Fig. A.1: The definition of the fluid pressure ratio λ is sensitive to the path used from the sea surface to the point of interest where the pressure is estimated. The black segment was proposed by *Hubbert and Rubey* [1959] and considered by *Pons and Leroy* [2012]. The red path was used by *Davis et al.* [1983] and the blue path was employed by *Dahlen* [1984]. The three different paths lead to the same fluid pressure at point P but to different pressure ratios.

The tangential stress τ_D, Figure A.1, to activate the decollement is given by

$$\tau_D = \tan(\varphi_D)(\sigma_n + p_D)\,, \tag{A.4}$$

in which φ_D, σ_n and p_D are the friction angle, the normal stress and the fluid pressure in the decollement, respectively. The fluid pressure within the decollement is parametrized following Dahlen's choice as described in Appendix A:

$$p_D = -\lambda_D^{(D2)}\sigma_z + (1-\lambda_D^{(D2)})\rho_f g D^{(D2)}\,. \tag{A.5}$$

The decollement tractions is now expressed in the (x,z) coordinate system also adopted in *Dahlen* [1984]'s (the blue coordinate in Figure A.1)

$$\begin{aligned}\sigma_n &= \sigma_z - \tau_{xz}\sin 2(\alpha+\beta) - \frac{1}{2}(\sigma_z-\sigma_x)[1-\cos 2(\alpha+\beta)]\,,\\ \tau_D &= \frac{1}{2}(\sigma_z-\sigma_x)\sin 2(\alpha+\beta) + \tau_{xz}\cos 2(\alpha+\beta)\,,\end{aligned} \tag{A.6}$$

in terms of the stress components within the cohesionless wedge. This state of stress is on the verge of Coulomb failure and satisfies the local conditions

$$\begin{aligned}\frac{1}{2}(\sigma_z-\sigma_x) &= \frac{-\bar\sigma_z}{\csc(\varphi_B)\,\sec(2\Psi_O)-1}\\ \tau_{xz} &= \frac{-\tan(2\Psi_O)\,\bar\sigma_z}{\csc(\varphi_B)\,\sec(2\Psi_O)-1}\,,\end{aligned} \tag{A.7}$$

in which φ_B is the bulk friction angle, and the angle Ψ_O is measured between the maximum principal stress direction σ_1 and the x-axis of the blue coordinate system (Figure A.1). Also, the effective, vertical stress $\bar\sigma_z$ in (A.7) is

$$\bar\sigma_z = \sigma_z + p_B = (1-\lambda_B^{(D2)})(\sigma_z + \rho_f g D^{(D2)}). \tag{A.8}$$

in which p_B, $\lambda_B^{(D2)}$ are the fluid pressure and the fluid pressure ratio in bulk material, respectively.

The set of five equations in (A.4) to (A.8) provides an implicit solution for the critical taper angle: $\alpha+\beta = \Psi_D - \Psi_O$ with

$$\begin{aligned}\Psi_D &= \frac{1}{2}\arcsin\left[\Big(\frac{1-\lambda_D^{(D2)}}{1-\lambda_B^{(D2)}}\Big)\frac{\sin(\varphi_D)}{\sin(\varphi_B)} + \Big(\frac{\lambda_D^{(D2)}-\lambda_B^{(D2)}}{1-\lambda_B^{(D2)}}\Big)\sin(\varphi_D)\cos(2\Psi_O)\right] - \frac{1}{2}\varphi_D\\ \Psi_O &= \frac{1}{2}\arcsin\Big(\frac{\sin(\alpha')}{\sin(\varphi_B)}\Big) - \frac{1}{2}\alpha'\\ \alpha' &= \arctan\left[\Big(\frac{1-\rho_f/\rho}{1-\lambda_B^{(D2)}}\Big)\tan\alpha\right].\end{aligned} \tag{A.9}$$

The quantity Ψ_D is the angle between σ_1 and the decollement, and this implicit definition is the only different term from the CCW theory, recalling the definition (13) and (19) in the contribution of *Dahlen* [1984], $\Psi_D = \frac{1}{2}\arcsin\left[\frac{\sin(\varphi'_D)}{\sin(\varphi_B)}\right] - \frac{1}{2}\varphi'_D$ with $\varphi'_D = \arctan\left[\left(\frac{1-\lambda_D^{(D2)}}{1-\lambda_B^{(D2)}}\right)\tan(\varphi_D)\right]$. Obviously, the formulations of *Dahlen* [1984] is also the exact solutions if the bulk material and decollement have the same fluid pressure ratio, $\lambda_D^{(D2)} = \lambda_B^{(D2)}$, or if they are both dry and subaeria.

The ECCW theory is now compared with the CCW theory using the coordinate definition considered by *Dahlen* [1984] in Figure A.2a and b, corresponding to the gravitational collapse and the tectonic collapse modes, respectively. The material properties are summarized in the third column of Table 2.1. For over-pressured decollement, the ECCW results does not differ significantly from the solutions of *Dahlen* [1984] and *Xiao et al.* [1991] in region I of Figure A.2a and b. However, the differences are significant for region II (gravitational collapse or tectonic extension) of interest to this contribution. The critical slope α_c predicted from ECCW theory in region II, Figure A.2a, is greater than the value of CCW theory. The ECCW theory produces a lower critical slope compared to the extensional CCW theory (region II in Figure A.2b).

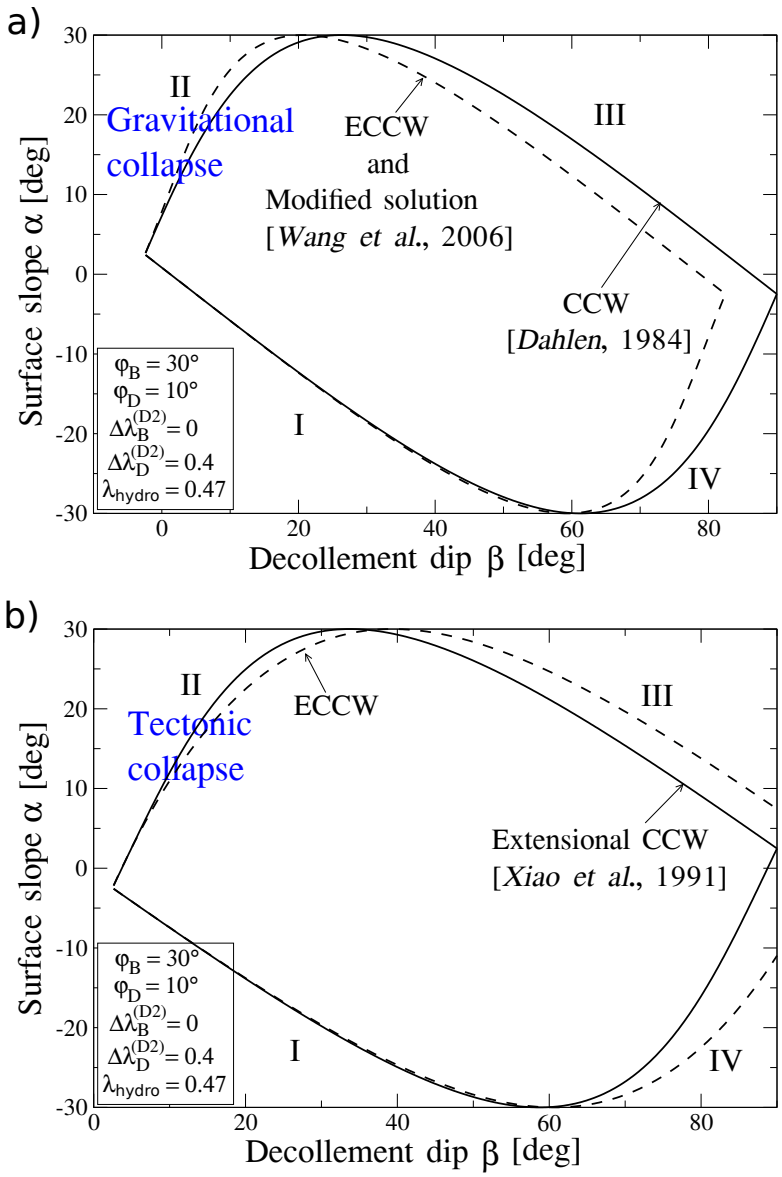


Fig. A.2: Comparison of the ECCW theory and the solution of *Wang et al.* [2006] with the original theory of *Dahlen* [1984] for gravitational collapse, a). Same comparison of the ECCW theory and the original extensional CCW theory of *Xiao et al.* [1991], b). The bulk and decollement pressure ratios are defined in the Dahlen's fluid ratio $\lambda^{(D2)}$.

Appendix B

Electronic Supplement to Chapter 2

This Electronic Supplement contains two types of information. The first two sections provide further comments on the theoretical background used in the main text. The last section complements the main paper with the derivation of the three upper bounds used in Section 2.4.

1 Theorem of virtual powers with acceleration contribution

This derivation is classical in mechanics and is provided here for sake of completeness and to make sure that the terminology is well defined and understood. The influence of the fluid phase is not included for simplicity but its influence is discussed in the main paper and presented at length in *Pons and Leroy* [2012]. Note also that the velocity is assumed continuous.

Consider the equation of motion over the domain Ω_t

$$\underline{\mathrm{div}}(\underline{\underline{\sigma}}) + \rho \underline{g} = \rho \underline{a} \quad \forall \underline{x} \in \Omega_t \,. \tag{B.1}$$

Multiply this vectorial equation by a virtual velocity field $\underline{\hat{U}}$. This velocity field is not necessarily the exact velocity field and is simply consistent with the boundary conditions. The result reads

$$\int_{\Omega_t} \underline{\hat{U}} \cdot \big(\underline{\mathrm{div}}(\underline{\underline{\sigma}}) + \rho \underline{g}\big) dV = \int_{\Omega_t} \underline{\hat{U}} \cdot \rho \underline{a} dV \,. \tag{B.2}$$

This is a weak (integral) form of the equation of motion which is equivalent to (B.1) in view of the arbitrariness of the virtual velocity field. Integrate by parts the first term in the left integrand to obtain

$$\int_{\Omega_t} \underline{\mathrm{div}}(\underline{\hat{U}} \cdot \underline{\underline{\sigma}}) + \underline{\hat{U}} \cdot \rho \underline{g} - \underline{\underline{\sigma}} : \underline{\underline{\nabla \hat{U}}} \, dV = \int_{\Omega_t} \underline{\hat{U}} \cdot \rho \underline{a} dV \,. \tag{B.3}$$

Application of the divergence theorem provides

$$\int_{\partial\Omega_t} \underline{\hat{U}} \cdot \underline{\underline{\sigma}} \cdot \underline{n}\, dS + \int_{\Omega_t} \underline{\hat{U}} \cdot \rho \underline{g} - \underline{\underline{\sigma}} : \underline{\underline{\nabla \hat{U}}}\, dV = \int_{\Omega_t} \underline{\hat{U}} \cdot \rho \underline{a} dV\,, \tag{B.4}$$

where $\partial\Omega_t$ is the boundary of the domain of normal $\underline{n}$. This boundary is divided into two parts $\partial\Omega_t^u$ and $\partial\Omega_t^T$ where the displacement and the stress vector $\underline{\underline{\sigma}} \cdot \underline{n}$ are given, respectively. The virtual velocity field is chosen to vanish over $\partial\Omega_t^u$ and the stress vector is equal to the force per surface area $\underline{T}^d$. Consequently, (B.4) is equivalent to

$$\int_{\partial\Omega_t^T} \underline{\hat{U}} \cdot \underline{T}^d\, dS + \int_{\Omega_t} \underline{\hat{U}} \cdot \rho \underline{g}\, dV - \int_{\Omega_t} \underline{\underline{\sigma}} : \underline{\underline{\nabla \hat{U}}}\, dV = \int_{\Omega_t} \underline{\hat{U}} \cdot \rho \underline{a} dV\,. \tag{B.5}$$

Terms in (B.5) have dimension of a power. The left-hand side is the difference between the external power and the internal power. The right-hand side corresponds to the sum of the acceleration times the virtual velocity and is thus called the acceleration power. This equation corresponds to equation (2.1) in the main paper with the addition of the fluid pressure, discussed at length in the work of *Pons and Leroy* [2012].

2 A weak expression of Archimedes theorem

Archimedes theorem states that the sum of the forces exerted by a fluid on a submerged body is equal to the upward force of magnitude equalling to the weight of the same body composed of the fluid phase. Apply this theorem to the triangular region *HIJ* in Figure B.1:

$$\int_J^H p(x_2)\, dS\, \underline{n}_{JH} + \int_J^I p(x_2)\, dS\, \underline{n}_{JI} + \int_H^I p(x_2)\, dS\, \underline{n}_{HI} + \int_{\partial\Omega} \rho_f \underline{g} dV = \underline{0}\,. \tag{B.6}$$

Consider the uniform virtual velocity $\underline{\hat{U}}$ for the region *HIJ* and multiply (B.6) by this vector:

$$\int_J^H p(x_2)\, dS\, \underline{n}_{JH} \cdot \underline{\hat{U}} + \int_J^I p(x_2)\, dS\, \underline{n}_{JI} \cdot \underline{\hat{U}} + \int_H^I p(x_2)\, dS\, \underline{n}_{HI} \cdot \underline{\hat{U}} + \int_{\partial\Omega} \rho_f \underline{g} dV \cdot \underline{\hat{U}} = 0\,. \tag{B.7}$$

This scalar equation is called in the main paper a weak form of Archimedes theorem and is used to simplify the effective external power in Section 2.3 for the gravitational collapse mode.

3 Derivation of three upper bounds

The objective is to complement Section 2.4 in the main paper by proposing the derivation of the upper bounds to the tectonic force necessary for the three collapse mechanisms. The least of

the three upper bounds identifies the dominant mechanism. It is used to compare our approach with the extensional ECCW theory and it is also used to interpret the experiments of *Xiao et al.* [1991].

Mechanism (1): decollement fully activated

The first collapse mechanism corresponds to the rigid translation of the wedge on the fully activated decollement at the uniform velocity of norm $\hat{U}_D$, a vector oriented by the angle φ_D from the decollement, see Figure 2.8(1). The velocity jump at the back-wall is the difference $\underline{\hat{U}}_{BW} - \underline{\hat{U}}_D$, a vector of norm $\hat{J}_{BW}$ and oriented by the angle φ_{BW} from the back-wall. The external effective power for this velocity field reads

$$\mathcal{P}'_{\text{ext}}(\underline{\hat{U}}) = Q_1 \hat{U}_{BW} + \rho \underline{g} S_{ABC} \cdot \underline{\hat{U}}_D + \int_A^B p_D \, dS \, \underline{n}_{AB} \cdot \underline{\hat{U}}_D + \int_B^C p \, dS \, \underline{n}_{BC} \cdot \underline{\hat{U}}_D + \int_A^C p_{AC} \, dS \, \underline{n}_{AC} \cdot \underline{\hat{J}}_{BW} \,, \tag{B.8}$$

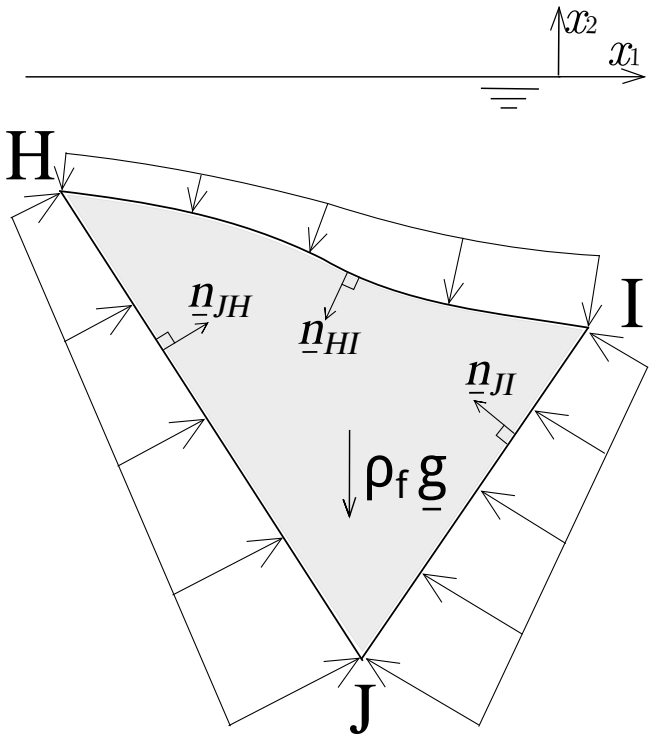


Fig. B.1: The Archimedes theorem applied in a triangular region.

in which $\underline{n}_{XY}$ is the normal vector to the surface XY. For the triangular geometry of interest, this expression simplifies to

$$\begin{aligned}\mathcal{P}'_{\text{ext}} &= Q_1\hat{U}_{BW} + (\rho-\rho_f)gS_{ABC}\hat{U}_D\sin(\beta-\varphi_D) + \Delta\lambda_D\rho gS_{ABC}\hat{U}_D\frac{\sin(\varphi_D)}{\cos\beta} \\ &\quad - \frac{1}{2}\Delta\lambda_B\rho gL_{AC}^2\hat{U}_D\cos(\beta-\varphi_D) + \frac{p(A)+p(C)}{2}L_{AC}\,,\end{aligned} \tag{B.9}$$

where the pressure terms were replaced by their spatial distribution in (2.9), and the scalar products in the integrals were evaluated using the optimal orientations in (2.11). The hodogragh of the velocity jump at the back-wall is presented in the right-hand side of Figure 2.8(1) and the law of the sines provides

$$\frac{1}{\cos(\varphi_{BW}+\varphi_D-\beta)} = \frac{\hat{J}_{BW}}{\sin(\beta-\varphi_D)} = \frac{\hat{U}_D}{\cos(\varphi_{BW})}\,, \tag{B.10}$$

having set to one the back-wall velocity norm ($\hat{U}_{BW}=1$). The maximum resisting power defined in (12) combined with the definition of the support function in (2.11) provides

$$\mathcal{P}'_{\text{mr}}(\underline{\hat{U}}) = C_D L_{AB}\cos(\varphi_D)\hat{U}_D + C_{BW}L_{AC}\cos(\varphi_{BW})\hat{J}_{BW}\,. \tag{B.11}$$

Consider now the MST in (2.13) for zero acceleration and observe that there is indeed an upper-bound to the force applied on the back-wall $Q_1 \leq Q_{u1}$. The exact expression for this upper bound is obtained by combining (B.9) and (B.11),

$$\begin{aligned}Q_{u1} &= C_D L_{AB}\cos(\varphi_D)\hat{U}_D + C_{BW}L_{AC}\cos(\varphi_{BW})\hat{J}_{BW} - (\rho-\rho_f)gS_{ABC}\hat{U}_D\sin(\beta-\varphi_D) \\ &\quad - \Delta\lambda_D\rho gS_{ABC}\hat{U}_D\frac{\sin(\varphi_D)}{\cos\beta} + \frac{1}{2}\Delta\lambda_B\rho gL_{AC}^2\hat{U}_D\cos(\beta-\varphi_D) - \frac{p(A)+p(C)}{2}L_{AC}\,.\end{aligned} \tag{B.12}$$

Mechanism (2): a normal fault rooting at the back-wall

The second collapse mechanism consists of a normal fault rooting at the base of the back-wall and dipping at γ, Figure 2.8(2), and there is no activation of the decollement. The half-graben has the uniform velocity field of norm $\hat{U}_{HG}$, which is oriented by the angle φ_{NF} from the normal fault, Figure 2.8(2). The jump in velocity across the back-wall interface is $\underline{\hat{J}}_{BW} = \underline{\hat{U}}_{BW} - \underline{\hat{U}}_{HG}$ and is oriented with the angle φ_{BW} from the back-wall, Figure 2.8(2). The external effective

power for this velocity field reads

$$\begin{aligned}\mathcal{P}'_{\text{ext}}(\underline{\hat{U}}) &= Q_2 + \rho \underline{g} S_{AEC} \cdot \underline{\hat{U}}_{HG} + \int_A^E p_{AE}\, dS\, \underline{n}_{AE} \cdot \underline{\hat{U}}_{HG} + \int_E^C p\, dS\, \underline{n}_{EC} \cdot \underline{\hat{U}}_{HG} + \int_A^C p_{AC}\, dS\, \underline{n}_{AC} \cdot \underline{\hat{J}}_{BW} \\ &= Q_2 + (\rho - \rho_f) g S_{AEC} \hat{U}_{HG} \sin(\gamma - \varphi_{NF}) + \Delta\lambda_B \rho g S_{AEC} \hat{U}_{HG} \frac{\sin(\varphi_{NF})}{\cos\gamma} \\ &- \frac{1}{2} \Delta\lambda_B \rho g L_{AC}^2 \hat{U}_{HG} \cos(\gamma - \varphi_{NF}) + \frac{p(A) + p(C)}{2} L_{AC}\,,\end{aligned} \tag{B.13}$$

where we again set $\hat{U}_{BW} = 1$. The hodogragh of the velocity jump at the back-wall is presented in Figure 2.8(2) and the law of the sines for the second failure mechanism provides

$$\frac{1}{\cos(\varphi_{BW} - \gamma + \varphi_{NF})} = \frac{\hat{J}_{BW}}{\sin(\gamma - \varphi_{NF})} = \frac{\hat{U}_{HG}}{\cos(\varphi_{BW})}\,. \tag{B.14}$$

The maximum resisting power defined in (2.12) combined with the definition of the support function in (2.11) provides

$$\mathcal{P}'_{\text{mr}}(\underline{\hat{U}}) = C_{NF} L_{AE} \cos(\varphi_{NF}) \hat{U}_{HG} + C_{BW} L_{AC} \cos(\varphi_{BW}) \hat{J}_{BW}\,. \tag{B.15}$$

Application of the MST provides again an upper bound to the force applied to the back-wall Q_{u2} and its expression relies on (B.13) and (B.15)

$$\begin{aligned}Q_{u2} &= C_{NF} L_{AE} \cos(\varphi_{NF}) \hat{U}_{HG} + C_{BW} L_{AC} \cos(\varphi_{BW}) \hat{J}_{BW} - (\rho - \rho_f) g S_{HG} \hat{U}_{HG} \sin(\gamma - \varphi_{NF}) \\ &- \Delta\lambda_B \rho g S_{HG} \hat{U}_{HG} \frac{\sin(\varphi_{NF})}{\cos\gamma} + \frac{1}{2} \Delta\lambda_B \rho g L_{AC}^2 \hat{U}_{HG} \cos(\gamma - \varphi_{NF}) - \frac{p(A) + p(C)}{2} L_{AC}\,.\end{aligned} \tag{B.16}$$

Mechanism (3): a normal fault and a shear plane rooting on the decollement

The third collapse mechanism consists of the normal fault GE dipping at γ and the shear plane GF dipping at θ, Figure 2.8(3). They both root at point G on the decollement which is activated from point A to G. The geometry of this third collapse mechanism is thus described with three parameters: γ, θ and the distance L_{AG}. The velocities of the BL and the HG are uniform and denoted $\underline{\hat{U}}_{BL}$ and $\underline{\hat{U}}_{HG}$ and they are oriented by the angles φ_D and φ_{NF} from the corresponding interface, see inset of Figure 2.8(3). There are two additional velocity discontinuities corresponding to the shear plane ($\underline{\hat{J}}_{SP} = \underline{\hat{U}}_{BL} - \underline{\hat{U}}_{HG}$) and to the interface with the back-wall ($\underline{\hat{J}}_{BW} = \underline{\hat{U}}_{BW} - \underline{\hat{U}}_{BL}$). These two jumps are oriented by the angles φ_{SP} and

φ_{BW} from the shear plane and the back-wall, respectively. The external effective power for this velocity field reads

$$\begin{aligned}\mathcal{P}'_{\text{ext}}(\hat{\underline{U}}) &= Q_3 + \rho \underline{g} S_{HG} \cdot \hat{\underline{U}}_{HG} + \rho \underline{g} S_{BL} \cdot \hat{\underline{U}}_{BL} + \int_G^E p_{GE}\, dS\, \underline{n}_{GE} \cdot \hat{\underline{U}}_{HG} + \int_E^F p\, dS\, \underline{n}_{EF} \cdot \hat{\underline{U}}_{HG} \\ &+ \int_G^F p_{GF}\, dS\, \underline{n}_{GF} \cdot \hat{\underline{J}}_{SP} + \int_A^G p_D\, dS\, \underline{n}_{AG} \cdot \hat{\underline{U}}_{BL} + \int_C^F p\, dS\, \underline{n}_{CF} \cdot \hat{\underline{U}}_{BL} + \int_A^C p_{AC}\, dS\, \underline{n}_{AC} \cdot \hat{\underline{J}}_{BW} \\ &= Q_3 + (\rho - \rho_f) g S_{HG} \hat{U}_{HG} \sin(\gamma - \varphi_{NF}) + (\rho - \rho_f) g S_{BL} \hat{U}_{BL} \sin(\beta - \varphi_D) \\ &+ \Delta\lambda_D \rho g S_{AGPC} \hat{U}_{BL} \frac{\sin(\varphi_D)}{\cos\beta} + \Delta\lambda_B \rho g S_{GEP} \hat{U}_{HG} \frac{\sin(\varphi_{NF})}{\cos\gamma} + \Delta\lambda_B \rho g S_{GFP} \hat{J}_{SP} \frac{\sin(\varphi_{SP})}{\cos\theta} \\ &- \frac{1}{2} \Delta\lambda_B \rho g L_{AC}^2 \hat{U}_{BL} \cos(\beta - \varphi_D) + \frac{p(A) + p(C)}{2} L_{AC},\end{aligned} \tag{B.17}$$

in which the point P was introduced to distinguish the areas, S_{AGPC}, S_{GEP} and S_{GFP} accounting for the fluid over-pressure power above discontinuities AG, GE and GF. The hodograghs of the velocity jumps at the shear plane and back-wall are presented in Figure 2.8(3) and the law of the sines provides

$$\begin{aligned}\frac{\hat{U}_{BL}}{\sin(\theta - \varphi_{SP} + \gamma - \varphi_{NF})} &= \frac{\hat{J}_{SP}}{\sin(\varphi_D - \beta + \gamma - \varphi_{NF})} = \frac{\hat{U}_{HG}}{\sin(\theta - \varphi_{SP} - \varphi_D + \beta)} \\ \frac{1}{\cos(\varphi_{BW} + \varphi_D - \beta)} &= \frac{\hat{J}_{BW}}{\sin(\beta - \varphi_D)} = \frac{\hat{U}_{BL}}{\cos(\varphi_{BW})}\,.\end{aligned} \tag{B.18}$$

The maximum resisting power defined in (2.12) combined with the definition of the support function in (2.11) provides

$$\begin{aligned}\mathcal{P}'_{\text{mr}}(\hat{\underline{U}}) &= C_D L_{AG} \cos(\varphi_D) \hat{U}_{BL} + C_{NF} L_{GE} \cos(\varphi_{NF}) \hat{U}_{HG} + C_{SP} L_{GF} \cos(\varphi_{SP}) \hat{J}_{SP} \\ &+ C_{BW} L_{AC} \cos(\varphi_{BW}) \hat{J}_{BW}\,.\end{aligned} \tag{B.19}$$

The tectonic upper bound Q_{u3} for mechanism (3) is then obtained by combining (B.17) and (B.19) and reads

$$\begin{aligned}Q_{u3} &= C_{NF} L_{GE} \cos(\varphi_{NF}) \hat{U}_{HG} + C_{SP} L_{GF} \cos(\varphi_{SP}) \hat{J}_{SP} + C_D L_{AG} \cos(\varphi_D) \hat{U}_{BL} + C_{BW} L_{AC} \cos(\varphi_{BW}) \hat{J}_{BW} \\ &- (\rho - \rho_f) g S_{HG} \hat{U}_{HG} \sin(\gamma - \varphi_{NF}) - (\rho - \rho_f) g S_{BL} \hat{U}_{BL} \sin(\beta - \varphi_D) \\ &- \Delta\lambda_D \rho g S_{AGPC} \hat{U}_{BL} \frac{\sin(\varphi_D)}{\cos\beta} - \Delta\lambda_B \rho g S_{GEP} \hat{U}_{HG} \frac{\sin(\varphi_{NF})}{\cos\gamma} - \Delta\lambda_B \rho g S_{GFP} \hat{J}_{SP} \frac{\sin(\varphi_{SP})}{\cos\theta} \\ &+ \frac{1}{2} \Delta\lambda_B \rho g L_{AC}^2 \hat{U}_{BL} \cos(\beta - \varphi_D) - \frac{p(A) + p(C)}{2} L_{AC}\,.\end{aligned} \tag{B.20}$$

Appendix C

Electronic Supplement to Chapter 3

The objective is to complement the main paper with the expression for the upper bound forces used in Sections 3.3, 3.4 and 3.5. The properties of the virtual velocity field and a summary of the maximum strength theorem are also proposed as a preliminary.

1 Preliminary

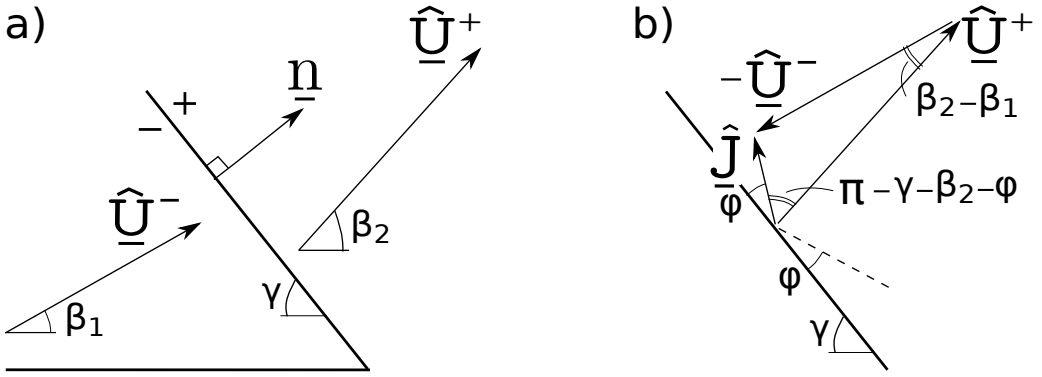


Fig. C.1: (a) The velocity jump $\underline{\hat{J}}$ over a discontinuity of normal $\underline{n}$, and (b) the associated hodograph.

The velocity dissipation (power) in this class of problems occurs over discontinuities within the structure or on its boundary (detachment, back wall). Consider such a velocity discontinuity dipping at γ and oriented by its normal $\underline{n}$, Figure C.1a. This oriented discontinuity sustains the velocity jump $\underline{\hat{J}}$ defined by the difference $\underline{\hat{U}}^+ - \underline{\hat{U}}^-$, between the velocities of the + and − regions. These velocities are virtual and are not necessary equal to the exact unknown velocity. Their dimension is immaterial to the problem. It has been shown theoretically in

Chen [1975] and *Salençon* [2002], despite different interpretations in these references, that the velocity jump is not parallel to the interface. Moreover, the absolute value of the angle between the velocity jump and this interface should be at least the friction angle φ, if slip is controlled by the classical Coulomb criterion. Most of the examples treated by the authors [*Maillot and Leroy*, 2006; *Cubas et al.*, 2008; *Pons and Leroy*, 2012; *Yuan et al.*, 2015] have pointed to the conclusion that this angle is optimum for the values of $\pm\varphi$, the sign depending on the overall sense of shear dictated by the global kinematics. This conclusion is applied to this contribution. Consequently, the velocities on the two sides and their jump are related by the hodograph presented in Figure C.1b for the example of a reverse sense of slip. The application of the law of sines to this triangular construction provides:

$$\frac{\hat{J}}{\sin(\beta_2 - \beta_1)} = \frac{\hat{U}^-}{\sin(\gamma + \beta_2 + \varphi)} = \frac{\hat{U}^+}{\sin(\gamma + \varphi + \beta_1)} \,. \tag{C.1}$$

These relations between the velocity norms are used in what follows to eliminate all velocity magnitudes except for the back-wall velocity which norm is set arbitrary to one.

Before proceeding to the presentation of the upper bound forces for various mechanisms, a summary of the maximum strength theorem [*Maillot and Leroy*, 2006], which is the kinematic approach of limit analysis is proposed. The starting point is the collapse mechanism corresponding to a mode of faulting in our structure, typically, the half-graben. The normal fault and the axial surface are velocity discontinuities and the other source of dissipation is the detachment or the initially blind fault considered in Sections 3.4 and 3.5 in the main paper.

The theorem of virtual power is applied to this collapse mechanism. This theorem is an integral expression of mechanical equilibrium. It states the equality between the external power and the internal power. The external power is composed of the power of the gravity and of the tectonic forces applied on the boundary on the velocity field. In this presentation, the fluid pressure is also introduced and it is proposed as part of the external forces (see *Pons and Leroy* [2012] or *Yuan et al.* [2015] for further discussion). The internal power is composed of the power of the forces acting on the various discontinuities described above. These forces are unknown and the internal power cannot be estimated although an upper bound force can be provided because of the convex shape of the strength domain in stress space (e.g. Coulomb strength limit). The reader will find further detailed information on this upper bound force calculation in *Salençon* [2002] and in *Maillot and Leroy* [2006], for an English version. It is this bounding which is at the core of the method and it leads to an upper bound to the tectonic force applied

on the boundary. There is an upper bound force for each collapse mechanism. The least upper bound is the closest to the exact, unknown tectonic force and the corresponding mechanism is considered to be dominant (active). This is how the dips of the normal fault and of the active axial surface are obtained for the half-graben collapse mechanism.

2 The upper bound forces for three mechanisms in Section 3.3

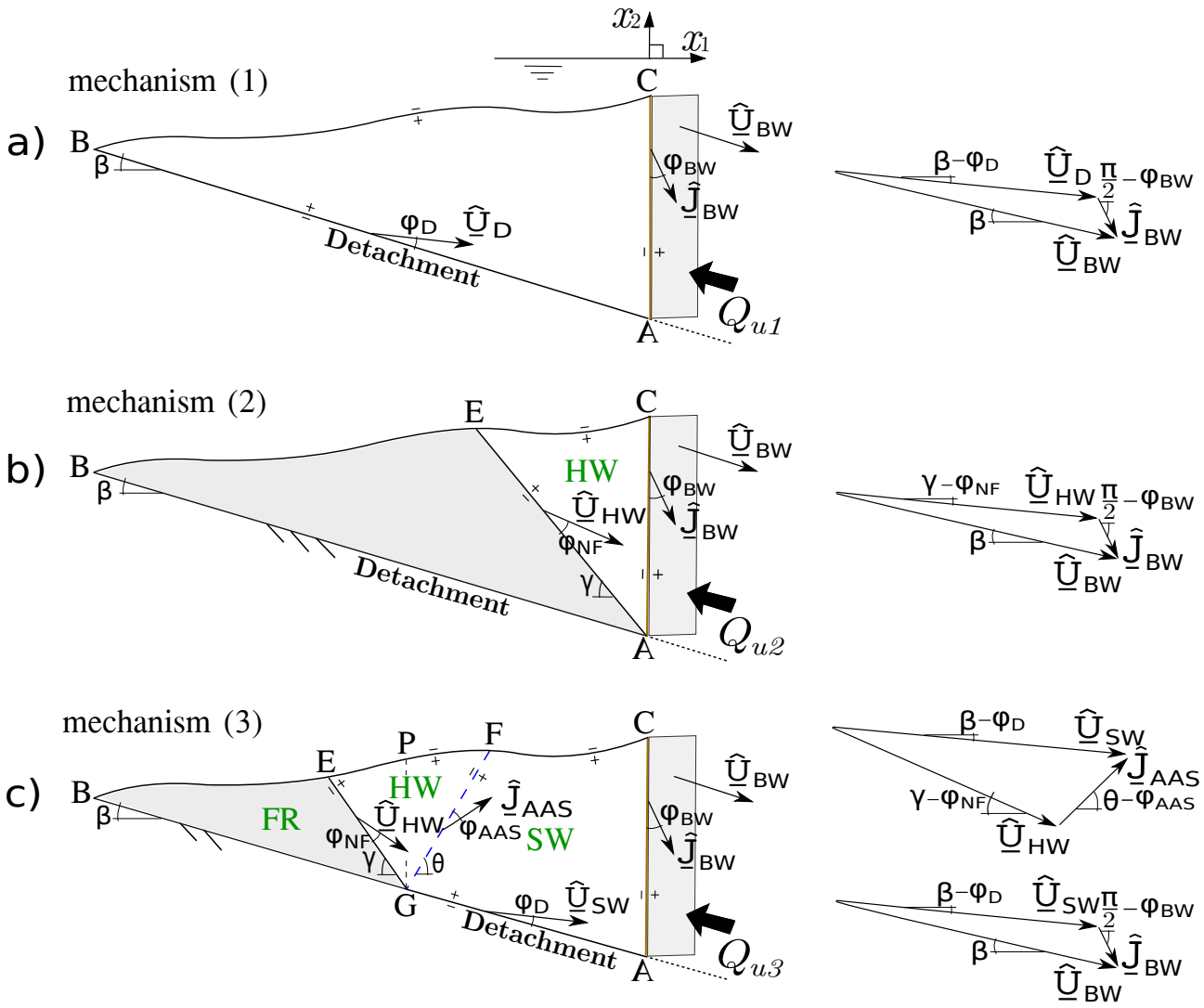


Fig. C.2: The virtual velocity field for the three mechanisms in Figure 1a. The hodographs of the velocities for the associated three mechanisms are presented on the right-hand side.

The three mechanisms have in common the back-wall velocity. It is assumed in what follows

to be parallel to the detachment such that the jump over AC is the vector $\underline{\hat{J}}_{BW}$ oriented at φ_{BW} from this interface. The back-wall velocity norm is set to one.

Notation is as follows: Coulomb properties are the friction angle φ and cohesion C. The subscripts for all material or geometric parameters (length L, surface S) identifies either a region (BW = Back Wall, HW = Hanging Wall, SW = Sliding Wall, FR = Frontal Region) or a line (XY between points X and Y, AAS for Active Axial Surface, NF for Normal Fault, D for Detachment) or a surface (ABC = all wedge). The wedge is composed of a bulk material (B) and is crossed by surfaces which could have either bulk or specific properties if inherited from a extension step to the other (for example softening on the normal fault). Fluid pressures are usually attached to material points ($p(A)$ for fluid pressure at point A). Fluid pressure ratio and the ratio difference to the hydrostatic pressure ratio are denoted λ and $\Delta\lambda$, respectively.

Mechanism (1): detachment fully activated

The first collapse mechanism corresponds to the rigid translation of the wedge on the fully activated detachment at the uniform velocity of norm $\hat{U}_D$, a vector oriented by the angle φ_D from the detachment, see Figure C.2a. The relations between the back-wall velocity and the jump over the back wall are obtained from the hodograph found in Figure C.2a and read:

$$\frac{1}{\cos(\varphi_{BW}+\beta-\varphi_D)} = \frac{\hat{J}_{BW}}{\sin(\varphi_D)} = \frac{\hat{U}_D}{\cos(\varphi_{BW}+\beta)}\,. \tag{C.2}$$

The application of the maximum strength theorem based on this velocity field provides the upper bound force Q_{u1}

$$\begin{aligned} Q_{u1} = {} & C_D L_{AB}\cos(\varphi_D)\hat{U}_D + C_{BW}L_{AC}\cos(\varphi_{BW})\hat{J}_{BW} - (\rho-\rho_f)gS_{ABC}\hat{U}_D\sin(\beta-\varphi_D) \\ & - \Delta\lambda_D\,\rho g S_{ABC}\hat{U}_D\frac{\sin(\varphi_D)}{\cos\beta} + \frac{1}{2}\Delta\lambda_{BW}\,\rho g L_{AC}^2\hat{U}_D\cos(\beta-\varphi_D) - \frac{p(A)+p(C)}{2}L_{AC}\cos\beta\,. \end{aligned} \tag{C.3}$$

Mechanism (2): a normal fault rooting at the back wall

The second collapse mechanism consists of a normal fault rooting at the base of the back wall and dipping at γ, Figure C.2b. There is no activation of the detachment. The hanging wall has the uniform velocity field of norm $\hat{U}_{HW}$, which is oriented by the angle φ_{NF} from the normal fault AE, Figure C.2(2). The hodograph of the velocity jump at the back wall is presented in

Figure C.2b and the law of the sines for the second failure mechanism provides

$$\frac{1}{\cos(\varphi_{BW}+\gamma-\varphi_{NF})}=\frac{\hat{J}_{BW}}{\sin(\beta-\gamma+\varphi_{NF})}=\frac{\hat{U}_{HW}}{\cos(\varphi_{BW}+\beta)}\,. \tag{C.4}$$

Application of limit analysis leads to the following expression for the upper bound force Q_{u2}

$$\begin{aligned}Q_{u2}=&\,C_{NF}L_{AE}\cos(\varphi_{NF})\hat{U}_{HW}+C_{BW}L_{AC}\cos(\varphi_{BW})\hat{J}_{BW}-(\rho-\rho_f)gS_{HW}\hat{U}_{HW}\sin(\gamma-\varphi_{NF})\\&-\Delta\lambda_{NF}\,\rho gS_{HW}\hat{U}_{HW}\frac{\sin(\varphi_{NF})}{\cos\gamma}+\frac{1}{2}\Delta\lambda_{BW}\,\rho gL_{AC}^2\hat{U}_{HW}\cos(\gamma-\varphi_{NF})-\frac{p(A)+p(C)}{2}L_{AC}\cos\beta\,.\end{aligned} \tag{C.5}$$

Note that the normal-fault fluid pressure ratio λ_{NF} takes the same value as the bulk ratio $\Delta\lambda_B$ for all calculations.

Mechanism (3): hanging wall bounded by a normal fault and an active axial surface

The third collapse mechanism consists of the normal fault GE dipping at γ and the active axial surface GF dipping at θ, Figure C.2c. They both root at point G on the detachment which is activated from point A to G. The geometry of this third collapse mechanism is thus described with three parameters: γ,θ and the distance L_{AG}. The velocities of the sliding wall and the hanging wall are uniform and denoted $\underline{\hat{U}}_{SW}$ and $\underline{\hat{U}}_{HW}$ and they are oriented by the angles φ_D and φ_{NF} from the corresponding interface, see Figure C.2c. There is also an additional velocity discontinuity corresponding to the active axial surface ($\underline{\hat{J}}_{AAS}=\underline{\hat{U}}_{SW}-\underline{\hat{U}}_{HW}$). The corresponding jump is oriented by the angle φ_{AAS} from the active axial surface. The hodographs of the velocity jumps at the active axial surface and at the back wall are presented in Figure C.2c and the law of the sines provides

$$\begin{aligned}\frac{\hat{U}_{SW}}{\sin(\theta-\varphi_{AAS}+\gamma-\varphi_{NF})}&=\frac{\hat{J}_{AAS}}{\sin(\varphi_D-\beta+\gamma-\varphi_{NF})}=\frac{\hat{U}_{HW}}{\sin(\theta-\varphi_{AAS}-\varphi_D+\beta)}\,,\\ \frac{1}{\cos(\varphi_{BW}+\beta-\varphi_D)}&=\frac{\hat{J}_{BW}}{\sin(\varphi_D)}=\frac{\hat{U}_{SW}}{\cos(\varphi_{BW}+\beta)}\,.\end{aligned} \tag{C.6}$$

The upper bound force reads

$$
\begin{aligned}
Q_{u3} = {} & C_{NF} L_{GE} \cos(\varphi_{NF}) \hat{U}_{HW} + C_{AAS} L_{GF} \cos(\varphi_{AAS}) \hat{J}_{AAS} + C_D L_{AG} \cos(\varphi_D) \hat{U}_{SW} + C_{BW} L_{AC} \cos(\varphi_{BW}) \hat{J}_{BW} \\
& - (\rho - \rho_f) g S_{HW} \hat{U}_{HW} \sin(\gamma - \varphi_{NF}) - (\rho - \rho_f) g S_{SW} \hat{U}_{SW} \sin(\beta - \varphi_D) \\
& - \Delta\lambda_D \, \rho g S_{AGPC} \hat{U}_{SW} \frac{\sin(\varphi_D)}{\cos\beta} - \Delta\lambda_{NF} \, \rho g S_{GEP} \hat{U}_{HW} \frac{\sin(\varphi_{NF})}{\cos\gamma} - \Delta\lambda_B \, \rho g S_{GFP} \hat{J}_{AAS} \frac{\sin(\varphi_{AAS})}{\cos\theta} \\
& + \frac{1}{2} \Delta\lambda_{BW} \, \rho g L_{AC}^2 \hat{U}_{SW} \cos(\beta - \varphi_D) - \frac{p(A) + p(C)}{2} L_{AC} \cos\beta \, .
\end{aligned}
\tag{C.7}
$$

Optimization

The upper bound force for mechanism 1 is constant for a given geometry. The upper bound forces for mechanisms 2 and 3 are dependent of the angle γ and of the three parameters θ, γ and L_{AG}, respectively. It is necessary for the last two mechanisms to minimize their upper bound forces in terms of these parameters. It is only then that the three upper bound forces can be compared and the dominant mechanism, associated to the least upper bound, be determined.

Consequence of the dimensional analysis

The structure of the definition of the three upper bound forces in equations (C.2) to (C.7) is as follows:

$$
\tilde{Q}_{ui} = a_i \tilde{C} + b_i + \Delta\lambda c_i + (\tilde{P}_A + \tilde{P}_C) d \, , \tag{C.8}
$$

for the three mechanisms ($i = 1, 2, 3$) after proper scaling by $\rho g L^2$ where L is the characteristic length of the structure (e.g. initial value of L_{AB}). Dimensionless stress-like quantities $(\tilde{C}, \tilde{P})$ are obtained by scaling with $\rho g L$. The parameters a_i, b_i, c_i, d in (C.8) are also dimensionless and, furthermore, independent of the structure characteristic length.

For cohesionless material ($\tilde{C} = 0$) and dry conditions ($\tilde{P} = 0$), equation (C.8) shows that the upper bound force is independent of its characteristic size. Consequently, the final shape of the structure is independent of this characteristic length. For cohesionless but saturated media, the conclusion is the same despite the presence of the fourth term in the right-hand side of (C.8). This is simply due to the fact that the fourth term is the same for the three collapse mechanisms.

Comparing the upper bound forces

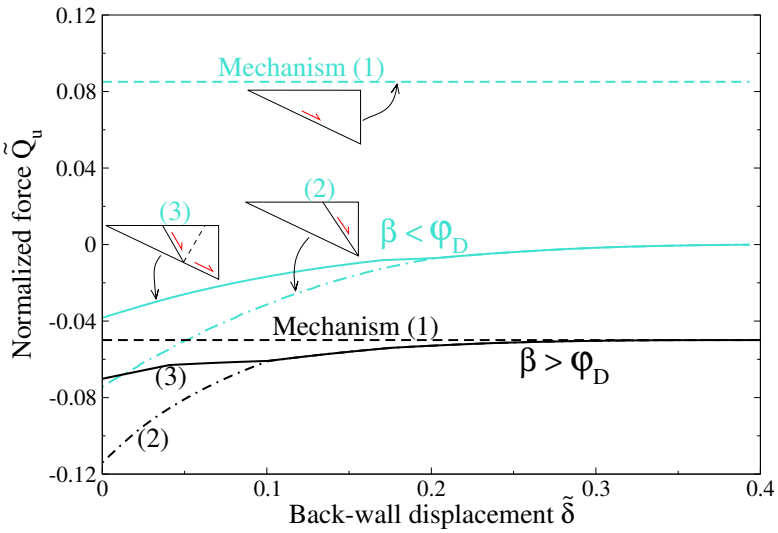


Fig. C.3: The normalized upper bound forces $\tilde{Q}_u = Q_u/(\rho g S_{ABC})$ versus the back-wall displacement for $\beta > \varphi_D$ (black curves) and $\beta < \varphi_D$ (green curves) in the dry case. Curves are dashed for mechanism 1, dot-dashed for 2 and solid for 3. Back-wall friction: $\varphi_{BW} = 30°$.

We examine the upper bound forces, normalised by the weight of the wedge $\rho g S_{ABC}$ (Figure C.3). This comparison is essential for the main paper since it provides the least upper bound associated with the active collapse mechanism at every increment of extension.

Negative upper bound values correspond to a compressive force at the back wall. Upper bound forces of mechanisms 2 and 3 vary with $\tilde{\delta}$ because they depend on the shape of the wedge surface, whereas mechanism 1, involving no internal deformation, depends only on the weight of the wedge. Its upper bound force is therefore constant. Consider first the case $\beta > \varphi_D$ (black curve in Figure C.3). Again, as seen from the cross-section and the G-gram, the least upper bound corresponds to mechanism 2 up to $\tilde{\delta} = 0.1$, then mechanism 3 becomes as optimal as mechanism 2, and finally, mechanism 1 produces the least upper bound for $\tilde{\delta} \geq 0.37$ (Figure C.3). At this stage, the wedge is critical and the three mechanisms correspond to the same upper bound value up to numerical accuracy. The wedge can be considered as critical in the sense of the extensional CCW theory [*Xiao et al.*, 1991; *Yuan et al.*, 2015], i.e., its taper is at the critical value, and all failure mechanisms are as likely to occur. The case $\beta < \varphi_D$ (Figure C.3, green curves) presents essentially the same features, with mechanisms 2 and 3 simultaneously active for $\tilde{\delta} \geq 0.2$, and upper bound magnitudes are decreasing towards zero,

because there is less and less material in contact with the back wall. Mechanism 1 has a positive upper bound meaning that its activation requires to pull on the back wall.

3 Upper bound for a normal fault piercing the cover, Sections 3.4 and 3.5

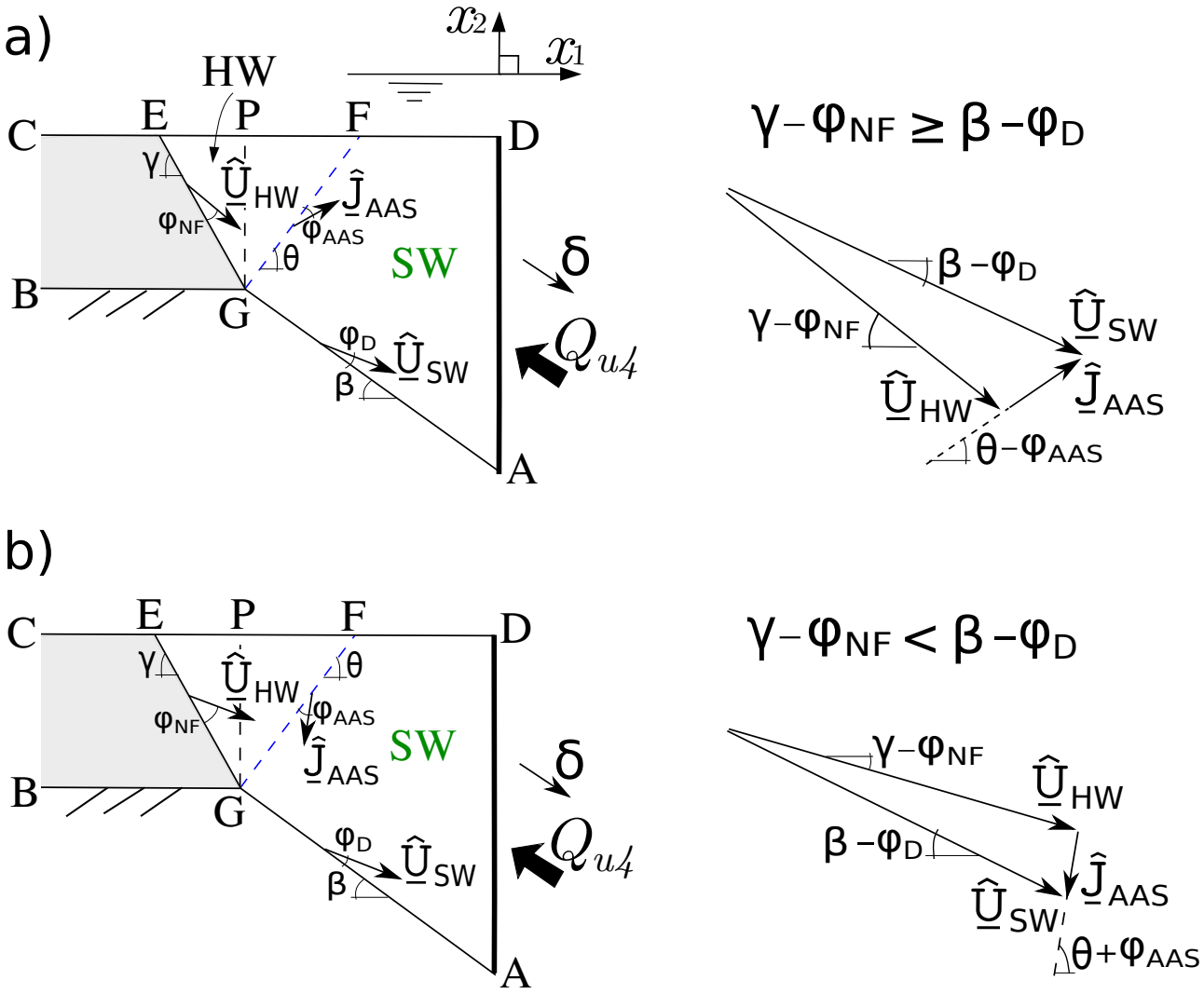


Fig. C.4: The virtual velocity field and associated velocity hodograph for the collapse mechanism 4.

The collapse mechanism 4 is proposed and composed of two discontinuities always rooting at point G, Figure 2 and Figure C.4. The normal fault GE dips at γ and the active axial surface GF at θ, Figure C.4. The velocities of sliding wall and hanging wall are uniform oriented by

the angles φ_D and φ_{NF} from AG and GE, respectively. The velocity discontinuity of active axial surface ($\underline{\hat{J}}_{AAS} = \underline{\hat{U}}_{SW} - \underline{\hat{U}}_{HW}$) is oriented by the angles φ_{AAS} from this surface. There are two possibilities for the sense of slip on the active axial surface, Figure C.4. The velocities are related by

$$\begin{aligned}
&\text{if} \quad \gamma - \varphi_{NF} \geq \beta - \varphi_D \quad \text{(case a)} : \\
&\frac{1}{\sin(\gamma - \varphi_{NF} + \theta - \varphi_{AAS})} = \frac{\hat{J}_{AAS}}{\sin(\gamma - \varphi_{NF} - \beta + \varphi_D)} = \frac{\hat{U}_{HW}}{\sin(\beta - \varphi_D + \theta - \varphi_{AAS})} \,,
\end{aligned} \tag{C.9}$$

$$\begin{aligned}
&\text{if} \quad \gamma - \varphi_{NF} < \beta - \varphi_D \quad \text{(case b)} : \\
&\frac{1}{\sin(\gamma - \varphi_{NF} + \theta + \varphi_{AAS})} = \frac{\hat{J}_{AAS}}{\sin(\beta - \varphi_D - \gamma + \varphi_{NF})} = \frac{\hat{U}_{HW}}{\sin(\beta - \varphi_D + \theta + \varphi_{AAS})} \,,
\end{aligned}$$

and deduced from the hodograph in Figure C.4. Note that only case (a) was found during the calculations. The upper bound force is

$$\begin{aligned}
Q_{u4} = \frac{1}{\cos(\varphi_D)} \Big[& C_D L_{AG} \cos(\varphi_D) + C_{NF} L_{GE} \cos(\varphi_{NF}) \hat{U}_{HW} + C_{AAS} L_{GF} \cos(\varphi_{AAS}) \hat{J}_{AAS} \\
& - (\rho - \rho_f) g S_{HW} \hat{U}_{HW} \sin(\gamma - \varphi_{NF}) - (\rho - \rho_f) g S_{SW} \sin(\beta - \varphi_D) \\
& - \Delta\lambda_D \, \rho g S_{AGPD} \frac{\sin(\varphi_D)}{\cos\beta} - \Delta\lambda_B \, \rho g S_{GEP} \hat{U}_{HW} \frac{\sin(\varphi_{NF})}{\cos\gamma} - \Delta\lambda_B \, \rho g S_{GFP} \hat{J}_{AAS} \frac{\sin(\varphi_{AAS})}{\cos\theta} \Big] \,.
\end{aligned} \tag{C.10}$$

Two parameters (θ, γ) are optimized to minimize the bound for mechanism 4.

4 Kinematics of hanging-wall deformation

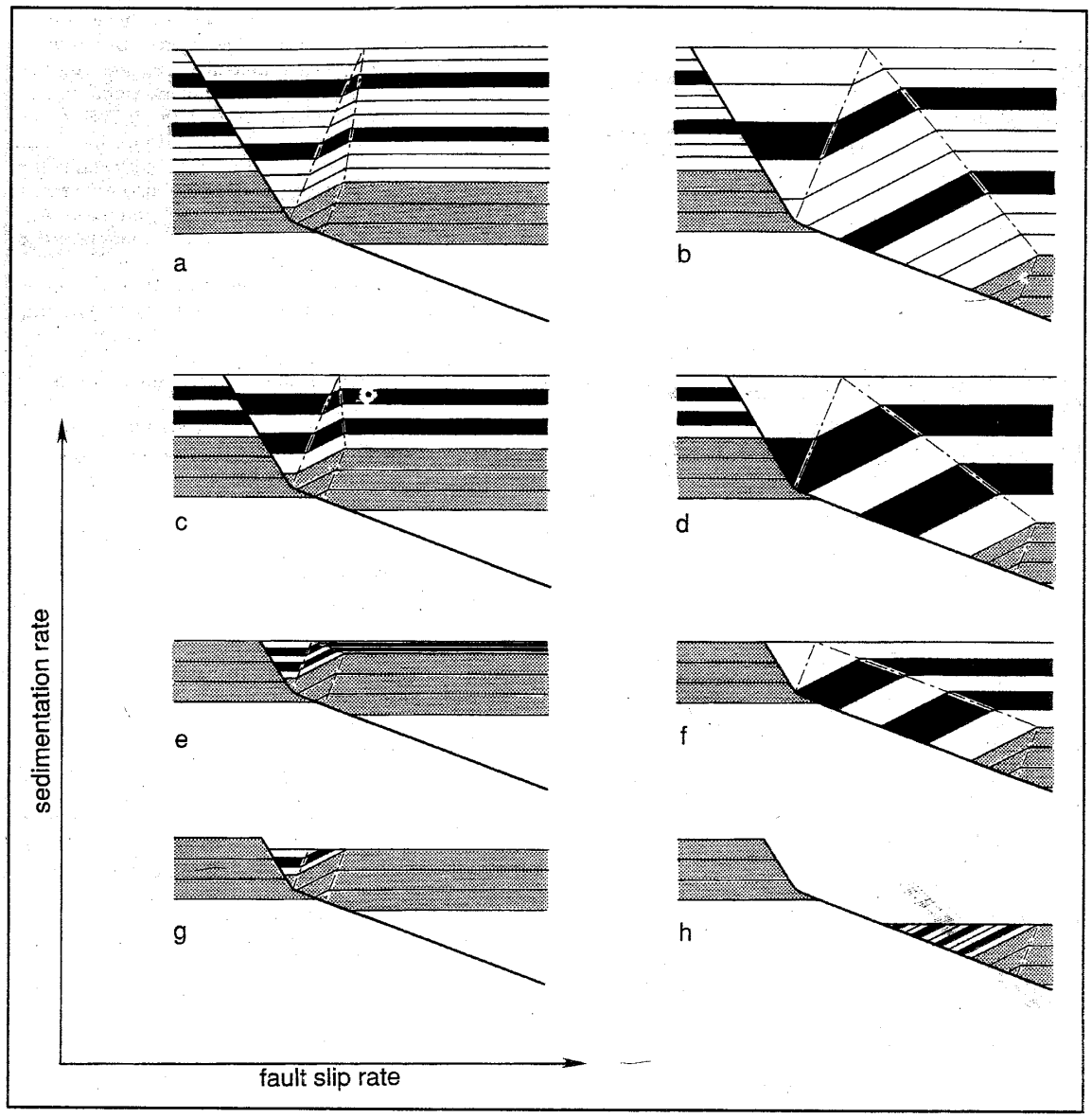


Fig. C.5: The kinematic models of hanging-wall deformation for a constant fault shape with varying sedimentation and fault slip [*Xiao and Suppe*, 1992]. This kinematics is compared with our Figure 10 in Section 3.4.3.

5 Cross-sections of Jeanne d'Arc Basin, Section 3.5

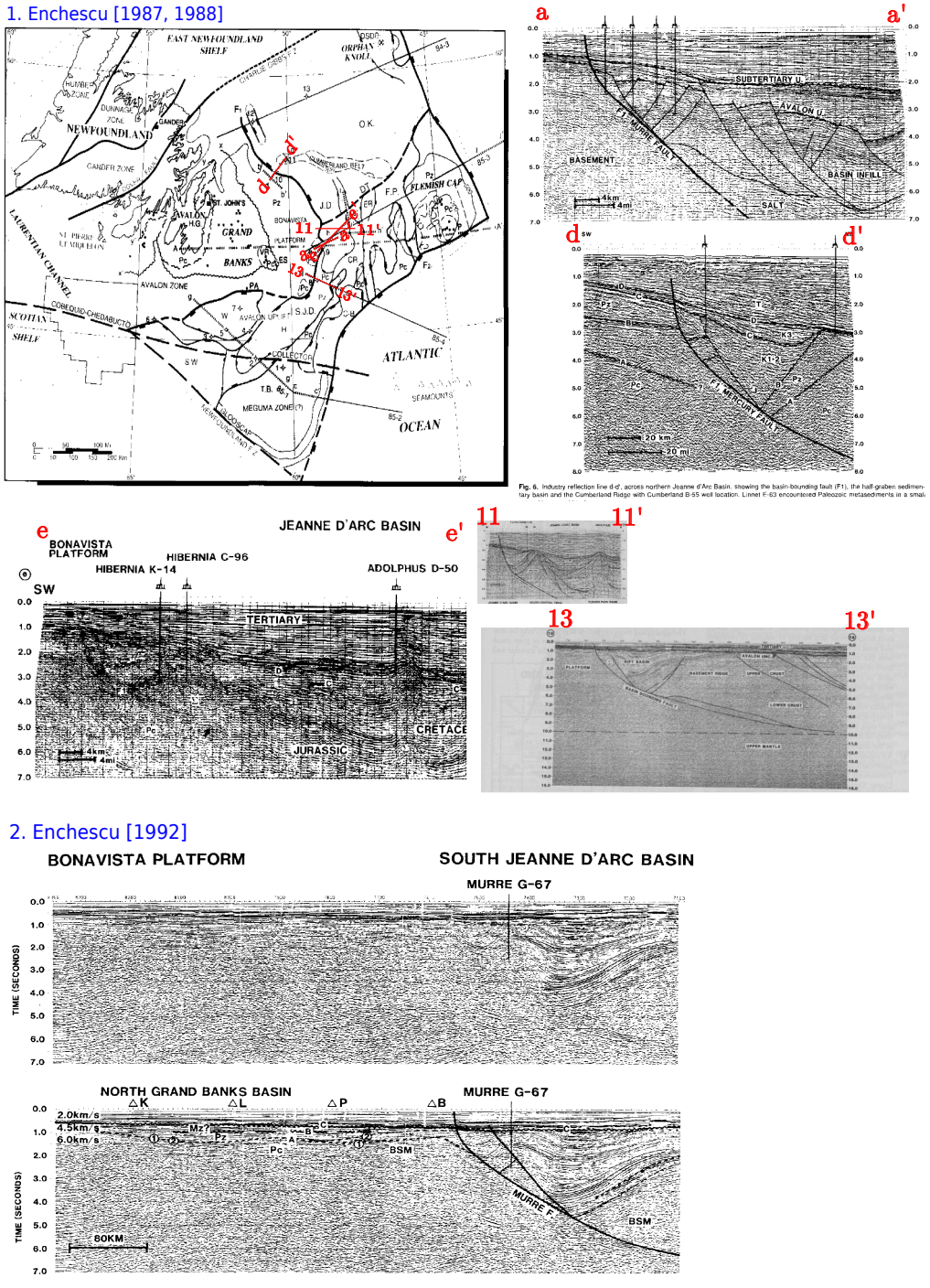


Fig. C.6: Several cross-sections in Jeanne d'Arc Basin [*Enachescu*, 1987; 1988; 1992]. The failure cross-sections across 200 km have almost the same structure, typically the presence of single block in the hanging wall.

6 Some results of inverse analysis for Section 3.5

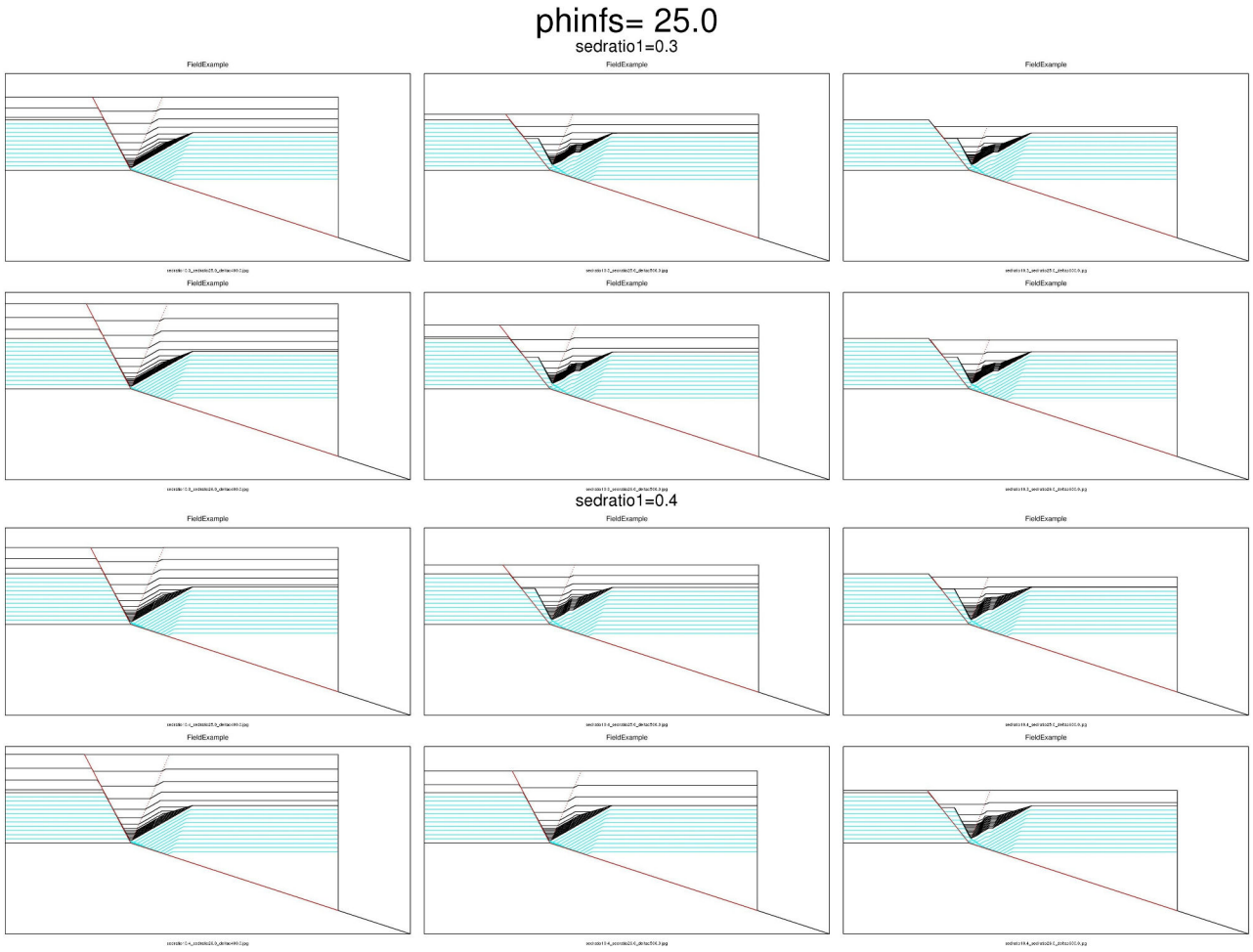


Fig. C.7: In this image, fault friction $\varphi_{NFS} = 25°$. $r_{S1} = 0.3, 0.4$ are the first and the last two rows, respectively. In each r_{S1} part, $r_{S2} = 5.0, 6.0$ correspond respectively to the first and the second row, and the results of $\delta_c = 6.5, 8.1, 9.8$ km are shown in the first, the second and the third column, respectively.

Appendix D

Appendix for Chapter 4

1 General solution of the kinematic approach of LA

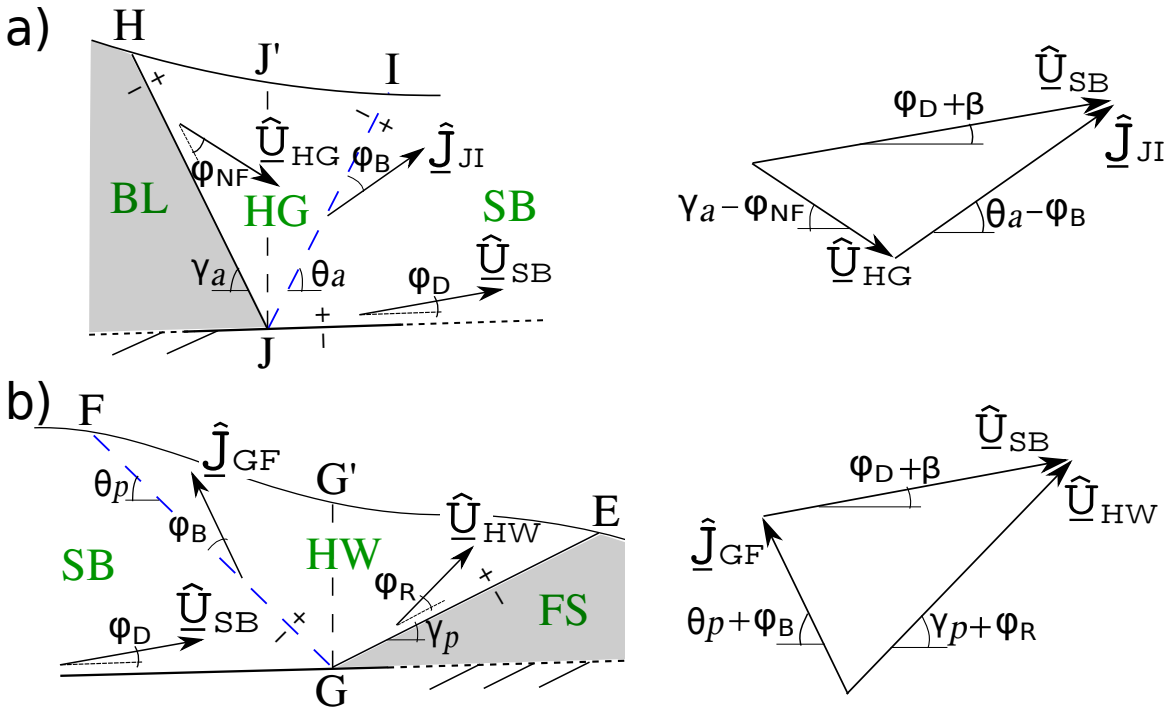


Fig. D.1: In (a) and (b), the virtual velocities for the collapse mechanism of Figure 4.10 and the hodographs of the velocity jumps across the axial surfaces *JI* and *GF*.

The objective of this appendix is to calculate the effective external power in (4.5) and the maximum resisting power in (4.6), and then generalize to the inclined layer and wedge prototype.

1.1 General prototype

The velocity field in equation (4.5) is uniform over three regions of our general prototype in Figure 4.1. The velocity of the sliding block is inclined by the angle φ_D from the detachment and has for norm $\hat{U}_{SB}$, Figure D.1. The half-graben velocity is inclined by the angle φ_{NF} from the normal fault JH and has the norm $\hat{U}_{HG}$, and the hanging-wall velocity is inclined by the angle φ_R from the thrust ramp GE and has the norm $\hat{U}_{HW}$. The velocity jumps at the axial surfaces JI and GF correspond to the difference $(\hat{\underline{U}}_{SB} - \hat{\underline{U}}_{HG})$ and $(\hat{\underline{U}}_{HW} - \hat{\underline{U}}_{SB})$, a vector of norm $\hat{J}_{JI}$ and $\hat{J}_{GF}$ oriented by the angle φ_B from the corresponding axial surface in Figure D.1a and D.1b, respectively. The hodographs of these two velocity jumps provide that information by application of the law of the sines. The general expressions are found in (4.9).

The effective external power $\mathcal{P}'_{\text{ext}}(\hat{\underline{U}})$ in (4.5) for this velocity field is

$$\begin{aligned}\mathcal{P}'_{\text{ext}}(\hat{\underline{U}}) = \rho \underline{g} \cdot (S_{HG}\hat{\underline{U}}_{HG} + S_{SB}\hat{\underline{U}}_{SB} + S_{HW}\hat{\underline{U}}_{HW}) \\ + \int_J^H p_{JH}\, dS\, \underline{n}_{JH} \cdot \hat{\underline{U}}_{HG} + \int_J^I p_{JI}\, dS\, \underline{n}_{JI} \cdot \hat{\underline{J}}_{JI} + \int_G^F p_{GF}\, dS\, \underline{n}_{GF} \cdot \hat{\underline{J}}_{GF} \\ + \int_G^E p_{GE}\, dS\, \underline{n}_{GE} \cdot \hat{\underline{U}}_{HW} + \int_J^G p_D\, dS\, \underline{n}_{JG} \cdot \hat{\underline{U}}_{SB} \\ + \int_H^I p_f\, dS\, \underline{n}_{HI} \cdot \hat{\underline{U}}_{HG} + \int_E^F p_f\, dS\, \underline{n}_{EF} \cdot \hat{\underline{U}}_{HW} + \int_F^I p_f\, dS\, \underline{n}_{FI} \cdot \hat{\underline{U}}_{SB}\,,\end{aligned} \tag{D.1}$$

in which, S_{HG}, S_{SB} and S_{HW} are the surface sizes of half-graben, sliding block and hanging wall, respectively. The first term in the right-hand side of (D.1) corresponds to the power of the velocity field on gravity in regions of half-graben, sliding block and hanging wall. The next five integrals are the contributions of the power of the velocity jumps on the fluid pressure field in (D.1) within the normal fault JH, the upslope axial surface JI, the thrust ramp GE, the downslope axial surface GF and the detachment JG, respectively. The last three terms result from the power of the fluid pressure on the topography. p_{XY} denotes the fluid pressure between point X and Y. $\underline{n}_{XY}$ indicates the norm vector of surface XY.

Expression (D.1) is now simplified by application of the following weak form of Archimedes' theorem as the Electronic Supplement in *Yuan et al.* [2015]: the power of the velocity field on the hydrostatic part of the pressure is equal to the opposite of the power of the same velocity field on the vertical forces resulting from the weight of the displaced regions, if assumed composed of a density ρ_f. The effective external power of (D.1) is expressed in terms of the departure of

the pressure from the hydrostatic condition as

$$\begin{aligned}\mathcal{P}'_{\text{ext}}(\hat{\underline{U}}) &= (\rho-\rho_f)\underline{g}\cdot\left(S_{HG}\hat{\underline{U}}_{HG}+S_{SB}\hat{\underline{U}}_{SB}+S_{HW}\hat{\underline{U}}_{HW}\right)\\ &+\int_J^H \Delta p_{JH}\,dS\,\underline{n}_{JH}\cdot\hat{\underline{U}}_{HG}+\int_J^I \Delta p_{JI}\,dS\,\underline{n}_{JI}\cdot\hat{\underline{J}}_{JI}+\int_G^F \Delta p_{GF}\,dS\,\underline{n}_{GF}\cdot\hat{\underline{J}}_{GF}\\ &+\int_G^E \Delta p_{GE}\,dS\,\underline{n}_{GE}\cdot\hat{\underline{U}}_{HW}+\int_J^G \Delta p_D\,dS\,\underline{n}_{JG}\cdot\hat{\underline{U}}_{SB}\,.\end{aligned} \tag{D.2}$$

The points J' and G' in Figure D.1a and D.1b are introduced on the topography to have the same x_1-coordinate with points J and G, respectively. The expression (D.2) combined with the fluid overpressure definition in (4.7) leads to an explicit form as

$$\begin{aligned}\mathcal{P}'_{\text{ext}}(\hat{\underline{U}}) &= (\rho-\rho_f)g\big[S_{HG}\hat{U}_{HG}\sin(\gamma_a-\varphi_{NF})-S_{SB}\hat{U}_{SB}\sin(\beta+\varphi_D)-S_{HW}\hat{U}_{HW}\sin(\gamma_p+\varphi_R)\big]\\ &+\rho g\Big[\Delta\lambda_{NF}\,S_{JJ'H}\hat{U}_{HG}\frac{\sin(\varphi_{NF})}{\cos(\gamma_a)}+\Delta\lambda_B\,S_{JJ'I}\hat{J}_{JI}\frac{\sin(\varphi_B)}{\cos(\theta_a)}+\Delta\lambda_B\,S_{GG'F}\hat{J}_{GF}\frac{\sin(\varphi_B)}{\cos(\theta_p)}\\ &+\Delta\lambda_R\,S_{GG'E}\hat{U}_{HW}\frac{\sin(\varphi_R)}{\cos(\gamma_p)}\Big]+\Delta\lambda_D\,\rho g S_{JJ'G'G}\hat{U}_{SB}\frac{\sin(\varphi_D)}{\cos\beta}\,,\end{aligned} \tag{D.3}$$

in which, $S_{JJ'H}$, $S_{JJ'I}$, $S_{GG'F}$, $S_{GG'E}$ and $S_{JJ'G'G}$ are the surface sizes of porous media above the segment JH, JI, GF, GE and JG, respectively (Figure D.1a and D.1b). The friction angles and overpressure ratios on the normal fault JH and on the thrust ramp GE are set to have the same values as the bulk materials for the stability analysis in this contribution.

The maximum resisting power in (4.6) for this velocity field is

$$\begin{aligned}\mathcal{P}'_{\text{mr}}(\hat{\underline{U}}) &= C_D L_{JG}\cos(\varphi_D)\hat{U}_{SB}+C_{NF}L_{JH}\cos(\varphi_{NF})\hat{U}_{HG}+C_B L_{JI}\cos(\varphi_B)\hat{J}_{JI}\\ &+C_R L_{GE}\cos(\varphi_R)\hat{U}_{HW}+C_B L_{GF}\cos(\varphi_B)\hat{J}_{GF}\,,\end{aligned} \tag{D.4}$$

corresponding to the sum of the contributions on the discontinuities JG, JH, JI, GE, GF, respectively.

1.2 Inclined layer

For the inclined layer of a topographic surface parallel to detachment in Figure D.2a, the length sizes used in (D.4) for the calculation of maximum resisting power are

$$L_{JH}=h/\sin(\gamma_a+\beta)\,,\quad L_{JI}=h/\sin(\theta_a-\beta)\,,\quad L_{GE}=h/\sin(\gamma_p-\beta)\,,\quad L_{GF}=h/\sin(\theta_p+\beta)\,. \tag{D.5}$$

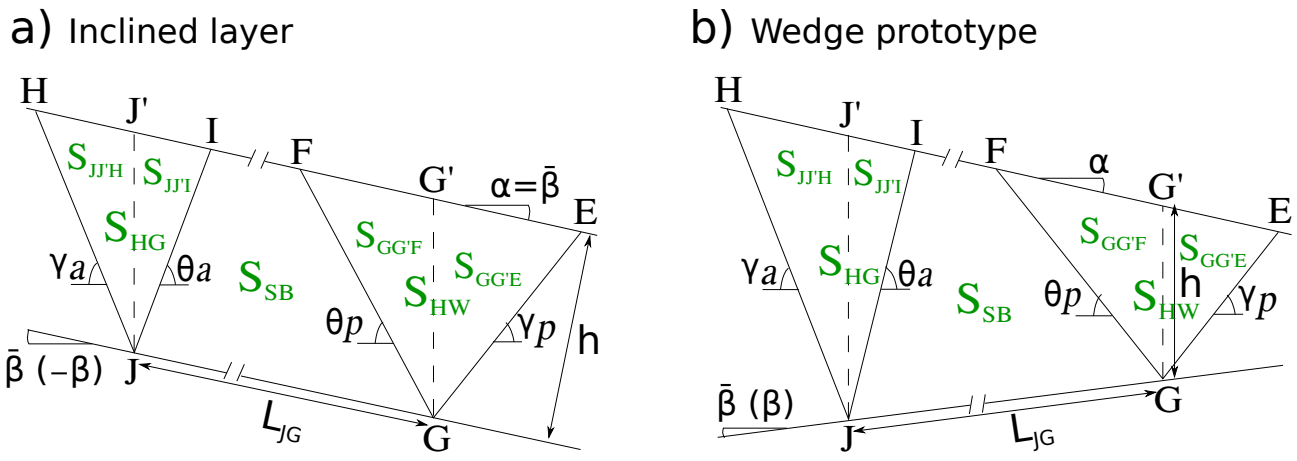


Fig. D.2: Geometries of (a) Inclined layer and (b) wedge prototype used to calculate the block sizes.

The surface sizes used in (D.3), Figure D.2a, are

$$S_{HG} = h^2\big[\cot(\gamma_a+\beta)+\cot(\theta_a-\beta)\big]/2\,, \quad S_{SB} = L_{JG}\,h - h^2\big[\cot(\theta_a-\beta)+\cot(\theta_p+\beta)\big]/2\,,$$
$$S_{HW} = h^2\big[\cot(\theta_p+\beta)+\cot(\gamma_p-\beta)\big]/2\,, \quad S_{JJ'H} = \frac{h^2\cos(\gamma_a)}{2\,\sin(\gamma_a+\beta)\cos\beta}\,, \quad S_{JJ'I} = \frac{h^2\cos(\theta_a)}{2\,\sin(\theta_a-\beta)\cos\beta}\,,$$
$$S_{GG'E} = \frac{h^2\cos(\gamma_p)}{2\,\sin(\gamma_p-\beta)\cos\beta}\,, \quad S_{GG'F} = \frac{h^2\cos(\theta_p)}{2\,\sin(\theta_p+\beta)\cos\beta}\,, \quad S_{JJ'G'G} = L_{JG}\,h\,. \tag{D.6}$$

Combining the (D.3), (D.6), we will have the explicit effective external power in (4.8) normalized by $\rho g h^2 \hat{U}_{BS}$ in the main text.

1.3 Triangular Wedge

For the wedge prototype used in Section 4.4, the reference length is $L_{GG'} = h$, Figure D.2b. The length sizes used in (D.4) for the maximum resisting power are

$$L_{JH} = \frac{L_{JJ'}\cos\alpha}{\sin(\gamma_a-\alpha)}\,, \quad L_{JI} = \frac{L_{JJ'}\cos\alpha}{\sin(\theta_a+\alpha)}\,, \quad L_{GE} = \frac{h\cos\alpha}{\sin(\gamma_p+\alpha)}\,, \quad L_{GF} = \frac{h\cos\alpha}{\sin(\theta_p-\alpha)}\,,$$
$$\text{with} \quad L_{JJ'} = L_{JG}\sin\beta + h + L_{JG}\cos\beta\,\tan\alpha\,, \tag{D.7}$$

and the surface sizes used in (D.3) correspond to

$$
\begin{aligned}
&S_{JJ'H} = \frac{L_{JJ'}^2 \cos(\gamma_a)\cos\alpha}{2\,\sin(\gamma_a-\alpha)}\,, \quad S_{JJ'I} = \frac{L_{JJ'}^2 \cos(\theta_a)\cos\alpha}{2\,\sin(\theta_a+\alpha)}\,, \quad S_{GG'E} = \frac{h^2 \cos(\gamma_p)\cos\alpha}{2\,\sin(\gamma_p+\alpha)}\,,\\
&S_{GG'F} = \frac{h^2 \cos(\theta_p)\cos\alpha}{2\,\sin(\theta_p-\alpha)}\,, \quad S_{JJ'G'G} = \frac{(h+L_{JJ'})L_{JG}\cos\beta}{2}\,,\\
&S_{HG} = S_{JJ'H} + S_{JJ'I}\,, \quad S_{HW} = S_{GG'E} + S_{GG'F}\,, \quad S_{SB} = S_{JJ'G'G} - S_{JJ'I} - S_{GG'F}\,.
\end{aligned}
\tag{D.8}
$$

We obtain the effective external power by using (D.3), (D.8) and velocity hodographs in (4.9) for the stability analysis in Section 4.4.

Appendix E

Electronic Supplement to Chapter 4

1 Different fluid pressure parametrizations

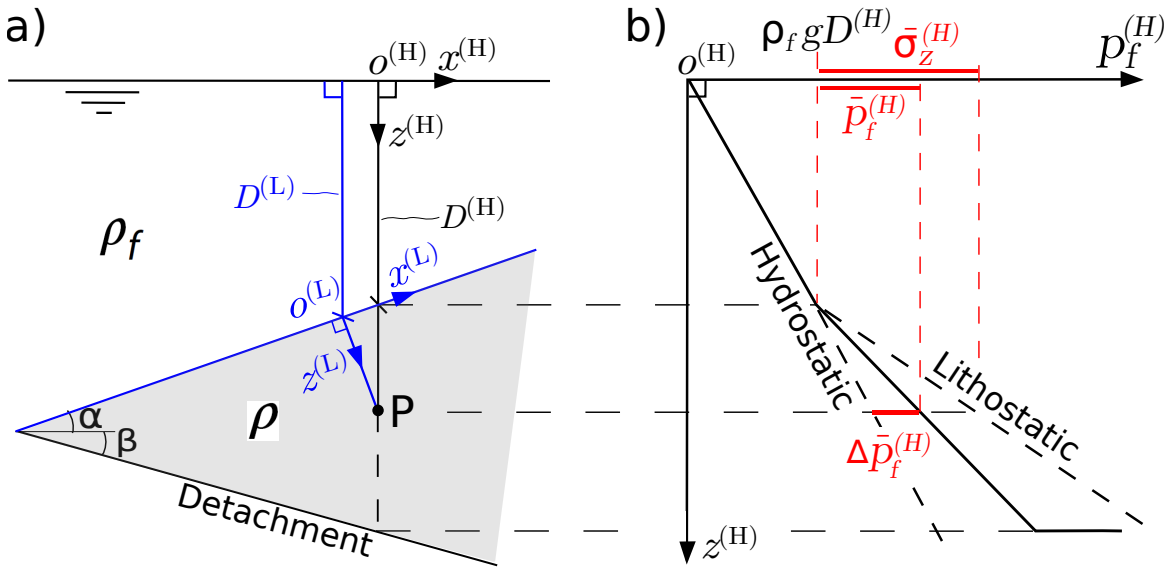


Fig. E.1: (a) The two definitions of fluid pressure ratio in different coordinates, the black segment was proposed by *Hubbert and Rubey* [1959] and blue segment was considered by *Lacoste et al.* [2012]. (b) The illustration of the definition for fluid pressure ratio $\lambda^{(H)}$ and overpressure ratio $\Delta\lambda^{(H)}$ in *Hubbert and Rubey* [1959].

This appendix is to build the relations between three different definitions of fluid pressure ratios. Accounting for these differences is crucial for the comparisons to analytical solutions in section 4.3. In this article we use the parametrization of *Hubbert and Rubey* [1959], identified with a superscript $^{(H)}$. In the main text however, we have removed the superscript to keep

with light notations. This parametrization relies on a vertical path from the sea level to the point of interest. This path corresponds to the black line in Figure E.1a and the associated fluid pressure is illustrated in Figure E.1b [*Pons and Leroy*, 2012] leading to

$$\lambda^{(H)} = -\frac{p_f^{(H)} - \rho_f g D^{(H)}}{\sigma_z^{(H)} + \rho_f g D^{(H)}} = \frac{\bar{p}_f^{(H)}}{\bar{\sigma}_z^{(H)}} \quad \text{with} \quad \bar{\sigma}_z^{(H)} = \rho g (z^{(H)} - D^{(H)}) \,. \tag{E.1}$$

From the illustration in Figure E.1b, the value of $\lambda^{(H)}$ is between ρ_f/ρ and 1, and the fluid overpressure ratio $\Delta\lambda^{(H)} = \Delta\bar{p}_f^{(H)}/\bar{\sigma}_z^{(H)}$ is in the range of $[0, 1-\rho_f/\rho]$. The fluid pressure jumps when it pass from the bulk materials to the detachment. Therefore, $\lambda_B^{(H)}$ and $\lambda_D^{(H)}$ are used to represent the fluid pressure ratio in bulk materials and on the detachment, respectively.

The path referred by blue line was defined by *Lacoste et al.* [2012] leading to a different fluid pressure ratio in (4.13). The equality of $p_f^{(H)} = p_f^{(L)}$ at the point P from equations (E.1) and (4.13) leads to the relation between the above two ratios as:

$$\lambda^{(L)} = \frac{\lambda^{(H)} - \lambda_{hydro}}{(1 - \lambda_{hydro}) \cos^2 \alpha} \quad \text{with} \quad \lambda_{hydro} = \rho_f/\rho \,. \tag{E.2}$$

For the sandbox experiments, the fluid pressure is usually applied by using vertical and upward air flows through the sand pack with a thickness h [*Mourgues and Cobbold*, 2003; 2006b; *Mourgues et al.*, 2014]. The pressure ratio in sandbox experiments [*Mourgues and Cobbold*, 2003] is defined as

$$\lambda^{(M)} = \frac{p_d - p_{at}}{\rho_s g h \cos \alpha} \tag{E.3}$$

in which, p_d and p_{at} are the air pressures on the detachment and atmospheric pressure on surface of sand pack, respectively, ρ_s is the density of sand. From (4.13) to (E.3), the value of ρ and ρ_f are replaced by ρ_s and 0, respectively, p_{at} is subtracted from $p_f^{(L)} - \rho_f g (D^{(L)} + z^{(L)} \cos \alpha)$ in (4.13) for the sandbox scale and $z^{(L)}$ equals to h at the detachment. Thus, the value of $\lambda^{(M)}$ equals to $\lambda^{(L)}$ and is in the range of $[0, 1]$.

2 Analytical collapse length and fault dips for an inclined layer

The objective of this appendix is to provide the analytical collapse length [*Lacoste et al.*, 2012] and fault dips [*Lehner*, 1986] of an inclined layer that are used for the comparisons in Section 4.3. Their geometrical and physical parameters are denoted to be consistent in the main text for our comparisons.

The link between the extensive and compressive domains of inclined layer was considered by *Lacoste et al.* [2012] with friction on the detachment of finite length. The force driving sliding is the weight of the layer, whereas the resisting forces are the friction at the layer detachment and the compressive domain resistance to shortening. The use of a global equilibrium condition in the inclined layer to obtain the collapse length for a given detachment dip $\bar{\beta}$, the equation (a11) in *Lacoste et al.* [2012],

$$\tilde{L}_{JGc} = \frac{2\sqrt{\tan^2(\varphi_B)\,(1-\lambda_B^{(L)})^2 - \tan^2\bar{\beta}}}{\left[\tan\bar{\beta} - \tan(\varphi_D)\,(1-\lambda_D^{(L)})\right]\cos(\varphi_B)}\,, \tag{E.4}$$

where $\lambda_B^{(L)}, \lambda_D^{(L)}$ and φ_B, φ_D are fluid pressure ratios (4.13) and friction angles in the bulk materials and on the detachment, respectively.

Our limit analysis approach consider the interaction of extensive and compressive domains, and the transitional region between the two domains. Thus the failure geometries are also essential for the validation of our mechanical approach, whereas the geometries are lack of prediction from *Lacoste et al.* [2012]. The theoretical dips of faults are obtained from the active and passive circles by the method of Mohr construction [*Lehner*, 1986], the optimum fault dips lead to

$$\begin{aligned}
\gamma_a &= \frac{\pi}{4} + \frac{\varphi_B}{2} - \frac{1}{2}\arcsin\left(\frac{\sin(\alpha')}{\sin(\varphi_B)}\right) - \frac{1}{2}\alpha' + \alpha \\
\theta_a &= \frac{\pi}{4} + \frac{\varphi_B}{2} + \frac{1}{2}\arcsin\left(\frac{\sin(\alpha')}{\sin(\varphi_B)}\right) + \frac{1}{2}\alpha' - \alpha \\
\gamma_c &= \frac{\pi}{4} - \frac{\varphi_B}{2} - \frac{1}{2}\arcsin\left(\frac{\sin(\alpha')}{\sin(\varphi_B)}\right) + \frac{1}{2}\alpha' - \alpha \\
\theta_p &= \frac{\pi}{4} - \frac{\varphi_B}{2} + \frac{1}{2}\arcsin\left(\frac{\sin(\alpha')}{\sin(\varphi_B)}\right) - \frac{1}{2}\alpha' + \alpha\,,
\end{aligned} \tag{E.5}$$

in which, γ_a, θ_a are active fault dips and γ_c, θ_p are passive fault dips, α' is a modified slope angle defined by

$$\alpha' = \arctan\left[\tan(\alpha)/(1-\lambda_B^{(L)})\right] \leq \varphi_B\,, \tag{E.6}$$

for the pertinent of (E.5) in arcsin formula. Note that the analytical collapse length (E.4) and fault dips (E.5) require to have the same definition of fluid pressure ratio $\lambda^{(H)}$ as in the main text for comparisons. The fluid pressure ratio from the above constraint leads to a critical value $\lambda_{Bc}^{(L)} = 1 - \tan(\alpha)/\tan(\varphi_B)$. With the (E.2), the critical fluid pressure ratio $\lambda_{Bc}^{(H)}$ and friction

coefficient μ'_{Bc} of bulk materials yields

$$\begin{aligned} \lambda_{Bc}^{(H)} &= (1-\lambda_{hydro})\big[1-\tan(\alpha)/\tan(\varphi_B)\big]\cos^2(\alpha)+\lambda_{hydro}\,, \\ \mu'_{Bc} &= \tan(\varphi_B)(1-\lambda_{Bc}^{(H)})/(1-\lambda_{hydro})\,. \end{aligned} \tag{E.7}$$

Appendix F

Appendix for Chapter 5

1 Geometric relations

The hanging wall is above n segmented faults which lie in layers of the same thickness. This hanging wall is discretized into n rigid blocks by active axial surfaces, illustrated in Figure 5.3a. γ_i, θ_i are the dips of the segmented fault E_iE_{i+1} and the active axial surface E_iF_i, respectively.

The detachment depth, point E_1 referenced to sea floor, is denoted as Z_D, Figure 5.2b. The depth of point E_i, Z_i referenced to the sea floor (Figure F.1a), is

$$Z_i = \frac{(n+1-i)Z_D}{n}\,, \quad i = 1, \cdots, n+1\,. \tag{F.1}$$

The size of the active axial surface E_iF_i can be calculated from the value of Z_i in (F.1) as

$$L_{E_iF_i} = \frac{Z_i \cos\alpha}{\sin(\theta_i + \alpha)}\,, \tag{F.2}$$

and the size of the segmented fault E_iE_{i+1} is

$$L_{E_iE_{i+1}} = \frac{Z_D \cos\alpha}{n \sin(\gamma_i - \alpha)}\,. \tag{F.3}$$

Assume the line of Z_{FRD} lies in the layer j (Figure 5.3a), an unknown integral value obtained from relation of $Z_{j+1} < Z_{FRD} \leq Z_j$. Segment E_iG_i is the section of active axial surface E_iF_i below Z_{FRD} (Figure F.1a), the size of this segment is

$$L_{E_iG_i} = \frac{(Z_i - Z_{FRD})\cos\alpha}{\sin(\theta_i + \alpha)}\,. \tag{F.4}$$

Segment E_jG_{j+1} is the normal fault in layer j below the line Z_{FRD}, Figure 5.3a, and this size is

$$L_{E_jG_{j+1}} = \frac{(Z_j - Z_{FRD})\cos\alpha}{\sin(\gamma_j - \alpha)}\,. \tag{F.5}$$

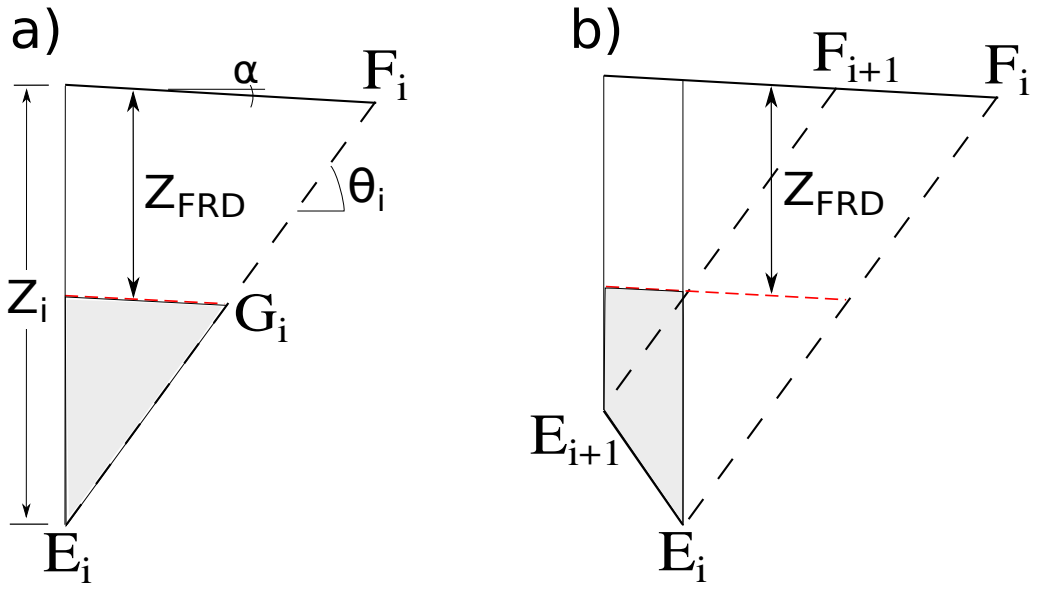


Fig. F.1: The power of fluid overpressure has two contributions: (a) above the partial active axial surface E_iG_i and (b) above the segmented fault E_iE_{i+1}. Shadow regions indicate the fluid overpressure zone used to calculate the power of fluid overpressure.

The size of the i^{th} block, $E_iF_iF_{i+1}E_{i+1}$, is

$$\Delta A_i = \frac{1}{2}Z_i^2 \cos\alpha\Big[\frac{\cos(\theta_i)}{\sin(\theta_i+\alpha)} + \frac{\cos(\gamma_i)}{\sin(\gamma_i-\alpha)}\Big] - \frac{1}{2}Z_{i+1}^2 \cos\alpha\Big[\frac{\cos(\theta_{i+1})}{\sin(\theta_{i+1}+\alpha)} + \frac{\cos(\gamma_i)}{\sin(\gamma_i-\alpha)}\Big], \tag{F.6}$$

and the size of the n^{th} block, $E_nF_nE_{n+1}$, is

$$\Delta A_n = \frac{1}{2}Z_n^2 \cos\alpha\Big[\frac{\cos(\theta_n)}{\sin(\theta_n+\alpha)} + \frac{\cos(\gamma_n)}{\sin(\gamma_n-\alpha)}\Big]. \tag{F.7}$$

The size of sliding block, ADE_1F_1, is

$$S_{SB} = S_{ADE_1E_1'} - \frac{1}{2}Z_D^2 \cos\alpha \frac{\cos(\theta_1)}{\sin(\theta_1+\alpha)}, \tag{F.8}$$

in which, $S_{ADE_1E_1'}$ is the surface size of ADE_1E_1' (a constant) above the detachment DE_1, Figure 5.3a.

2 Velocity relations and Limit Analysis

The velocity in the region $E_iF_iF_{i+1}E_{i+1}$ above the i^{th} segmented fault has a constant magnitude $\hat{U}_i$. The hodograph of velocity jump across the active axial surface E_iF_i, Figure 5.3c, provides

that information by application of the law of the sines

$$\frac{\hat{J}_i}{\sin(\gamma_i-\gamma_{i-1})}=\frac{\hat{U}_{i-1}}{\sin(\gamma_i+\theta_i-2\varphi_B)}=\frac{\hat{U}_i}{\sin(\gamma_{i-1}+\theta_i-2\varphi_B)}\,. \tag{F.9}$$

The region of sliding block slides on the detachment AE_1 at an uniform velocity of norm $\hat{\underline{U}}_{SB}$, a vector oriented by the angle φ_D from the detachment, Figure 5.3a. The relations of the velocities across E_1F_1 deduced from the hodograph in Figure 5.3d as

$$\frac{1}{\sin(\gamma_1+\theta_1-2\varphi_B)}=\frac{\hat{J}_1}{\sin(\gamma_1-\varphi_B-\beta+\varphi_D)}=\frac{\hat{U}_1}{\sin(\theta_1-\varphi_B+\beta-\varphi_D)}\,. \tag{F.10}$$

This hodograph of (F.9) and (F.10) are valid when the internal angles in sine's functions are positive. The construction of above velocity relations leads to the kinematically admissible and pertinent virtual velocities in the hanging wall and sliding block regions.

Combinng the geometric relations in (F.1-F.8) and the velocity hodographs in (F.9-F.10), the effective external power in (5.3) is expressed as

$$\begin{aligned}\mathcal{P}'_{\text{ext}}(\hat{\underline{U}})&=(\rho-\rho_f)g\Big[\sum_{i=1}^{n}\Delta A_i\,\hat{U}_i\sin(\gamma_i-\varphi_B)+S_{SB}\sin(\beta-\varphi_D)\Big]\\&+\Big[\sum_{i=1}^{j-1}(\Delta p_{E_i}+\Delta p_{E_{i+1}})L_{E_iE_{i+1}}\hat{U}_i+\Delta p_{E_j}L_{E_jG_{j+1}}\hat{U}_j+\sum_{i=1}^{j}\Delta p_{E_i}L_{E_iG_i}\hat{J}_i\Big]\sin(\varphi_B)/2\\&+(\Delta p_D+\Delta p_{E_1})L_{DE_1}\sin(\varphi_D)/2+Q\cos(\varphi_D)\,,\end{aligned} \tag{F.11}$$

in which, the first term on the right-hand side is the power of the gravity field on the velocity field composed of the number of blocks in hanging wall and sliding block regions. The next terms corresponds to the power of fluid overpressure along all the discontinuities composed of the segmented faults $(E_1E_2, E_2E_3, \cdots, E_{j-1}E_j, E_jG_{j+1})$, the active axial surfaces $(E_1G_1, E_2G_2, \cdots, E_jG_j)$ and the detachment DE_1. The last term $Q\cos(\varphi_D)$ is the power of the tectonic force at the back wall acting on its velocity of norm $\hat{U}_{SB}$, having set to one $(\hat{U}_{SB}=1)$.

The maximum resisting power in (5.5) for the proposed velocity field is

$$\mathcal{P}'_{\text{mr}}(\hat{\underline{U}})=\sum_{i=1}^{n}C_BL_{E_iE_{i+1}}\hat{U}_i\cos(\varphi_B)+\sum_{i=1}^{n}C_BL_{E_iF_i}\hat{J}_i\cos(\varphi_B)+C_DL_{DE_1}\cos(\varphi_D)\,, \tag{F.12}$$

in which, the terms on the right-hand side are the maximum resisting powers along the segmented fault E_iE_{i+1}, the active axial surface E_iF_i, and along the detachment fault DE_1, respectively.

Bibliography

Abe, S., H. Van Gent, and J. L. Urai (2011), Dem simulation of normal faults in cohesive materials, *Tectonophysics*, *512*(1), 12–21.

Adam, J., and C. D. Reuther (2000), Crustal dynamics and active fault mechanics during subduction erosion. application of frictional wedge analysis on to the north chilean forearc, *Tectonophysics*, *321*, 297–325.

Albertz, M., C. Beaumont, and S. J. Ings (2010), Geodynamic modeling of sedimentation-induced overpressure, gravitational spreading, and deformation of passive margin mobile shale basins, *AAPG Memoir*, pp. 29–62.

Anderson, E. M. (1951), *The Dynamics of Faulting, Etc.(Revised.)*., Edinburgh, London.

Anderson, R., M. Zoback, and G. Thompson (1983), Implications of selected subsurface data on the structural form and evolution of some basins in the northern Basin and Range province, Nevada and Utah, *Geological Society of America Bulletin*, *94*(9), 1055–1072.

Bilotti, F., and J. H. Shaw (2005), Deep-water niger delta fold and thrust belt modeled as a critical-taper wedge: The influence of elevated basal fluid pressure on structural styles, *AAPG Bulletin*, *89*(11), 1475–1491.

Bose, S., and S. Mitra (2009), Deformation along oblique and lateral ramps in listric normal faults: Insights from experimental models, *AAPG Bulletin*, *93*(4), 431–451.

Chen, W. (1975), *Limit analysis and soil plasticity*, Elsevier, Amsterdam.

Cobbold, P., and L. Castro (1999), Fluid pressure and effective stress in sandbox models, *Tectonophysics*, *301*(1-2), 1–19.

Cobbold, P., R. Mourgues, and K. Boyd (2004), Mechanism of thin-skinned detachment in the amazon fan: assessing the importance of fluid overpressure and hydrocarbon generation, *Marine and Petroleum Geology*, *21*(8), 1013 – 1025.

Cobbold, P. R., B. J. Clarke, and H. Loseth (2009), Structural consequences of fluid overpressure and seepage forces in the outer thrust belt of the Niger Delta, *Petroleum Geoscience*, *15*(1), 3–15.

Corredor, F., J. H. Shaw, and F. Bilotti (2005), Structural styles in the deep-water fold and thrust belts of the niger delta, *AAPG Bulletin*, *89*(6), 753–780.

Corredor, F., J. Shaw, and F. Bilotti (2005), Structural styles in the deep-water fold and thrust belts of the Niger Delta, *AAPG Bulletin*, *89*(6), 753–780.

Crans, W., and G. Mandl (1980), On the theory of growth faulting part i (a): genesis of the "unit", *Journal of Petroleum Geology*, *3*(2), 209–236.

Crans, W., G. Mandl, and J. Haremboure (1980), On the theory of growth faulting: a geomechanical delta model based on gravity sliding, *Journal of Petroleum Geology*, *2*(3), 265–307.

Crook, A., D. Owen, S. Willson, and J. Yu (2006), Benchmarks for the evolution of shear localisation with large relative sliding in frictional materials, *Computer methods in applied mechanics and engineering*, *195*(37), 4991–5010.

Cubas, N., Y. M. Leroy, and B. Maillot (2008), Prediction of thrusting sequences in accretionary wedges, *Journal of Geophysical Research*, *113*(B12), 1–21.

Cubas, N., C. Barnes, and B. Maillot (2013a), Inverse method applied to a sand wedge: estimation of friction parameters and uncertainty analysis, *Journal of Structural Geology*, *55*, 101–113.

Cubas, N., J.-P. Avouac, Y. Leroy, and A. Pons (2013b), Low friction along the high slip patch of the 2011 mw 9.0 tohoku-oki earthquake required from the wedge structure and extensional splay faults, *Geophysical Research Letters*, *40*, doi:10.1002/grl.50682.

Cubas, N., J.-P. Avouac, P. Souloumiac, and Y. Leroy (2013c), Megathrust friction determined from mechanical analysis of the forearc in the maule earthquake area, *Earth and Planetary Science Letters*, *381*, 92–103.

Dahl, N. (1987), Eksperimentelle ekstensjonsbrudd i sand som følge av verticale basement-bevegelser, Master's thesis, University of Aarhus, Aarhus, Denmark.

Dahlen, F. (1990), Critical taper model of fold-and-thrust belts and accretionary wedges, *Annual Review of Earth and Planetary Sciences*, *18*, 55.

Dahlen, F. A. (1984), Noncohesive critical Coulomb wedges: an exact solution, *Journal of Geophysical Research*, *89*(B12), 10,125–10,133.

Damuth, J. E. (1994), Neogene gravity tectonics and depositional processes on the deep niger delta continental margin, *Marine and Petroleum Geology*, *11*(3), 320–346.

Davis, D., J. Suppe, and F. A. Dahlen (1983), Mechanics of fold-and-thrust belts and accretionary wedges, *Journal of Geophysical Research*, *88*(B2), 1153–1172.

Davis, R. O., and A. P. S. Selvadurai (2005), *Plasticity and Geomechanics*, Cambridge University Press.

Deemer, S., J. Hall, K. Solvason, K. H. Lau, K. Louden, S. Srivastava, and J.-C. Sibuet (2009), Structure and development of the southeast newfoundland continental passive margin: derived from screech transect 3, *Geophysical Journal International*, *178*(2), 1004–1020.

Delouis, B., H. Philip, L. Dorbath, and A. Cisternas (1998), Recent crustal deformation in the antofagasta region (northern chile) and the subduction process, *Geophysical Journal International*, *132*, 302–338.

Dula, W. (1991), Geometric models of listric normal faults and Rollover Folds, *AAPG Bulletin*, *75*(10), 1609–1625.

Egholm, D. L., M. Sandiford, O. R. Clausen, and S. B. Nielsen (2007), A new strategy for discrete element numerical models: 2. sandbox applications, *Journal of Geophysical Research*, *112*(B05204), doi:10.1029/2006JB004558.

Enachescu, M. (1987), Tectonic and structural framework of the northeast newfoundland continental margin, *12*, 117–146.

Enachescu, M. E. (1988), Extended basement beneath the intracratonic rifted basins of the grand banks of newfoundland, *Canadian Journal of Exploration Geophysics*, *24*(1), 48–65.

Enachescu, M. E. (1992), Enigmatic basins offshore newfoundland, *Canadian Journal of Exploration Geophysics*, *28*(1), 44–61.

Erickson, S. G., L. M. Strayer, and J. Suppe (2001), Mechanics of extension and inversion in the hanging walls of listric normal faults (paper 2001jb000245), *Journal of Geophysical Research*, *106*(11), 26–655.

Exadaktylos, G., I. Vardoulakis, M. Stavropoulou, and P. Tsombos (2003), Analogue and numerical modeling of normal fault patterns produced due to slip along a detachment zone, *Tectonophysics*, *376*(1-2), 117–134.

Finch, E., S. Hardy, and R. Gawthorpe (2004), Discrete-element modelling of extensional fault-propagation folding above rigid basement fault blocks, *Basin Research*, *16*(4), 489–506.

Galland, O., P. Cobbold, E. Hallot, J. d'Ars, and G. Delavaud (2006), Use of vegetable oil and silica powder for scale modelling of magmatic intrusion in a deforming brittle crust, *Earth and Planetary Science Letters*, *243*(3-4), 786–804.

Ge, H., M. P. Jackson, and B. C. Vendeville (1997), Kinematics and dynamics of salt tectonics driven by progradation, *AAPG bulletin*, *81*(3), 398–423.

Gemmer, L., S. J. Ings, S. Medvedev, and C. Beaumont (2004), Salt tectonics driven by differential sediment loading: stability analysis and finite-element experiments, *Basin Research*, *16*(2), 199–218.

Gemmer, L., C. Beaumont, and S. J. Ings (2005), Dynamic modelling of passive margin salt tectonics: effects of water loading, sediment properties and sedimentation patterns, *Basin Research*, *17*(3), 383–402.

Goodwyne, O. K. (2012), Pressure prediction and underbalanced drilling in the deepwater niger delta, Ph.D. thesis, Durham University.

Grasemann, B., S. Martel, and C. Passchier (2005), Reverse and normal drag along a fault, *Journal of Structural Geology*, *27*(6), 999–1010.

Groshong, R. H. (1989), Half-graben structures: Balanced models of extensional fault-bend folds, *Geological Society of America Bulletin*, *101*(1), 96–105.

Hardy, S. (2013), Propagation of blind normal faults to the surface in basaltic sequences: Insights from 2d discrete element modelling, *Marine and Petroleum Geology*, *48*, 149–159.

Hillis, R. R. (2001), Coupled changes in pore pressure and stress in oil fields and sedimentary basins, *Petroleum Geoscience*, *7*(4), 419–425.

Hillis, R. R. (2003), Pore pressure/stress coupling and its implications for rock failure, *Geological Society, London, Special Publications*, *216*(1), 359–368.

Holland, M., H. van Gent, L. Bazalgette, N. Yassir, E. H. H. Strating, and J. L. Urai (2011), Evolution of dilatant fracture networks in a normal faultevidence from 4d model experiments, *Earth and Planetary Science Letters*, *304*(3), 399–406.

Holland, M., J. L. Urai, and S. Martel (2006), The internal structure of fault zones in basaltic sequences, *Earth and Planetary Science Letters*, *248*(1-2), 301–315.

Hooper, R., R. Fitzsimmon, N. Grant, and B. Vendeville (2002), The role of deformation in controlling depositional patterns in the south-central Niger Delta, West Africa, *Journal of Structural Geology*, *24*(4), 847–859.

Hubbert, M. K., and W. W. Rubey (1959), Role of fluid pressure in mechanics of overthrust faulting, i, mechanics of fluid-filled solids and its application to overthrust faulting, *Geological Society of America Bulletin*, *70*, 115–166.

Jackson, J., and D. McKenzie (1983), The geometrical evolution of normal fault systems, *Journal of Structural Geology*, *5*(5), 471–482.

Jackson, J., and N. White (1989), Normal faulting in the upper continental crust: observations from regions of active extension, *Journal of Structural Geology*, *11*(1-2), 15–36.

Kampfer, G., and Y. Leroy (2009), Imperfection and burial-depth sensitivity of the initiation and development of kink-folds in laminated rocks, *Journal of the Mechanics and Physics of Solids*, *57*, 1314–1339.

Kampfer, G., and Y. M. Leroy (2012), The competition between folding and faulting in the upper crust based on the maximum strength theorem, *Proceedings of the Royal Society A: Mathematical, Physical and Engineering Sciences*, *468*(2141), 1280–1303.

Keen, C., R. Boutilier, B. De Voogd, B. Mudford, and M. Enachescu (1987), Crustal geometry and extensional models for the grand banks, eastern canada: constraints from deep seismic reflection data, *12*, 101–115.

Kettermann, M., and J. L. Urai (2015), Changes in structural style of normal faults due to failure mode transition: first results from excavated scale models, *Journal of Structural Geology*, *74*, 105–116.

King, R. C., M. R. Tingay, R. R. Hillis, C. K. Morley, and J. Clark (2010), Present-day stress orientations and tectonic provinces of the nw borneo collisional margin, *Journal of Geophysical Research*, *115*(B10415), doi:{10.1029/2009JB006997}.

Kohli, A. H., and M. D. Zoback (2013), Frictional properties of shale reservoir rocks, *Journal of Geophysical Research-Solid Earth*, *118*(9), 5109–5125.

Kooi, H. (1997), Insufficiency of compaction disequilibrium as the sole cause of high pore fluid pressures in pre-cenozoic sediments, *Basin Research*, *9*(3), 227–241.

Kostenko, O., S. Naruk, W. Hack, M. Poupon, H. Meyer, M. Mora-Glukstad, C. Anowai, and M. Mordi (2008), Structural evaluation of column-height controls at a toe-thrust discovery, deep-water niger delta, *AAPG Bulletin*, *92*(12), 1615–1638.

Krueger, S. W., and N. T. Grant (2011), *The growth history of toe thrusts of the Niger Delta and the role of pore pressure*, vol. 94, chap. Thrust fault-related folding, pp. 357–390, AAPG Memoir.

Kvalstad, T. J., L. Andresen, C. F. Forsberg, K. Berg, P. Bryn, and M. Wangen (2005), The Storegga slide: evaluation of triggering sources and slide mechanics, *Marine and Petroleum Geology*, *22*(1-2), 245–256.

Lacoste, A., B. C. Vendeville, R. Mourgues, L. Loncke, and M. Lebacq (2012), Gravitational instabilities triggered by fluid overpressure and downslope incision - insights from analytical and analogue modelling, *Journal of Structural Geology*, *42*, 151 – 162.

Lallemand, S., P. Schnurle, and J. Malavieille (1994), Coulomb theory applied to accretionary and nonaccretionary wedges: Possible causes for tectonic erosion and/or frontal accretion, *Journal of Geophysical Research*, *99*, 12,033–12,055.

Leduc, A. M., R. J. Davies, A. L. Densmore, and J. Imber (2012), The lateral strike-slip domain in gravitational detachment delta systems: A case study of the northwestern margin of the Niger Delta, *AAPG Bulletin*, *96*(4), 709–728.

Lehner, F. K. (1986), Noncohesive critical Coulomb wedges: an exact solution - Comments, *Journal of Geophysical Research*, *91*(B1), 793–796.

Maillot, B. (2013), A sedimentation device to produce uniform sand packs, *Tectonophysics*, *593*, 85–94.

Maillot, B., and Y. M. Leroy (2006), Kink-fold onset and development based on the maximum strength theorem, *Journal of the Mechanics and Physics of Solids*, *54*(10), 2030–2059.

Maloney, D., R. Davies, J. Imber, S. Higgins, and S. King (2010), New insights into deformation mechanisms in the gravitationally driven Niger Delta deep-water fold and thrust belt, *AAPG Bulletin*, *94*(9), 1401–1424.

Mandl, G., and W. Crans (1981), Gravitational gliding in deltas, *In: McClay, K.R., Price, N.J. (Eds.) Thrust and Nappe Tectonics Geological Society of London Special Publication*, *9*, 41–54.

Martel, S. (2004), Mechanics of landslide initiation as a shear fracture phenomenon, *Marine Geology*, *203*(3), 319–339.

Mary, B., B. Maillot, and Y. M. Leroy (2013a), Deterministic chaos in frictional wedges revealed by convergence analysis, *International Journal for Numerical and Analytical Methods in Geomechanics*, doi:10.1002/nag.2177.

Mary, B., B. Maillot, and Y. M. Leroy (2013b), Predicting orogenic wedge styles as a function of analogue erosion law and material softening, *Geochemistry, Geophysics, Geosystems*, *14*, doi:10.1002/ggge.20262.

Mary, B. C. L. (2012), Mécanique du prisme d'accrétion par l'approche cinématique de l'analyse limite et contributions expérimentales, Doctoral thesis, Université de Cergy-Pontoise, France.

McClay, K., T. Dooley, and G. Lewis (1998), Analog modeling of progradational delta systems, *Geology*, *26*(9), 771–774.

McDermott, K., P. Belligham, J. Pindell, R. Graham, and B. Horn (2014), Some insights into rifted margin development and the structure of the continentocean tran-sition using a global deep seismic reflection database, 4th Atlantic Conjugate Margins Conference.

Michalowski, R. (1995), Slope stability analysis: a kinematical approach, *Géotechnique*, *45*(2), 283–293.

Morgan, R. (2006), The niger delta: an active passive margin, *GEO ExPro*, *4*(5), 36.

Morley, C. (2003), Mobile shale related deformation in large deltas developed on passive and active margins, *Geological Society, London, Special Publications*, *216*(1), 335–357.

Morley, C., R. King, R. Hillis, M. Tingay, and G. Backe (2011), Deepwater fold and thrust belt classification, tectonics, structure and hydrocarbon prospectivity: a review, *Earth-Science Reviews*, *104*(1), 41–91.

Morley, C. K., M. Tingay, R. Hillis, and R. King (2008), Relationship between structural style, overpressures, and modern stress, baram delta province, northwest borneo, *Journal of Geophysical Research*, *113*(B09410), doi:{10.1029/2007JB005324}.

Mourgues, R., and P. Cobbold (2003), Some tectonic consequences of fluid overpressures and seepage forces as demonstrated by sandbox modelling, *Tectonophysics*, *376*, 75–97.

Mourgues, R., and P. Cobbold (2006a), Thrust wedges and fluid overpressures: Sandbox models involving pore fluids, *Journal of Geophysical Research - Solid Earth*, *111*(B5), doi:{10.1029/2004JB003441}.

Mourgues, R., and P. R. Cobbold (2006b), Sandbox experiments on gravitational spreading and gliding in the presence of fluid overpressures, *Journal of Structural Geology*, *28*(5), 887–901.

Mourgues, R., E. Lecomte, B. Vendeville, and S. Raillard (2009), An experimental investigation of gravity-driven shale tectonics in progradational delta, *Tectonophysics*, *474*(3-4), 643–656.

Mourgues, R., A. Lacoste, and C. Garibaldi (2014), The Coulomb critical taper theory applied to gravitational instabilities, *Journal of Geophysical Research - Solid Earth*, *119*(1), 754–765.

Nirrengarten, M., G. Manatschal, X. P. Yuan, N. J. Kusznir, and B. Maillot (2016), Application of the critical coulomb wedge theory to hyper-extended, magma-poor rifted margins, *Earth and Planetary Science Letters*, doi:10.1016/j.epsl.2016.03.004.

Nollet, S., G. J. K. Vennekate, S. Giese, P. Vrolijk, J. L. Urai, and M. Ziegler (2012), Localization patterns in sandbox-scale numerical experiments above a normal fault in basement, *Journal of Structural Geology*, *39*, 199–209.

OptumG2 (2014), Optum computational engineering, www.optumce.com.

Ortiz, M., Y. Leroy, and A. Needleman (1987), A finite element method for localized failure analysis, *Computer Methods in Applied Mechanics and Engineering*, *61*(2), 189 – 214.

Panien, M., G. Schreurs, and A. Pfiffner (2006), Mechanical behaviour of granular materials used in analogue modelling: insights from grain characterisation, ring-shear tests and analogue experiments, *Journal of Structural Geology*, *28*(9), 1710 – 1724, doi:10.1016/j.jsg.2006.05.004.

Pashin, J., and R. Groshong (1998), Structural control of coalbed methane production in Alabama, *International Journal of Coal Geology*, *38*(1-2), 89–113.

Patton, T. L. (2005), Sandbox models of downward-steepening normal faults, *AAPG Bulletin*, *89*(6), 781–797.

Paul, B. (1961), A modification of the coulomb-mohr theory of fracture, *Journal of Applied Mechanics*, *28*(2), 259–268.

Pons, A., and Y. M. Leroy (2012), Stability of accretionary wedges based on the maximum strength theorem for fluid-saturated porous media, *Journal of the Mechanics and Physics of Solids*, *60*, 643–664.

Pons, A., and R. Mourgues (2012), Deformation and stability of over-pressured wedges: Insight from sandbox models, *Journal of Geophysical Research*, *117*(B09404), doi:10.1029/2012JB009379.

Resor, P. G., and D. D. Pollard (2012), Reverse drag revisited: Why footwall deformation may be the key to inferring listric fault geometry, *Journal of Structural Geology*, *41*, 98–109.

Rigo, A., H. LyonCaen, R. Armijo, A. Deschamps, D. Hatzfeld, K. Makropoulos, P. Papadimitriou, and I. Kassaras (1996), A microseismic study in the western part of the Gulf of Corinth (Greece): Implications for large-scale normal faulting mechanisms, *Geophysical Journal International*, *126*(3), 663–688.

Roscoe, K., and J. Burland (1968), On the generalized stress-strain behaviour of wet clay.

Roscoe, K. H., A. Schofield, and C. Wroth (1958), On the yielding of soils, *Geotechnique*, *8*(1), 22–53.

Rouby, D., T. Nalpas, R. Jermannaud, C. Robin, F. Guillocheau, and S. Raillard (2011), Gravity driven deformation controlled by the migration of the delta front: The Plio-Pleistocene of the Eastern Niger Delta, *Tectonophysics*, *513*(1-4), 54–67.

Rowan, M. G., F. J. Peel, and B. C. Vendeville (2004), Gravity-driven fold belts on passive margins, *AAPG Memoir*, pp. 157–182.

Russell, L., and S. Snelson (1994), Structure and tectonics of the albuquerque basin segment of the rio grande rift: Insights from reflection seismic data, *Geological Society of America Special Papers*, *291*, 83–112.

Saffer, D. (2003), Pore pressure development and progressive dewatering in underthrust sediments at the Costa Rican subduction margin: Comparison with northern Barbados and Nankai, *Journal of Geophysical Research*, *108*(B5), 1–16.

Salençon, J. (1974), *Théorie de la plasticité pour les applications à la mécanique des sols*, Eyrolles, Paris.

Salençon, J. (2002), *De l'élasto-plasticité au calcul à la rupture*, École Polytechnique, Palaiseau, and Ellipses, Paris.

Salisbury, M., and C. Keen (1993), Listric faults imaged in oceanic crust, *Geology*, *21*(2), 117–120.

Sallarès, V., and C. R. Ranero (2005), Structure and tectonics of the erosional convergent margin off antofagasta, north chile (23°30's), *Journal of Geophysical Research*, *110*(B06101), doi:10.1029/2004JB003418.

Sapin, F., M. Pubellier, J.-C. Ringenbach, and T. Rives (2009), The brunei fold-and-thrust belt: Tectonically-or gravity-driven?, *AAPG Hedberg October*.

Schöpfer, M. P. J., C. Childs, and J. J. Walsh (2007), Two-dimensional distinct element modeling of the structure and growth of normal faults in multilayer sequences: 1. Model calibra-

tion, boundary conditions, and selected results, *Journal of Geophysical Research-Solid Earth*, *112*(B10), doi:{10.1029/2006JB004902}.

Shaw, J. H., E. Novoa, and C. D. Connors (2004), Structural controls on growth stratigraphy in contractional fault-related folds.

Silva, S., R. Maciel, and M. Severino (1998), Cenozoic tectonics of amazon mouth basin, *Geo-Marine Letters*, *18*(3), 256–262.

Sinclair, I. K. (1995), Transpressional inversion due to episodic rotation of extensional stresses in jeanne d'arc basin, offshore newfoundland, *Geological Society, London, Special Publications*, *88*, 249–271.

Sorel, D. (2000), A pleistocene and still-active detachment fault and the origin of the corinth-patras rift, greece, *Geology*, *28*(1), 83–86.

Souloumiac, P., Y. M. Leroy, K. Krabbenhøft, and B. Maillot (2009), Predicting stress in fault-bend fold by optimization, *Journal of Geophysical Research*, *114*, B09,404.

Souloumiac, P., B. Maillot, and Y. M. Leroy (2012), Bias due to side wall friction in sand box experiments, *Journal of Structural Geology*, *35*, 90–101.

Suppe, J. (1983), Geometry and kinematics of fault-bend folding, *American Journal of Science*, *283*, 684–721.

Suppe, J. (2007), Absolute fault and crustal strength from wedge tapers, *Geology*, *35*(12), 1127–1130, doi:10.1130/G24053A.1.

Suppe, J. (2014), Fluid overpressures and strength of the sedimentary upper crust, *Journal of Structural Geology*, *69, Part B*, 481 – 492.

Tankard, A., H. Welsink, and W. Jenkins (1989), Structural styles and stratigraphy of the jeanne d'arc basin, grand banks of newfoundland, *Extensional tectonics and stratigraphy of the North Atlantic margins: AAPG Memoir*, *46*, 265–282.

Terzaghi, K., K. Terzaghi, C. Engineer, A. Czechoslowakia, K. Terzaghi, I. Civil, A. Tchécoslovaquie, and E. Unis (1951), *Mechanism of landslides*, Harvard University, Department of Engineering.

Tingay, M. R., R. R. Hillis, R. E. Swarbrick, C. K. Morley, and A. R. Damit (2009), Origin of overpressure and pore-pressure prediction in the baram province, brunei, *AAPG Bulletin*, *93*(1), 51–74.

Trautmann, C. H., F. Kulhawy, and T. D. O'Rourke (1985), Sand density measurements for laboratory studies, *Geotechnical Testing Journal*, *8*(4), 159–165.

Trudgill, B. D., M. G. Rowan, J. C. Fiduk, P. Weimer, P. E. Gale, B. E. Korn, R. L. Phair, W. T. Gafford, G. R. Roberts, and S. W. Dobbs (1999), The perdido fold belt, northwestern deep gulf of mexico, part 1: Structural geometry, evolution and regional implications1, *AAPG bulletin*, *83*(1), 88–113.

Utili, S., and G. B. Crosta (2011), Modeling the evolution of natural cliffs subject to weathering: 1. limit analysis approach, *Journal of Geophysical Research*, *116*, doi:{10.1029/2009JF001557}.

van Gent, H. W., M. Holland, J. L. Urai, and R. Loosveld (2010), Evolution of fault zones in carbonates with mechanical stratigraphy - Insights from scale models using layered cohesive powder, *Journal of Structural Geology*, *32*(9, SI), 1375–1391.

Van Wees, J. D., S. Cloetingh, and G. De Vicente (1996), The role of pre-existing faults in basin evolution: constraints from 2d finite element and 3d flexure models, *Geological Society, London, Special Publications*, *99*(1), 297–320.

Vendeville, B. C. (2005), Salt tectonics driven by sediment progradation: Part imechanics and kinematics, *AAPG bulletin*, *89*(8), 1071–1079.

Vogler, H., and B. Robison (1987), Exploration for deep geopressured gas: Corsair trend, offshore texas, *AAPG Bulletin*, *71*(7), 777–787.

von Huene, R., and C. R. Ranero (2003), Subduction erosion and basal friction along the sediment-starved convergent margin off antofagasta, chile, *Journal of Geophysical Research*, *108*(B2), doi:10.1029/2001JB001569.

Wang, K., J. He, and Y. Hu (2006), A note on pore fluid pressure ratios in the coulomb wedge theory, *Geophysical Research Letters*, *33*(L19310), doi:10.1029/2006GL027233.

Weber, K., and E. Daukoru (1975), Petroleum geology of the niger delta, in *9th World petroleum congress proceedings*, vol. 2, pp. 209–221.

Wernicke, B. (1995), Low-angle normal faults and seismicity: A review, *Journal of Geophysical Research*, *100*(B10), 20,159–20,174.

Withjack, M., and S. Callaway (2000), Active normal faulting beneath a salt layer: An experimental study of deformation patterns in the cover sequence, *AAPG Bulletin*, *84*(5), 627–651.

Withjack, M., and E. Peterson (1993), Prediction of normal-fault geometries - A sensitivity analysis, *AAPG Bulletin*, *77*(11), 1860–1873.

Withjack, M. O., and R. W. Schlische (2005), A review of tectonic events on the passive margin of eastern north america, in *Petroleum Systems of Divergent Continental Margin Basins: 25th Bob S. Perkins Research Conference, Gulf Coast Section of SEPM*, pp. 203–235, SEPM.

Withjack, M. O., and R. W. Schlische (2006), Geometric and experimental models of extensional fault-bend folds, *Geological Society, London, Special Publications*, *253*(1), 285–305.

Withjack, M. O., Q. T. Islam, and P. R. Lapointe (1995), Normal faults and their hanging-wall deformation - an experimental study, *AAPG Bulletin*, *79*(1), 1–18.

Wu, S., and A. W. Bally (2000), *Slope Tectonics-Comparisons and Contrasts of Structural Styles of Salt and Shale Tectonics of the Northern Gulf of Mexico with Shale Tectonics of Offshore Nigeria in Gulf of Guinea*, pp. 151–172, American Geophysical Union, doi:10.1029/GM115p0151.

Xiao, H.-B., and J. Suppe (1989), Role of compaction in listric shape of growth normal faults, *AAPG Bulletin*, *73*(6), 777–786.

Xiao, H.-B., and J. Suppe (1992), Orgin of rollover, *AAPG Bulletin*, *76*(4), 509–529.

Xiao, H.-B., F. A. Dahlen, and J. Suppe (1991), Mechanics of extensional wedges, *Journal of Geophysical Research*, *96*(B6), 301–318.

Yuan, X. P., Y. M. Leroy, and B. Maillot (2015), Tectonic and gravity extensional collapses in overpressured cohesive and frictional wedges, *Journal of Geophysical Research - Solid Earth*, *120*, doi:10.1002/2014JB011612.

Yue, L.-F., and J. Suppe (2014), Regional pore-fluid pressures in the active western taiwan thrust belt: A test of the classic hubbert–rubey fault-weakening hypothesis, *Journal of Structural Geology*, *69*, 493–518.

Zhang, X., K. Krabbenhoft, D. M. Pedroso, A. V. Lyamin, D. Sheng, M. V. da Silva, and D. Wang (2013), Particle finite element analysis of large deformation and granular flow problems, *Computers and Geotechnics*, *54*, 133–142.

Zhao, W. L., D. M. Davis, F. A. Dahlen, and J. Suppe (1986), Origin of convex accretionary wedges: Evidence from barbados, *Journal of Geophysical Research*, *91*(B10), 10,246–10,258.

Résumé

Dans ce manuscrit nous développons l'approche cinématique 2D du calcul à la rupture pour examiner les effondrements en extension (ou failles normales) de la croûte supérieure cassante qui résultent de surpressions de fluides. Les sujets d'intérêt liés à la déformation en extension sont (1) les roles de la pression des fluides, des processus de surface, et des propriétés des matériaux et des failles sur la stabilité des structures d'extension; (2) la formation de failles normales à faible pendage et de failles listriques; (3) la distribution de la déformation au dessus d'un glissement à faible pendage; et (4) l'influence de l'adoucissement mécanique des failles et des processus de sédimentation sur cette distribution.

Cette approche mécanique est vérifiée par la théorie du prisme critique de Coulomb, et la généralise pour étudier la topographie complexe de la péninsule de Mejillones dans le Nord du Chili. Cette approche est aussi appliquée à l'instabilité gravitaire dans le delta du Niger en reliant les structures compressives en bas de pente aux structure extensives en amont par un détachement profond. Nous prédisons des surpressions de fluides beaucoup plus élevée que celles obtenues par application du prisme de Coulomb. Enfin, cette méthodologie est appliquée à l'étude de la forme de failles normales reliant un détachement profond à la surface. Dans le cas du delta du Niger, nous montrons que les failles à faible pendage et les failles listriques impliquent que la profondeur de rétention des fluides est faible. La version séquentielle de l'analyse limite ouvre de nouvelles voies pour suivre l'évolution structurale dans le temps du jeu sur les failles normales. Les simulations montrent en particulier qu'une faille normale tourne vers des pendage plus faibles au fur et à mesure de la dénudation du mur, formant une région qui passe du mur au toit de la faille active en rotation. La prédiction de cette région est illustrée par des expériences analogiques et des exemples de terrain.

Mots Clés

surpression de fluide, théorie du prisme critique, calcul à la rupture, extension tectonique, modélisation analogique, instabilité gravitaire

Abstract

This manuscript develops a 2D kinematic approach of Limit Analysis to examine the extensional failures in the brittle, upper crust resulting from fluid overpressures and normal faulting. There are many interesting topics related to the extensional deformation such as (1) the roles of fluid pressure, topographic processes, material and fault properties on the stability of extensional structures; (2) the formation of low-angle and listric normal fault; (3) the deformation pattern due to slip on a low-angle fault; and (4) the influence of fault softening and sedimentation processes on this deformation pattern.

This mechanical approach applied to a wedge-shape prototype is validated by the critical Coulomb wedge (CCW) theory, and it generalizes the CCW theory to investigate the complex topography on the Mejillones peninsula, Northern Chile. Additionally, this approach is also applied to investigate gravity instability of Niger Delta by linking down-slope compressional to up-slope extensional failures through a deep detachment. We predict much higher fluid overpressures than that of the CCW theory. Finally, this Limit Analysis methodology is applied to investigate the shape of normal fault linking a low detachment to the surface. The application to Niger Delta implies that the formation of very low-angle and strongly listric faults results from a shallow fluid-retention depth. The sequential version of Limit Analysis opens new ways to envision the structural evolution through time resulting from normal faulting. The simulations show in particular that the normal fault rotates during extension, forming a region of Foot-to-Hanging Wall (FHW) where the material in the footwall is sheared upon entering the hanging wall. The creation of the FHW region is illustrated by sandbox experiments and field examples.

Keywords

fluid pressure, critical Coulomb wedge theory, limit analysis, extensional tectonics, analogue modeling, gravity instability